A NEW CONFIGURATION FOR A LIQUID HELIUM TEMPERATURE CRYOCOOLER

by

JAMES ALAN CRUNKLETON

B.M.E., Georgia Institute of Technology

1981

S.M.M.E., Massachusetts Institute of Technology

1984

Submitted to the Department of Mechanical Engineering in Partial Fulfillment of the Requirements for the Degree of

DOCTOR OF PHILOSOPHY

at the

MASSACHUSETTS INSTITUTE OF TECHNOLOGY

September 1987

© Massachusetts Institute of Technology 1987

Signature of Author Signature redacted

Department of Mechanical Engineering
July 15, 1987

Certified by Signature redacted

Joseph L. Smith, Jr.
Thesis Supervisor

Signature redacted

Accepted by

Ain A. Sonin
Chairman, Departmental Committee on Graduate Students

MASS. INST. TECH.
JUL 2 '87
LIBRARIES

Archives

For my Dad,

Buren L. Crunkleton

A NEW CONFIGURATION FOR A LIQUID HELIUM TEMPERATURE CRYOCOOLER

by

JAMES ALAN CRUNKLETON

Submitted to the Department of Mechanical Engineering
on July 15, 1987 in partial fulfillment of the
requirements for the Doctor of Philosophy

ABSTRACT

The primary efforts over the last several years in miniature liquid helium temperature refrigerator development have focused on the modification of two-stage totally regenerative cycle cryocoolers by adding a Joule-Thomson loop. Such efforts have focused on increased reliability without regard to thermodynamic efficiency. This project is intended to identify a cycle configuration along with physical components that comprise a thermodynamically efficient cryocooler that is compact and easy to fabricate. Analytical work began with a computerized optimization study of a modified Collins cycle which includes variations in performance characteristics using different physical components. The computer study identified a multi-staged cryocooler design that incorporates the integration of a heat exchanger and expansion engine in a concentric tube configuration.

The basic configuration for a single stage is a long displacer in a close-fitting, thin-walled cylinder. The displacer-to-cylinder gap is the high-pressure passage of the heat exchanger, and the low-pressure passage is formed by a thin tube over the OD of the cylinder. The inlet valve is at room temperature and the exhaust valve operates at the refrigeration temperature. The mass flow and pressure in the displacer-to-cylinder gap are periodic, while the low-pressure return flow is nearly constant in order to increase counterflow heat exchange efficiency. A heat exchanger design algorithm has been developed which accounts for the periodic mass flow rate in the displacer-to-cylinder gap, relative motion between the displacer and cylinder, and counterflow heat exchange.

A single-stage prototype has been built and tested. With no applied heat load at the cold end, the cryocooler operates at 34 K without precooling and at 19.5 K with liquid nitrogen precooling. Performance parameters, such as adiabatic engine efficiency and heat exchange temperature difference, were defined and calculated for the integral expander and exchanger. The salient loss mechanism was a result of counterflow heat exchange. This counterflow heat exchange loss was larger than expected because of non-periodic displacer motion, which resulted from slow time response of the hydraulic drive mechanism to pressure changes in the expander working volume.

Thesis Supervisor: Dr. Joseph L. Smith, Jr.

Title: Professor of Mechanical Engineering

ACKNOWLEDGEMENTS

I would like to thank Professors Joseph L. Smith and Ernesto E. Blanco for their support and enthusiasm throughout this work. I particularly wish to acknowledge Prof. Smith, who has been an inspiring teacher and friend.

Hugh Ekberg was instrumental during the experimental phase of the project. His dedication and enthusiasm were a constant source of inspiration that always kept spirits high in "that cold, dark, dirty lab." Hugh assembled the compression system and the hydraulic drive mechanism. He also assisted in countless other smaller jobs whenever needed. For example, Hugh machined the Rulon end piece for the displacer, which, according to Hugh, was a primary reason for the better-than-expected cryocooler performance.

I also want to thank two other students, Chin-Min Wang and Mike Turek, for taking time to help out with the experiment. Chin-Min helped during the early stages with design of the expansion valve and with the hydraulic tube forming experiment. Mike worked on the electronic control unit.

Jay and George Smith of Smith Bros. Machine Shop went out of their way to make sure the cryocooler parts were delivered on time to keep the project on schedule. Jay delivered valve parts about 10 pm one Friday night so that they could be assembled over the weekend.

My girlfriend, Bedana, was a source of endless support throughout the final year of work, particularly near the end. Thanks for all your love and patience, B, especially on those (rare?) occasions when I was "out of control."

I especially want to acknowledge the support of my family throughout this work: my dad, Buren; my mom, Edna; and my "little" sister, Sherri. Although there was time for few visits home, family bonds seem to have strengthened over the past couple of years. Phone calls at the end of the day, flowers on Valentine's day, and a few "care packages" were very motivating during those last few months of the project.

Table of Contents

Abstract . . . 3
Acknowledgements . . . 4
Table of Contents . . . 5
List of Figures . . . 8
List of Tables . . . 12
List of Symbols . . . 13
Chapter 1 Introduction . . . 16
1.1 Cryocooler Considerations . . . 16
1.2 Cryogenic Refrigeration at the MIT Cryogenic Eng. Lab. . . . 17
1.3 Current Investigation . . . 21
Chapter 2 Component Analysis For an SVC Cycle Cryocooler . . . 23
2.1 Introduction . . . 23
2.2 The SVC Cycle with Physical Components . . . 24
2.2.1 Selection of the SVC Cycle . . . 25
2.2.2 SVC Cycle Physical Configuration . . . 26
2.3 Description of the Computer Programs . . . 29
2.4 Results of the Computer Analysis . . . 32
2.4.1 Effects of Parameter Variation on SVC Cycle Performance . . . 32
2.4.2 Cycle Performance Evaluation Using Entropy Generation . . . 34
2.5 Implications for Additional Cryocooler Miniaturization . . . 49
2.6 The Integral Heat Exchanger and Expansion Engine . . . 53
2.7 Implications for Multi-Staged Cryocooler Design . . . 56
Chapter 3 Performance Algorithm for an Integral Concentric Tube Heat Exchanger and Expansion Engine . . . 61
3.1 Description of the Model . . . 62
3.2 Average Enthalpy Flow Rate at a Cross Section . . . 70
3.2.1 Simplifying Assumptions . . . 71
3.2.2 Method of Solution . . . 72
3.3 The Performance Algorithm . . . 77
3.4 Results from the Performance Algorithm . . . 79
3.4.1 Results for a Single-Stage Cryocooler of 50 cm Length . . . 79

3.4.2 Results for a Single-Stage Cryocooler of 12 cm Length 90
Chapter 4 Single-Stage Cryocooler Experiment 92
4.1 The Integral Heat Exchanger and Expander Unit 94
4.1.1 Design of the Integral Unit 94
4.1.2 Hydroforming of the Concentric Tubes 101
4.1.3 Fabrication of the Spiral Spacer 106
4.2 Inlet and Exhaust Valves 113
4.3 Hydraulic Drive Mechanism 117
4.4 Electronic Control System 119
4.5 Experimental Results 124
4.5.1 Measured Heat Leaks 127
4.5.2 Cryocooler Performance 129
4.5.3 Cryocooler Performance with Precooling 141
4.5.4 Calculations of Experimental Efficiencies 151
4.6 Discussion of Results 164
4.6.1 Problems with the Cryocooler 164
4.6.2 Discussion of Cryocooler Performance 165
4.6.3 A Discussion of Heat Exchange Performance 169
Chapter 5 Conclusions and Recommendations 174
5.1 Summary of Analytical Results 174
5.2 Summary of Experimental Results 175
5.3 Recommendations 176
Appendix A Computer Program Descriptions with Results for the System Analysis 178
A.1 Computer Program Descriptions for the System Analysis 178
A.1.1 Program SYSITER 182
A.1.2 Subprogram SYSLEAK 190
A.2 Results from the Computer Analysis 198
Appendix B Detailed Development of the Performance Algorithm 224
B.1 The Average Enthalpy Flow Rate at a Cross Section 224
B.1.1 Simplifying Assumptions 225
B.1.2 Net Enthalpy Flow Through a Plane 226

B.1.3 Derivation of the Energy Equations 229
B.1.4 Substitution of Energy Equations into Enthalpy Flux Equation . . 238
B.2 Performance Algorithm with Computer Code 241
Appendix C Details of the Single-Stage Cryocooler Experiment 256
C.1 Instrumentation and Data Acquisition 256
C.1.1 Pressure Instrumentation 256
C.1.2 Temperature Instrumentation 259
C.1.3 Mass Flow Rate Measurement 261
C.2 Compression System 262
References 265
Biographical Note 269

LIST OF FIGURES

1.1 The Collins cycle using two dry expansion engines 18

1.2 The SVC cycle using two dry expansion engines 20

2.1 SVC cycle configuration used for the cycle analysis 27

2.2 Entropy generation versus engine speed 39

2.3 Total mass flow rate versus engine speed 40

2.4 Total entropy generation versus heat exchange temperature ratio 42

2.5 Total entropy generation versus total heat exchanger length 44

2.6 Entropy generation in the gas versus engine speed 45

2.7 Entropy generation in the engines versus engine speed 47

2.8 Total mass flow rate versus refrigeration heat load 50

2.9 Heat exchange temperature ratio versus refrigeration heat load 51

2.10 Comparison of entropy generation in the gas and due to axial conduction versus heat load 52

2.11 Schematic of the flow circuit for the integral expander and exchanger 55

2.12 Variation of SVC cycle configuration with integral expander and exchanger . . 58

2.13 Independent heat exchanger and expansion engine configuration using conduction paths 59

3.1 Schematic of the flow circuit for the integral expander and exchanger 63

3.2 Coordinate system used to develop heat transfer equations for the average enthalpy flow equation 64

3.3 Control volume used for the performance algorithm 65

3.4 Average enthalpy flow rate at a cross section versus the ratio of high-pressure side gap width to cylinder diameter 81

3.5 Refrigeration heat load versus the ratio of high-pressure side gap width to cylinder diameter 83

3.6 First law balance for the control volume of Fig. (3.3) versus the ratio of high-pressure side gap width to cylinder diameter 84

3.7 Wall temperatures versus time for the case of $z_H = z_L = 2.5(10^{-5})$ mm 85

3.8 Wall temperatures versus time for the case of $z_H = z_L = 2.5(10^{-3})$ mm 87
3.9 Wall temperatures versus time for $z_H = 0.127$ mm and $z_L = 0.254$ mm 88
3.10 Refrigeration temperature versus load for $z_H = 0.127$ mm and $z_L = 0.254$ mm 89
4.1 Schematic of integral heat exchanger and expansion engine 93
4.2 Photograph of complete experiment 95
4.3 Photograph of cryocooler 95
4.4 Cross section of integral exchanger and expander 96
4.5 Dimensional specifications for the concentric tubes and spiral spacers
97
4.6 Definition of tube straightness, d 102
4.7 Schematic of outer shell forming apparatus 103
4.8 Photograph of tubes, mylar, and hydraulic pump 105
4.9 Photograph of tape applicator for spiral spacers 108
4.10 Photograph of cylinder with spiral spacer and end pieces 110
4.11 Photograph of outer shell with end pieces 110
4.12 Cross section of jig used to assemble cylinder and outer shell 111
4.13 Photograph of assembled cylinder and outer shell 112
4.14 Exhaust valve 114
4.15 Inlet valve 115
4.16 Photographs of inlet and exhaust valves 116
4.17 Schematic of hydraulic system with accompanying legend 118
4.18 a Schematic of electronic control circuit for hydraulic directional control valve 120
4.18 b Schematic of the electronic control circuit for the inlet and exhaust valve solenoids 121
4.18 c Relay circuit between electronic control unit and solenoids 122
4.19 Representative p-v plot used to define each part of cycle 125
4.20 Experimental set-up for static and displacer motion heat leaks 128
4.21 Refrigeration temperature versus mass flow rate at constant engine speed for the case of no heat load and no precooling 130

4.22 Temperature versus engine speed at constant mass flow rate for the case of no heat load and no precooling 131
4.23 Pressure versus volume for no heat load and no precooling 133
4.24 Displacer position versus time for no heat load and no precooling 134
4.25 Low-pressure mass flow rate at room temperature versus time for the case of no heat load and no precooling 135
4.26 Pressure drop over the low-pressure return passage versus time for no heat load and no precooling 136
4.27 Outer shell wall temperature versus position for the case of no heat load and no precooling 138
4.28 Refrigeration temperature versus heat load for no precooling 139
4.29 Pressure versus volume for 11 W load and no precool 140
4.30 Refrigeration temperature versus engine speed at constant mass flow rate for the case of LN_2 precool and no load 142
4.31 Refrigeration temperature versus mass flow rate at constant engine speed for LN_2 precooling and no heat load 143
4.32 Pressure versus volume with liquid nitrogen cooling and no heat load . . . 144
4.33 Low-pressure mass flow rate at room temperature versus time for liquid nitrogen cooling and no heat load 146
4.34 Pressure drop over the low-pressure return passage versus time for liquid nitrogen cooling and no heat load 147
4.35 Outer shell wall temperature versus position for the case of liquid nitrogen cooling and no heat load 148
4.36 Refrigeration temperature versus heat load with LN_2 cooling 149
4.37 Pressure versus volume with 6.25 W load and LN_2 cooling 150
4.38 Temperature versus time at the cold end for the case of no precooling and no load 168
4.39 Pressure versus volume with data points for no precooling and no load . . 170
A.1 Numbering system for SVC cycle 185
A.2 Mass flow rate versus $TE(2)$ 200

A.3 Mass flow rate versus wet expander efficiency 201
A.4 Mass flow rate versus vapor compressor efficiency 202
B.1 Control volumes for the heat transfer equations 227
B.2 Control volume used for the performance algorithm 243
C.1 Temperature sensor and heater locations with legend 257
C.2 Schematic of the compression system 263

LIST OF TABLES

2.1 Input parameters for SVC cycle analysis 35

2.2 Computer output specifications for a representative 1 W cryocooler 48

2.3 Computer output specifications for a representative 0.25 W cryocooler 54

3.1 Inputs and outputs to performance algorithm 69

3.2 Inputs to the performance algorithm for the 50 cm cryocooler 80

3.3 Inputs to the performance algorithm for the 12 cm cryocooler 91

4.1 Displacer, cylinder, and outer shell tube dimensions 106

4.2 Hydraulic pressures and yield stresses for the tube forming 106

4.3 Experimental and theoretical values for no precool and no load 152

4.4 Experimental and theoretical values for no precool and 11W load 153

4.5 Experimental and theoretical values for precool and no load 154

4.6 Experimental and theoretical values for precool and 6.25W load 155

A.1 Inputs and outputs to program SYSITER and subroutine SYSLEAK 179

A.2 Subprograms of program SYSITER 183

A.3 SVC cycle considered in Section A.2 198

B.1 Inputs and outputs to the performance algorithm 246

C.1 Pressure and mass flow rate calibration curves 256

C.2 Forward diode sensor voltage (in volts) at the specified temperature for a 10 μA current 261

LIST OF SYMBOLS

$\Delta T / T$: Heat exchange temperature ratio.

η_E: Expander adiabatic efficiency.

ϵ: Efficiency of blowdown.

γ: Amount of mass (g).

ω: Circular frequency (rad/s).

ρ: Density (g/cc).

ξ: Position of displacer.

$A_n to I_n$: Fourier series constants.

A_{cd}: Cross sectional area of the displacer.

c_m: Wall specific heat (J/g-K).

c_p: Gas specific heat (J/g-K).

C_F: Flow coefficient.

D: Diameter (mm).

h: Enthalpy flow rate (W).

L: Heat exchanger length (cm).

m: Mass flow rate (g/s).

M: Time-averaged mass flow rate (g/s).

P: Absolute pressure (atm).

q: Heat flow (W).

$q(1), q(2)$: Lumped heat leak before the dry expanders (W).

s: Engine stroke (mm).

S_{gen}: Entropy generation (W/K).

$TE(1), TE(2)$: Dry expansion engine inlet temperature (K).

t: Thickness (mm).

t: Time (s).

V: Volumetric ratio.

W: Work (W).

x: Axial coordinate for cylinder and shell.

y: Axial coordinate for displacer.

z: Heat exchange gap width (mm).

Subscripts

0: At $x = 0$.

A: Beginning of blowdown portion of exhaust stroke.

b: Of blowdown.

B: End of blowdown portion of exhaust stroke.

C: End of constant pressure exhaust.

c: Of the cylinder.

c: Cyclic.

C: Due to conduction.

C: Of the clearance volume.

d: Of the displacer.

D: Of the displacement volume.

e: Of exhaust.

E: Expander.

exh: Average for the exhaust portion of stroke.

h: Due to heat exchange.

H: On the high-pressure side.

ind: Indicated by measurements.

L: On the low-pressure side.

L: Due to the heat load.

m: Of the exchanger wall.

n: Order of Fourier series.

nc: Non-cyclic.

p: Of the displacer.

R: Of refrigeration.

RL: At the refrigeration temperature.

s: Of the outer shell.

VC: Of the vapor compressor.

WE: Of the wet expander.

W: Of the working volume.

Chapter 1
Introduction

Miniature liquid-helium-temperature cryocoolers that are efficient, compact, and reliable are not generally available. The primary efforts in liquid helium cryocooler development have been focused on the modification of two-stage, 10 K to 15 K units intended for cryopumping applications. The Stirling and Gifford-McMahon cycles have been modified by using a Joule-Thomson loop to reach 4.2 K. Such efforts have focused on reliability rather than thermodynamic efficiency.

A new configuration for a liquid helium temperature cryocooler has been developed and will be described in this thesis. The remainder of this introductory chapter will briefly describe the cryocoolers available in order to indicate a need for the present work. The scope of this project will then be outlined.

1.1 Cryocooler Considerations

A myriad of cycles and cycle combinations can be contrived that will provide liquid helium temperature refrigeration.[1,2,3,4] Large scale refrigeration and liquefaction is generally provided by a Collins or modified Collins cycle. Smaller scale refrigeration at 4.2 K is most popularly obtained using a regenerative cycle such as the Stirling or Gifford-McMahon in combination with a Joule-Thomson (J-T) loop.[5] A cascaded J-T refrigeration system has been investigated that uses helium, hydrogen, and nitrogen as the working fluids.[6] A more exotic system is the gas sorption J-T refrigerator developed for space applications.[7] Presently under development are small turbo-Brayton cycle cryocoolers.[8] To reach temperatures less than 1 K, magnetic refrigeration systems may be used.[9,10]

Practical considerations narrow this field of possible cryocooler configurations that may be feasible for liquid helium temperatures to only a few.[11,12,13,14] The Stirling/J-T and Gifford-McMahon/J-T combination cycles are the most common cryocoolers available. The totally regenerative cycles must, however, be combined with a J-T loop to reach temperatures below about 12 K, due to diminishing heat

capacity of regenerator materials. These cycle combinations require two warm compressors or the modification of a single compressor because efficient operating pressures and pressure ratios for the regenerative cycle and J-T loop are not compatible. The use of two separate cooling systems also results in a cumbersome manufacturing procedure.

Although the Collins cycle is much more thermodynamically efficient than the Stirling/J-T or Gifford-McMahon/J-T cycles,[14] the Collins cycle has not yet been modified for cryocooler use. One of the primary reasons is questionable reliability of the cold valves, in terms of mechanical integrity and vulnerability to gas contamination. Manufacture of heat exchangers has also been a major deterrent.

Regardless of the particular cycle chosen, scaling a large scale refrigeration system to cryocooler size introduces additional design considerations. First, the selection of a heat exchanger or regenerator configuration must take into consideration two loss mechanisms not significant in large scale systems: flow maldistribution[15] and axial conduction.[16,17] Also, since miniaturization of heat exchangers or regenerators results in very small flow passages, gas contamination[18–23] must be reduced to much lower levels than in larger systems.

1.2 Cryogenic Refrigeration at the MIT Cryogenic Engineering Laboratory

The MIT Cryogenic Engineering Laboratory has long been involved in helium-temperature refrigeration research. A majority of the emphasis has been placed on the continuing improvement of the Collins cycle refrigerator shown in Figure (1.1). Use of a wet expander to replace the J-T expansion valve was one of the first major cycle modifications intended to improve cycle efficiency. Other analytical studies and extensive experiments include work with the Stirling cycle,[24,25] thermal regenerators,[26–30] pulse tube refrigerators,[31] and miniature expansion engines.[32] More recently, entropy minimization techniques have been used to develop design criteria for miniature parallel plate counterflow heat exchangers.[16]

Recent efforts have also focused on the basic refrigeration process. Minta[33–37] has performed cycle optimization studies to develop the saturated vapor compres-

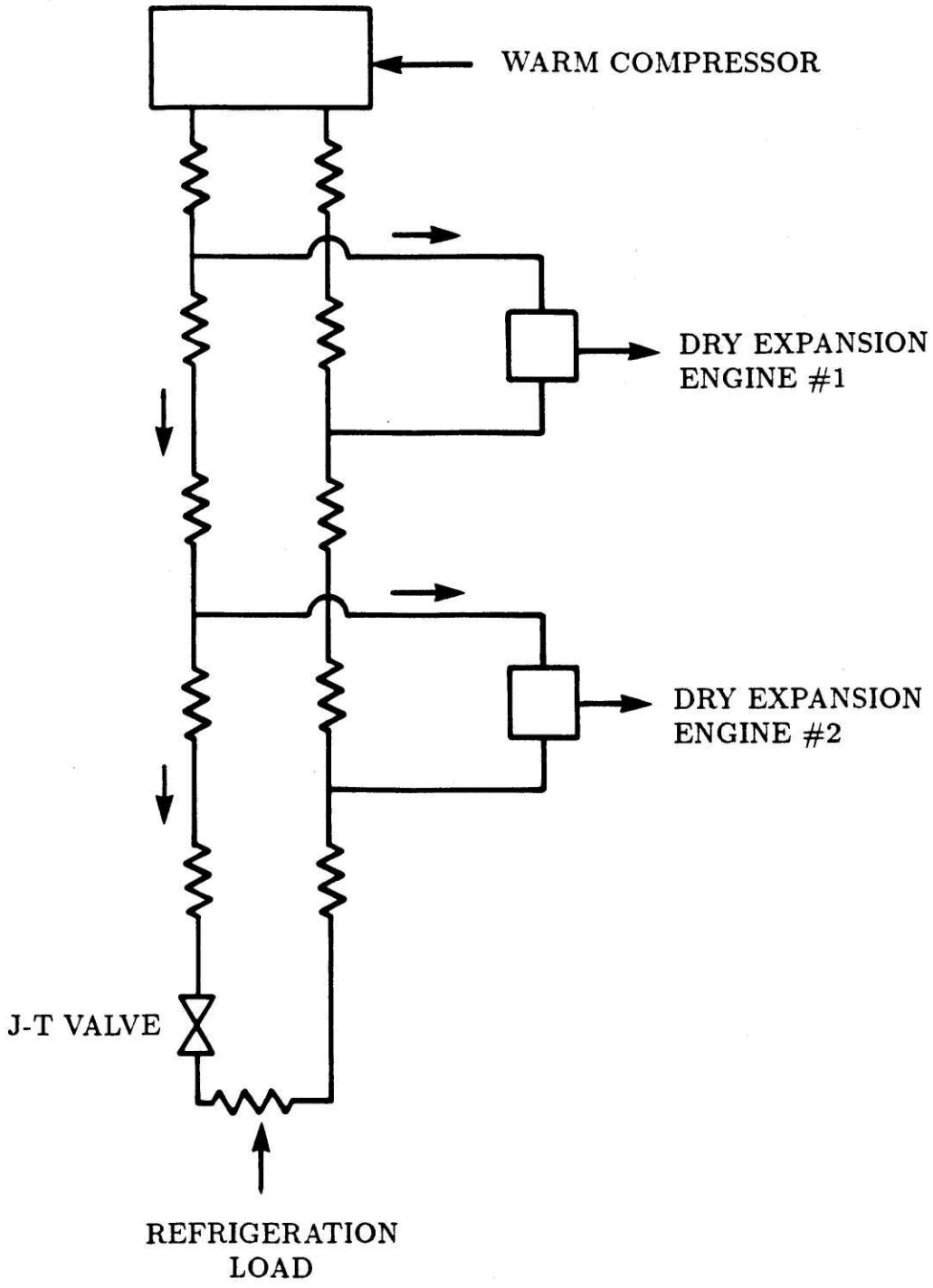

Fig. (1.1) The Collins cycle using two dry expansion engines.

sion (SVC) cycle shown in Figure (1.2). These cycle studies reveal that an optimal thermodynamic cycle consists of a multiple-expander precooling stage to closely match the heat capacity rates of the counter-current fluid streams. Also, cycle pressure levels and cycle pressure ratios must be as high as practical for optimal performance. Heat exchange performance is increased by raising the pressure on the low-pressure side of the heat exchanger. Raising the pressure increases the helium density and therefore places the gas closer to the heat exchanger walls. A vapor compressor is used to increase the return pressure. Raising the return pressure also reduces the power requirement at the warm compressor.

The superiority of the SVC cycle over the original Collins cycle may be illustrated by differentiating the two cycles. First, the Collins cycle employs dry expansion engines and a J-T expansion valve. The expansion engines remove more energy from the gas as the expansion ratio increases, so a high expansion ratio is desired. The J-T valve, however, must be operated in a range of temperatures and pressures that have the largest J-T coefficient, which limits the maximum pressure that can effectively be used for the cycle. These conflicting operating specifications result in a cycle where the low pressure is set by the refrigeration temperature desired while the cycle high pressure is determined by a compromise between the performances of the expanders and the J-T stage. Operation at pressures below 1 atm on the low-pressure side results in a significant increase in both the heat exchanger size and the power requirement at the warm compressor.

The SVC cycle has several advantages over the original Collins cycle. First, the higher pressure level in the low-pressure return side results in improved heat transfer, substantially reducing the required heat exchanger size. Second, the increased suction pressure at the warm compressor inlet reduces the compressor size. Another advantage is that pressure levels may be chosen with regard to best performance of the expansion engines and heat exchangers, without compromise to J-T valve performance. This allows the wet expander to operate over a higher pressure ratio, thus increasing refrigeration potential.

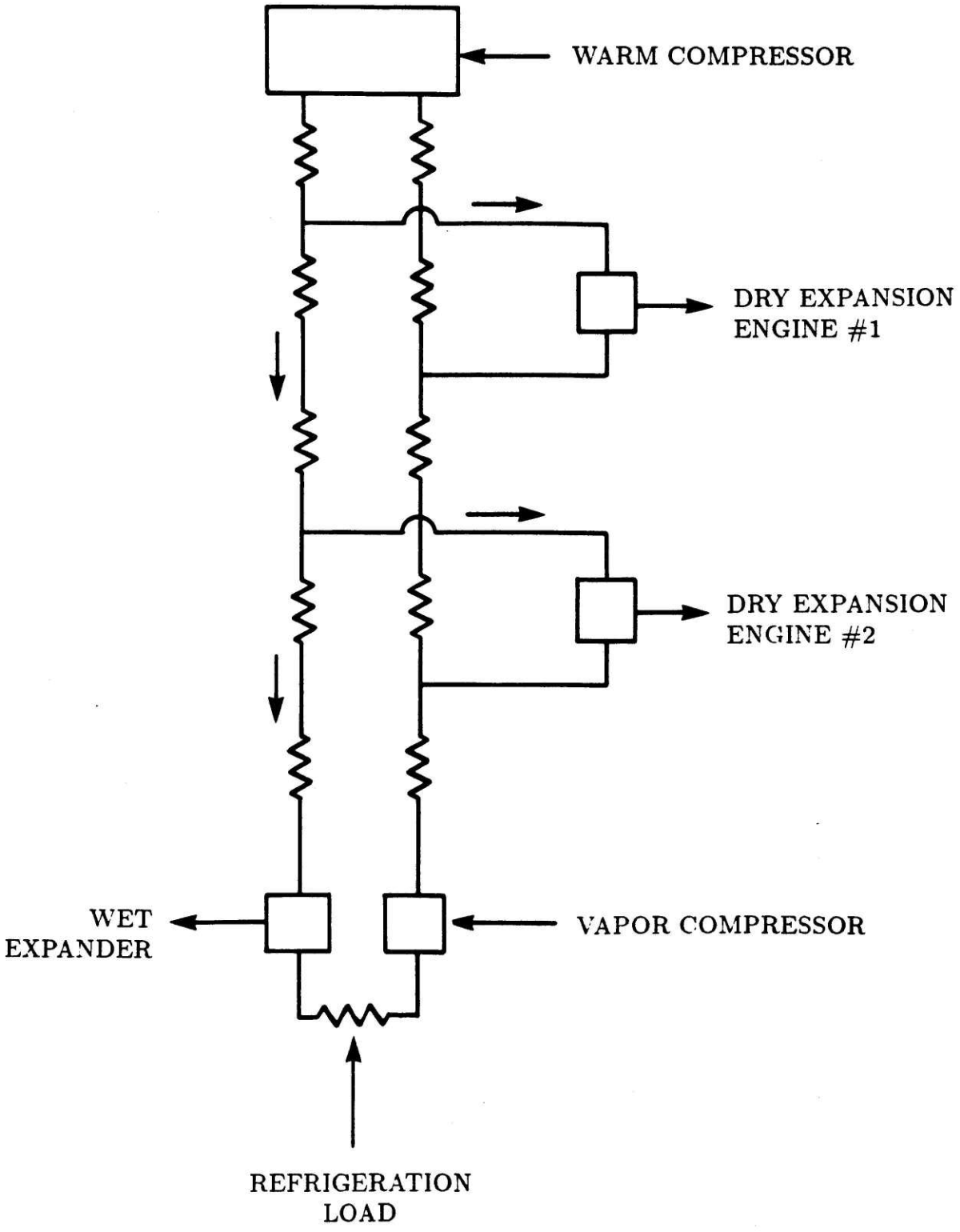

Fig. (1.2) The saturated vapor compression cycle using two dry expansion engines.

1.3 Current Investigation

The overall goal of this project was to find a cryocooler configuration that exploits the high thermodynamic efficiency of the SVC cycle while consisting of compact, reliable, easy to fabricate components. A cryocooler producing 1 W of refrigeration at 4.2 K was considered, with a pressure ratio of 10:1. System analyses consisting of computer algorithms were used to identify physical components that must be developed for the miniature SVC cycle. Using these results, a single-stage cryocooler was designed. Then, in an effort to validate some of the theoretical results and to demonstrate an appropriate fabrication procedure, a single-stage cryocooler was built and tested.

To provide theoretical information on the effects of design parameters on refrigerator performance, a computer algorithm for the SVC cycle was developed. This algorithm allowed variations in such input parameters as the inlet temperatures to the dry expansion engines and heat exchange pinch point locations. The algorithm designed physical components for a complete system by determining heat exchanger and expansion engine dimensions. This information was used to obtain comparative values of entropy generation due to various mechanisms such as expander and compressor irreversibilities, heat exchange temperature difference, fluid friction, heat conduction, and radiation heat leak. Using information obtained from this computer analysis along with practical considerations such as reliability and ease of manufacture indicated a cryocooler configuration that was thermodynamically efficient, yet capable of being mass produced. The optimization study identified a cryocooler design that incorporated the integration of a heat exchanger and expansion engine into a concentric tube configuration.

Design of the integral exchanger and expander required development of a comprehensive performance algorithm which consisted of two parts: one part to model heat exchange and another to model an adiabatic expansion process followed by a lumped heat input. The model for heat exchange included both regenerative and counterflow mechanisms. The result of this heat exchange model was an average

enthalpy flow at a cross section perpendicular to the engine axis consisting of enthalpy flows due to heat exchange and displacer motion. The results were first used to obtain performance predictions for a single-stage cryocooler experiment. Then, results from the algorithm were compared with the experimental results to better understand which loss mechanisms were most prevalent.

In an effort to verify the analytical predictions, a single-stage cryocooler using the integral concentric tube heat exchanger and expansion engine was built. The fabrication procedure used for the experiment should be adaptable to large scale production. The cryocooler was tested both with and without auxiliary liquid nitrogen precooling in an effort to obtain an understanding of the practical utility of the new cryocooler. Various performance parameters were then defined in an effort to quantify cryocooler performance and to indicate which thermodynamic losses dominated.

Chapter 2

Component Analysis for an SVC Cycle Cryocooler

2.1 Introduction

The purpose of this chapter is to identify a cryocooler physical configuration that is thermodynamically efficient, reliable, and easily manufacturable. The cryocooler must also be comparable in size to those currently being used for refrigeration loads of approximately 1 W at 4.2 K. The saturated vapor compression (SVC) cycle will be the thermodynamic cycle used due to its high thermodynamic efficiency and its suitability for use at liquid-helium temperatures, when compared to the Stirling and Gifford-McMahon cycles. The SVC cycle is a modified Collins cycle which operates at higher inlet and exhaust pressures and at higher pressure ratios. A wet expander is used to eliminate thermodynamic irreversibilities associated with Joule-Thomson expansion valves and a vapor compressor raises the low-pressure return side pressure to increase heat exchange efficiency.

Reliability and ease of manufacture are important considerations at this stage of cryocooler development. Because the intake and exhaust valves operate at the refrigeration temperature in the SVC cycle, reliability has been a major concern which has resulted in the use of regenerative-type cryocoolers. Also, during this stage of development, manufacturability of the miniature heat exchangers and expansion engines must be considered. Starting with these design criteria and after considering other configurations, an integral heat exchanger and expansion engine using a concentric tube heat exchanger enclosing a displacer and cylinder was selected. In this chapter, the integral configuration will be introduced for use in the cryocooler analysis.

Since overall cycle performance is under investigation, analyzing the system in closed form would be very cumbersome. For this reason, the first step in finding an adequate cryocooler configuration is to develop a computer program that places physical dimensions on heat exchangers and expansion engines for the SVC cycle. The program also computes the entropy generated in each component, which may be

compared to the entropy generation in the overall system or to entropy generation in the other components. The resulting data base is used to identify the effects of varying design parameters and which physical components contribute most to cycle inefficiencies in terms of entropy generation. Information obtained from this data base would be difficult to obtain in a closed form mathematical solution.

Several important observations are identified in this chapter that result from the computer analysis. For example, cycle performance is not as sensitive to changes in the vapor compressor efficiency as it is to changes in wet expander efficiency. The analysis also indicates optimal inlet temperatures for the dry expanders and the performance sensitivity to operation at other than these optimal inlet temperatures. Another result is that a heat exchanger is required that operates between the temperature at the coldest dry expander exhaust and the wet expander inlet temperature.

This chapter first discusses reasons for choosing the SVC cycle for cryocooler use and then gives details of the SVC cycle analysed. The cycle description is followed by an overall description of the computer programs used to analyse the SVC cycle with physical components. The results mentioned above are then described in more detail. Also, the theoretical implications of further miniaturizing the SVC cycle are investigated. Finally, the implications for cryocooler design obtained from the analysis are given.

2.2 The SVC Cycle with Physical Components

This section will describe the SVC cycle cryocooler analysed using the computer analysis. Reasons for selection of the SVC cycle among the possible alternatives will be given. The integral heat exchanger and expansion engine will then be introduced as a primary component in the configuration considered. The specific case analysed will then be described.

2.2.1 Selection of the SVC Cycle

The cycles used most commonly for cryocoolers are the Stirling and Gifford-McMahon. The performance of these cycles is poor when operation at liquid helium temperatures is necessary due to the diminishing heat capacity of regenerator materials at low temperatures. To reach liquid helium temperatures, the Stirling and Gifford-McMahon cycles must be modified by adding a Joule-Thomson (J-T) loop which is in parallel with the main cycle. Since the Collins cycle uses counterflow heat exchangers, diminishing heat capacity does not limit the heat exchanger performance. Reference (14) compared the Collins cycle with the Stirling/J-T and the Gifford-McMahon/J-T combination cycles to find that the Collins cycle is the most thermodynamically efficient of the three, requiring much less power input per Watt of refrigeration. The study also found that using a wet expander and vapor compressor have potential to increase the system performance.

More recently, SVC cycle optimization studies by Minta[33-37] based on the minimization of entropy generation indicate that an optimal thermodynamic cycle consists of a multiple-expander precooling stage to closely match the heat capacity rates of the counter-current fluid streams. This difference in heat capacity between the high-pressure helium and the low-pressure helium results from a strong pressure and temperature dependence of the helium heat capacity below 70 K. The optimal cycle requires that the heat exchange temperature ratio be constant over the heat exchange temperature span. This result is expressed as

$$\Delta T / T = \text{constant},$$

where ΔT is the heat exchange temperature difference between the high- and low-pressure streams and T is temperature of the low-pressure stream. Also, optimal cycle performance requires that cycle pressure levels and cycle pressure ratios be kept as high as practical.

Based on these studies, the SVC cycle is used as a starting point for analysis. Results are used to further increase system performance and to simplify manufactur-

ing of the cryocooler by modifying components normally used in large-scale Collins type cycles. These modifications result in a cycle configuration that deviates somewhat from the standard SVC cycle configuration used in the analysis that follows. For example, the integral heat exchanger and expansion engine described later uses an inlet valve which operates at room temperature and an exhaust valve that operates at the refrigeration temperature. Examination of the SVC cycle shown in Figure (2.1) indicates that this cycle must be modified if it is to use the integral exchanger and expander with a room temperature valve. Analysis of the resulting cycle configuration, however, yields the same general trends as those observed in the SVC configuration of Fig. (2.1) because the cryocooler components are used in an analogous fashion to keep the heat exchange temperature ratio constant over the exchanger length. More discussion about the possible cycle configurations given at the end of this chapter. At this point, one should only note that the counterflow heat exchanger used in the computer analysis is modified in a later section by using the results from the analysis to find a more efficient configuration.

2.2.2 SVC Cycle Physical Configuration

The purpose of the computer analysis to be described later in this chapter is to help in the design of a helium-temperature cryocooler providing 1 W of refrigeration. The analysis includes losses that depend on the component dimensions of a specified physical system. Since developing the computer programs was a preliminary step in the project, a cycle configuration had to be chosen. In other words, an iterative procedure was used to evolve a physical configuration that would meet the design criteria. The concentric tube heat exchanger was not the first heat exchanger type considered for the integral heat exchanger and expansion engine configuration. Another heat exchanger configuration considered consists of multiple small diameter tubes wrapped around a mandrel. High-pressure gas would flow inside the tubes and low-pressure gas would flow over the tubes. This exchanger was not as efficient as the concentric tube exchanger and was not easily mass produced.

As a primary design criterion, the size of the cryocooler had to be comparable to

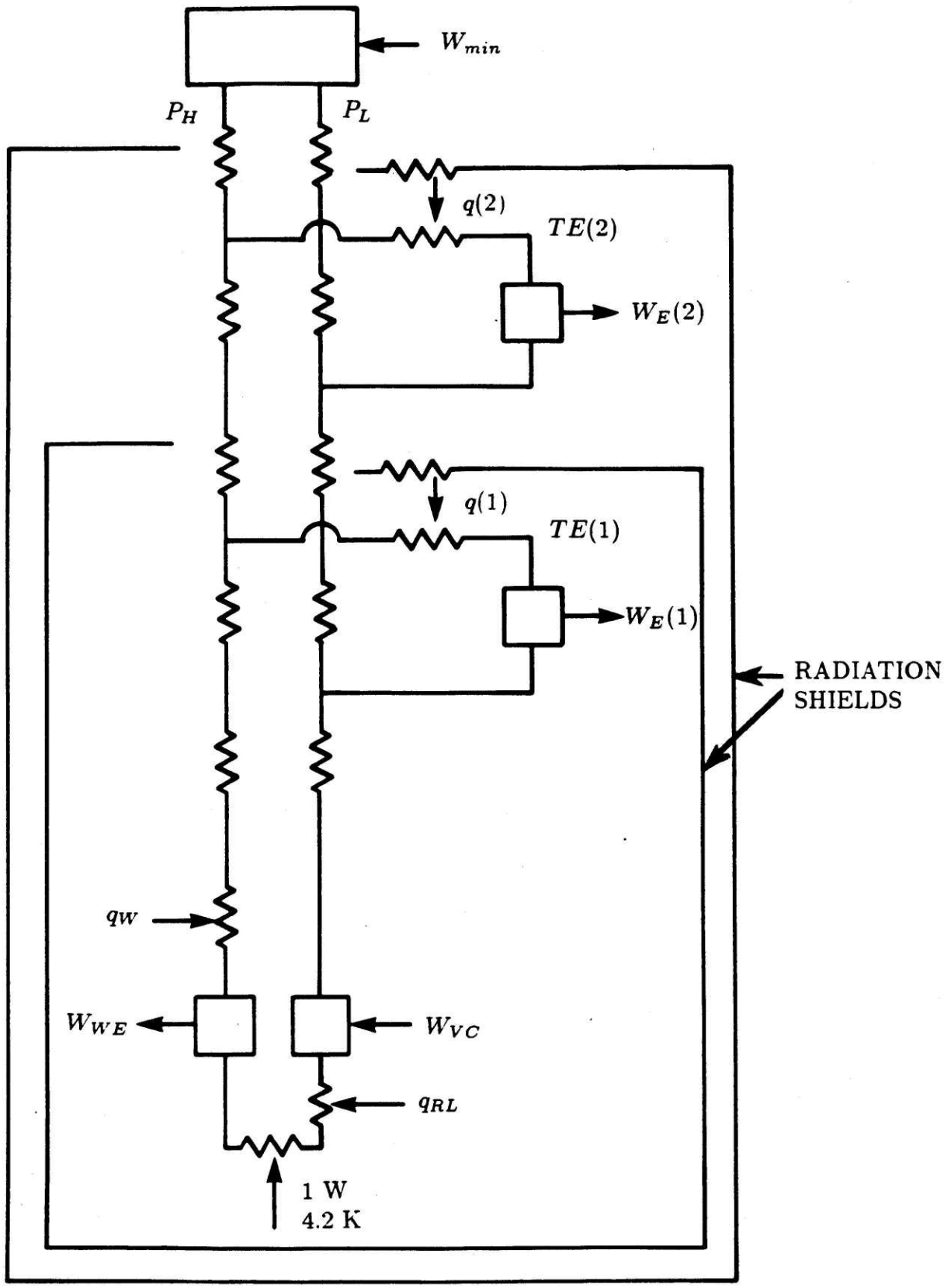

Fig. (2.1) SVC cycle configuration used for the cycle analysis.

those currently available which use other cycle configurations. A survey of miniature cryocoolers[1] available in 1984 indicates that the cold box for this project should be less than 60 cm high with sides of 20 cm. The integral heat exchanger and expansion engine chosen for this project not only reduces the overall size of the system but also reduces the cross-sectional area for axial conduction.

Heat exchanger selection for the integral exchanger and expander arrangement involves consideration of refrigerator capacity and physical size. Conventional heat exchanger configurations such as finned tube or stacked plate arrangements are much too bulky and difficult to manufacture if scaled to cryocooler dimensions. Also, thermodynamic losses that are negligible in large-scale helium-temperature refrigerators may be significant for cryocoolers. These thermodynamic losses which are unique to miniature refrigerators include flow maldistribution and conduction heat leak irreversibilities.

A flow maldistribution loss occurs when a heat exchanger flow is divided into many passages, some of which having a larger resistance to fluid flow. The result is different mass flow rates among the passages. The effect of this flow maldistribution on thermal performance is severe and becomes more pronounced as heat exchange effectiveness increases. For this reason, very little is gained by increasing the heat exchange effectiveness if flow maldistribution is present. The result of a study by Fleming[15] indicates that continuous mixing of a uniform side flow (*i.e.*, either the high-pressure or low-pressure side fluid flows through one passage, thereby being continuously mixed) throughout the exchanger significantly reduces the effect of flow maldistribution.

The conduction loss is the result of transverse (stream-to-stream) conduction, which is essential to heat exchange between streams, and axial conduction which is totally undesirable. Conduction loss minimization has been investigated for the simple heat exchange configurations of parallel plates[16] and concentric tubes.[17] These studies included the effects of axial conduction, transverse conduction, and flow friction losses. The results of theses studies indicate that an optimal value of heat exchanger wall conductivity exists, and that this value varies with fluid

parameters and operating conditions.

A concentric tube heat exchanger will be used in the computer analysis. The concentric tube heat exchanger encloses a cylinder and expansion engine. The outer wall of the cylinder will be an inner shell for the heat exchanger. A primary reason for choosing the concentric tube heat exchanger over other types is because the concentric tube heat exchange surface area requirement is of the same magnitude as the surface area of the cylinder wall required to keep axial conduction heat leak small. Also, in an effort to keep flow maldistribution losses to a minimum, the low-pressure return flow will be directed in a spiral direction, using a spiral flow passage tilted at a helix angle measured from the axial direction of the engine (*e.g.*, a helix angle of 0 degrees results in flow only in the axial direction). The equivalent diameters obtainable for flow on the high- and low-pressure sides are on the order of 0.25 mm. The small equivalent diameter on the high-pressure side results in laminar flow for the cases considered. On the low-pressure side, the flow may be turbulent in some cases. Both conditions must therefore be included in the computer analysis.

For analysis using the SVC cycle shown in Fig. (2.1), both the inlet and exhaust valves will be located at the cold end of the expansion engine. The flows on the high- and low-pressure sides will be taken as steady. Three of these integral heat exchanger and expansion engines will be used in the analysis. In the computer programs, the integral exchanger and wet expander will be assumed to be of the same bore as the colder integral exchanger and dry expander. Two radiation shields will be used, one operating at the inlet temperature to the warmer dry expander and the other operating at the inlet temperature to the cooler dry expander.

2.3 Description of the Computer Programs

Computer programs have been developed that compute state properties and mass flow rates at several state points in the SVC cycle based on input specifications and inputs resulting from component performance. In order to observe the effect on cycle performance of varying component dimensions and operation specifications, the programs have been used to obtain several data points.

Since the computer programs design the cryocooler components for each set of input values, thermodynamic losses can be computed based on an actual system. The losses included in this analysis are:

1) expander and compressor inefficiencies,
2) heat exchange temperature difference,
3) fluid friction,
4) heat conduction, and
5) radiation heat leak.

What follows is a brief description of the computer programs. The computer analysis consists of two primary algorithms:

1) One algorithm is used to compute properties of the helium gas and the mass flow rate at several locations for the SVC cycle shown in Figure (2.1). This algorithm is concerned primarily with the thermodynamic cycle. Heat leaks are included in this algorithm using a lumped parameter model. The lumped heat leaks due to axial conduction and radiation are input before the engines, as shown in Figure (2.1). The main program does not perform calculations to determine losses for the components; hence, no component specifications are required in this part of the program.
2) A second algorithm computes heat exchanger and expansion engine dimensions. After these components are designed, axial conduction and radiation heat leaks are computed. Also, the pressure drops through each heat exchanger are computed along with the absolute pressure at the inlet and outlet to each heat exchanger. Due to the small equivalent diameters for the cases considered, flow on the high-pressure side was always laminar. On the low-pressure side, the flow was usually turbulent at lower temperatures. Equations for both laminar and turbulent flows were included in the algorithm.

By examining these two algorithms, one will observe that their use to design a cryocooler is an iterative process. An initial set of specifications is input to

the first algorithm. After mass flow rates and helium properties are computed at the points of interest for the SVC cycle, the second algorithm uses outputs from the first algorithm to compute physical dimensions for the specified components. Component inefficiencies result in heat leaks, fluid friction pressure drops, and heat exchange temperature differences. These outputs from the second algorithm are then input to the first algorithm.

The first algorithm is generally applicable to any cryocooler component configuration that uses the SVC cycle. The second algorithm is a subroutine that is not generally applicable; it is presently set up for use with an integral concentric tube heat exchanger and expansion engine. The subroutine is easily modified to analyze similar configurations, however. To analyze a different heat exchanger configuration, the equations for heat exchange coefficient and pressure drop need to be modified. Also, the cross-sectional area for axial conduction and the area exposed to radiation heat leak must be changed.

A subroutine called PINCH is used to determine heat exchange pinch points, which are locations of minimum temperature difference in the heat exchanger stack. These pinch points are due to the high-pressure stream having a larger heat capacity rate than the low-pressure stream. The result is that, over a length of counterflow heat exchange, the temperature of the low-pressure stream changes more than that of the high-pressure stream. At the pinch points, the heat exchange temperature difference is a minimum. As discussed earlier, results from Minta indicate that the heat exchange temperature ratio should be kept constant over the heat exchanger stack length by use of multiple expansion engines. To prevent the heat exchange temperature difference from becoming too large, expansion engines extract mass flow from the high-pressure side and add it to the low-pressure side to better match the heat capacity rates. Subprogram PINCH determines pinch point locations in a single heat exchanger.

A more detailed description of the computer programs is given in Appendix A. Tables are included that list all of the input and output parameters. Also, results from other investigators are included that are not discussed in this chapter.

2.4 Results of the Computer Analysis

This section begins with general results that do not require the choice of specific cryocooler components. These results include selection of optimal dry expander inlet temperatures, the sensitivity of cycle performance to variations in engine efficiencies, and the effect of heat exchange pinch point locations at the cold end on system performance. An evaluation of component performance based on entropy generation follows. Entropy generation in the components due to various mechanisms is compared for different values of engine speed for a system using the integral concentric tube heat exchanger and expansion engine. These results indicate that, for the case considered, the magnitude of entropy generation in the engines is comparable to that in the heat exchanger stack, while the magnitude of entropy generated due to radiation and conduction is quite small.

2.4.1 Effects of Parameter Variations on SVC Cycle Performance

The results reported in this sub-section were generated using only the computer algorithm for the SVC cycle — the subroutine used to design an integral expander and exchanger unit was not used. The trends in the results are therefore not dependent on the specific components chosen and are generally valid for any SVC cryocooler. For a slightly more detailed explanation of the results and for representative plots of the observed trends, refer to Appendix A.

With other cycle parameters held constant, optimal dry expander inlet temperatures which minimize entropy generation in the system may be found using an iterative method.[36] Although the same general trends result, these optimal inlet temperatures are actually different for different component dimensions due to variations in the magnitudes of lumped parameter heat inputs before the expansion engines, heat exchange efficiency, and flow friction in the heat exchangers. Only the inlet temperatures to the dry expansion engines may be optimized; the inlet temperature to the wet expander depends on the specified temperature in the refrigeration zone.

Overall system performance is not particularly sensitive to small changes in the optimal dry expander inlet temperatures. Trends in the total mass flow rate at the warm compressor are compared by varying the inlet temperature to one dry expander while holding all other inputs constant. The results indicate that variations in the inlet temperature to the warmer dry expansion engine of 15 K causes the entropy generation in the system to increase by less than 5%. A variation in the inlet temperature to the cooler dry expander of 2 K results in the system entropy generation increasing by approximately 5%. The system is more sensitive to variation in inlet temperature for the cooler dry expander because the gas specific heat varies significantly with temperature at the cooler temperatures.

Individual variations in the adiabatic efficiency of the wet expander, cold vapor compressor, or dry expanders indicate varying magnitudes of effect on the total entropy generation for the cryocooler system. The system is most sensitive to variations in wet expander performance. For example, if a wet expander with an adiabatic efficiency of 0.9 is replaced with a less efficient wet expander with an efficiency of 0.8, the change in overall cryocooler entropy generation will increase by as much as 35 percent. Also, the magnitude of entropy generation in the wet expander is larger than in the other engines.

Overall system performance is much less sensitive to vapor compressor efficiency than to wet expander efficiency. Likewise, the magnitude of entropy generated in the vapor compressor is smaller than in the other engines. This result indicates that improvements on vapor compressor efficiency are not as beneficial to overall cycle performance as improvements on wet expander efficiency. One should note, however, that the vapor compressor must perform the function of raising the return-side pressure; otherwise, system performance will deteriorate due to a decrease in heat exchange efficiency. In other words, operating the return passage at a lower pressure implies operation at a lower gas density, which results in a mass flow of higher velocity with less mass near the exchanger wall. The overall result is lower heat exchange efficiency and, thus, lower system efficiency.

Another important observation is that, for best system performance, a cold

heat exchanger must be located between the outlet from the coldest dry expander and the inlet to the wet expander. Furthermore, the exchanger must be designed to have pinch point locations at both the outlet from the coldest dry expander and at the inlet to the wet expander. Note that a pinch point is always located at the exhaust from a dry expander in order to match the capacity rates, but the inlet to the wet expander must be designed to be a pinch point location if better system performance is desired. As a final note, use of this cold heat exchanger is, in general, a good design rule; however, if an inefficient heat exchange configuration ($\Delta T / T > 0.06$) is to be used, the inlet to the wet expander does not necessarily have to be a pinch point location to achieve best performance.

2.4.2 Cycle Performance Evaluation Using Entropy Generation

In this section entropy generation in the cryocooler components is investigated. The specific losses observed are entropy generation due to heat exchange temperature difference, expander and compressor inefficiencies, fluid friction, axial conduction, and radiation. The SVC cycle cryocooler considered is shown in Fig. (2.1). Table (2.1) lists the input parameters for the analysis.

An entropy generation technique is useful to analyse system performance because magnitudes of inefficiencies in each cryocooler component may be compared with a universal scale. This type of analysis indicates which components require the most effort in efficient cryocooler development.

General trends and overall results are developed in the remainder of this chapter for a specific cryocooler. The primary cycle configuration considered in this analysis is shown in Fig. (2.1). The system consists of two integral heat exchanger and dry expansion engine units, an integral heat exchanger and wet expander unit, and a vapor compressor. The heat exchangers used are the concentric-tube counterflow type. Two radiation shields are used to limit the radiation heat leak to the cold components. The radiation shields are cooled by helium gas. In this analysis, the two shields are assumed to be isothermal and to operate at the temperatures of their respective expansion engine inlet temperatures. In other words, helium gas exits

Table (2.1) Input parameters for SVC cycle analysis.

Parameter	Value
Refrigeration load	1 W
Refrigeration temperature	4.2 K
Wet expander efficiency	0.80
Vapor compressor efficiency	0.80
Dry expander efficiencies	0.75
Inlet high pressure	40 atm
Inlet low pressure	4 atm
Total heat exchange area	400 cm^2
Engine bore/stroke ratio	1.0
Displacer-to-cylinder gap	0.127 mm
Cylinder-to-outer shell gap	0.254 mm
Displacer tube thickness	0.89 mm
Cylinder tube thickness	0.71 mm
Outer shell tube thickness	0.51 mm
Spiral spacer angle	78°
Surface emissivities	0.05

the high-pressure side of the heat exchanger, passes through the radiation shield, and then enters the inlet valve for the expansion engine.

As mentioned previously, other heat exchange configurations were considered in this analysis in an effort to find the one best suited for the cryocooler under development. The trends reported in this section are the same for other heat exchange configurations; the magnitudes of the various irreversibilities, however, depend on the specific configuration. One may also note that other concentric tube arrangements could have been selected. Here, the concentric tube heat exchangers are assumed to be integral with the expansion engines so that the cylinder wall is also the inner shell wall for the heat exchanger. In this arrangement, three integral expander and exchanger units are used. Another arrangement consists of a single exchanger integral with the wet expander, where only a single counterflow heat exchanger with plumbing for the other engines is used.

The cryocooler has a refrigeration load of 1 W at 4.2 K and 1 atm. Results discussed earlier indicate that cycle pressure levels and pressure ratios should be as high as practical. The warm compressor in the analysis has a pressure ratio of 10:1; the high-pressure gas leaving the compressor after-coolers is at 40 atm.

Because the specific heat of the components operating near liquid helium temperatures diminishes, the wet expander and vapor compressor probably operate more efficiently than the dry expansion engines. The wet expander and vapor compressor are assumed to have adiabatic efficiencies of 0.80 and both dry expansion engines are assumed to operate at 0.75 adiabatic efficiency.

Axial conduction is shown to be a major driving force in the results presented in this section. For this reason, computation of the axial conduction heat leak is based on a design with practical physical components. Using the thermodynamic cycle configuration shown in Fig. (2.1) in combination with the integral exchanger and expander results in a rather clumsy system design because only one heat exchanger extends from room temperature. Thus, if the configuration of Fig. (2.1) were used, the heat exchangers would not enclose the entire length of each expander, except on the warmer integral unit. On the colder dry expander and the wet expander, the heat exchanger would enclose only the colder portion of the cylinder. A more practical system would use heat exchangers that also extend from room temperature. Configurations used for this type of modification will be discussed in much more detail in later sections. (Figures (2.12) and (2.13) indicate these configurations.) For now, the physical configuration used to compute the axial conduction heat leak assumes three walls for axial conduction: a displacer wall, a cylinder wall, and an outer shell wall. Each of the three walls extends from room temperature to the expander inlet temperature. The thickness of each wall is given in Table (2.1). Note that only the axial conduction heat leak is based upon the three wall physical configuration. All other computations are based directly on the cycle configuration of Fig. (2.1).

Several physical parameters had to be preselected. The total heat exchange area for the heat exchanger stack is 400 cm^2. This value is an input to the overall

analysis but is an output from the computer program. For this reason, inputs to the program must be varied until a total heat exchange surface area of 400 cm^2 results. The value of helix angle used for the low-pressure return side spiral flow passage is 78°. The bore-to-stroke ratio for the expansion engines and vapor compressor is 1.0. The major inputs to the analysis for this case are included in Table (2.1).

Choosing an appropriate amount of total surface area for heat exchange is an iterative process, depending on several input parameters. Two of the more important input parameters are the heat exchange gap widths and the heat exchange temperature ratio. The heat exchange area that evolved for this analysis is 400 cm^2. This value allows consideration of total stack lengths in the range of 40 cm to 80 cm while maintaining a realistic range of values for such parameters as heat exchanger temperature ratio and engine efficiencies.

The total heat exchange surface area is an output from the computer program and is proportional to the product of exchanger length and diameter. The actual length and diameter of each integral unit is computed as follows using the cycle configuration of Fig. (2.1). The expander working volume for the two dry expanders is computed first, based on the expander mass flow rates computed in the cycle analysis. The dimensions for the working volume depend on the engine speed and the bore-to-stroke ratio, along with the gas properties. The engine bore computed is the dimension upon which the displacer, cylinder, and outer shell diameters are based. The length of exchanger is then computed using these diameters. The length depends on the amount of heat exchange area required to obtain the end-to-end temperature change. The bore-to-stroke ratio is preselected to be unity. For this reason, the exchanger dimensions depend very strongly on the engine speed.

An iterative method was used to find trends in overall cryocooler performance. With the input parameters held constant, the speed of the engines was varied. All of the engines operate at the same number of revolutions per minute. For a set value of engine speed, the heat exchanger performance must be sufficient to require only 400 cm^2 of heat exchange area. One measure of the performance is the heat exchange temperature ratio at the pinch points, $\Delta T / T$. The same value of temperature

ratio is used at all pinch points. This ratio is an input to the computer program. The iteration scheme, therefore, consists of finding the value of $\Delta T/T$ required for a given engine speed with the heat transfer area set at 400 cm^2.

The engine speeds considered range from 20 RPM to 220 RPM. The above iteration method was used for each engine speed. A second iteration to find the optimal expander inlet temperatures is nested in the above iteration. These optimal inlet temperatures vary with changes in cryocooler specifications. For example, a reduction in engine speed results in a shorter exchanger stack, which results in a higher heat exchange temperature ratio and higher total mass flow rate. To optimally match the heat capacity flow rates for this new situation requires finding new optimal inlet temperatures for the dry expanders.

Trends in entropy generation with respect to engine speed will now be discussed. Figure (2.2) is a plot of entropy generation versus RPM. The total entropy generated is plotted along with component values of irreversibilities due to heat exchange temperature difference, engine losses, radiation heat leak, and conduction heat leak. The figure indicates that optimal system performance in terms of entropy generation occurs in the range of 100 RPM to 140 RPM. A plot of mass flow rate at the warm compressor versus engine speed is shown in Fig. (2.3). As in Fig. (2.2), the curve becomes flat above approximately 100 RPM. This mass flow rate curve, however, does not indicate the magnitudes of the various loss mechanisms. The shapes of the individual curves shown in Fig. (2.2) will now be discussed.

The magnitude of entropy generation resulting from conduction, as shown in Figure (2.2), is quite small when compared with the total entropy generation. The overall trends, however, follow the trends in axial conduction very closely. The total entropy generation is observed to consist primarily of entropy generations due to heat exchange and engine inefficiencies, both of which follow the general trends of the axial conduction entropy generation curve. At lower engine speeds, the value of axial conduction entropy generation peaks, as does the total mass flow. Higher engine speeds correspond to small diameter, long integral exchanger and expander units; thus, the axial conduction heat leak is small at the higher speeds. Overall

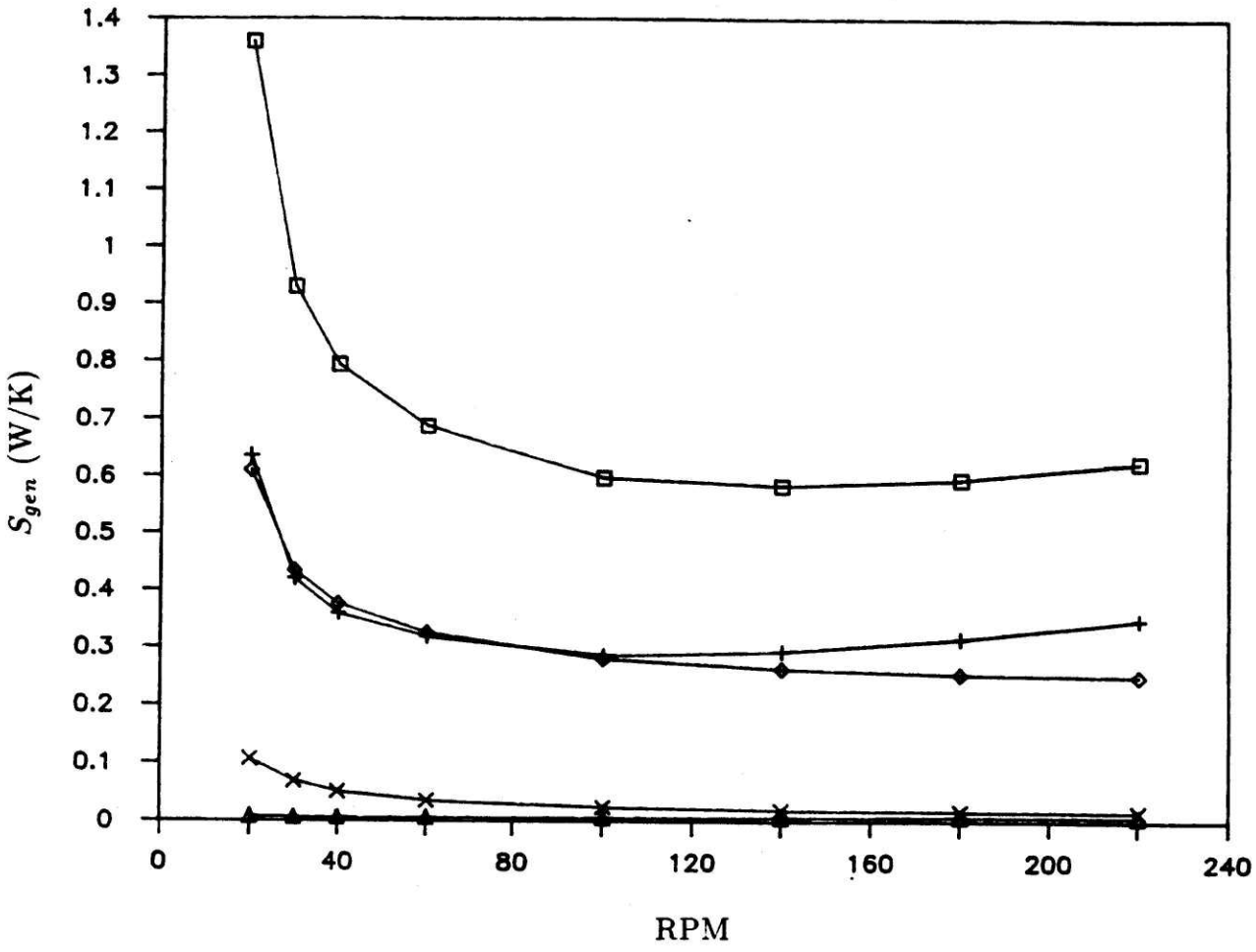

Fig. (2.2) Entropy generation versus engine speed.

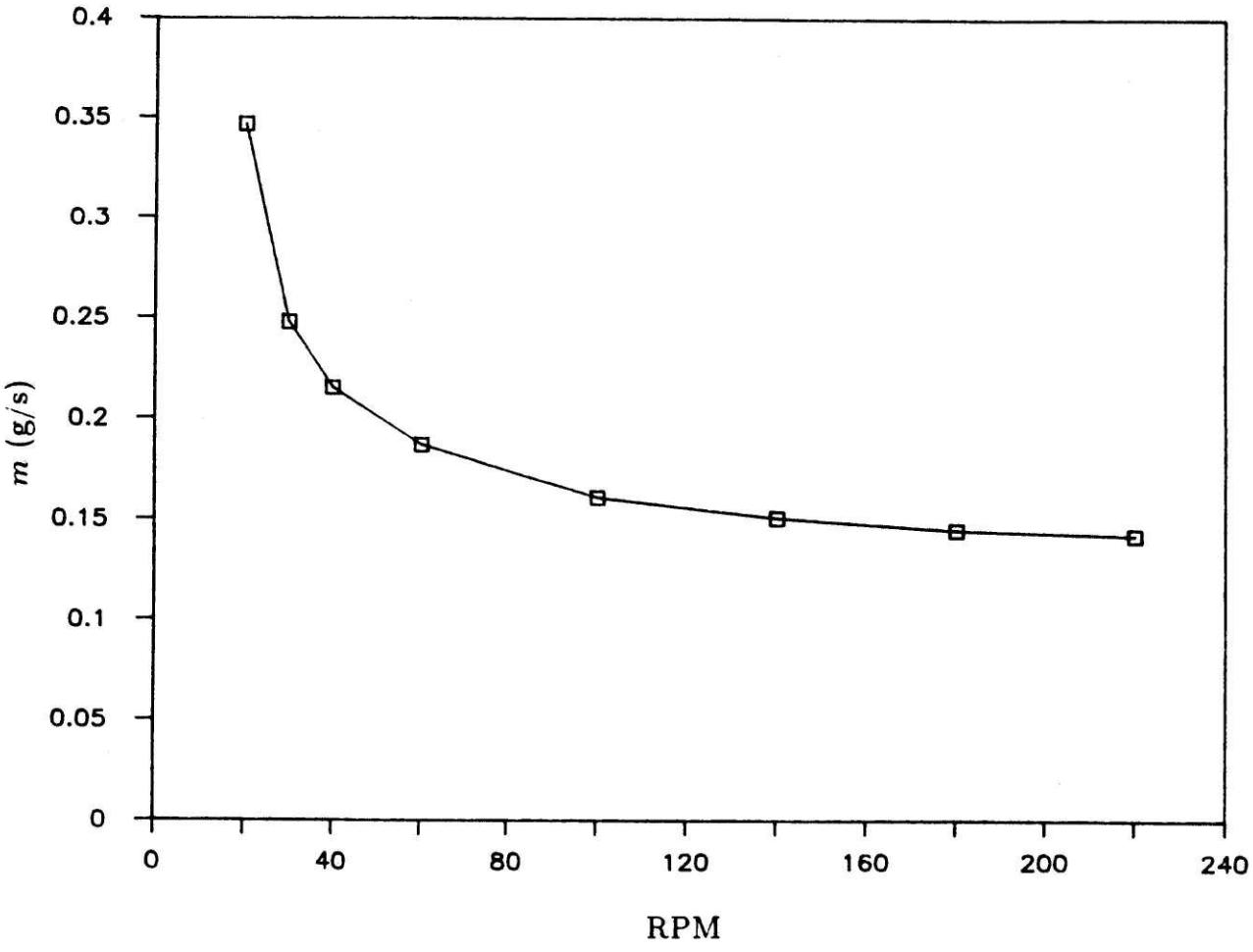

Fig. (2.3) Total mass flow rate versus engine speed.

system performance also peaks at higher engine speeds. The increase in entropy generations due to heat exchange temperature differences and engine inefficiencies are directly proportional to the increase in mass flow rate through the exchangers and engines, respectively. For this reason, the influence of axial conduction on overall performance may be explained as follows. A shorter heat exchanger stack length results in increased axial conduction. This additional axial conduction heat leak must be removed at an expander by an increase in work removed, which requires a larger mass flow rate through the expander. The larger mass flow through the expander results in an increase in entropy generation since the engine entropy generation is proportional to the mass flow rate times the change in entropy, where the change in entropy is constant for a given expander inlet temperature and adiabatic efficiency. The entropy flow equation is

$$S_{gen,engines} = M\,(s_{in} - s_{out}) \tag{2.1}$$

where M is the time-averaged mass flow rate. The larger mass flow rate required to remove the axial conduction also results in a larger mass flow rate through the heat exchangers. The entropy generation in the heat exchangers is proportional to the mass flow rate times the heat exchange temperature ratio. In the heat exchangers, the increased mass flow also results in an increased temperature ratio, which further compounds the entropy generation. The temperature ratio increases with an increase in mass flow because of a decreased time for heat exchange while the gas is at each position. These results indicate that increased axial conduction is the primary driver for increased mass flow at the warm compressor.

Thermodynamic losses due to heat exchange can be further investigated by examining system entropy generation versus the heat exchange temperature ratio at the heat exchange pinch points, $\Delta T / T$, as shown in Fig. (2.4). When observing trends in temperature ratio, one should note that heat exchange temperature difference increases as the exchanger mass flow rate increases, as discussed in the preceeding paragraph. By comparing with Fig. (2.2), an increase in $\Delta T / T$ corresponds to a decrease in engine speed and, thus, a decrease in stack length. For

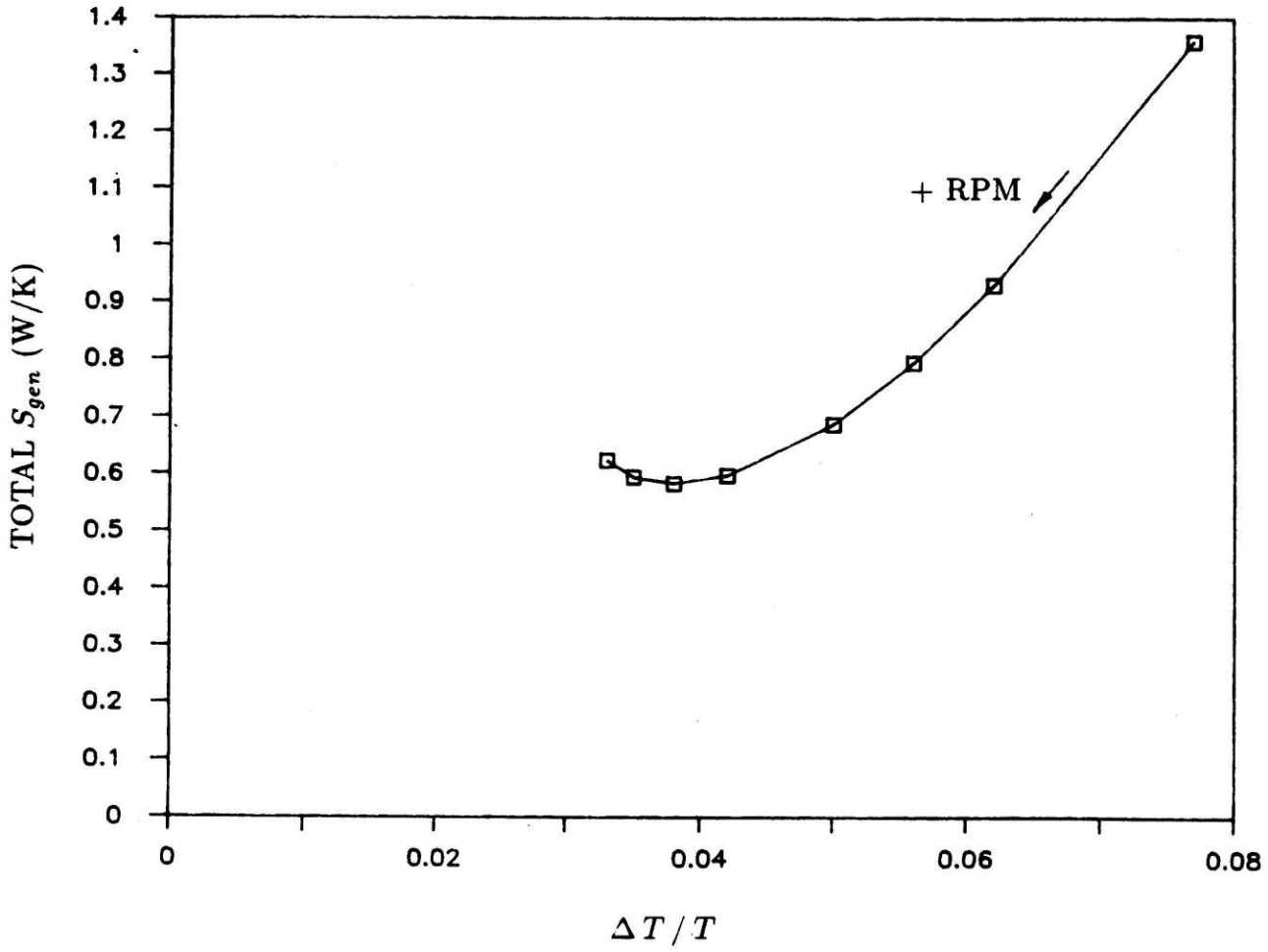

Fig. (2.4) Total entropy generation versus heat exchange temperature ratio.

the specified cycle, the optimal temperature ratio is approximately 0.037. Entropy generation due to heat exchange temperature difference always decreases with decreasing $\Delta T / T$, since entropy generation due to heat exchange is proportional to the product of temperature ratio and mass flow rate through the exchanger. For $\Delta T / T > 0.037$, increased entropy generation is due primarily to increased temperature difference between the high-pressure and low-pressure streams.

Figure (2.4) indicates other loss mechanisms dominating the total entropy generation below $\Delta T / T = 0.037$. The cryocoolers with $\Delta T / T < 0.037$ have longer fluid flow passages than those with higher values of temperature ratio. For this reason, the increase in total entropy generation for small $\Delta T / T$ results primarily from increased entropy generation due to fluid friction. This increase in total entropy generation could be reduced if the resistance to fluid flow were reduced on the low-pressure return side by decreasing the helix angle for the spiral flow passage.

Figure (2.5) is a plot of total entropy generation in the system versus the heat exchanger stack length. This figure indicates that for minimal entropy generation, the stack length would be approximately 100 cm. A primary design criterion, however, limits the design length to 60 cm. Designing for a shorter stack length results in an increased heat exchange temperature difference, as indicated by Figure (2.4). As explained earlier, this result is due to an increase in the temperature gradient in the axial direction, which results in increased axial conduction.

Another observation concerning Figure (2.5) should be made at this time. Since the heat exchange area for an integral unit is proportional to the product of exchanger length and diameter, the bore to stroke ratio that was preselected for this analysis affects the exchanger length. In other words, changing the bore to stroke ratio to the appropriate value would result in a heat exchanger stack length of 60 cm at an engine speed of minimal entropy generation. Without a better understanding of engine efficiency with regard to the bore to stroke ratio and engine speed, however, this exercise could not yield more accurate performance predictions.

Entropy generation in the helium gas is plotted in Figure (2.6). Real gas properties are used to generate the total gas entropy generation in the heat exchangers.

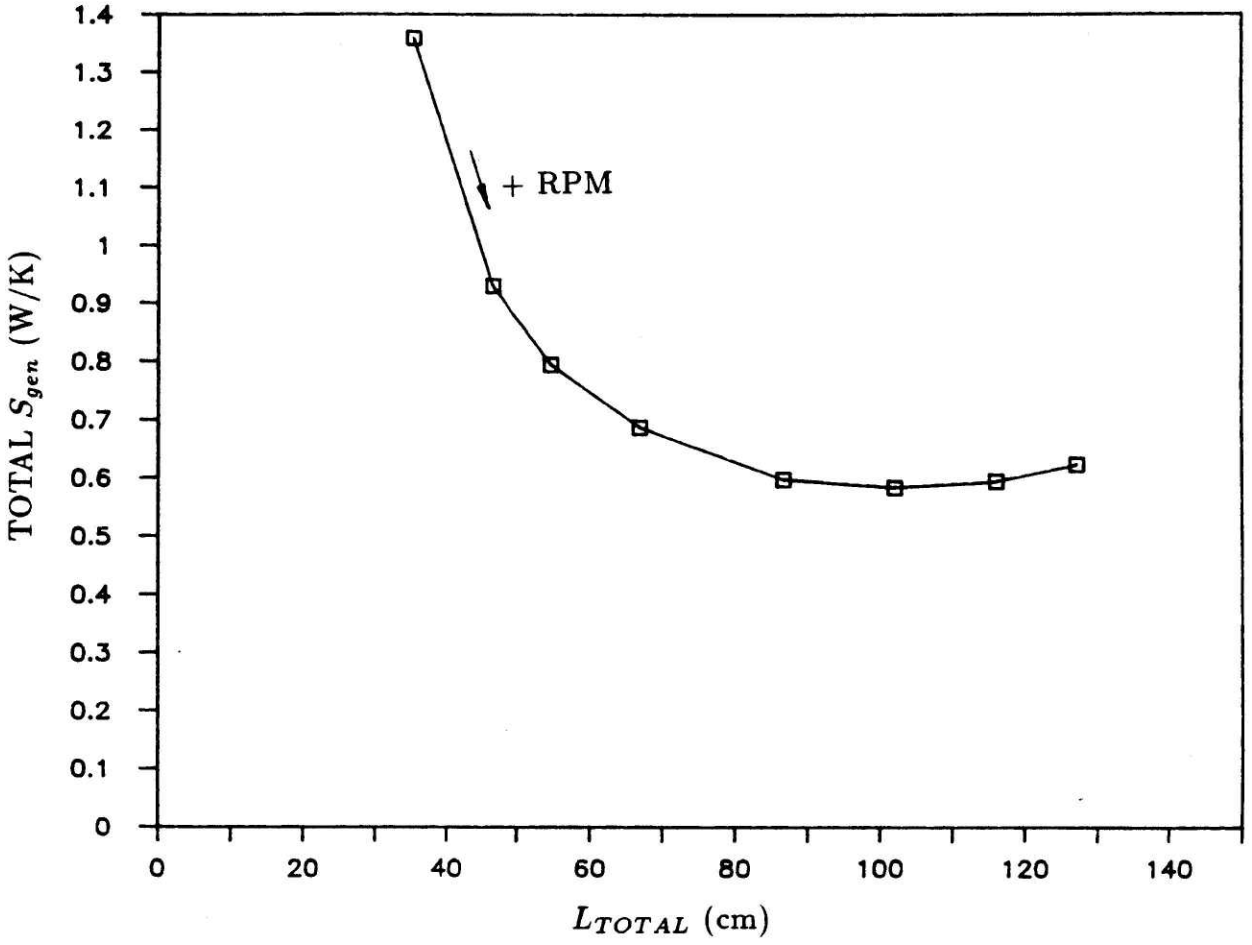

Fig. (2.5) Total entropy generation versus total heat exchanger length.

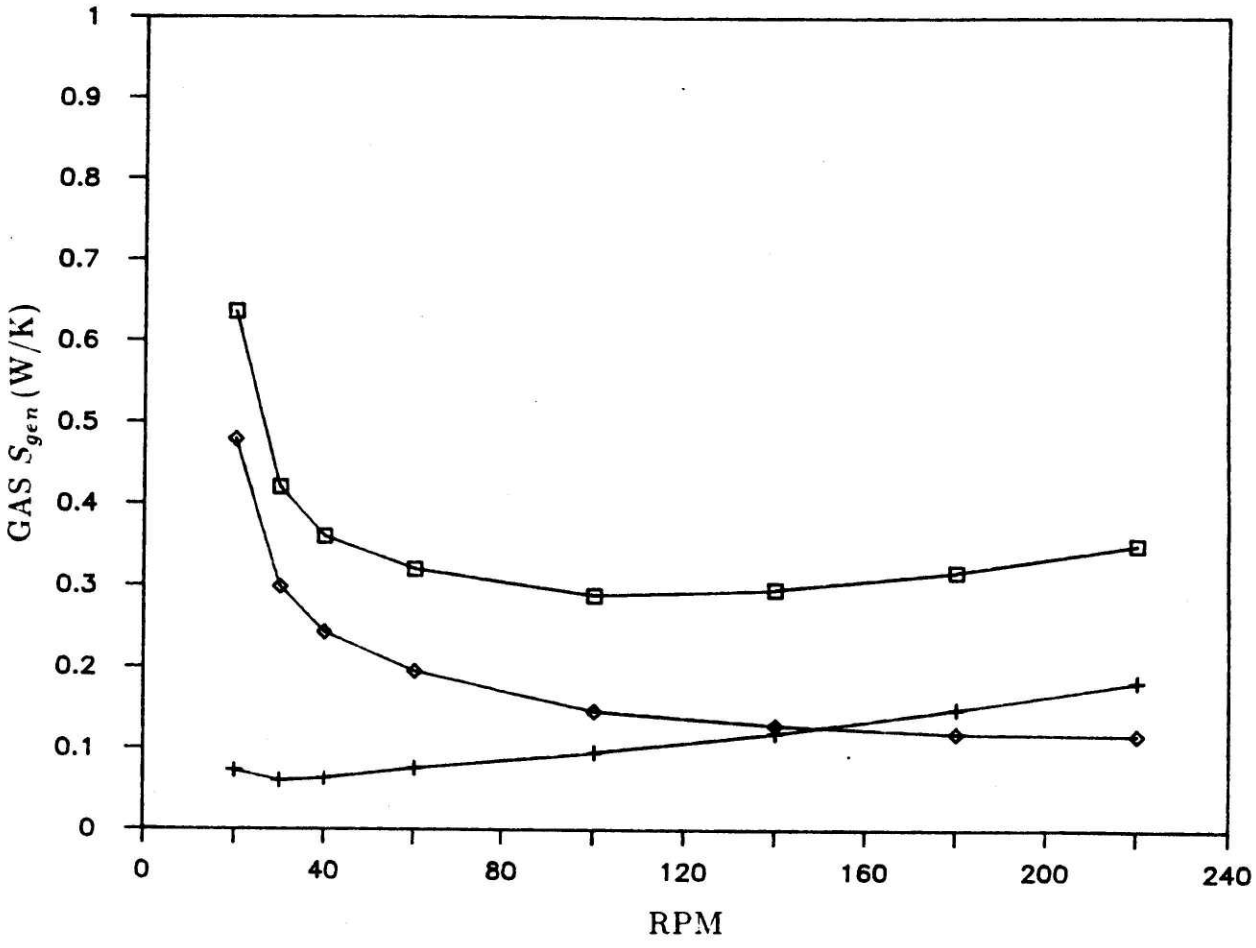

Fig. (2.6) Entropy generation in the gas versus engine speed.

The distribution of total entropy generation in the gas is observed to have a minimum when the cryocooler is designed to operate at about 100 RPM. To better understand this distribution, ideal gas relations were used to plot individual entropy generation values due to changes in pressure and temperature. Only data from heat exchangers operating above 70 K was used for these ideal gas plots. At lower engine speeds, entropy generation is due mostly to changes in temperature. This trend is indicative of the increase in heat exchange $\Delta T / T$ for lower engine speeds, resulting from a shorter stack length and increased axial conduction, as discussed earlier. Entropy generation in the gas due to pressure changes increases linearly with engine speed. This trend is the result of increased heat exchanger length with increasing engine speed, since the pressure drop in the heat exchanger is directly proportional to the heat exchanger length. Again, if necessary, this entropy generation may be controlled by a change in the helix angle of the low-pressure side of the heat exchangers or by variation in the bore to stroke ratio. Also, the magnitude of pressure drop is much larger in the warmer heat exchangers than in the colder ones.

Figure (2.7) is a plot of entropy generation in the engines versus engine speed. Individual contributions of entropy generation from the wet expander, vapor compressor, and dry expansion engines are plotted along with their sum. The entropy generation is observed to increase substantially at the low values of engine speed because the mass flow through the expander must be higher to remove the additional axial conduction heat leak that occurs for the slower engine speeds and, thus, shorter stack lengths. This increase may be explained by looking at Eqn. (2.1) for entropy generation in the engines. Notice that the change in entropy of the gas, $(s_{in} - s_{out})$, depends only on the engine inlet state and the adiabatic engine efficiency; thus, for small variations in the inlet conditions for different engine speeds, the change in entropy of the gas is nearly constant. The rapid increase in $S_{gen,engine}$ at lower engine speeds is therefore due to an increase in mass flow rate.

Results from this section indicate the interdependencies of the various cryocooler components. Although experiments must be performed to better predict

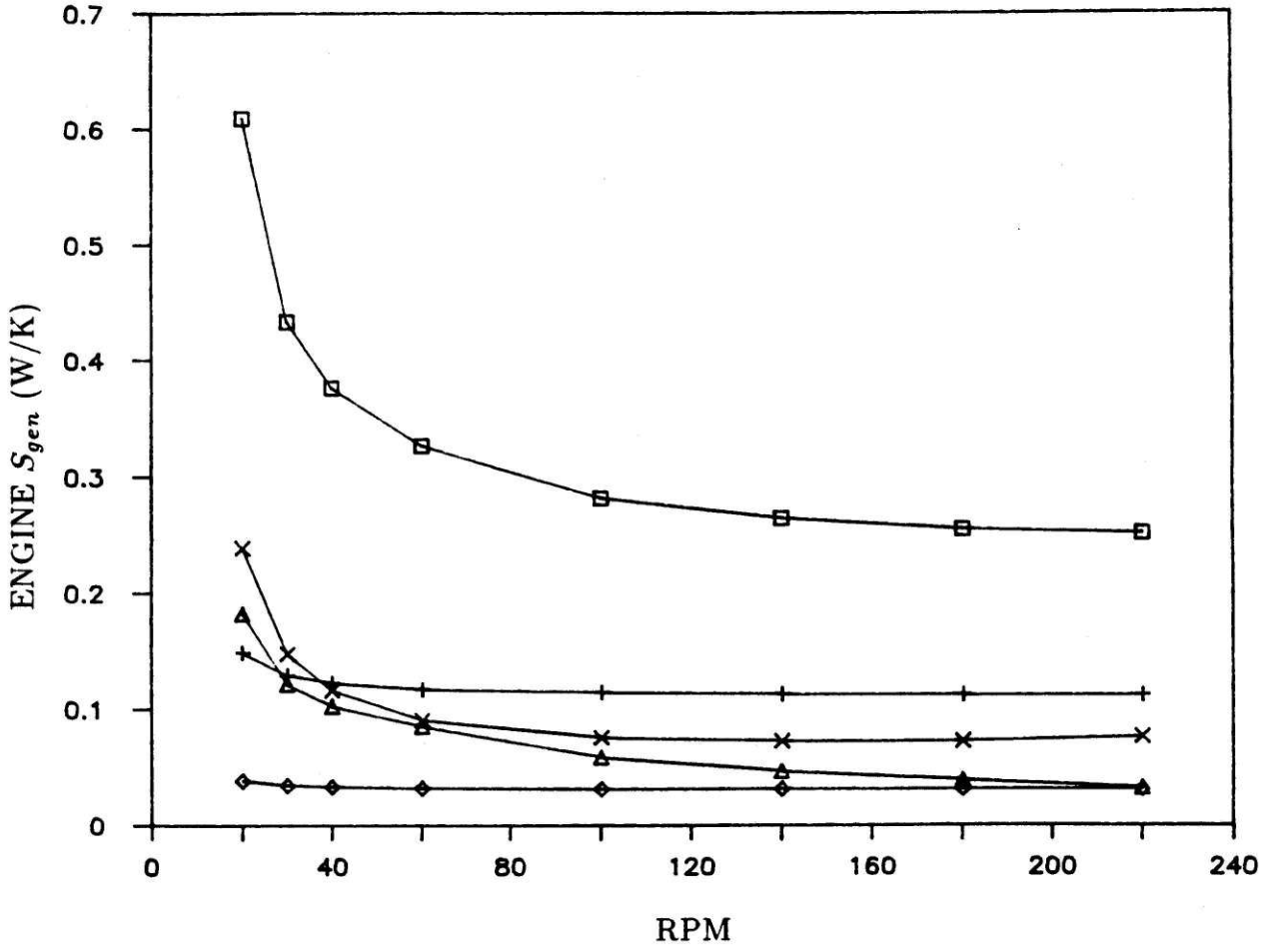

Fig. (2.7) Entropy generation in the engines versus engine speed.

Table (2.2) Computer output specifications for a representative 1 W cryocooler.

Parameter	Value
Engine speed	60 RPM
$TE(1)$	36.6 K
$TE(2)$	137 K
$\Delta T / T$	0.05
Mass flow at 4.2 K	0.085 g/s
Mass flow rate through engine (1)	0.050 g/s
Mass flow rate through engine (2)	0.052 g/s
Total mass flow rate	0.187 g/s
Bore and stroke of engine (1)	19 mm
Bore and stroke of engine (2)	22 mm
Total heat exchanger/wet expander length	62 cm
Length of engine (1)	35 cm
Length of engine (2)	12 cm
Lumped heat leak at 4.2 K	0 W
Lumped heat leak before wet expander	0.02 W
Lumped heat leak before engine (1)	0.41 W
Lumped heat leak before engine (2)	4.9 W

component performances, this analysis does indicate some general results that may be used for a preliminary cryocooler design. First, the mass flow rate at the warm compressor should be less than 0.2 g/s. For a three-stage warm compressor with intercooling and isentropic efficiencies of 0.85 per stage, the power requirement is less than 400 W. This power requirement is much less than that required for Stirling/J-T or Gifford-McMahon/J-T combination cycles. The analysis also indicates cryocooler dimensions that may be expected to yield the specified operating conditions with good thermodynamic efficiency. The cryocooler length specified as a design criterion is 60 cm. For this length, the analysis indicates that a bore and stroke of approximately 20 mm X 20 mm is needed. A detailed list of computer outputs for a representative cryocooler is given in Table (2.2).

The most important result of this analysis has been to identify an integral concentric tube heat exchanger and expander configuration that may be feasible for cryocooler use. After examining the effects of scaling the cryocooler to different heat capacities at liquid helium temperatures, the remainder of this document will focus on development of the integral expander and exchanger.

2.5 Implications for Additional Cryocooler Miniaturization

Up to this point, the cryocoolers considered were designed to sustain an applied heat load of 1 W at 4.2 K. The possibility of using the concentric tube arrangement for applications requiring further miniaturization is examined next. Cryocooler capacities in the range of 0.15 W to 0.3 W are considered. Since the applied heat load is a variable, the engine speed is preselected to be 80 RPM. This engine speed resulted in efficient operation in the longer cryocooler considered in the previous section, so it is used again here. The overall length specification will be reduced to a range averaging about 25 cm. This length is somewhat arbitrarily chosen to be about half of the length of the cryocoolers considered in the previous section. For this length, approximately 100 cm^2 of heat exchange area is needed for heat exchange temperature ratios in the range of 0.02 to 0.07. Otherwise, the system considered here is the same as in Section (2.4.2); specifications are given in Table (2.1), except that the total heat exchange area is 100 cm^2, the engine speed is 80 RPM, and the applied heat load is the variable.

The mass flow rate at the warm compressor is shown as a function of applied heat load in Fig. (2.8). The increase in mass flow rate is primarily due to increased heat exchange irreversibilities, as indicated in Fig. (2.9) by the plot of heat exchange temperature ratio versus load. Irreversibility due to axial conduction becomes important as the applied heat load is reduced. Figure (2.10) is a plot of both entropy generation due to irreversibilities in the gas and due to axial conduction versus heat load. Entropy generation in the gas includes losses due to both temperature and pressure changes.

Other observations can be made by examining the optimal values of dry ex-

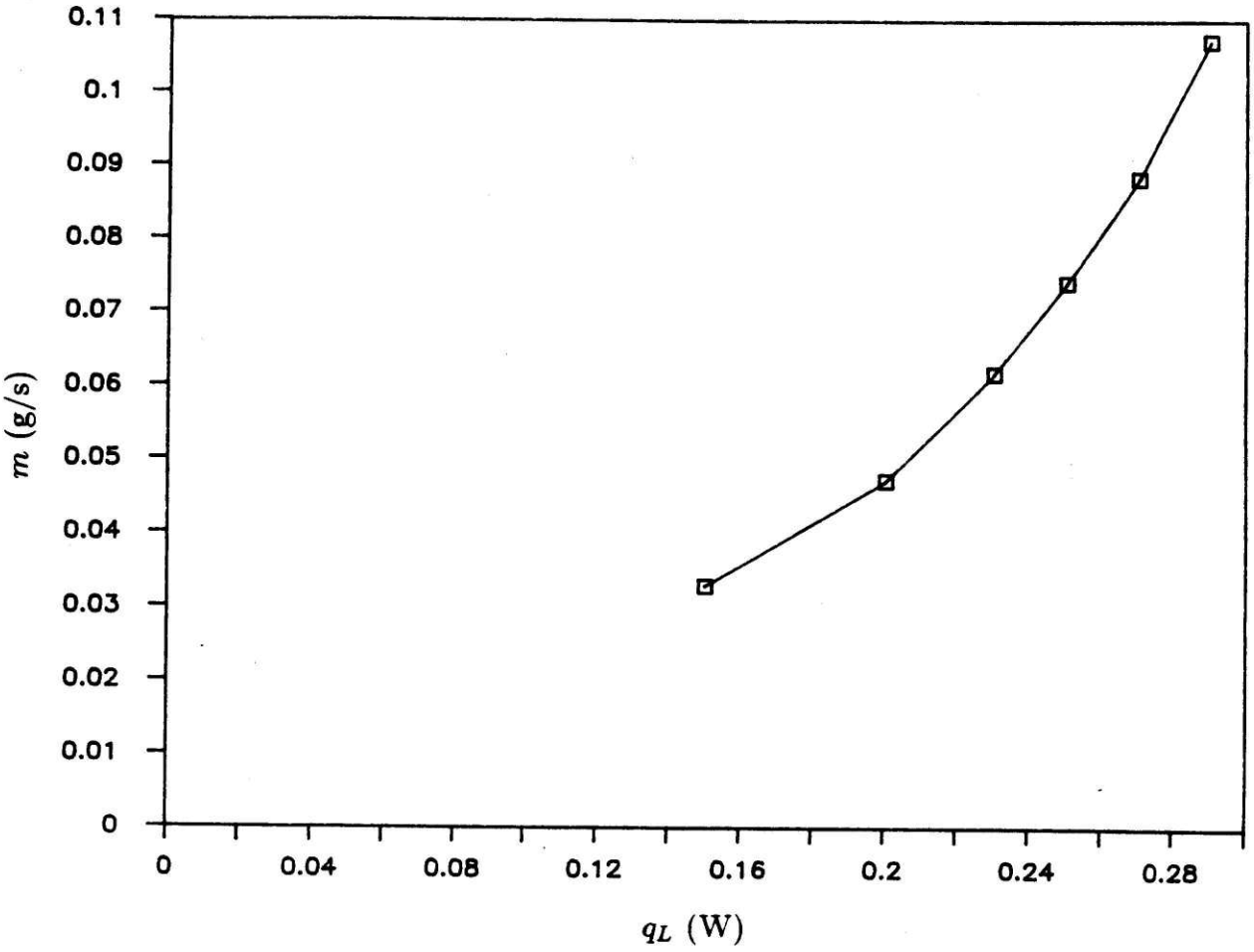

Fig. (2.8) Total mass flow rate versus refrigeration heat load.

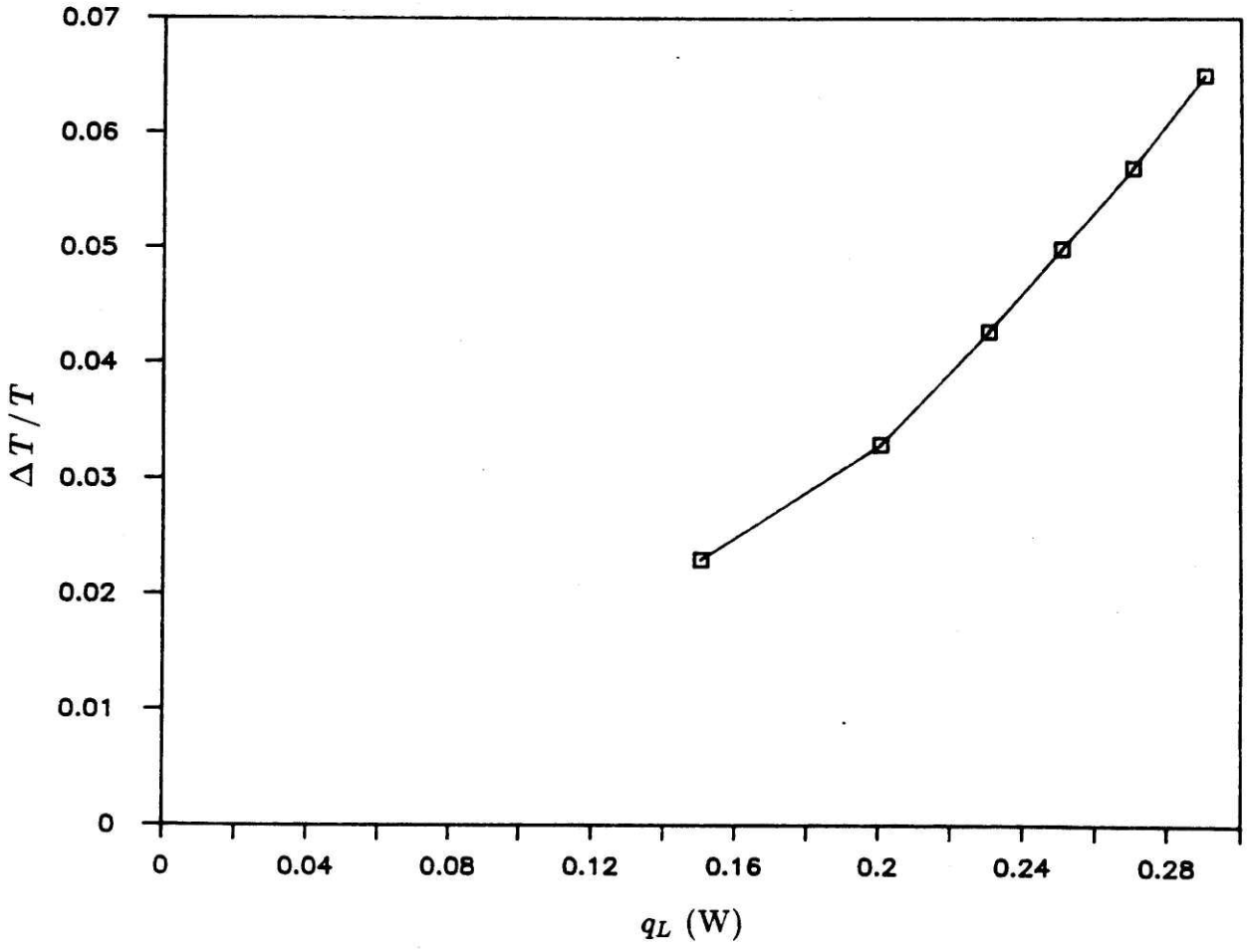

Fig. (2.9) Heat exchange temperature ratio versus refrigeration load.

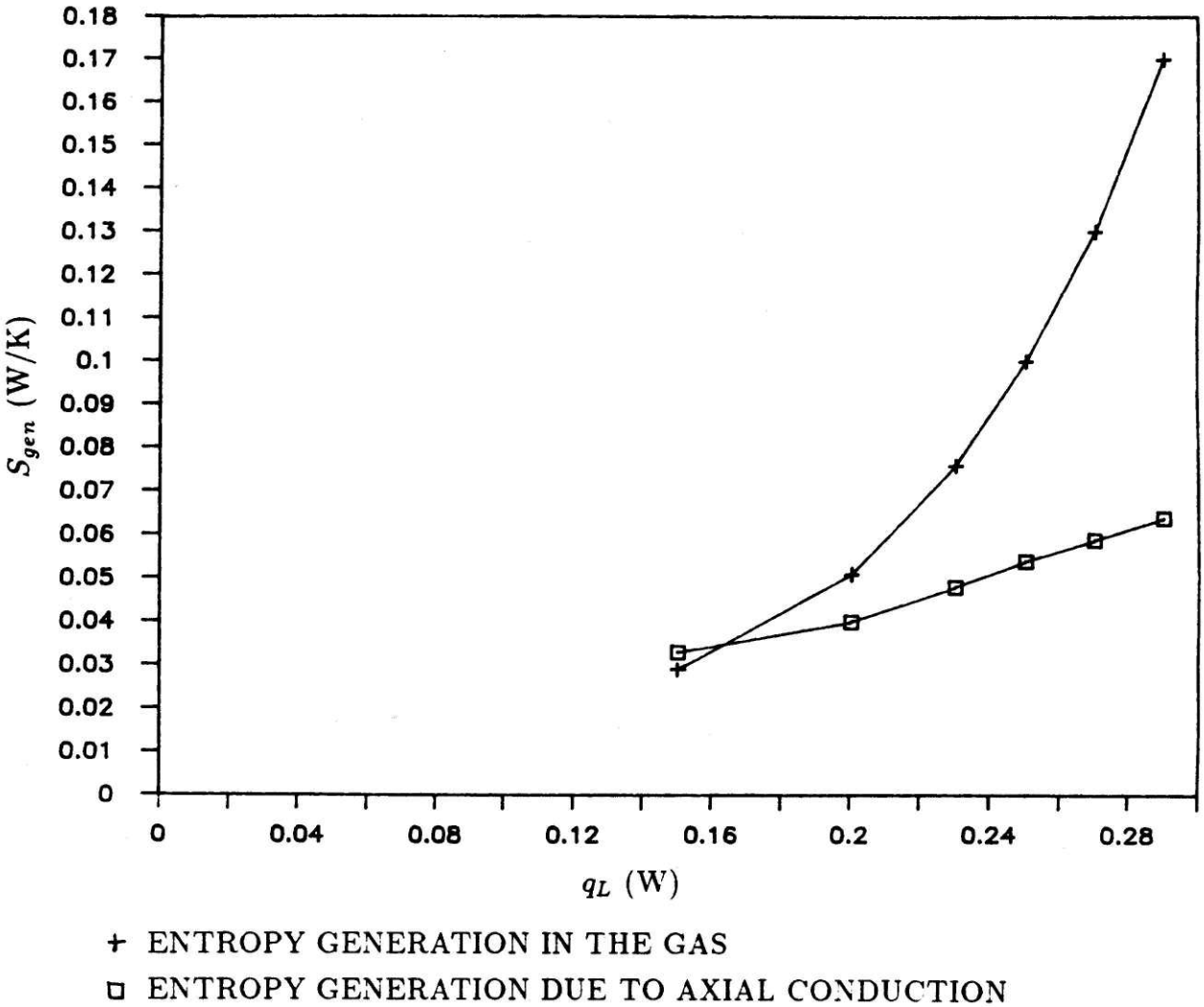

Fig. (2.10) Comparison of entropy generation in the gas and due to axial conduction versus heat load.

pander inlet temperatures. As stated in the preceeding section, the inlet temperature to the coldest dry expander must be chosen to yield pinch point locations at the outlet from the coldest dry expander and the inlet to the wet expander, with a heat exchanger located between. This design rule remains valid for smaller systems with smaller applied heat loads. As before, the rule should be used only for exchangers with $\Delta T / T < 0.06$.

Another observation is that the optimal inlet temperature to the warmer dry expander increases as the magnitude of applied heat load decreases. The resulting higher optimal inlet temperature to the warm expander may be explained as a result of trade offs between heat exchange irreversibilities and conduction heat leak irreversibilities. As another point, the lumped axial conduction heat leak is removed at the expansion engines, as discussed earlier. Since axial conduction is larger at warmer temperatures due to larger stainless steel thermal conductivity, most of the axial conduction heat leak is removed at the warmer dry expansion engine.

The computer results indicate that the concentric tube heat exchanger and expansion engine configuration is thermodynamically suited for cryocoolers designed for heat loads of less than 1 W at 4.2 K. Results for a representative cryocooler with a 0.25 W heat load are given in Table (2.3). Engine bores of 14 mm should be no more difficult to fabricate than those for the 1 W cryocoolers.

2.6 The Integral Heat Exchanger and Expansion Engine

Results from previous sections indicate that the integral concentric tube heat exchanger and expansion engine may be adequate for cryocoolers employing the saturated vapor compression cycle. This section discusses modifying the concentric tube heat exchanger for use in a miniature system. The modification consists of using the gap between the displacer and cylinder as the high-pressure heat exchange passage. An outer shell is then placed over the cylinder to form the low-pressure side. Spiral spacers separate the cylinder from the outer shell. In this arrangement, the inlet valve is located at room temperature and the exhaust valve is located at the refrigeration temperature. A discussion of how this integral exchanger and expander

Table (2.3) Computer output specifications for a representative 0.25 W cryocooler.

Parameter	Value
Engine speed	80 RPM
$TE(1)$	36.6 K
$TE(2)$	155 K
$\Delta T / T$	0.05
Mass flow at 4.2 K	0.023 g/s
Mass flow rate through engine (1)	0.028 g/s
Mass flow rate through engine (2)	0.024 g/s
Total mass flow rate	0.074 g/s
Bore and stroke of engine (1)	14 mm
Bore and stroke of engine (2)	14 mm
Total heat exchanger/wet expander length	24 cm
Length of engine (1)	14 cm
Length of engine (2)	5.5 cm
Lumped heat leak at 4.2 K	0 W
Lumped heat leak before wet expander	0.03 W
Lumped heat leak before engine (1)	0.82 W
Lumped heat leak before engine (2)	4.0 W

can be used in the SVC cycle follows. The standard SVC cycle configuration must be modified. This modification relaxes two constraints that are indigenous to the standard SVC cycle configuration: constant mass flow rate in the heat exchange passages and constant high-side and low-side pressures.

The integral configuration is modified as shown in Figure (2.11). The basic configuration is a long displacer in a close-fitting thin-walled cylinder. The inlet valve admits high pressure helium gas to the warm end of the displacer-to-cylinder gap. The gas flows through the gap to the expansion volume at the cold end of the displacer. The exhaust valve in the cold head of the cylinder exhausts the gas after expansion to the return side pressure. The gas then returns to the warm end of the engine between an outer shell and the cylinder. A spiral spacer guides the flow

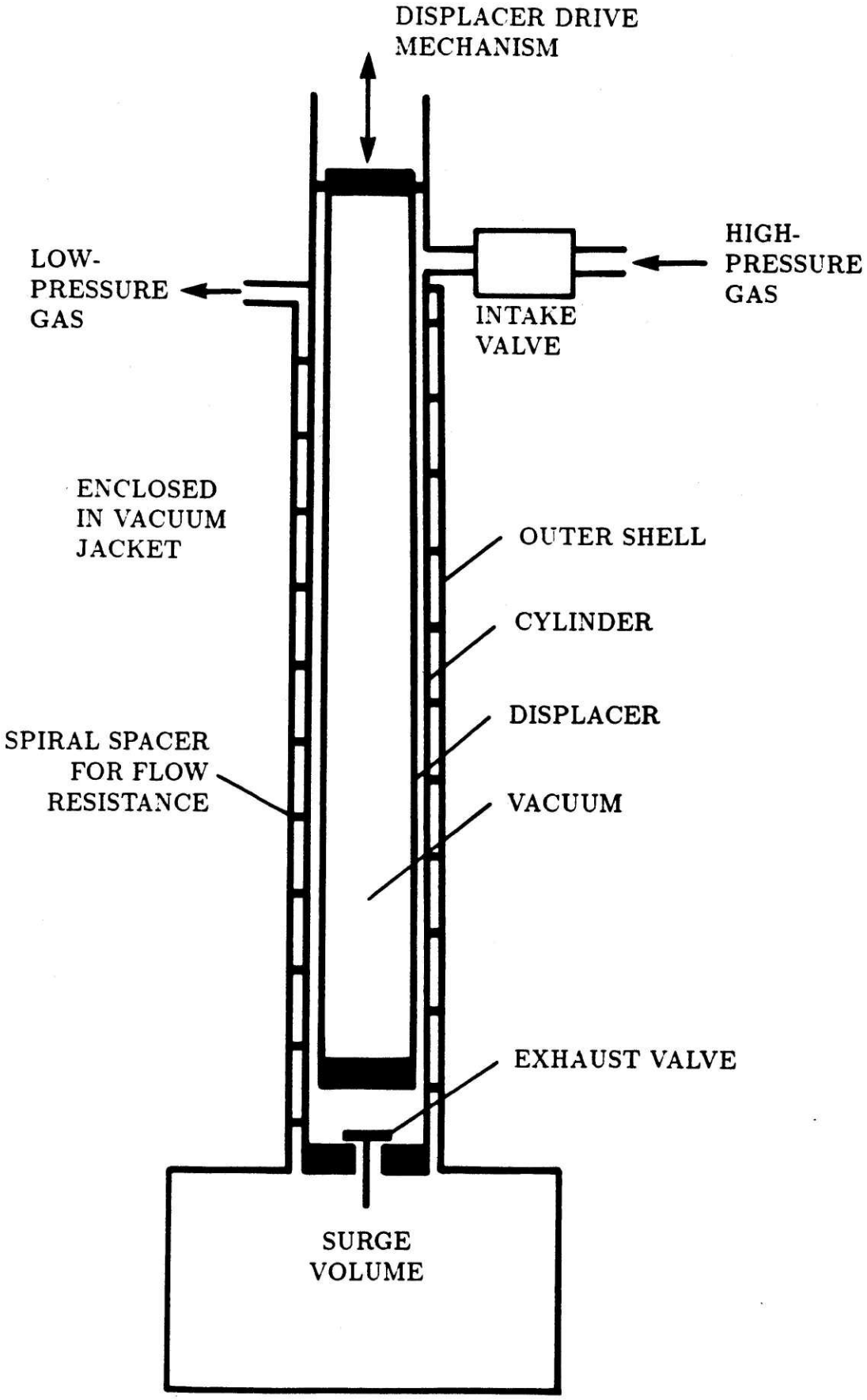

Fig. (2.11) Schematic of the flow circuit for the integral expander and exchanger.

around the cylinder in an effort to minimize the flow maldistribution loss.

One reason for using the cylinder as the wall between the high- and low-pressure streams is because axial conduction is reduced. Using the cylinder as the heat exchange surface eliminates the need for another tube to serve that purpose. Reducing the number of concentric tubes needed also makes the integral unit easier to manufacture. An assembly procedure for the concentric tube configuration will be described in Chapter 4.

Placing the inlet valve at room temperature and the exhaust valve at the refrigeration temperature has two important implications. First, a valve operating at room temperature is considered to be more reliable than one at cold temperatures. At cold temperatures, condensation of gas contaminants may result in valve leakage. Also, opening and closing a cold valve requires either a cold valve actuator or a valve actuator operating at room temperature that provides a path for thermal conduction to the cold box. Second, the cylinder head needs to accommodate enough space for only one valve, which allows design of the exhaust valve for minimal pressure drop and results in a less cumbersome manufacturing procedure.

2.7 Implications for Multi-Staged Cryocooler Design

Other cycle configurations employing the integral exchanger and expander described in the previous section can be devised by modifying the SVC cycle configuration shown in Fig. (2.1). Before looking at these modifications, a couple of points concerning the cycle shown in Fig. (2.1) will be mentioned to better indicate how the cryocooler components achieve SVC cycle refrigeration. In the SVC cycle configuration considered so far, both the inlet and exhaust valves operate at the refrigeration temperature. The low-pressure exhaust from a dry expansion engine is used to help keep the heat exchange temperature ratio, $\Delta T / T$, constant along the stack length. Keeping the temperature ratio constant is achieved by increasing the mass flow rate on the low-pressure side of the heat exchanger, thereby closely matching the heat capacity rates on the high- and low-pressure sides. Second, the cycle shown in Figure (2.1) requires complicated plumbing that would be difficult to

use in a miniature system. Headers would be needed to limit flow maldistribution at the plumbing connections for the dry expanders. Also, extraction of high-pressure gas for the expanders would be difficult.

The cycle configuration shown in Figure (2.12) operates similar to the one in Figure (2.1) except that the high- and low-pressure streams are separated into three streams at the room temperature inlet. This configuration has at least two advantages over the one shown in Figure (2.1). First, the helium gas for the dry expanders is not extracted from the high-pressure stream, which eliminates the need for tedious plumbing requirements. Second, the heat exchangers each extend from the cryocooler top plate which is at room temperature. A disadvantage of this configuration is that additional valves would be needed to properly divide the low-pressure flow to match the heat capacity rates.

Another approach to keeping the temperature ratio constant along the heat exchanger stack is to remove energy directly from an adjacent heat exchanger as shown in the cycle configuration of Figure (2.13). This configuration has the same advantages as the one shown in Figure (2.12). Another advantage is the use of a thermal conduction path to eliminate the need for connecting the integral exchanger and expander units using helium gas flow tubes. This thermal conduction path adds an additional heat exchange irreversibility, but simplifies assembly of the cryocooler. The irreversibility due to mixing of the engine exhaust with low-pressure flow, as in the configurations of Figures (2.1) and (2.12), is eliminated. This mixing irreversibility results from improper design or from operation at other than the design values.

An analytical study of these two configurations would yield the same theoretical trends as those for the configuration in Figure (2.1). Keeping the heat exchange temperature ratio constant over the exchanger stack length is the strategy of all three SVC configurations considered. The magnitudes of the irreversibilities will be different for the three configurations because the physical components are different. For this reason, optimal values of such parameters as dry expander inlet temperature may differ among the three configurations.

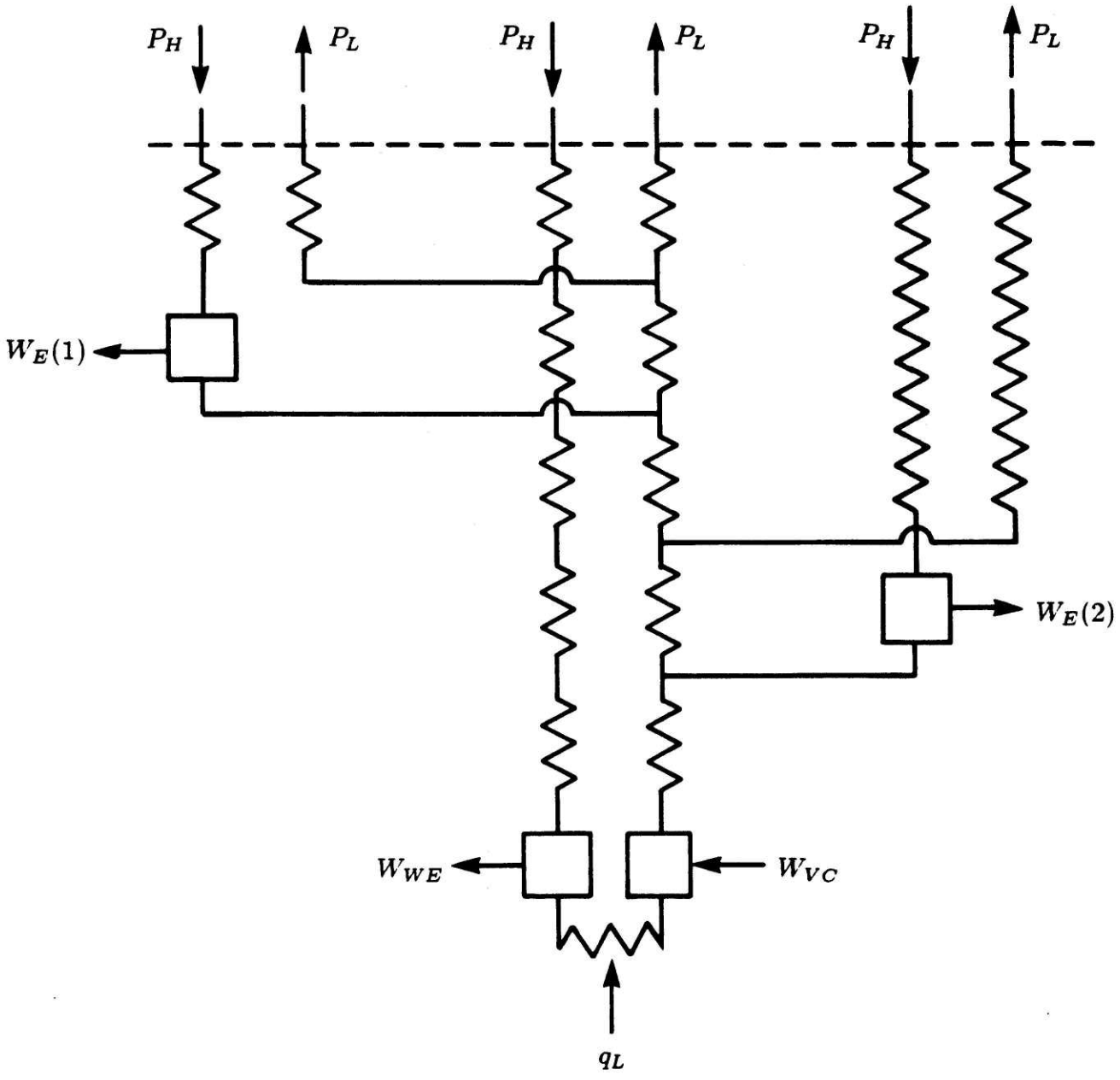

Fig. (2.12) Variation of SVC cycle configuration used with integral expander and exchanger.

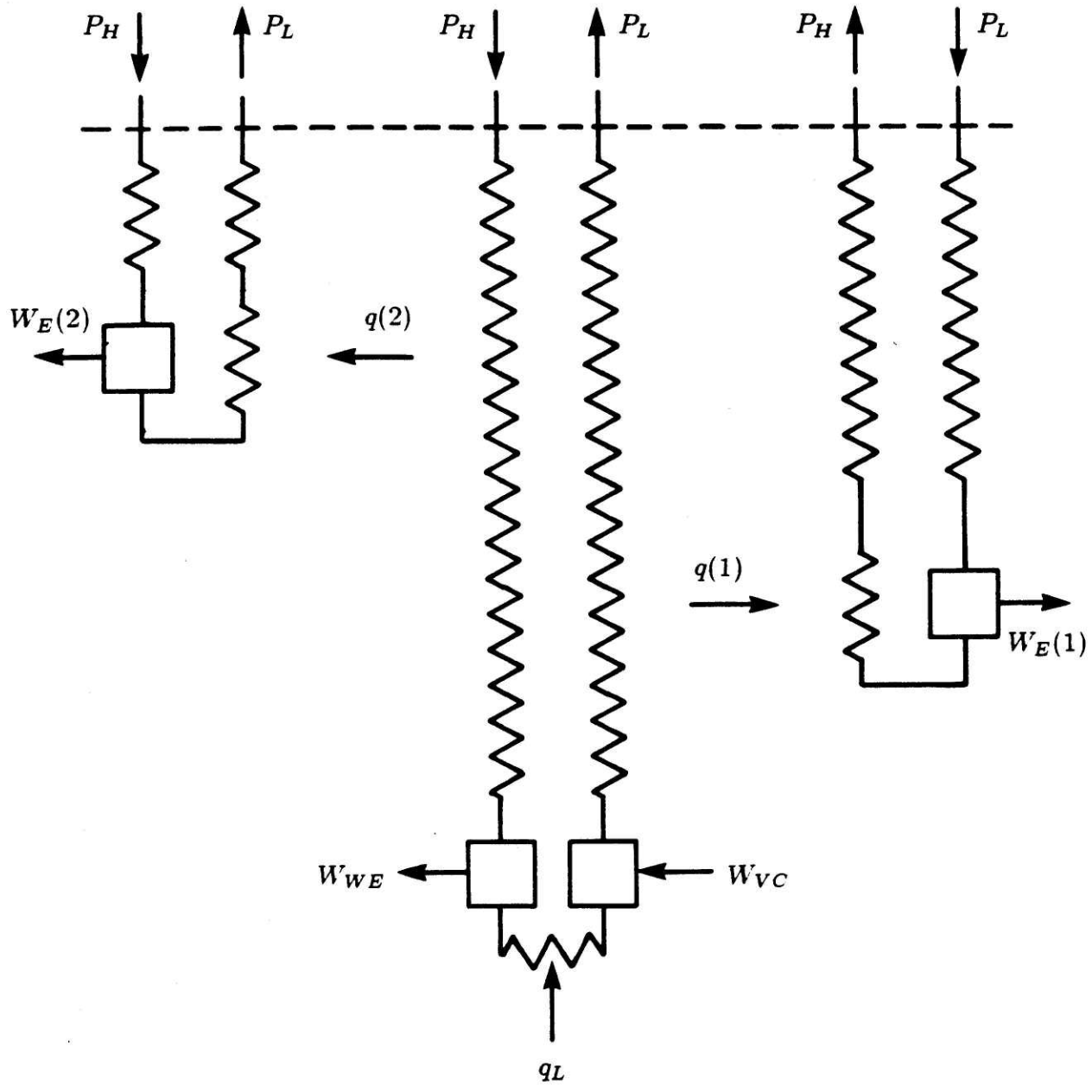

Fig. (2.13) Independent heat exchanger and expansion engine configuration using conduction paths.

The remaining chapters are devoted to the analytical and experimental development of an integral heat exchanger and expansion engine that could be easily used in the modified SVC cycle configuration shown in Fig. (2.13).

Chapter 3

Performance Algorithm for an Integral Concentric Tube Heat Exchanger and Expansion Engine

In Chapter 2, an integral heat exchanger and expansion engine was identified as a major component for a cryocooler using a modified SVC cycle. This chapter presents an algorithm that is used to design the single-stage cryocooler of Chapter 4. The overall performance algorithm consists of two integral algorithms: one used to model the heat exchange and another to model an adiabatic expansion process followed by a lumped heat input. An overall description of the model is first given, which includes the input and output parameters. The heat exchange algorithm is next developed in terms of an average enthalpy flow at a cross section. This average enthalpy flow consists of enthalpy flows due to counterflow heat exchange and displacer motion. The performance algorithm is then described and several results are given. In this chapter, descriptions of the various performance algorithm components include very few equations. For a detailed mathematical development of the average enthalpy flow at a cross section and of the performance algorithm, refer to Appendix B.

Design of the integral heat exchanger and expander component is intended to combine the advantages of regenerative heat exchange and counterflow heat exchange in a single package that uses a displacer type expansion engine. In totally regenerative cycles, the pressure ratio is effectively limited by the gas volume in the regenerator, which must be large enough so that the low-pressure flow pressure drop through the regenerator matrix is not excessive. In the integral expander and exchanger configuration, the displacer-to-cylinder gap-regenerator passes high-pressure flow, allowing the pressure ratio to be chosen for greater work extraction rather than minimal pressure drop. Because the low-pressure return flow effectively adds heat capacity to the regenerator walls, counterflow heat exchange significantly reduces vulnerability to diminishing regenerator wall heat capacity at low temperatures, adding yet another advantage to the integral configuration.

3.1 Description of the Model

A schematic of the situation to be modeled is shown in Fig. (3.1). When the inlet valve opens, high pressure gas enters the gap between the displacer and cylinder at room temperature and flows axially to fill the dead volume. The remainder of the intake portion of the cycle occurs after the dead volume is pressurized and the displacer begins to move so that gas flows into the working volume at a high rate. After the intake valve closes, expansion begins and a decreasing amount of gas flows into the working volume. At the end of expansion, the displacer changes direction and the exhaust valve opens, so the gas in the working volume is forced into a surge volume. The exhaust valve then closes and the remaining gas in the working volume is recompressed. The gas in the surge volume returns to room temperature on the low-pressure side of the counterflow heat exchanger between the cylinder and an outer shell.

As stated earlier, the complete performance algorithm for the situation shown in Fig. (3.1) consists of two analyses. The first analysis involves modeling of the heat exchange process. The output from the analysis is an average enthalpy flow into the cold end due to counterflow heat exchange and displacer motion. The output from the first analysis is an input to the second analysis. The second analysis is a simple energy balance on the cold end, consisting of an average enthalpy flow, conduction heat leak, applied heat load, and work output. In the remainder of this section a brief introduction to the two analyses will be given in an effort to identify the primary inputs and outputs to the overall performance algorithm.

Coordinates for the enthalpy flow analysis at a cross section are shown in Fig. (3.2). For determining the rate of enthalpy flow at any cross section (*i.e.*, at any x), the x coordinate is measured from a position at the axial center of the heat exchanger. To find the average rate of enthalpy flow over the exchanger length to be used in the energy balance of Fig. (3.3) to be used in the second analysis, the position of $x = 0$ is relocated to the cold end of the heat exchanger. In both cases, the y coordinate, which is attached to the displacer, coincides with the x coordinate

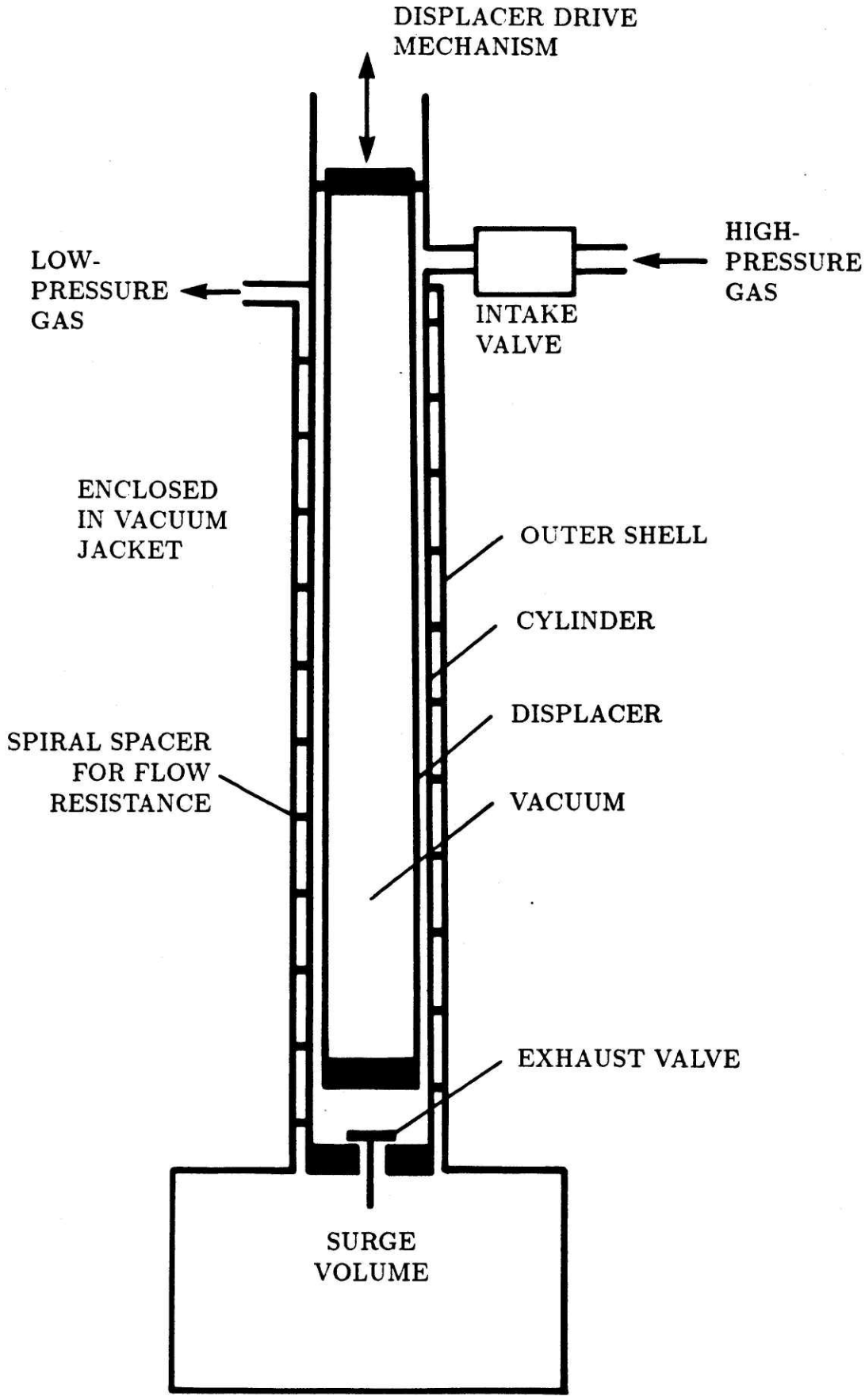

Fig. (3.1) Schematic of the flow circuit for the integral expander and exchanger.

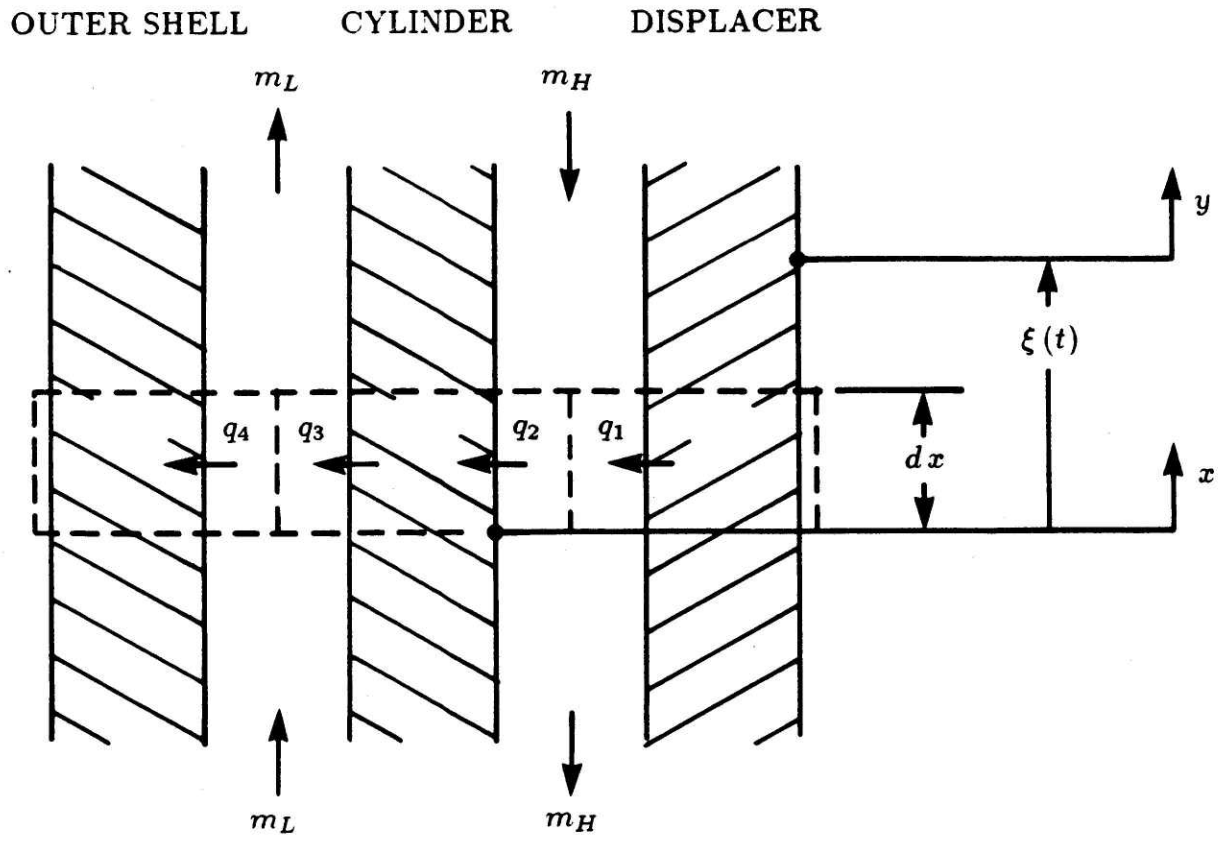

Fig. (3.2) Coordinate system used to develop heat transfer equations for the average enthalpy flow rate equation.

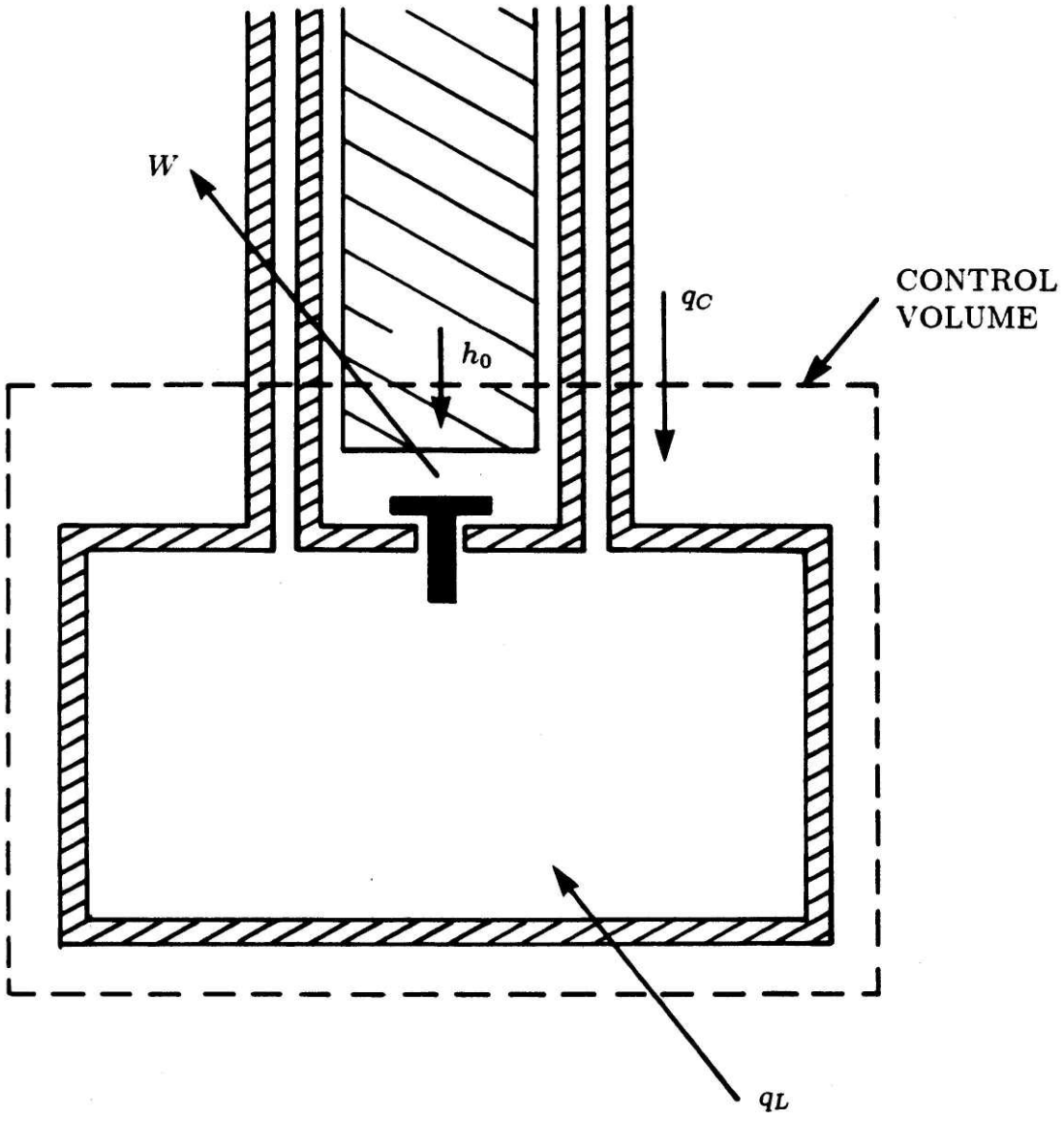

Fig. (3.3) Control volume used for the performance algorithm.

at $t = 0$.

The heat exchange model requires defining the mass flow rates and the displacer position as inputs. To make the flow on the low-pressure return side more steady, a surge volume is located at the cold exhaust and an appropriate flow resistance is built into the return passage to form a flow circuit with resistive and capacitive (RC) characteristics. Rather than complicate the mathematical expression for the return mass flow rate by using a constant mass flow with a sinusoidal mass flow superimposed, the mass flow rate on the low-pressure side is assumed to be constant.

The flow on the high-pressure side is periodic. Flow between the displacer and cylinder is maximum just after the intake valve opens and during the initial portion of expansion. Mass flow toward the cold end is small when the displacer is moving downward and the exhaust valve is open. When the exhaust valve closes, recompression begins. At this time, flow between the displacer and cylinder is toward the warm end. Using the coordinate system described earlier, general expressions for the displacer position and the high-pressure side mass flow rate are selected. Since these expressions must be general enough to describe most cases of interest, Fourier series are used. Nondimensional expressions for the displacer position, ξ, and the high-pressure side mass flow rate, m_H, are

$$\frac{\xi}{s} = \sum_{n=1}^{\infty} G_n \sin n\omega t \tag{3.1}$$

$$\frac{m_H c_p z_H}{2\pi D_H s k_g} = \sum_{n=1}^{\infty} (H_n \cos n\omega t + I_n \sin n\omega t) + \frac{M_H c_p z_H}{2\pi D_H s k_g} \tag{3.2}$$

where the symbols are defined as

ξ: The displacer position as a function of time.

s: The stroke for the displacer.

G_n, H_n, I_n: Fourier series constants.

ω: Circular frequency of the displacer.

t: Time variable.

m_H: Mass flow rate on the high-pressure side.

c_p: Specific heat at constant pressure for the gas.

z_H: Displacer-to-cylinder gap width.

D_H: Average diameter of the displacer-to-cylinder gap.

k_g: Thermal conductivity of the gas.

M_H: Time-averaged mass flow rate.

As defined, actual mass flow rates that may mathematically consist of a constant with sinusoidal terms are expressed with the small case letter, m. Time-averaged mass flow rates are expressed with the capital letter, M. Both Eqns. (3.1) and (3.2) are intended to be general enough for most cases of interest. The development presented in this chapter will assume that the mass flow equation is a sinusoid, so that $H_n = 0$. Both the position and the mass flow rate are assumed to be first order functions of time so that $n = 1$. For sinusoidal motion with the x and y coordinates being coincident at $t = 0$, the coefficient $G_1 = 0.5$. Enthalpy flow expressions for the more general case are given in Appendix B.

The remainder of the inputs to the heat transfer analysis are given in the first half of Table (3.1). The only inputs listed in this part of the table that are not inputs to the heat transfer analysis are the adiabatic engine efficiency, η_E, and the conduction heat leak, q_C, which are used only in the energy balance of the second analysis. Outputs from the heat exchange analysis include the average cyclic and non-cyclic average enthalpy flow at the cold end and the cold-end temperatures of the displacer, cylinder, and outer shell as functions of time.

The second analysis of the performance algorithm is based on an energy balance on the control volume shown in Fig. (3.3). Energy is removed from the control volume in the form of work, W. The refrigeration load is q_L. Heat leak due to axial conduction is q_C. The total enthalpy flow into the cold section, h_0, consists of enthalpy flow due to counterflow heat exchange, h_{nc0}, and due to displacer motion heat leak, h_{c0}. These enthalpy flow values are inputs to the cold-end energy balance from the heat transfer analysis. Outputs from the energy balance analysis include the work, W, and load, q_L. The conduction heat leak was decoupled from the other

heat exchange terms to reduce the complexity of the heat exchange analysis without compromising accuracy.

All inputs and outputs to the overall performance algorithm are given in Table (3.1). The inputs include all of the physical dimensions and operating specifications, such as engine speed and pressures. Inputs based upon performance estimates include the refrigeration temperature, end-to-end temperature difference, and average mass flow rate.

Two important performance parameters which must be input to the performance algorithm are the adiabatic engine efficiency and the heat exchanger performance. Estimates of both are based upon efficiencies obtained by other experiments in this laboratory. The adiabatic engine efficiency is an input to the energy balance analysis. The heat exchanger performance is an input to the heat transfer analysis. A temperature difference at the cold end is computed for each run based on a single estimate of heat exchanger performance that is internal to the computer code, rather than inputing the value of temperature difference for each run. The time-averaged temperature difference at the cold end varies due to input variations of the high- and low-pressure radial gaps. The single estimate of heat exchanger performance consists of an estimate of heat exchange temperature ratio for reference values of high- and low-pressure gaps. For all of the results presented in this chapter, the reference heat exchanger performance will be for a temperature ratio of 0.15 at 80 K. Thus,

$$\left.\frac{\Delta T}{T}\right)_{h0,ref} = 0.15 \text{ at } T = 80\,\text{K}$$

for the case of

$$z_{H,ref} = 0.127\text{mm}$$

$$z_{L,ref} = 0.254\text{mm}$$

where $z_{H,ref}$ is the reference value of high-pressure radial gap width and $z_{L,ref}$ is the reference low-pressure radial gap width. The temperature difference at the cold

Table (3.1) Inputs and outputs to performance algorithm

Input Parameters

Parameter	Definition
D_H	diameter of high-pressure stream gap
D_L	diameter of low-pressure stream gap
D_c	mean diameter of cylinder
t_d	displacer wall thickness
t_c	cylinder wall thickness
t_s	outer shell wall thickness
ω	circular frequency of displacer
s	stroke
η_E	adiabatic engine efficiency
$\left.\frac{\Delta T}{T}\right)_{h0,ref}$	heat exchanger performance parameter (fixes value of A_{HE})
ρ_m	wall density
c_m	wall specific heat
M_L	time averaged mass flow rate
L	overall exchanger length
q_C	axial conduction heat leak
P_H	mean high-pressure side pressure
P_L	low-pressure side pressure
ΔT	end-to-end temperature difference
T_R	refrigeration temperature
z_H	high-pressure side radial gap
z_L	low-pressure side radial gap

end is computed using

$$\Delta T)_{h0} = \frac{z_H + z_L}{z_{H,ref} + z_{L,ref}} \Delta T)_{h0,ref} \tag{3.3}$$

where the subscript "ref" indicates reference values. When using Eqn. (3.3) to compute $\Delta T)_{h0}$ for the various values of z_H and z_L, the total heat exchange surface

Table (3.1) (cont.)

Output Parameters

Parameter	Definition
h_{c0}	periodic enthalpy flow at $x = 0$
h_{nc0}	non-periodic enthalpy flow at $x = 0$
h_0	enthalpy flow at $x = 0$
q_L	refrigeration load
W	work output of expansion engine
$T_d(-\xi, t)$	displacer temperature at $x = 0$
$T_c(0, t)$	cylinder temperature at $x = 0$
$T_s(0, t)$	outer shell temperature at $x = 0$

area, A_{HE}, remains constant. The total heat exchange area is calculated as

$$A_{HE} = \pi D_c L$$

where D_c is the mean cylinder diameter and L is the total exchanger length. Both D_c and L are inputs to the analysis. As explained in Appendix B, only a single estimate must be made of the heat exchanger performance, upon which all estimates of temperature difference are based.

3.2 Average Enthalpy Flow Rate at a Cross Section

The integral exchanger and expander uses both regenerative and counterflow heat exchange. Since heat exchange irreversibilities account for most of the performance degradation, the heat exchange model must not only give a reasonable estimate of exchanger performance but also indicate performance trends resulting from parameter variations. Presented in this section is a model of the combined regenerative and counterflow heat exchange. The most important output is an expression for the average enthalpy flow at the cold end, which consists of periodic and non-periodic terms. Values obtained from use of this expression are inputs to the energy balance portion of the performance algorithm. Another output of this analysis is the cold-end temperatures of the displacer, cylinder, and outer shell.

3.2.1 Simplifying Assumptions

Several assumptions are made in an effort to make solving the energy equations less cumbersome while retaining the most important terms. The work of compression and expansion due to pressure changes is assumed negligible when compared to the combined heat capacity of the walls and low-pressure return stream. The advantage of this assumption is that gas compressibility can be neglected. In other words, no temperature fluctuation of the gas and walls results from energy addition to the gas during expansion and compression. The temperature fluctuations are assumed to be the result of displacer motion. This assumption becomes less valid as the temperature is reduced below about 30 K. The low-pressure mass flow, however, which would not be present in a totally regenerative cycle, limits the temperature fluctuation.

Assumptions were made involving the wall and gas thermal conductivities. As discussed earlier, the thermal conduction of the gas and walls in the axial direction is not included in the heat exchange analysis; instead, the axial conduction is an input to the energy balance part of the performance algorithm. In the radial direction, the gas thermal conductivity is much smaller than that of the walls; thus, the vast majority of the temperature difference between the displacer and outer shell is in the gas. For this reason, the walls are assumed to be at a single temperature, so the wall conductivity is not an input. The gas flows in small radial gaps, which results in laminar flow. Since the walls are assumed to have a much higher heat capacity than that of the gas, the gas temperature at any cross section is approximately the average of the enclosing wall temperatures. In other words, the gas conduction can be considered to be quasi-static.

The core of the heat exchange analysis is based on a segment of heat exchanger equal to the stroke length. Assuming that the heat exchanger is long compared with the stroke length allows end effects to be considered negligible. Also, focusing on a short exchanger length allows the material properties to be considered constant and the temperature gradient to be assumed linear over the short length. Variations in

the properties and temperature gradient are included by integrating the equation for a short exchanger section over the entire length.

3.2.2 Method of Solution

By first finding a net enthalpy flow through a plane perpendicular to the exchanger axis for one cycle, an average rate of enthalpy flow through an exchanger cross section is obtained by dividing by the period for one cycle. The resulting average enthalpy flow equation includes a heat flow term that must be solved for and then substituted back into the enthalpy flow equation. The result is an expression for average enthalpy flow at any cross section along the exchanger length. The effects of property changes on the temperature gradient are included by assuming a specific form for the temperature distribution and then applying exchanger end conditions to obtain the average rate of enthalpy flow into the cold section of the cryocooler.

To begin development of the average rate of enthalpy flow at a cross section, Fourier series expressions for the displacer, cylinder, and outer shell walls are selected. The cylinder and outer shell wall temperatures are based on the stationary coordinate system, x, so that

$$T_c = T_c(x,t) \tag{3.4a}$$

$$T_s = T_s(x,t) \tag{3.4b}$$

where T_c is the cylinder temperature and T_s is the outer shell temperature. The variable x is defined in Fig. (3.2). The displacer temperature is based on the moving coordinate system, y, so that

$$T_d = T_d(y,t) \tag{3.5}$$

where the variable y is defined in Fig. (3.2). All three temperatures must be evaluated at the same position in an energy balance. The position of $x = 0$ is chosen which is assumed to be at the vertical center of the exchanger so that end

effects are negligible. The temperatures at a location $x = 0$ for the cylinder, outer shell, and displacer are represented using Fourier series as

$$T_c(0,t) - T_c(0,0) = s\,\frac{\partial T}{\partial x}\sum_{n=1}^{\infty}\left(C_n\,\cos n\omega t + D_n\,\sin n\omega t\right) \tag{3.6}$$

$$T_s(0,t) - T_s(0,0) = s\,\frac{\partial T}{\partial x}\sum_{n=1}^{\infty}\left(E_n\,\cos n\omega t + F_n\,\sin n\omega t\right) \tag{3.7}$$

$$T_d(-\xi,t) - T_d(-\xi,0) = s\,\frac{\partial T}{\partial x}\sum_{n=1}^{\infty}\left(A_n\,\cos n\omega t + B_n\,\sin n\omega t\right) \tag{3.8}$$

where,

$\partial T / \partial x$: The linear temperature gradient over the heat exchanger.

$A_n, B_n, C_n, D_n, E_n, F_n$: Fourier constants.

In this chapter, only the case of $n = 1$ is considered. The accuracy of higher order terms and products of higher order terms is not necessary at this stage of analysis and would make solution of the equations much more cumbersome.

Using the coordinate system of Fig. (3.2), the enthalpy flow through a plane for one cycle at $x = 0$ can now be expressed as:

$$\Delta H = \oint m_H\,c_p\,T_H(0,t)\,dt - \oint m_L\,c_p\,T_L(0,t)\,dt - \oint \rho_m\,A_{cd}\,c_m\,T_d(-\xi,t)\,\frac{d\xi}{dt}\,dt \tag{3.9}$$

where T_H is the gas temperature in the displacer-to-cylinder gap, T_L is the gas temperature in the cylinder-to-outer shell gap, and A_{cd} is the cross sectional area of the displacer in a plane perpendicular to the axis of the exchanger. In Eqn. (3.9), the enthalpy flow is defined as positive toward the cold end. The first two terms are for the high- and low-pressure gas streams, respectively. The third term is the enthalpy flow through a plane due to movement of the displacer, which may be rewritten in terms of q_1 (see Fig. (3.2)) by applying the first law to a length dy on the displacer using the assumption of a linear temperature gradient over a short length. Dividing the result by the period of one cycle results in an average enthalpy flow rate:

$$h = \frac{\omega}{2\pi} \oint m_H \, c_p \, T_H(x,t) \, dt - \frac{\omega}{2\pi} \oint m_L \, c_p \, T_L(x,t) \, dt + \frac{\omega}{2\pi} \oint \left(\int_0^t \frac{d\,q_1}{d\,y} dt \right) \frac{d\,\xi}{d\,t} dt \tag{3.10}$$

where $dq_1 \,/\, dy$ is the heat leaving the displacer through the area encircling the displacer of dy width. The unknowns in Eqn. (3.10) are the gas temperatures, T_H and T_L, and the cyclic displacer energy flow, $dq_1 \,/\, dy$. An earlier assumption allows the gas temperatures to be approximated as the average of the enclosing wall temperatures. Thus,

$$T_H = \frac{T_d + T_c}{2}$$

$$T_L = \frac{T_c + T_s}{2}$$

The assumption of a linear temperature gradient over a length of exchanger equal to the stroke length allows the energy flow to also be expressed in terms of the wall temperatures. The assumptions, thus, allow the unknowns in Eqn. (3.10) to be obtained in terms of the Fourier series coefficients for the wall temperatures of Eqns. (3.6) to (3.8). Determining the coefficients requires the simultaneous solving of seven control volume energy equations. Solution of the energy equations yields expressions for the Fourier series constants for the displacer, cylinder, and outer shell temperatures. The procedure is straightforward but is quite cumbersome. Details are given in Section (B.1.3) of Appendix B.

Expressions for T_H, T_L, and $dq_1 \,/\, dy$ may then be substituted into the rate of enthalpy flow equation, Eqn. (3.10), which, after straightforward integration for the case of $n = 1$, yields

$$h = \frac{\pi \, D_H \, s^2 \, k_g}{2 \, z_H} \frac{\partial T}{\partial x} (S_1 - G_1 \, K_1) + M_L \, c_p \, (T_H(0,0) - T_L(0,0)) \tag{3.11}$$

where,

$$S_1 = (B_1 + D_1 - G_1)I_1 \tag{3.12}$$

The constant, K_1, consists of a combination of Fourier series constants along with physical dimensions, wall and gas properties, and operating conditions. The combination of expressions for K_1 will not be repeated here, but may be found in Section (B.1.3) of Appendix B. The heat exchange temperature difference at $x = 0$ and $t = 0$ is now defined, for convenience, as

$$\Delta T)_{h0} = T_H(0,0) - T_L(0,0) \tag{3.13}$$

At $t = 0$, the displacer is in its midpoint position, according to Eqn. (3.1); thus, the heat exchange temperature difference used in Eqn. (3.11) is the temperature difference at $x = 0$ when the displacer is in its midpoint position. Moreover, this temperature difference can be considered to be a time-averaged temperature difference for heat exchange.

Equation (3.11) is valid at any position along the heat exchanger. The temperature gradient, $\partial T / \partial x$, is assumed linear over a length of exchanger equal to the stroke. For the entire length, the temperature gradient may vary due to the finite gas specific heat and due to changing gas properties. This variation in temperature gradient is taken into account by assuming a specific form for the linear temperature distribution and applying a first law energy balance to the total heat exchanger length. Up until now, the position of $x = 0$ has been located at the axial center of the heat exchanger. At this point, the position of $x = 0$ is moved to the cold end of the heat exchanger so that Eqn. (3.11) can be integrated over the total exchanger length to get an expression for the average enthalpy flow into the cold end that takes variations of temperature gradient into account. The temperature distribution assumed takes the form

$$\frac{T - T_0}{\Delta T} = \Theta\left(\frac{x}{L}\right)^2 + (1 - \Theta)\frac{x}{L} \tag{3.14}$$

where T_0 is an average temperature at $x = 0$ for the displacer, cylinder, and outer shell, L is the exchanger length, and ΔT is the end-to-end temperature difference. An energy balance, which requires that the enthalpy flux at each end of the heat exchanger to be equal, is used to determine an expression for the constant, Θ. A final expression for the rate of enthalpy flow at $x = 0$ may now be written:

$$h_0 = \frac{\pi D_H s^2 k_{g0}}{2 z_H} \frac{\partial T}{\partial x}\Big)_0 (S_{10} - G_{10} K_{10}) + M_L c_p (T_H(0,0) - T_L(0,0)) \qquad (3.15)$$

where,

$$\frac{\partial T}{\partial x}\Big)_0 = \frac{\Delta T}{L}(1 - \Theta) \qquad (3.16)$$

These expressions are used in the performance algorithm as the rate of enthalpy flow at the cold end. The first term of Eqn. (3.15) is the cyclic enthalpy flow due to displacer motion, and will later be referred to as h_{c0}. The expression $(S_{10} - G_{10} K_{10})$ is a constant which depends on the input values. Variations of this constant expression results in the performance trends to be discussed in the next section. The second term of Eqn. (3.15) is due to the counterflow heat exchange temperature difference. This term is not periodic and will later be referred to as h_{nc0}. Since the counterflow heat exchange temperature difference varies with displacer position, the temperature difference used is a time-averaged value.

The heat exchange temperature difference at the cold end, $\Delta T)_{h0}$, is computed based on an estimate of heat exchanger performance. As mentioned earlier and explained in detail in Appendix B, only one estimate of the performance needs to be made, upon which all estimates of heat exchange temperature difference are based. The performance, for a group of integral expander and exchanger units all with the same heat exchange surface area, A_{HE}, is expressed in terms of a reference heat exchange temperature ratio at the cold end, along with a single set of representative values of the high- and low-pressure side gap widths. The temperature ratio is

$$\frac{\Delta T}{T}\Big)_{h0} = \frac{T_H(0,0) - T_L(0,0)}{T_L(0,0)} \qquad (3.17)$$

where the temperature difference is the value when the displacer is at its midpoint position, as defined by Eqn. (3.1). The reference values given at the end of Section (3.1) will be used in this chapter. As explained in Appendix B, estimates of the heat exchange temperature difference for other values of gap widths are computed based on this efficiency.

3.3 The Performance Algorithm

In this section, Eqn. (3.15) obtained in Section (3.2) for the average rate of enthalpy flow into the cold end due to counterflow heat exchange and displacer motion, h_0, will be used with an energy balance on the cold end to obtain a performance algorithm for the cryocooler. The energy balance for the control volume is shown in Fig. (3.3). The energy balance requires that

$$W = q_L + q_C + h_0 \tag{3.18}$$

where W is the rate of work extracted from the working volume, q_L is the applied heat load, and q_C is the conduction heat leak. To obtain a value for W, the expander efficiency must be estimated in terms of an adiabatic engine efficiency. The adiabatic engine efficiency is defined as

$$\eta_E = \frac{h_{in} - h_{out}}{h_{in} - h_{out,s}} \tag{3.19}$$

where h is the enthalpy. Subscripts are defined as "in" for going into the engine, "out" for exiting the engine, and "s" for the isentropic expansion state.

A logical sequence of events to describe the refrigeration process had to be devised in order to construct a performance algorithm. The final version of the algorithm is obtained by modifying the original algorithm to better correlate with experimental data. A description of the final version follows. The energy added to the exhaust stream is in the form of a lumped heat leak consisting of the average rate of enthalpy flow at $x = 0$, the conduction heat leak, and the applied heat load. The model begins by adiabatically expanding the high-pressure gas at $T_H(0,0)$ to

the exhaust pressure and the adiabatic expansion temperature, where $T_H(0,0)$ is the displacer-to-cylinder gas temperature at $x = 0$ when the displacer is in its midpoint position.

The reasons for selecting $T_H(0,0)$ as the expander inlet temperature are not immediately obvious and are explained as follows. In a real integral expander and exchanger, the temperature of the gas entering the working volume during expansion changes appreciably during the expansion process. The average value of displacer-to-cylinder gas temperature entering the working volume is approximately the value when the displacer is in its midpoint position. For this reason, $T_H(0,0)$ is used as the expander inlet temperature in the adiabatic engine efficiency of Eqn. (3.19).

The value of $T_H(0,0)$ may be expressed in terms of the refrigeration temperature, T_R, which is an input listed in Table (3.1), and the heat exchange temperature difference, $\Delta T)_{h0}$, as

$$T_H(0,0) = T_R + \Delta T)_{h0} \tag{3.20}$$

where $\Delta T)_{h0}$ was defined earlier as

$$\Delta T)_{h0} = T_H(0,0) - T_L(0,0) \tag{3.13}$$

In these equations, $T_R = T_L(0,0)$, the temperature after the lumped heat leak has been added to the gas at the adiabatic expansion temperature.

After the adiabatic expansion temperature is known, the rate of work removed from the cold end is computed. The calculation of the rate of work removal does not include dead or clearance volume effects. The dead volume is the volume between the displacer and cylinder, which is not a part of the active displacement or working volume. The amount of dead volume varies as the displacer-to-cylinder gap varies. The heat load applied to the cold end is then

$$q_L = W - h_0 - q_C \tag{3.21}$$

The computer program used for the algorithm is described in Section (B.2.1) of Appendix B. Results from the algorithm will be described next.

3.4 Results from the Performance Algorithm

In this section, the computerized algorithm is used to identify performance trends for the integral expander and exchanger. The results indicate important design parameters such as the heat exchange gap widths, which are used for the design of a single-stage cryocooler in Chapter 4. The specific cases investigated are based upon results for the cryocooler described in Tables (2.1) and (2.2) of Chapter 2, which provides 1 W of cooling at 4.2 K. The first case looks at a single-stage cryocooler which is 50 cm long. The second case considers a much shorter cryocooler of 12 cm length, which corresponds to a first stage for the 1 W refrigerator of Chapter 2.

3.4.1 Results for a Single-Stage Cryocooler of 50 cm Length

A single-stage cryocooler of 50 cm length and 26 mm bore and stroke is examined in this sub-section to identify important design parameters such as the heat exchange gap widths. The computerized performance algorithm is used for the refrigerator described in Table (3.2). With the exceptions of z_H and z_L, the values given in the table are for the experiment described in Chapter 4 without liquid nitrogen precooling. Appropriate values for z_H and z_L are outputs from the analysis. Variation in magnitude of the average enthalpy flow rate with high-pressure side gap width is discussed first. Then, temperature versus time plots for the displacer, cylinder, and outer shell are given for different values of high- and low-pressure side gap widths. Finally, the theoretical results used to design the single-stage cryocooler experiment of Chapter 4 are presented.

The average enthalpy flow rate at a cross section varies with the ratio of radial high-pressure gap width to cylinder diameter (z_H / D_c) as shown in Fig. (3.4). The low-pressure side radial gap is $z_L = 0.254$ mm. Note that z_H is the only dimension

Table (3.2) Inputs to the performance algorithm for the 50 cm cryocooler

Parameter	Value
D_H	26.44 mm
D_L	28.22 mm
D_c	27.28 mm
t_d	0.838 mm
t_c	0.686 mm
t_s	0.457 mm
ω	10.5 rad/s
s	25.4 mm
η_E	0.75
$\left(\frac{\Delta T}{T}\right)_{h0,ref}$	0.15 at 80 K (A_{HE} = 437 cm^2)
ρ_m	8.17 g/cc
c_m	0.239 J/g-K
M_L	0.1 g/s
L	51 cm
q_C	1 W
P_H	40 atm
P_L	4 atm
ΔT	215 K
T_R	variable
z_H	variable
z_L	variable

being varied and that T_R = 85 K. The value of cyclic enthalpy flow rate (h_{c0}) has a maximum at a small value of z_H. The magnitude of h_{c0} decreases as z_H increases from this value because the thermal communication between the cylinder and the reciprocating displacer decreases. As z_H is decreased from its value at maximum h_{c0}, the magnitude of cyclic enthalpy flow rate decreases because the temperature of the displacer, as observed from a stationary point on the cylinder, varies less as the radial gap decreases (*i.e.*, as the thermal communication between the displacer

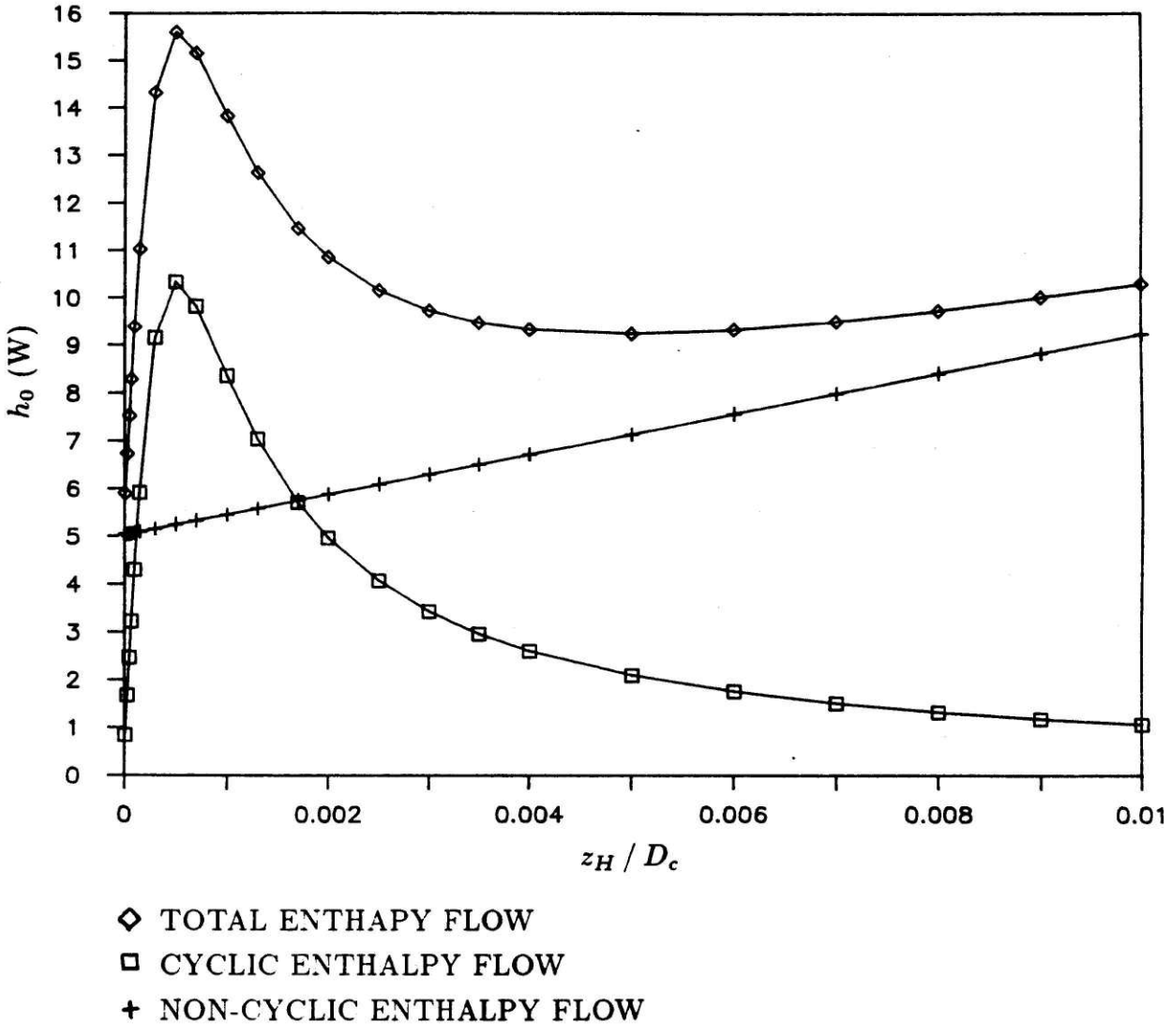

Fig. (3.4) Average enthalpy flow rate at a cross section versus the ratio of high-pressure side gap width to cylinder diameter.

and cylinder increases). The result is that the enthalpy of the displacer at a cross section (*i.e.*, at a given x) varies less.

The non-periodic enthalpy flow rate at a cross section increases with $z_H \,/\, D_c$ as shown in Fig. (3.4). This increase is due to increasing heat exchange temperature difference as the magnitude of z_H increases, which reduces the thermal communication between the displacer and cylinder.

The sum of the periodic and non-periodic terms of enthalpy flow rate indicates an optimal value for a practical choice of the high-pressure side radial gap width, as shown in Fig. (3.4). At this minimal value of total enthalpy flow rate, the refrigeration load is at a maximum, as shown in Fig. (3.5). As mentioned earlier, the effects of increased or decreased dead volume between the displacer and cylinder on the work output is not included.

An energy balance on the cold end as shown in Fig. (3.3) yields

$$W = q_L + q_C + h_0 \tag{3.22}$$

The magnitude of each term is plotted in Fig. (3.6). The value of conduction heat leak is taken as $q_C = 1$ W. The magnitude of work output is observed to decrease with increasing $z_H \,/\, D_c$ for a set refrigeration temperature and adiabatic engine efficiency. Again, dead volume effects are not included.

The next series of plots is temperature versus time for the displacer, cylinder, and outer shell. Different values of high- and low-pressure gap widths are considered in an effort to indicate theoretical trends in temperature versus time that may be compared with results in Fig. (3.4). The inputs are listed in Table (3.2) with $T_R = 80$ K. The first gap widths considered are impractically small, but give a very useful indication of theoretical trends. When $z_H = z_L = 2.5\,(10^{-5})$ mm, the thermal communication among the three walls is very good, causing the walls to equilibrate almost instantaneously with piston motion, as shown in Fig. (3.7). With these conditions, the average rate of enthalpy flow is small, as shown in Fig. (3.4). When the radial gaps are increased to $z_H = z_L = 2.5\,(10^{-3})$ mm, the temperature differences between adjacent walls increases, resulting in the plot shown in Fig.

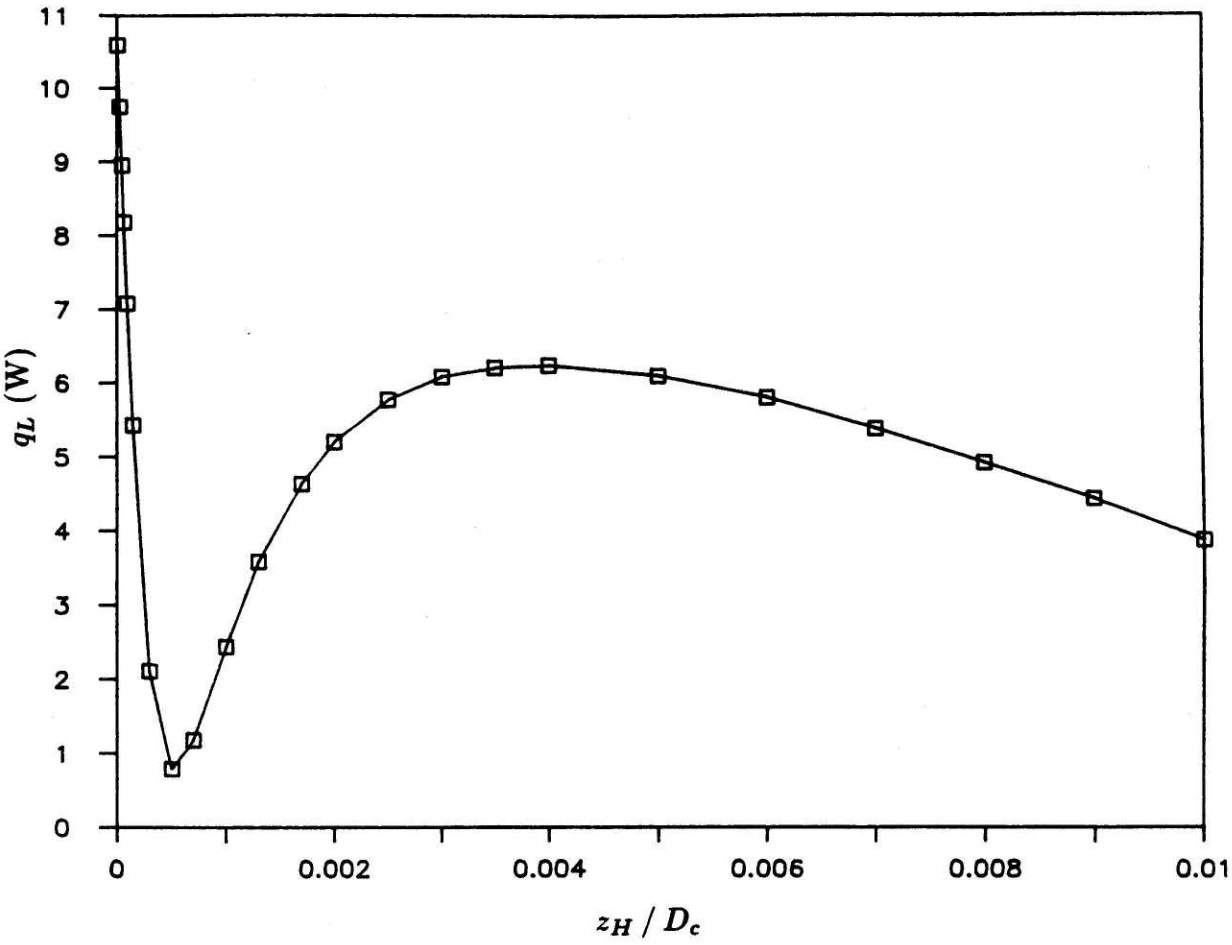

Fig. (3.5) Refrigeration heat load versus the ratio of high-pressure side gap width to cylinder diameter.

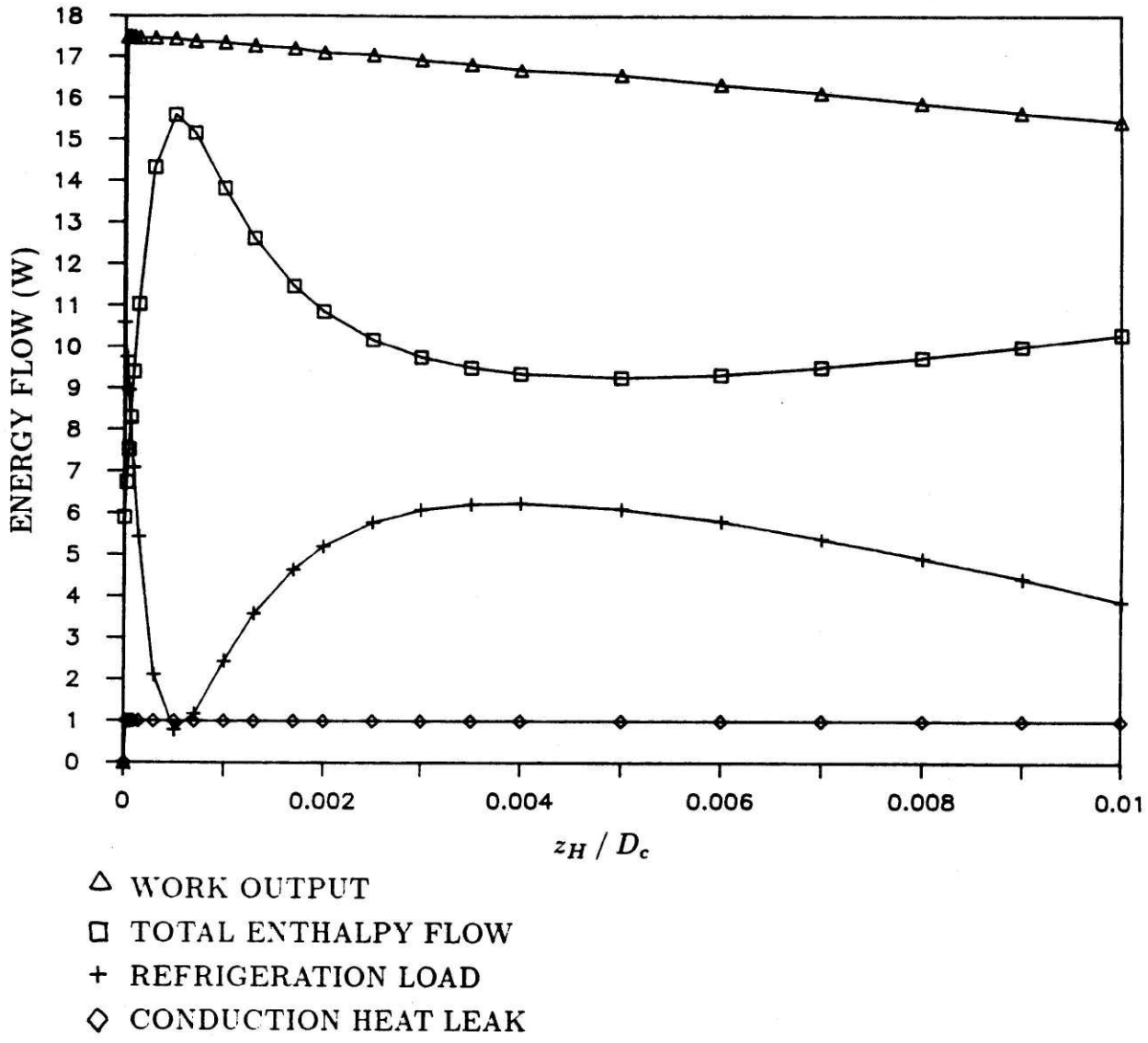

Fig. (3.6) First law balance for the control volume of Fig. (3.3) versus the ratio of high-pressure side gap width to cylinder diameter.

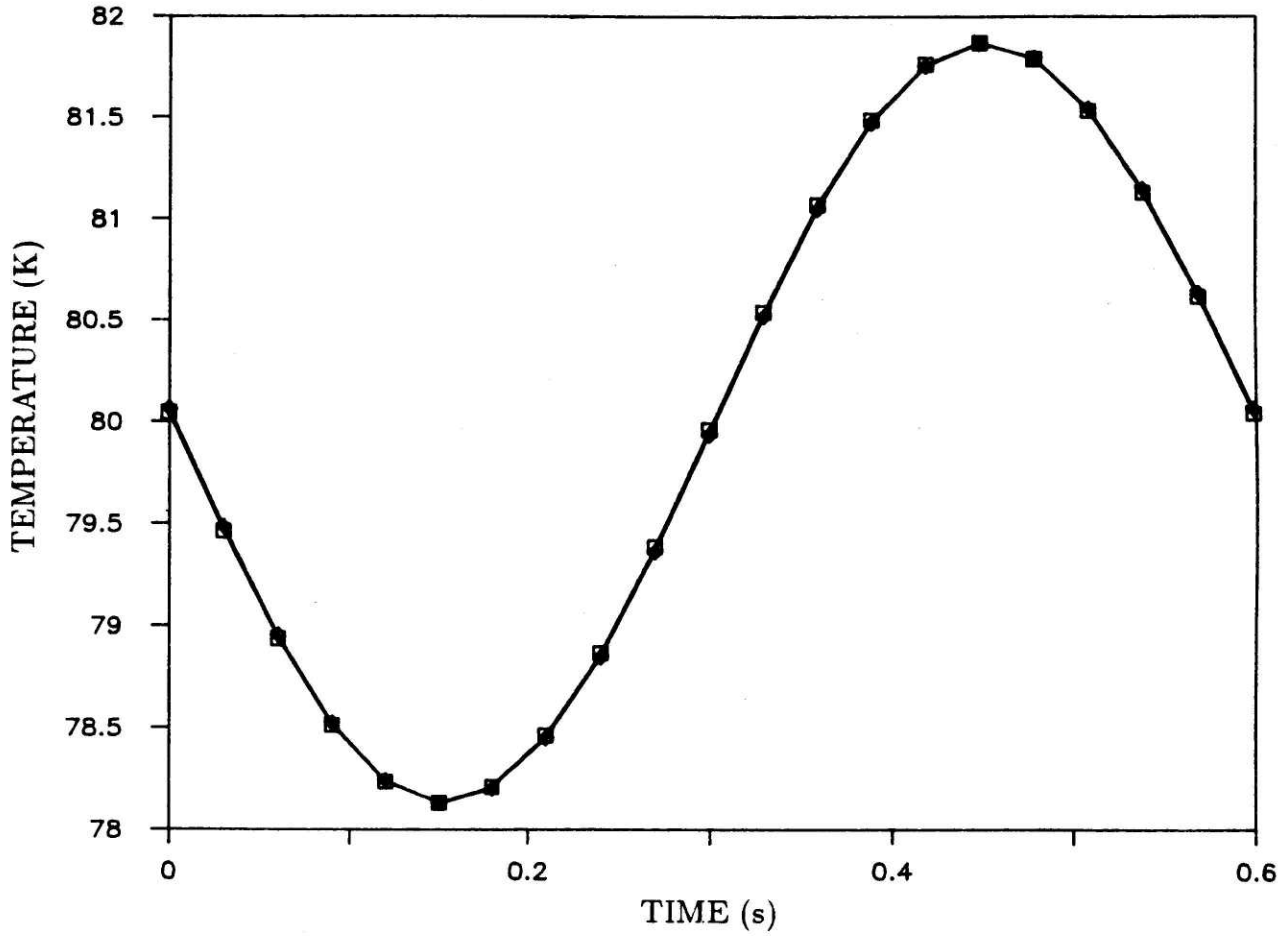

Fig. (3.7) Wall temperatures versus time for the case of $z_H = z_L = 2.5(10^{-5})$ mm.

(3.8). In this plot, thermal communication is still very efficient, but the average rate of enthalpy flow is near a maximum value, for reasons discussed earlier.

The remaining plots are for the integral heat exchanger and expander to be designed in Chap. 4, which has $z_H = 0.127$ mm and $z_L = 0.254$ mm. A temperature versus time plot for the case of $T_R = 80$ K is shown in Fig. (3.9). Note that on the plot of enthalpy flow rate versus z_H, the value of h_0 is near a minimum. The average temperature difference between the cylinder and outer shell is shown to be about 8 K, while the temperature difference between the displacer and cylinder is about 4 K.

Another plot of interest when trying to predict experimental results is the plot of refrigeration temperature versus refrigeration load, as shown in Fig. (3.10). This plot indicates that the minimum temperature that may be reached by the experiment with no refrigeration load is about 57 K. This plot assumes a mass flow rate of 0.1 g/s. This constant value of mass flow can be realized in an actual experiment over a range of refrigeration temperatures by adjusting the amount of recompression. This plot cannot, however, be extrapolated indefinitely to high temperatures without a reduction in mass flow rate. One should also note that adjusting the amount of recompression changes the adiabatic efficiency of the engine.

The performance algorithm can also be used to predict the heat leak due to displacer motion. In the experiment, the displacer motion heat leak will be measured using liquid nitrogen to cool the refrigeration zone. Using the information given in Table (3.2) with $z_H = 0.13$ mm, $z_L = 0.25$ mm, $T_R = 80$ K and $M_L = 0$ g/s, the resulting output is $q_L = -3.1$ W. In other words, 3.1 W must be removed from the cold end by the liquid nitrogen in order to sustain 80 K. The 3.1 W of heat removal consists of 1 W due to axial conduction and 2.1 W due to displacer motion. Since the mass flow rate is zero, the non-cyclic enthalpy flow due to counterflow heat exchange temperature difference is zero.

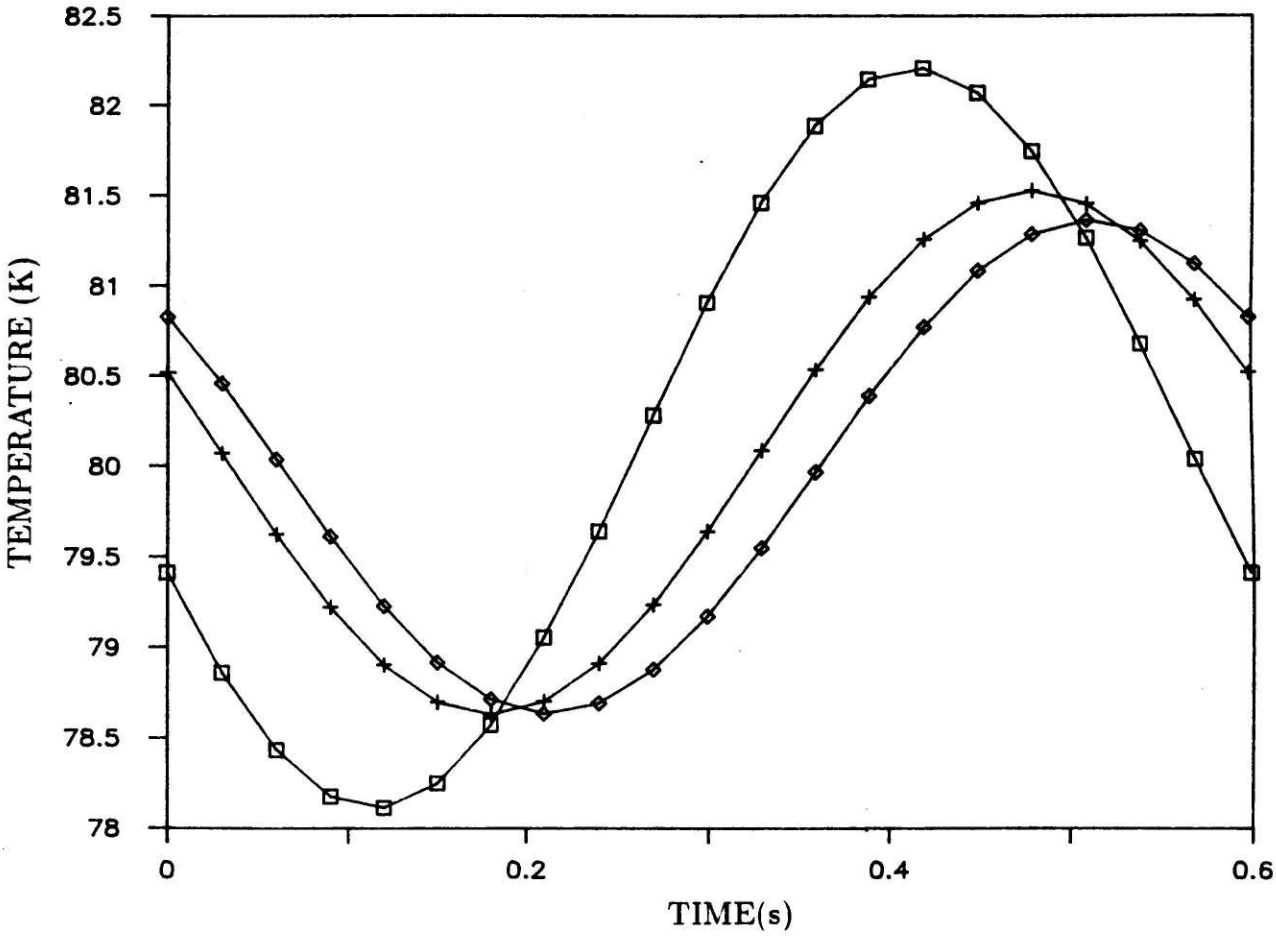

Fig. (3.8) Wall temperatures versus time for the case of $z_H = z_L = 2.5(10^{-3})$ mm.

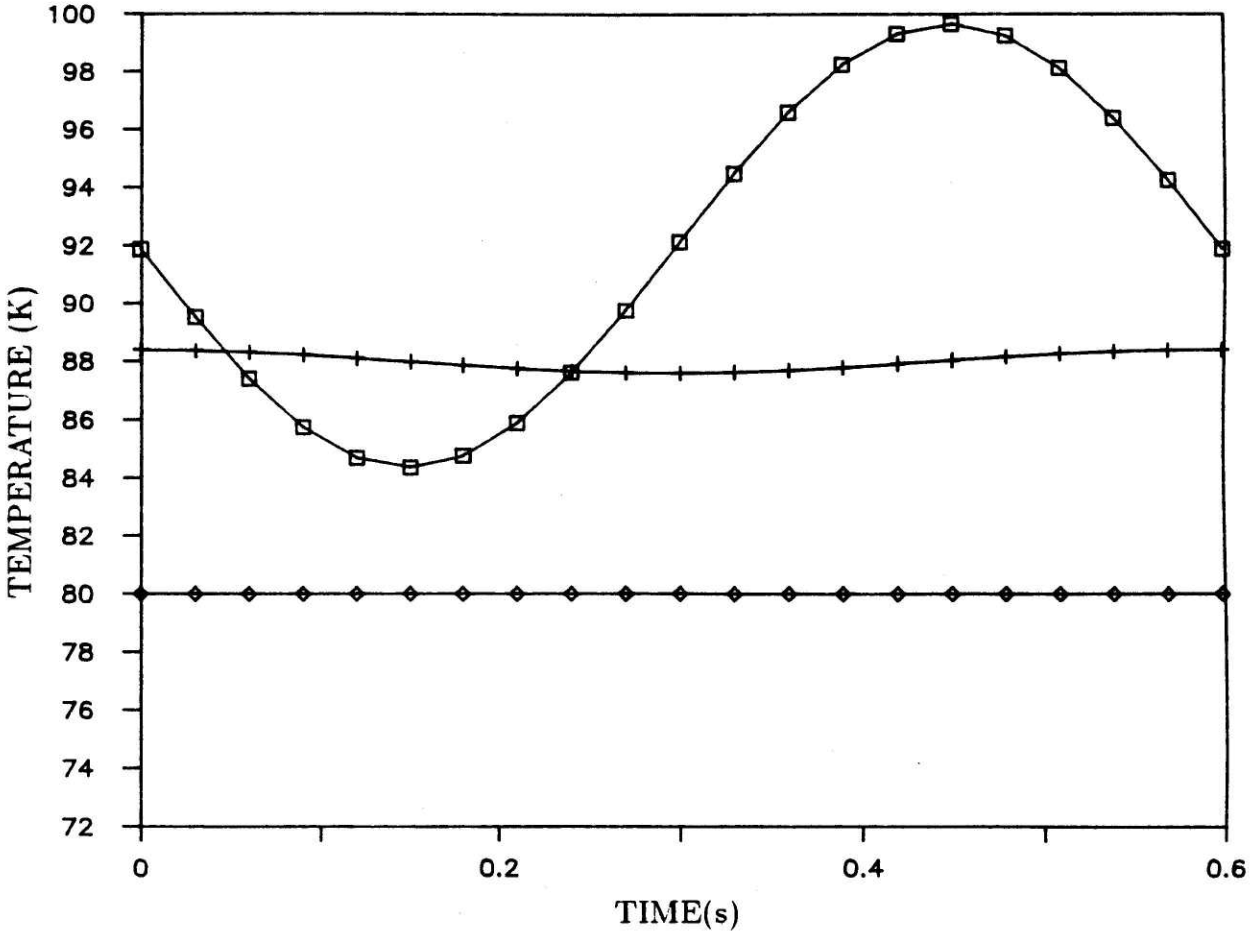

Fig. (3.9) Wall temperatures versus time for the case of $z_H = 0.127$ mm and $z_L = 0.254$ mm.

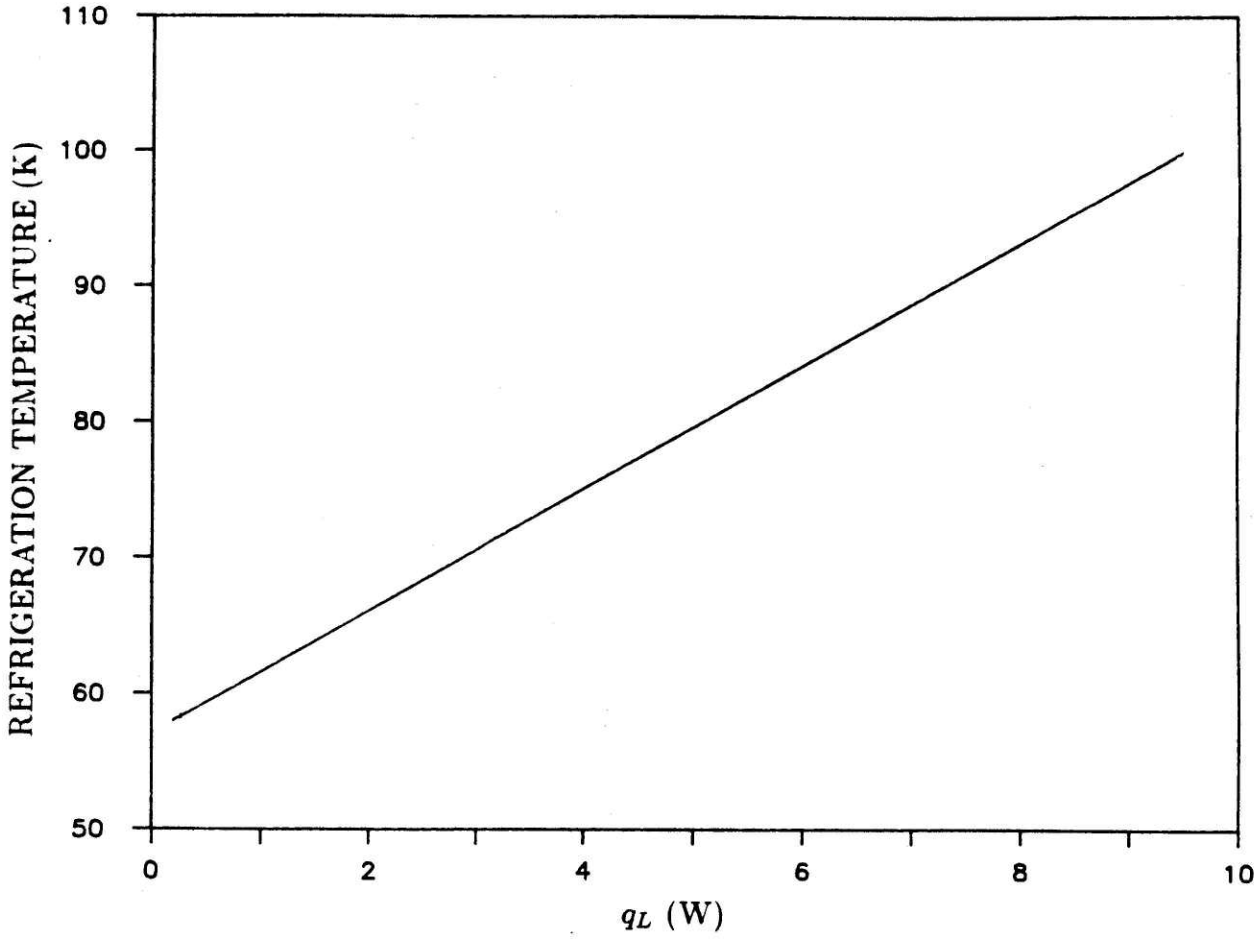

Fig. (3.10) Refrigeration temperature versus heat load for the case of $z_H = 0.127$ mm and $z_L = 0.254$ mm.

3.4.2 Results for a Single-Stage Cryocooler of 12 cm Length

This section uses the performance algorithm to design a single-stage expander and heat exchanger that could be used as the first stage in the liquid helium temperature cryocooler described in Table (2.2) of Chapter 2. The integral exchanger and expander length is 12 cm and the bore is 22 mm. This exercise also gives some indication of the usefulness of results from Chapter 2. The results listed in Table (2.2) of Chapter 2 specify that the mass flow through engine (2) is 0.052 g/s. The inputs to the performance algorithm are given in Table (3.3). As usual, the refrigeration temperature for the algorithm corresponds to the gas temperature after the lumped heat leak and heat load are added.

The overall cryocooler configuration assumed is that of Fig. (2.13), where the temperature ratio is controlled along the exchanger length by using exhaust from a warmer engine to remove energy directly from an adjacent integral expander and exchanger unit used to reach a colder temperature. The heat load that must be sustained by the warmer integral unit is equivalent to the energy that must be removed from the adjacent heat exchanger to obtain the specified temperature ratio at the heat exchange pinch point locations. The heat load, as defined in Fig. (2.13) of Chapter 2, may be calculated for the warmer integral unit using the equation

$$q(2) = m\, c_p\, \Delta T \tag{3.23}$$

where m is the mass flow through the warmer unit, c_p is the constant pressure specific heat, and ΔT is the temperature change of the gas. Using the results from Chapter 2 to obtain the appropriate ΔT, the heat load that must be sustained by the warmer engine is 13 W. Again, the shortest integral expander and exchanger of Fig. (2.13), which has a heat load of $q(2)$, is being considered.

Inputing the above information into the computer algorithm resulted in a 12 cm cryocooler that could sustain only a 6 W heat load. A heat load of 13 W required an increase in mass flow rate of approximately 50%, from 0.052 g/s to 0.08 g/s. Since the performance algorithm includes losses, such as displacer motion, which

Table (3.3) Inputs to the performance algorithm for the 12 cm cryocooler

Parameter	Value
D_H	21.8 mm
D_L	23.6 mm
D_c	22.9 mm
t_d	0.51 mm
t_c	0.51 mm
t_s	0.51 mm
ω	6.28 rad/s
s	21.8 mm
η_E	0.75
$\left(\frac{\Delta T}{T}\right)_{h0,ref}$	0.15 at 80 K ($A_{HE} = 86$ cm^2)
ρ_m	8.17 g/cc
c_m	0.239 J/g-K
M_L	0.052 g/s
L	12 cm
q_C	4.9 W
P_H	40 atm
P_L	4 atm
ΔT	163 K
T_R	137 K
z_H	0.13 mm
z_L	0.25 mm

are not included in the cycle analysis, this discrepancy in mass flow rates would be expected. For the case of 0.08 g/s mass flow rate, the heat leak due to heat exchange temperature difference is 6.6 W and due to displacer motion is 4.6 W.

Chapter 4

Single-Stage Cryocooler Experiment

In Chapter 2, a computer analysis for the SVC cycle identifies a major component for a cryocooler using a modified SVC cycle. This component consists of an integral concentric tube heat exchanger and expansion engine. Since development of the integral unit requires analytical prediction of performance characteristics, a performance algorithm is developed in Chapter 3. The present chapter describes an experiment used to further increase our ability to predict the performance of the integral exchanger and expander under development. A description of the experimental apparatus is first given. The experimental results obtained are then described, along with a detailed discussion of the results.

Shown in Fig. (4.1) is the integral concentric tube heat exchanger and expansion engine. All of the parts are made of 304 stainless steel, with exception to the room temperature parts for the exhaust valve which are made of brass. Displacer support disks and outer shell round-out-rings are used to maintain the shape of the integral unit during pressure cycling. The total heat exchanger length is 53 cm. The inlet valve, located at the room temperature end, is solenoid operated. The exhaust valve operates at the refrigeration temperature and is operated by a solenoid located at room temperature. A teflon coated stainless steel tube inside a stainless steel sheath provides the mechanical connection between the warm solenoid and the cold valve. Aluminized superinsulation covers all internal parts. The primary component of the stroking mechanism is a hydraulic system used to absorb the expander power output during the expansion stroke and to supply power during the exhaust and recompression stroke. An electronic linear position transducer is connected to the hydraulic cylinder shaft. The position transducer output is supplied to an electronic control circuit which is then connected to the inlet valve, exhaust valve, and hydraulic directional control valve solenoids. The control circuit was designed so that actuation timings for the three solenoids are independent. Also shown in the figure is a liquid nitrogen cooled radiation shield and heat exchanger. The experi-

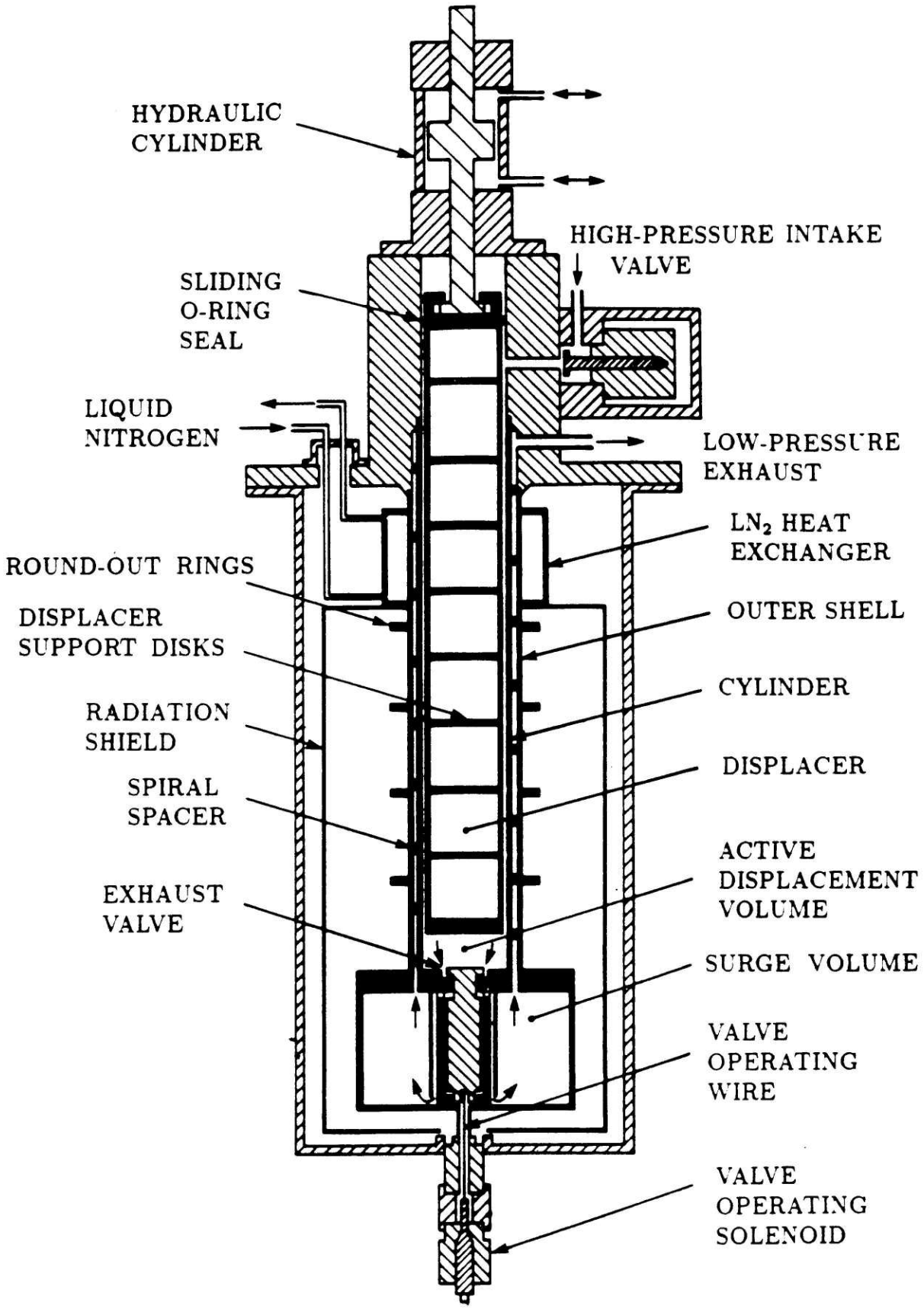

Fig. (4.1) Schematic of integral heat exchanger and expansion engine.

ment was first run without liquid nitrogen cooling. The radiation shield was used with liquid nitrogen only during testing with auxiliary cooling. Each of the above components will now be described in more detail. A photograph of the complete experiment is shown in Fig. (4.2). Another photograph of just the cryocooler is shown in Fig. (4.3).

4.1 The Integral Heat Exchanger and Expander Unit

Construction of the integral heat exchanger and expander unit is described in terms of design, fabrication, and assembly. Design of the unit includes the choice of physical dimensions for the specified flow conditions, temperature range, and length criterion. The salient fabrication techniques developed include a hydroforming process for the concentric tubes and a process for constructing the spiral spacers. Since the cylinder and outer shell concentric tubes have a slight interference fit, assembly required use of a thermal expansion technique.

4.1.1 Design of the Integral Unit

Figure (4.4) shows a cross section of the integral concentric tube heat exchanger. The incoming flow between the displacer and cylinder is periodic. The low-pressure return side was designed to have RC circuit characteristics that maintain a flow rate that is approximately steady. Fig. (4.5) shows dimensions for a spiral spacer used to obtain the RC characteristics.

The cryocooler heat exchanger is designed to minimize flow maldistribution and to enhance counterflow heat exchange. Designing a heat exchanger for very high efficiency is a frivolous effort if flow maldistribution is present; moreover, flow maldistribution becomes more dominant on heat exchange performance as heat transfer efficiency is increased. The incoming flow between the displacer and cylinder is periodic and is directed axially. At the warm end, an O-ring seals the high-pressure gas and maintains the displacer concentric with the cylinder. Also, high-pressure flow is uniformly distributed at the warm end using a shallow groove around the

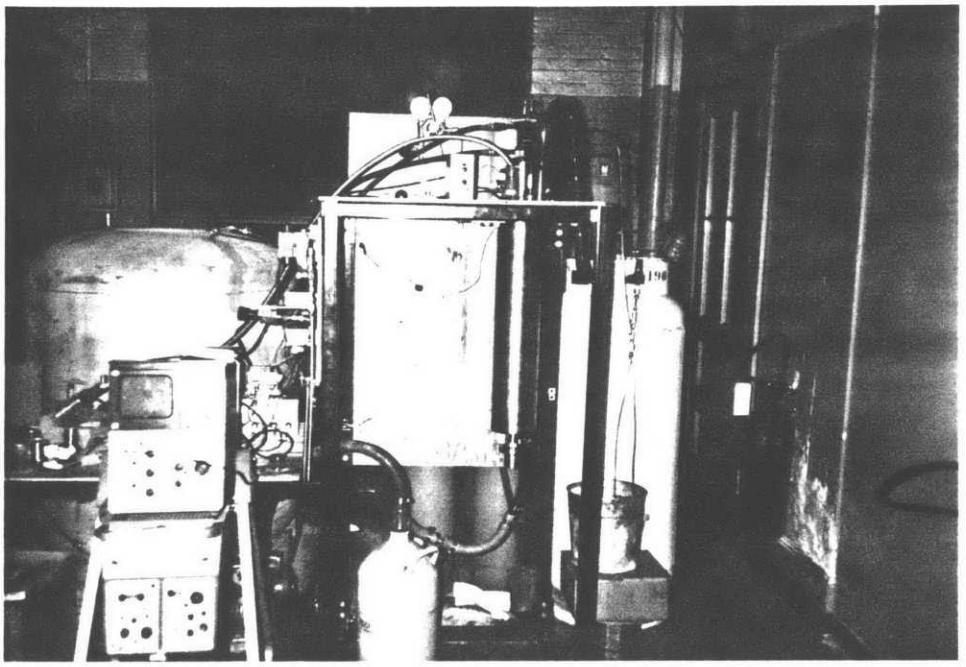

Fig. (4.2) Photograph of complete experiment.

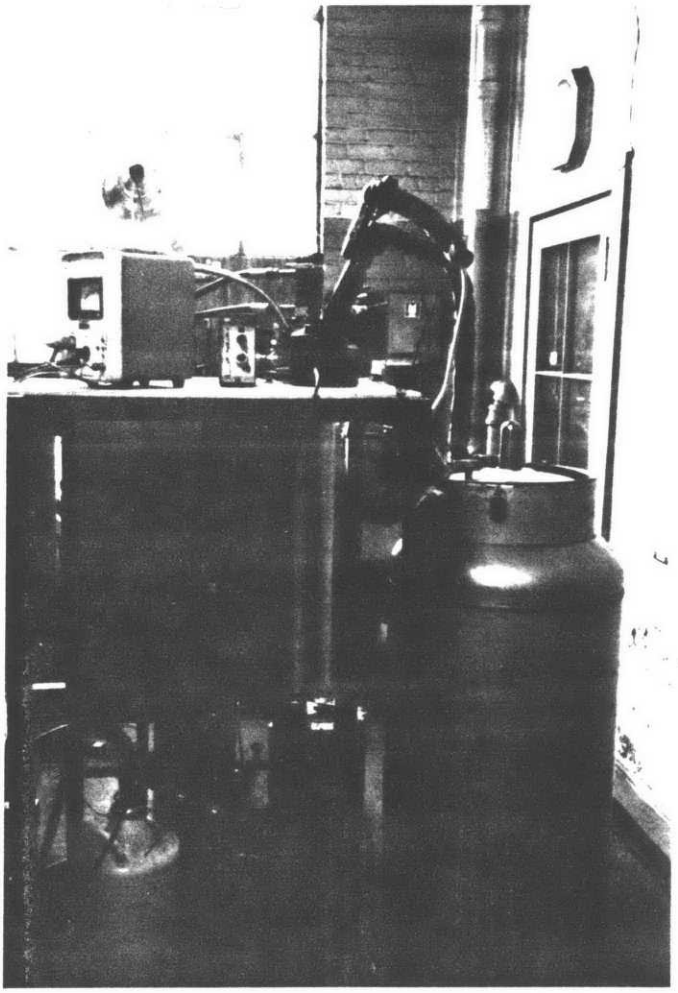

Fig. (4.3) Photograph of cryocooler.

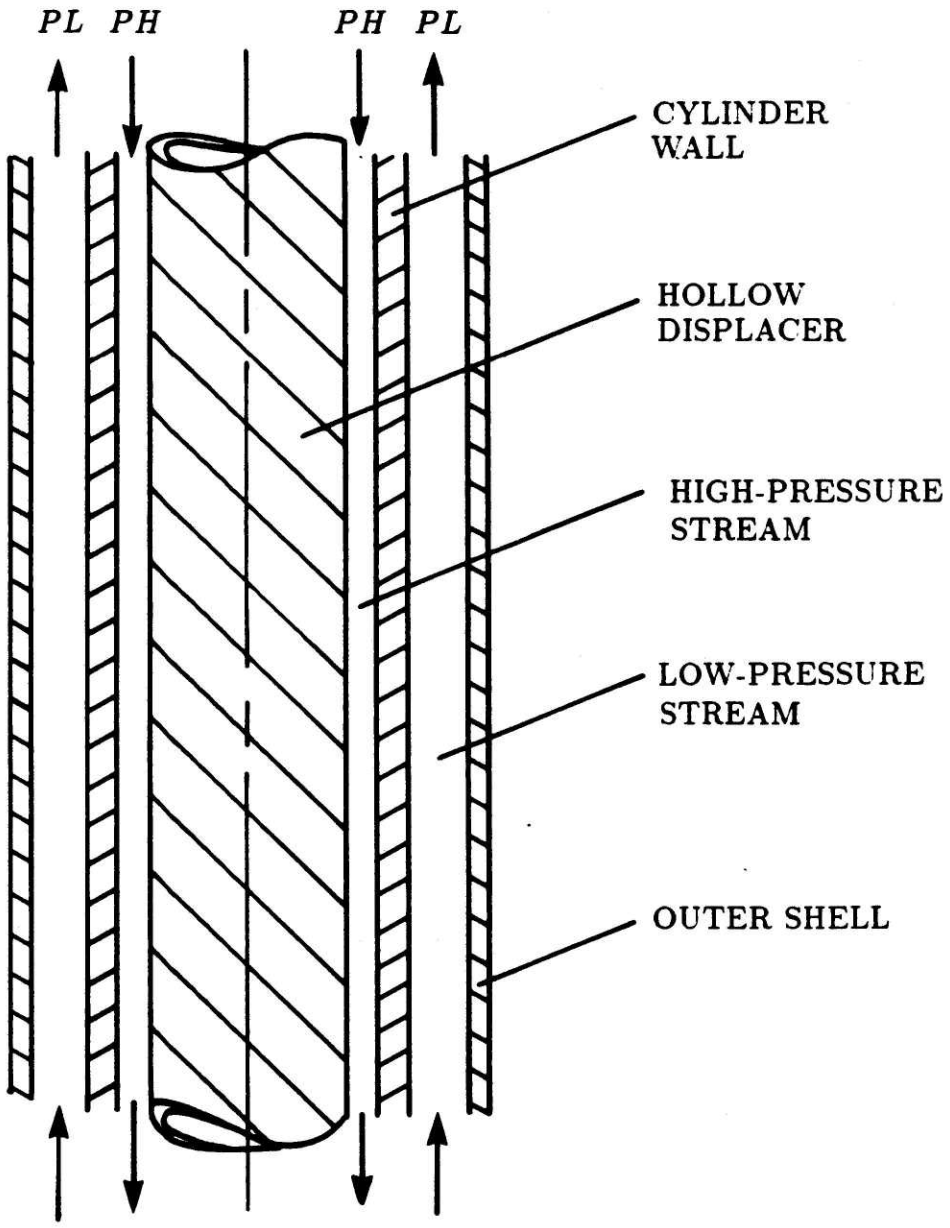

Fig. (4.4) Cross section of integral concentric tube heat exchanger and expansion engine.

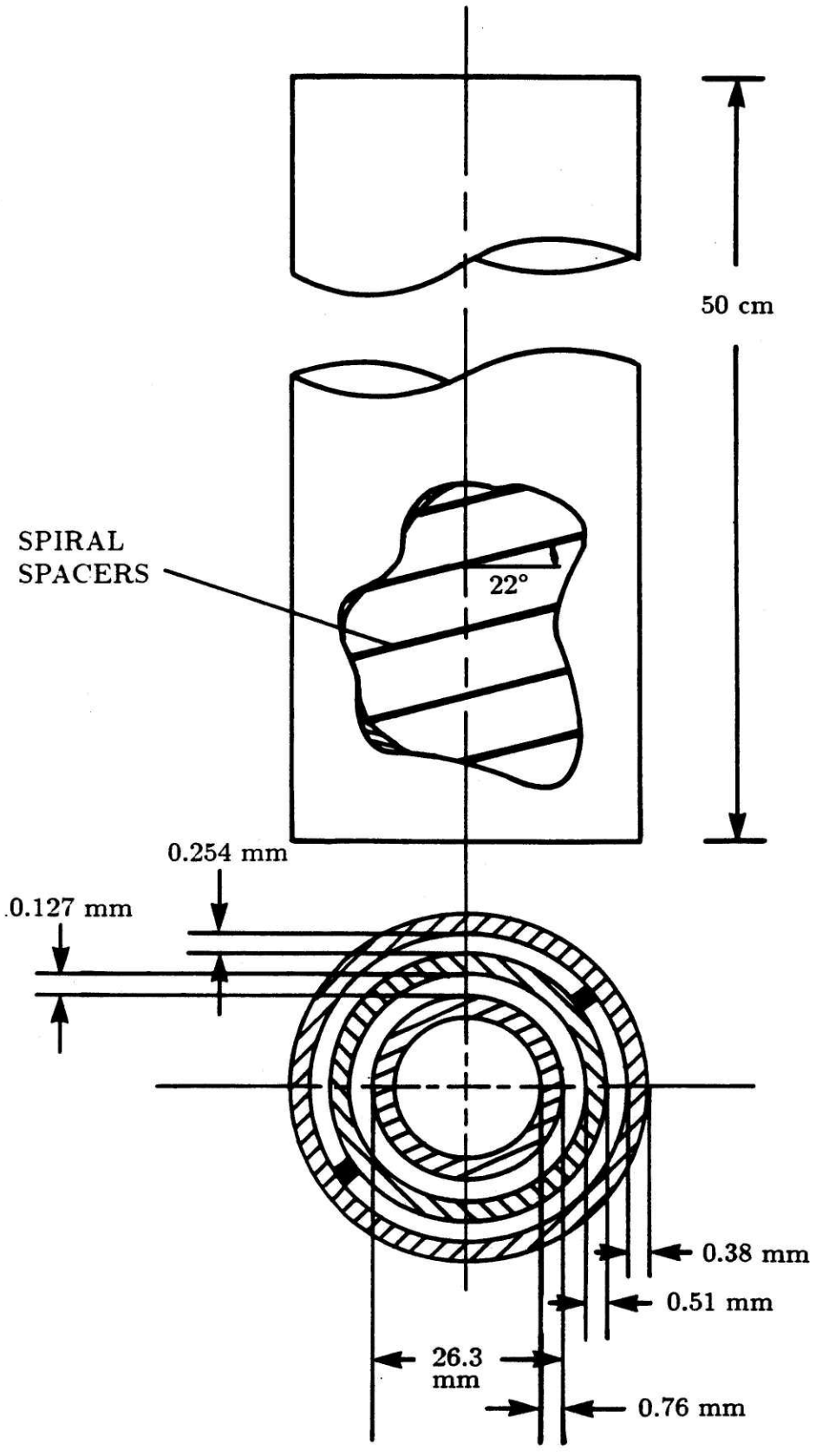

Fig. (4.5) Dimensional specifications for the concentric tubes and spiral spacers.

cylinder at the inlet valve port. Flow maldistribution is further reduced between the displacer and cylinder by placing a Rulon centering piece on the cold end of the displacer.

The effects of flow maldistribution between the displacer and cylinder are reduced by returning the low-pressure side flow to the warm end through spiral passages which encircle the cylinder. Two spiral spacers minimize the amount of leakage in the axial direction. The spacers encircle the cylinder at an angle of 68° measured from the vertical axis.

Overall design specifications are based on results from Chapter 2. The results indicate that the wet expander will operate with a mass flow rate of approximately 0.09 g/s and be about 55 cm long. Although not expected to reach liquid helium temperatures, the single-stage unit was designed to sustain a time-averaged mass flow rate of approximately 0.09 g/s. As discussed in Chapter 2, practical considerations for a maximum intake pressure resulted in a design intake pressure of 40 atm. For increased heat transfer effectiveness, a return pressure of 4 atm was chosen.

The choice of physical dimensions for the single-stage cryocooler required several considerations. In accordance with the cryocooler physical size criteria given in Chapter 2, the heat exchanger length was limited to 53 cm. Results from Chapter 3 were used to select the radial gaps between the displacer and cylinder to be 0.127 mm and between the cylinder and outer shell to be 0.254 mm. The choice of bore and stroke required a compromise between operation with and without a liquid nitrogen precooling heat exchanger. The bore to stroke ratio was chosen to be approximately unity. Diameters for the tubes were also restricted by commercially available tube sizes.

Using the above information as a starting point, the displacement was computed using two criteria. First, a mass flow rate due to approximately 1 atm of blowdown when the exhaust valve opens was computed. The amount of mass flow rate due to this blowdown is

$$m_b = \frac{\Delta \rho \, V}{\tau} \tag{4.1}$$

where,

$$V = \frac{\pi D_p^2 s}{4} \tag{4.2}$$

where τ is the period for one cycle, D_p is the displacer diameter, and s is the total stroke. The value used for the change in exhaust density, $\Delta\rho$, is based on an initial state before blowdown and the final state after reversible, adiabatic expansion. Equation (4.1) does not include the blowdown effect due to the dead volume between the displacer and cylinder. Including this dead volume effect would increase the calculated value of mass flow due to blowdown. Not including the dead volume while designing the cryocooler did not result in any problems while running the experiment because the mass flow rate was easily adjustable, as will be discussed later. The effect of dead volume on the blowdown mass flow will be included when analyzing the experimental results. Blowdown is assumed to occur from an initial pressure that is 1 atm above the exhaust pressure. The total displacement, V, was selected based on conditions when operating without precooling. The second equation needed to determine the required displacement volume is for constant pressure mass flow. The mass flow rate at constant pressure while the exhaust valve is open, m_e, is calculated in terms of the corresponding volume displaced as

$$\Delta V = \frac{m_e \tau}{\rho} \tag{4.3}$$

$$\Delta V = \frac{\pi D_p^2 s_e}{4} \tag{4.4}$$

where s_e is the distance moved by the displacer when the exhaust valve is open, and ρ is the density of the exhaust gas at constant temperature and pressure while the valve is open. The value of s_e used in these calculations was chosen to be half of the total stroke. The estimated exhaust temperature at 4 atm was 50 K. Also, the hydraulic drive mechanism was assumed to operate the unit at 100 RPM. The most readily available tube sizes that could meet these criteria were 1 in (25.4 mm) outer diameter.

The final displacer diameter after hydraulic forming is 26.29 mm, as shown in Fig. (4.5). Note that the outer diameter of the displacer includes the thickness of a teflon coating used to reduce friction. The stroke of the hydraulic piston is 26.67 mm.

The gap between the displacer and cylinder is based upon results from the performance algorithm described in Chapter 3 and Appendix B. The performance algorithm indicates that, for the specified conditions, the radial gap between the displacer and cylinder should be chosen at a value that limits the heat leak due to displacer motion while maintaining high heat transfer effectiveness. The radial gap between the displacer and cylinder was chosen to be 0.127 mm. The effects due to the resulting dead volume were not included in the work output computation of the performance algorithm.

The performance algorithm is subject to several assumptions. One of these assumptions is non-periodic flow on the low-pressure side. This steady flow is obtained by providing a surge volume at the cold exhaust and an appropriate flow resistance in the return passage, to form a flow circuit with resistive and capacitive (RC) characteristics. Figure (4.1) includes this configuration.

The low-pressure return side arrangement was designed to yield an RC time constant approximately equal to the period for one cycle. Obtaining this time constant for a set of operating conditions required proper choices of radial gap between the cylinder and outer shell, spiral passage helix angle, and surge volume at the cold end. These dimensions were chosen based on two criteria. First, a value for the magnitude of expansion volume that was comparable with the valve housing volume was selected. Then, the required flow resistance was computed using expressions for the return side pressure drop developed in detail in Appendix A for the cycle analysis. The second criterion was based on entropy generation in the helium gas. Entropy generation due to pressure drop was chosen to be 10% of the total entropy generation in the gas due to pressure drop and temperature difference. Entropy generation on the high-pressure side due to pressure drop was neglected. The pressure drop equations were used by dividing the heat exchanger

length into several segments and evaluating the pressure drop for each segment. Based on the entropy generation analysis, the pressure drop on the low-pressure side was designed to be about 0.4 atm when the experiment operates without liquid nitrogen auxiliary cooling. The experiment had 150 cc of surge volume at the cold end. The helix angle for operation at approximately 100 RPM was computed to be 68°. The radial gap between the cylinder and outer shell was 0.254 mm. Note that the choice of radial gap and helix angle was also dependent upon the fabrication procedure, which will be discussed next.

4.1.2 Hydroforming of the Concentric Tubes

A precise fabrication technique had to be developed for the three tubes comprising the displacer, cylinder and outer shell. Minimizing flow maldistribution required a technique that would maintain constant gap widths between tubes. Eliminating friction due to displacer motion and easing assembly of the tubes required that the tubes be very straight. Also, for the cryocooler to be viable for further development, the fabrication technique had to be simple and relatively inexpensive. Using these criteria, a hydraulic tube forming technique was implemented.

All three tubes were hydroformed within the same forming cylinder. This cylinder was gun drilled using 1117 free-cutting steel to very close tolerances as follows:

- 0.08 mm straightness on 76 cm length,
- 29.46 mm inner diameter with 0.01 mm tolerance,
- 4.7 mm wall with 0.1 mm tolerance, and
- 0.4 μm surface finish.

The "straightness" specification is defined in Fig. (4.6). This specification will also be used to specify straightness of the tubes.

The hydroforming process will now be described. The outer shell was formed first. A schematic of this forming process is shown in Fig. (4.7). End plugs were welded into the thin-walled tube to be formed. This tube was then filled with hydraulic fluid and placed inside the forming cylinder. The tube was then pressurized

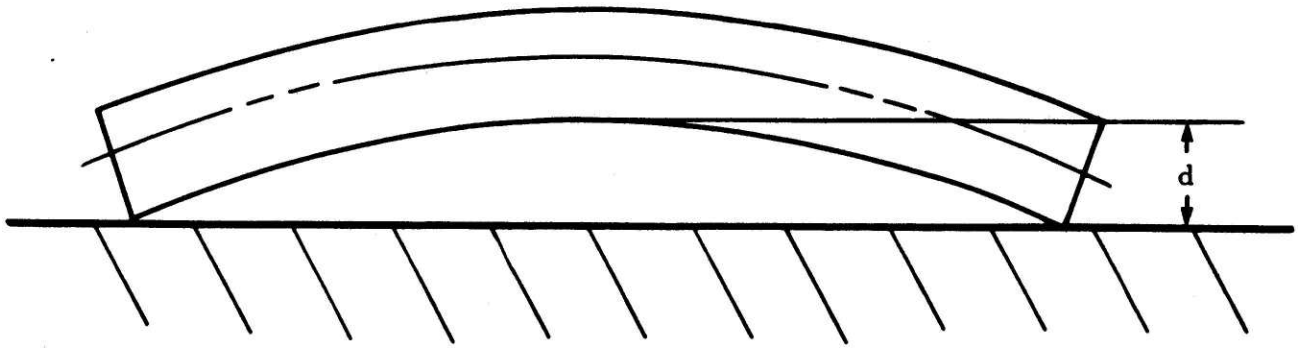

Fig. (4.6) Definition of tube straightness, d.

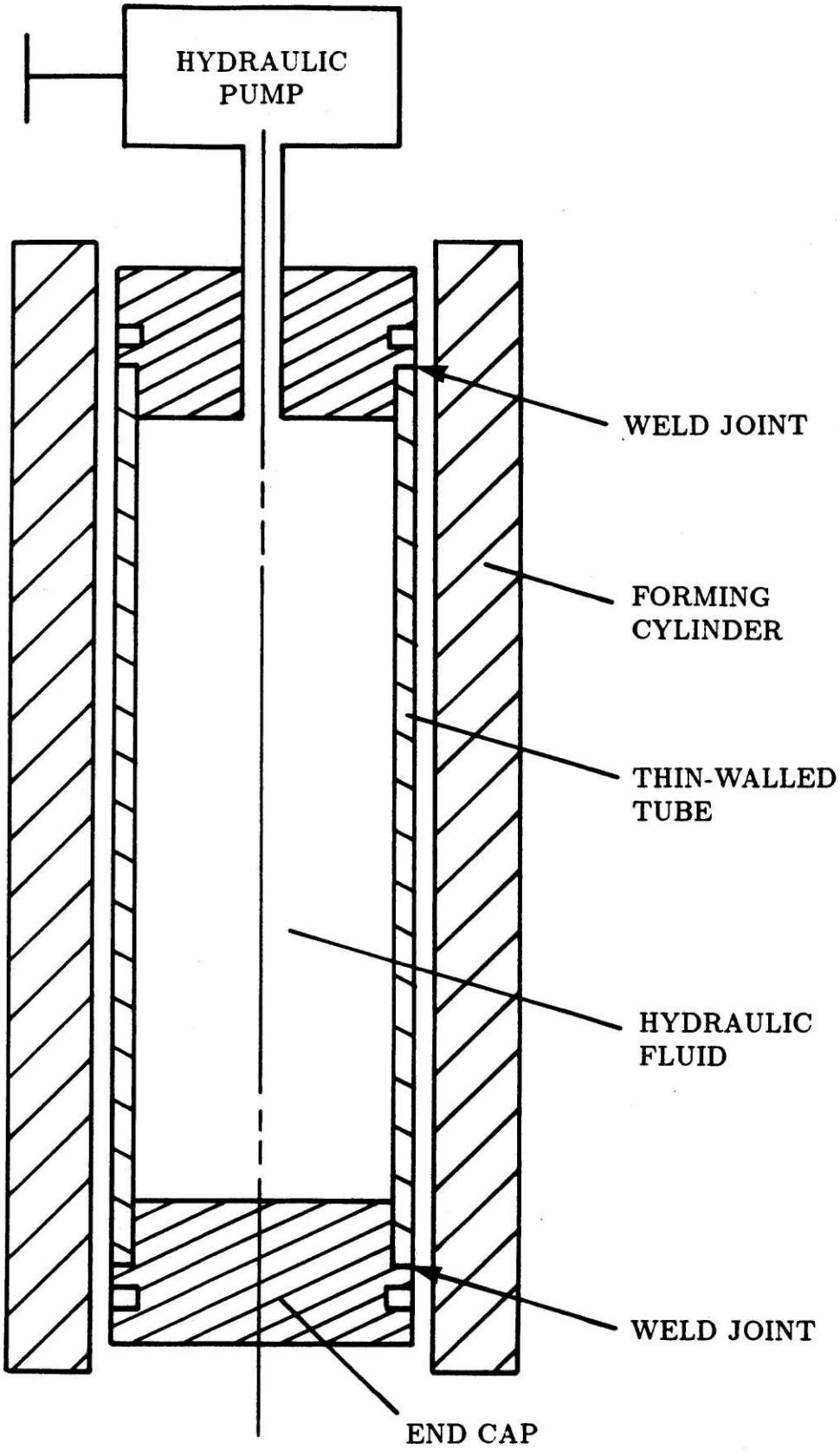

Fig. (4.7) Schematic of outer shell forming apparatus.

until it pressed against the forming cylinder. The pressure was then relieved and the formed tube was removed. The end plugs were next removed and the inside of the tube was cleaned.

To obtain a 0.254 mm radial gap between the cylinder and outer shell, two layers of mylar, each 0.127 mm thick, were placed inside the outer shell. Care was taken to fit each mylar sheet tightly into the outer shell without overlap. The cylinder was next formed against the mylar spacers. A single layer of mylar was then used to obtain the 0.127 mm radial gap between the displacer and cylinder. After the mylar spacer was in place, the teflon coated displacer was formed.

Separation of the formed tubes required use of a threaded shaft which separated two tubes at a time. The threaded shaft was screwed into the end cap of one tube and then turned to push against the opposite end cap of another tube, thereby pushing the tubes apart. The force required to push the tubes apart is small compared to the force required for plastic deformation. This method was first used to separate the displacer from the yet unseparated cylinder and outer shell. After the displacer was removed, the method was repeated for the cylinder and outer shell. A photograph of the tubes, mylar sheet, and hydraulic pump is given in Fig. (4.8).

Table (4.1) gives the initial and final diameters for the 304 stainless steel tubes along with the final straightness for each tube. A few points should be mentioned about these results. First, the displacer was coated with S-400 teflon before the forming process. The teflon did not peel or crack during the process. Second, as indicated in Table (4.1), the cylinder tube had to be plastically yielded approximately 10%, which is about twice as much as the displacer or outer shell. For this reason, the cylinder tube was annealed once after being formed 5% in an effort to prevent necking of the tube wall. A separate forming cylinder was used for this preforming process. The hydroforming process resulted in tubes of surprising straightness. Table (4.1) indicates that straightness improves as tube thickness increases; indeed, for the displacer, no unstraightness could be measured with the available instruments. The unstraightness measurements for the cylinder and outer shell indicated that the tubes were in a continuous bow, as indicated in Fig. (4.6).

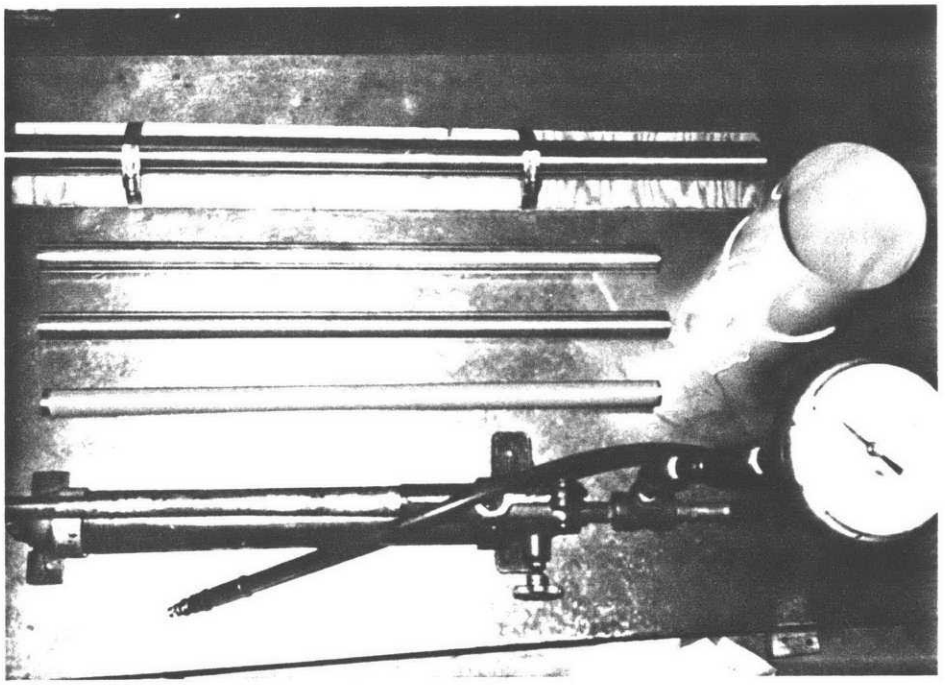

Fig. (4.8) Photograph of tubes, mylar, and hydraulic pump used for the hydroforming process.

Table (4.1) Displacer, cylinder, and outer shell tube dimensions.

Tube	Initial O.D. (mm)	Initial Wall (mm)	Final O.D. (mm)	Final I.D. (mm)	Final Straightness (mm)
Displacer	25.4	0.89	26.3	24.7	–
Cylinder	25.4	0.71	28.0	26.6	0.051
Outer shell	28.6	0.51	29.4	28.5	0.051

Table (4.2) Hydraulic pressures and yield stresses for the tube forming.

Tube	P_y (MPa)	σ_y (MPa)	P_b (MPa)	σ_b (MPa)	P_{max} (MPa)
Displacer	23	335	30	462	46
Cylinder	10	188	17	365	24
Outer shell	7	184	13	369	21

Table (4.2) gives the hydraulic pressures and yield stresses required for the tube forming. The first two values are the hydraulic pressure and tube yield stress for each tube when plastic deformation began. The next two values are the hydraulic pressure and yield stress when the tube bottomed against the forming surface. The final value is the maximum hydraulic pressure applied to ensure that the tube firmly bottomed against the forming surface. The values listed in this table were easily observed by a sudden change in the rate of change in hydraulic pressure as fluid was pumped into the tube. Pressure increased very slowly during plastic deformation; when the tubes were elastically deformed during initial tube pressurization or during the bottoming stage, pressure increased rapidly as hydraulic fluid was added to the tube.

4.1.3 Fabrication of the Spiral Spacer

A schematic of the flow arrangement that includes the spiral spacers is shown in Fig. (4.5). Two spiral spacers are used in the low-pressure return side in an effort to reduce flow maldistribution and to create RC circuit characteristics. The radial thickness of the spacers is 0.254 mm and the helix angle (as shown in Fig. (4.5))

is 68°. For these spiral spacers to be effective, leakage around the spacers had to be kept minimal. The spiral spacers are made of Stycast 2850 epoxy from Emerson Cummings. This epoxy has been used successfully in low-temperature applications at the MIT Cryogenic Engineering Laboratory. A description of the fabrication procedure will be given next and will be followed by the assembly procedure for the cylinder and outer shell.

The hydraulically formed cylinder tube was first placed on a case-hardened carbon steel mandrel so that the thin-walled tube would remain straight during the spiral spacer fabrication. The mandrel had been centerless ground to a diameter that allowed very little clearance between it and the inner diameter of the cylinder. The mandrel was also straight to within 0.03 mm on the length, as defined in Fig. (4.6). The mandrel was then mounted in a lathe. Much care was taken to center both ends of the mandrel so that the spiral spacers would be of the same thickness over the entire length. To provide a 68° helix angle, the lathe was modified so that the carriage moved at a pitch of 35.6 mm per spindle revolution.

Two grooves, approximately 0.75 mm wide and 0.495 mm deep, which would be filled with the epoxy were next constructed. Three layers of kapton tape (0.127 mm kapton with 0.038 mm adhesive) were applied to the cylinder for each spiral spacer. A tape applicator was made to accommodate both rolls of tape. One layer of tape consisting of two rows was placed on the cylinder during each pass to form one groove; three passes were required per spacer. A photograph of the tape application is given in Fig. (4.9). The kapton tape used was not cut at the factory to a constant width. For this reason, extra care had to be taken to ensure that the three layers of tape were flush on the edge where epoxy would be filled.

The resulting grooves were then filled with Stycast 2850 epoxy and allowed to harden. The tape was then removed. The result was two spiral spacers which had to then be machined to a diameter that would allow assembly of the cylinder and outer shell tubes. A carbide tool was used to turn the spacers to a diameter required to give 0.013 mm of interference with the outer shell. This interference was necessary to ensure minimal helium flow leakage in the axial direction. The

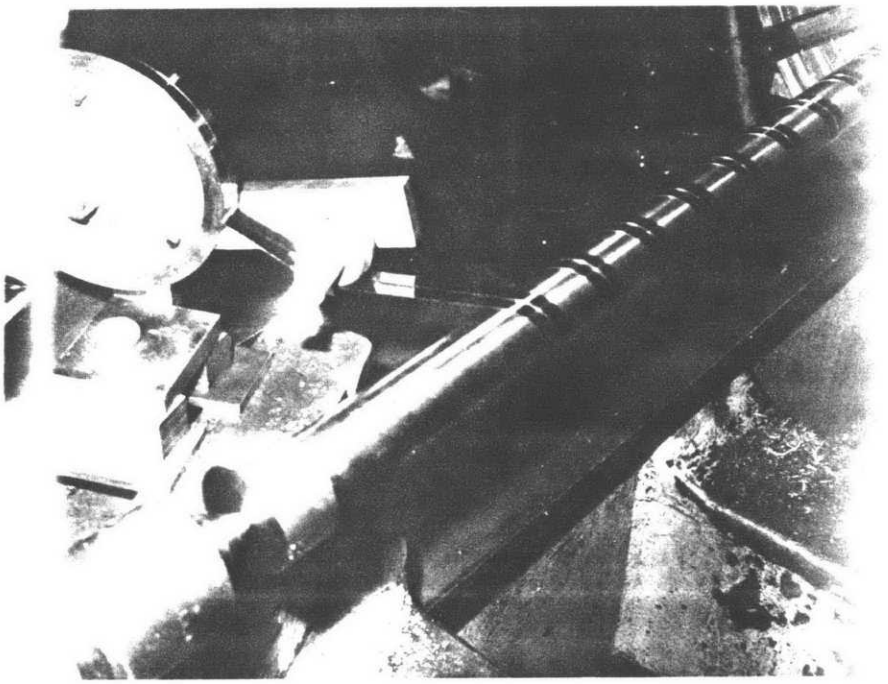

Fig. (4.9) Photograph of the tape applicator used to make casting grooves for the spiral spacers.

carbide tool was moved at the spiral spacer pitch so that the tool was continuously in contact with the epoxy spacer.

At this point, the tubes for the cylinder and outer shell were complete. Before assembly, however, end pieces for the warm end had to be welded to both the cylinder and outer shell. The cylinder end piece had to be honed to match the cylinder tube ID. Also, the exhaust valve housing had to be welded to the cold end. Photographs of the completed cylinder and outer shell are given in Figs. (4.10) and (4.11), respectively.

Assembly of the resulting cylinder and spiral spacers with the outer shell required raising the temperature of the outer shell and lowering the temperature of the cylinder in an effort to prevent damaging the spiral spacers. The jig used for assembly is shown in Fig. (4.12). The jig allowed the cylinder to be filled with liquid nitrogen supplied from a pressurized dewar. The nitrogen boil-off gas was then vented through an exhaust tube located inside the cylinder so that the gas entered the exhaust tube at the top end of the cylinder and exhausted at the bottom end, at the same level where the liquid nitrogen entered. To prevent air from condensing on the cylinder, room temperature nitrogen flowed in an annular space located outside the cylinder. This nitrogen was routed so that air could not enter the cold area. The outer shell was heated using heating tape. When the cylinder was at approximately 80 K and the outer shell was at approximately 400 K, the outer shell was lowered onto the cylinder. Lowering of the outer shell was done manually, which provided adequate speed control and allowed aligning of the outer shell with the cylinder. A photograph of the assembled unit is given in Fig. (4.13). The cylinder and outer shell assembly was completed by TIG welding together the warm end pieces.

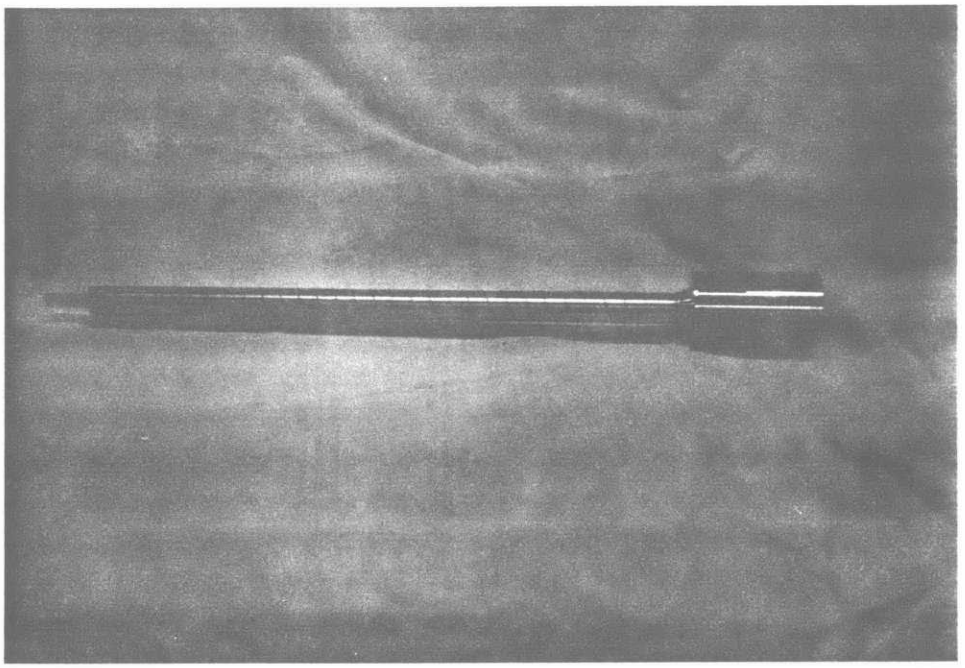

Fig. (4.10) Photograph of cylinder with spiral spacer and end pieces.

Fig. (4.11) Photograph of outer shell with end pieces.

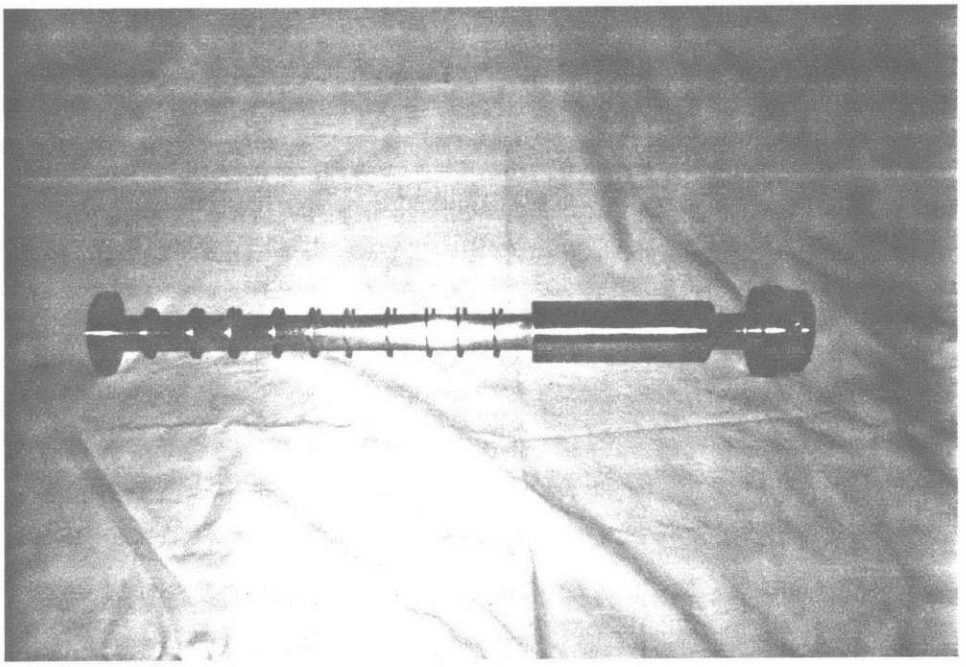

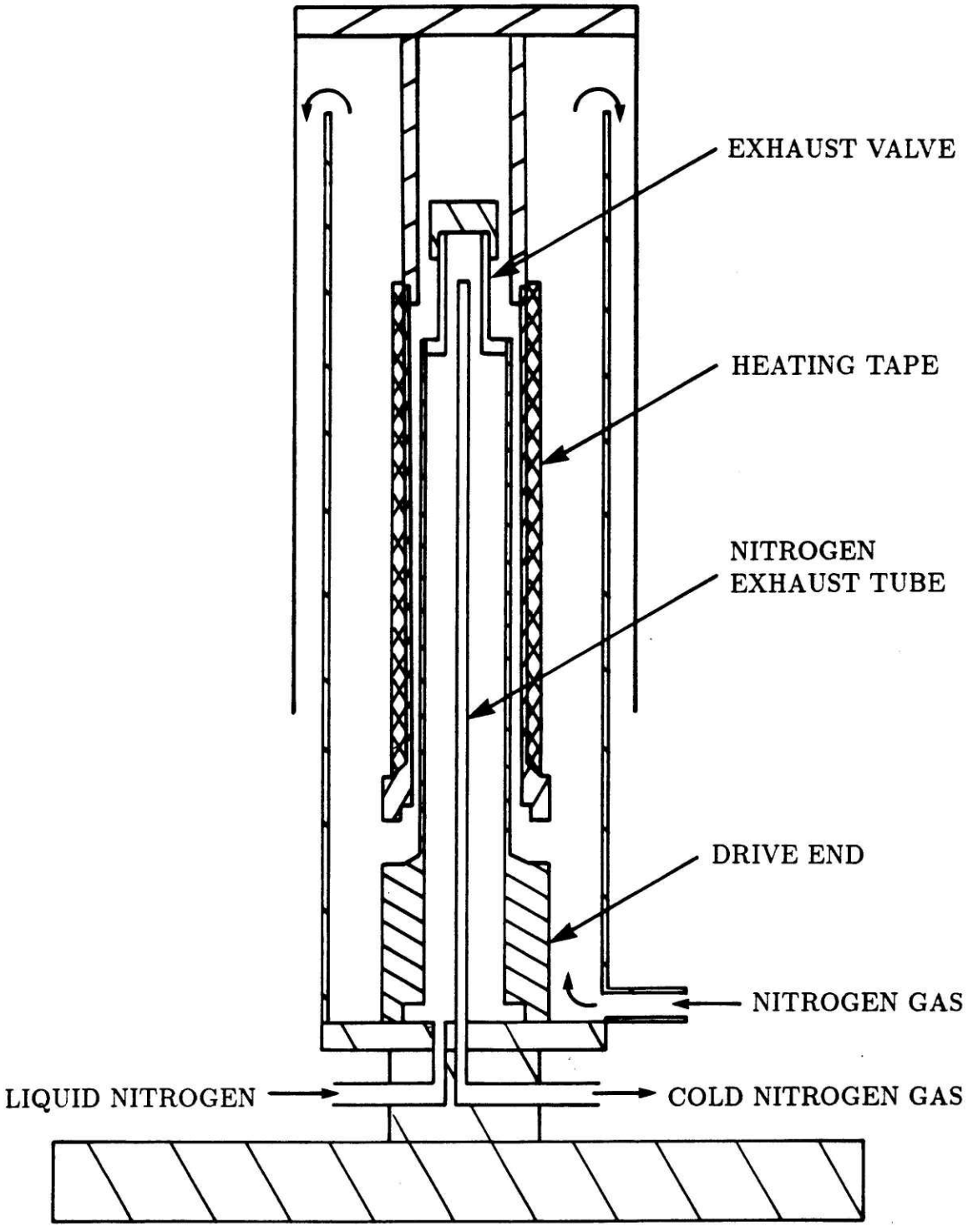

Fig. (4.12) Cross section of jig used to assemble cylinder and outer shell.

Fig. (4.13) Photograph of assembled cylinder and outer shell without surge volume.

4.2 Inlet and Exhaust Valves

Valving considerations played a major role in the cryocooler development. For adequate cryocooler performance, the inlet and exhaust valves had to provide:

1) sufficient valve sealing to prevent gas leakage from high to low pressure when the valve was closed,
2) minimum resistance to gas flow when the valve was open, and
3) quick response to input signals to open and close.

Sealing for both valves was achieved by using Kel-F valve washers, which provided compliance between the valve plunger and the stainless steel valve seats. Also to provide sealing, the pressure on the contact surface was maintained at two times the magnitude of the pressure difference between the high- and low-pressure sides.

Flow passages for both valves were designed large enough to make pressure drops through the valves very small. This design was possible since only one valve was located at the cold end, which leaves room for a large exhaust valve. A drawing of the exhaust valve is shown in Figure (4.14). The valve plunger was teflon coated. Flow entered the exhaust valve from the expansion space, flowed between the moving valve and the valve guide until arriving at radial exit holes, and then flowed between the valve guide and a flow guide tube until exiting at the valve base. Directing the flow along the entire length of the valve guide was intended to keep the valve and surge volume isothermal. Figure (4.15) shows the inlet valve. Flow entered through the valve housing and flowed between the teflon coated plunger and valve guide inside of three equally spaced grooves cut in the plunger along the valve axis. Photographs of both valves mounted on the experiment are shown in Figure (4.16).

Quick valve response to input signals was essential. Earlier experiments at the MIT Cryogenic Engineering Laboratory indicated that sluggish valve response causes the system to be unpredictable when valve timing was changed slightly. These earlier systems used a pneumatic system to provide valve timing and to power the valves.

For the inlet and exhaust valves in this experiment, valve timing was electron-

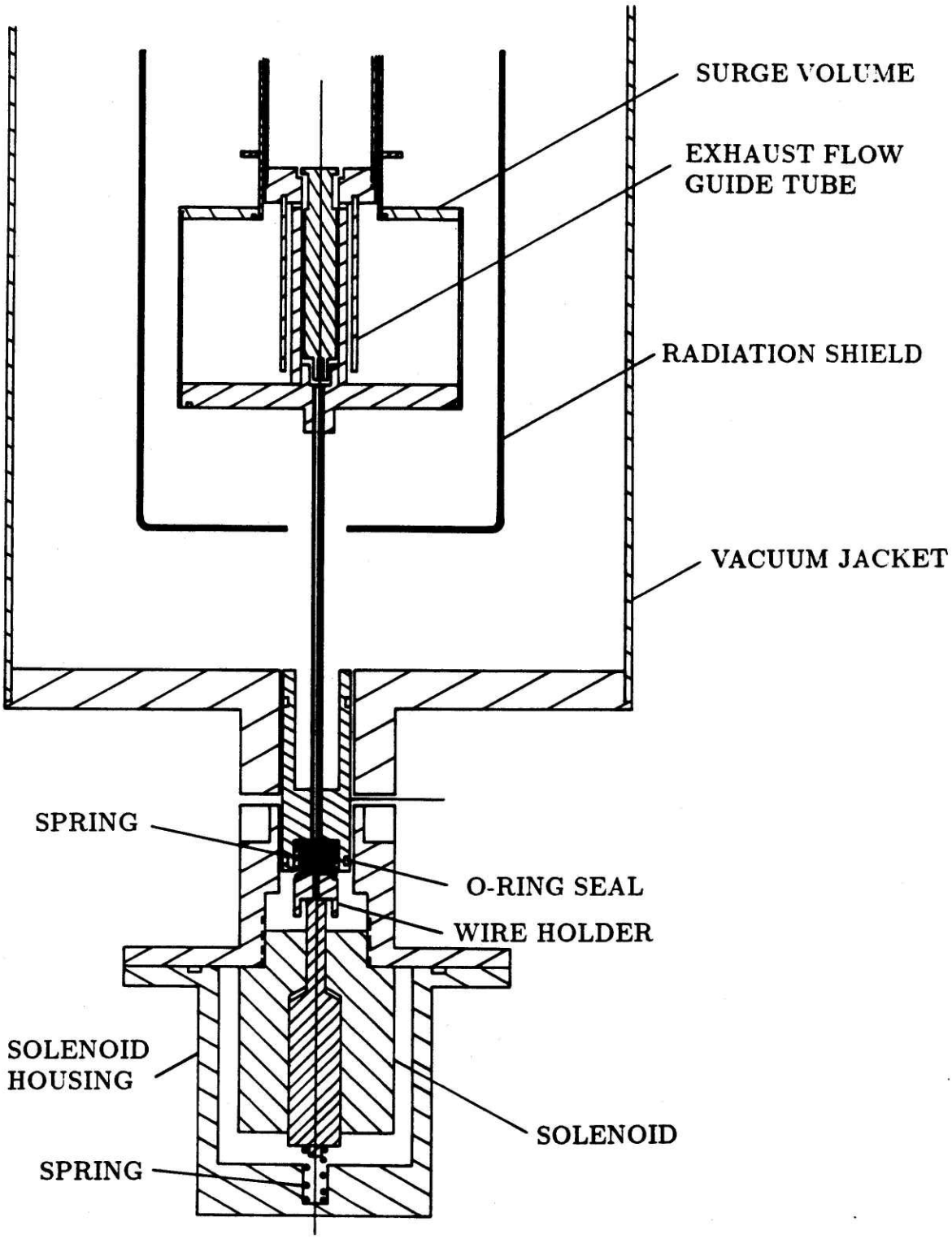

Fig. (4.14) Exhaust valve.

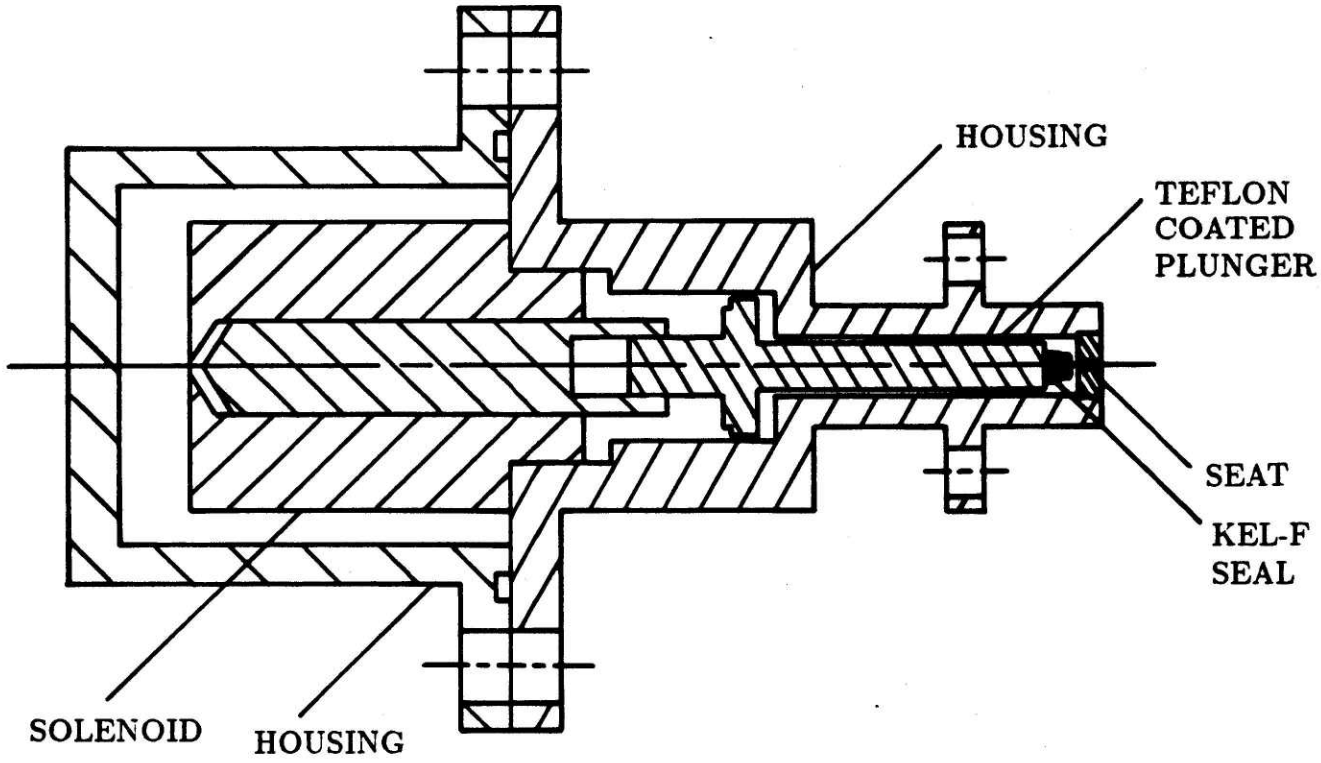

Fig. (4.15) Inlet valve.

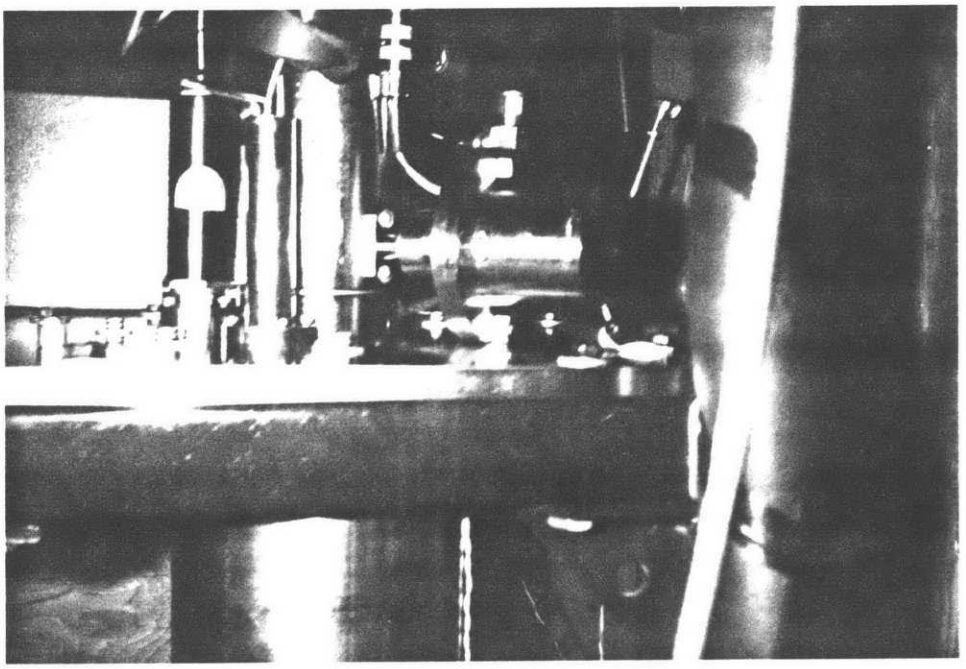

INLET
VALVE

Fig. (4.16) Photographs of inlet and exhaust valves.

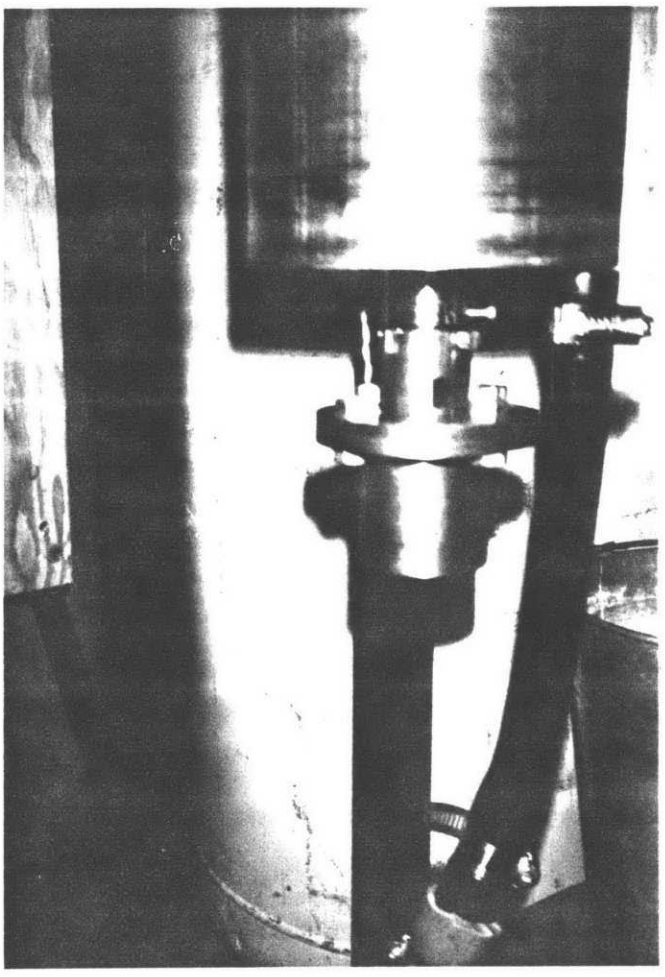

EXHAUST VALVE

ically controlled by a signal from a linear displacement transducer attached to the hydraulic piston. Power to move the valves was provided by commercial solenoid plungers. For the exhaust valve, the solenoid used was a Guardian Tubular Solenoid TP12X13, Stock Number 67F5620. This is a push type solenoid/plunger requiring a nominal 24 V dc input to obtain a force of 33 N when the plunger is 3.2 mm off its seat. The inlet valve used a Guardian Tubular Solenoid T12X13, Stock Number 24F2978, which is a pull type solenoid/plunger using a 24 V dc input for a force of 42 N at a stroke of 3.2 mm. Both valves use the solenoid force to open the valve and spring force to close.

4.3 Hydraulic Drive Mechanism

The drive mechanism for the expander must absorb the energy transferred to room temperature from the expansion work and must maintain displacer motion. A hydraulic system was chosen for this experiment. During the expansion portion of the cycle, the hydraulic system is used to dissipate work. Then, during the exhaust and recompression portions of the cycle, the system supplies the needed power to maintain motion. Also, when displacer motion heat leak is measured, power is supplied by the hydraulic system to move the displacer for the complete cycle.

A schematic of the hydraulic system is shown in Figure (4.17) with an accompanying legend. All components are from Pneumatic and Hydraulic Distributors, Inc. The supply pump is a model PAVC233OR2. The hydraulic system was designed to yield maximum flexibility. To achieve constant piston motion, the pump was operated as a pressure source and two pressure compensated flow control valves were used to control the stroke speed. Flow control valve, G, was used to set the speed of the displacer for the exhaust and recompression portions of the stroke. A second flow control valve, B, was used to set the speed of the intake and expansion work portions of the stroke. The relief valve, F, allowed independent operation of the two flow control valves. As will be discussed later, slow response of the pressure compensated valve, B, when the directional control valve switched resulted in fast displacer motion during the initial stage of the expansion stroke.

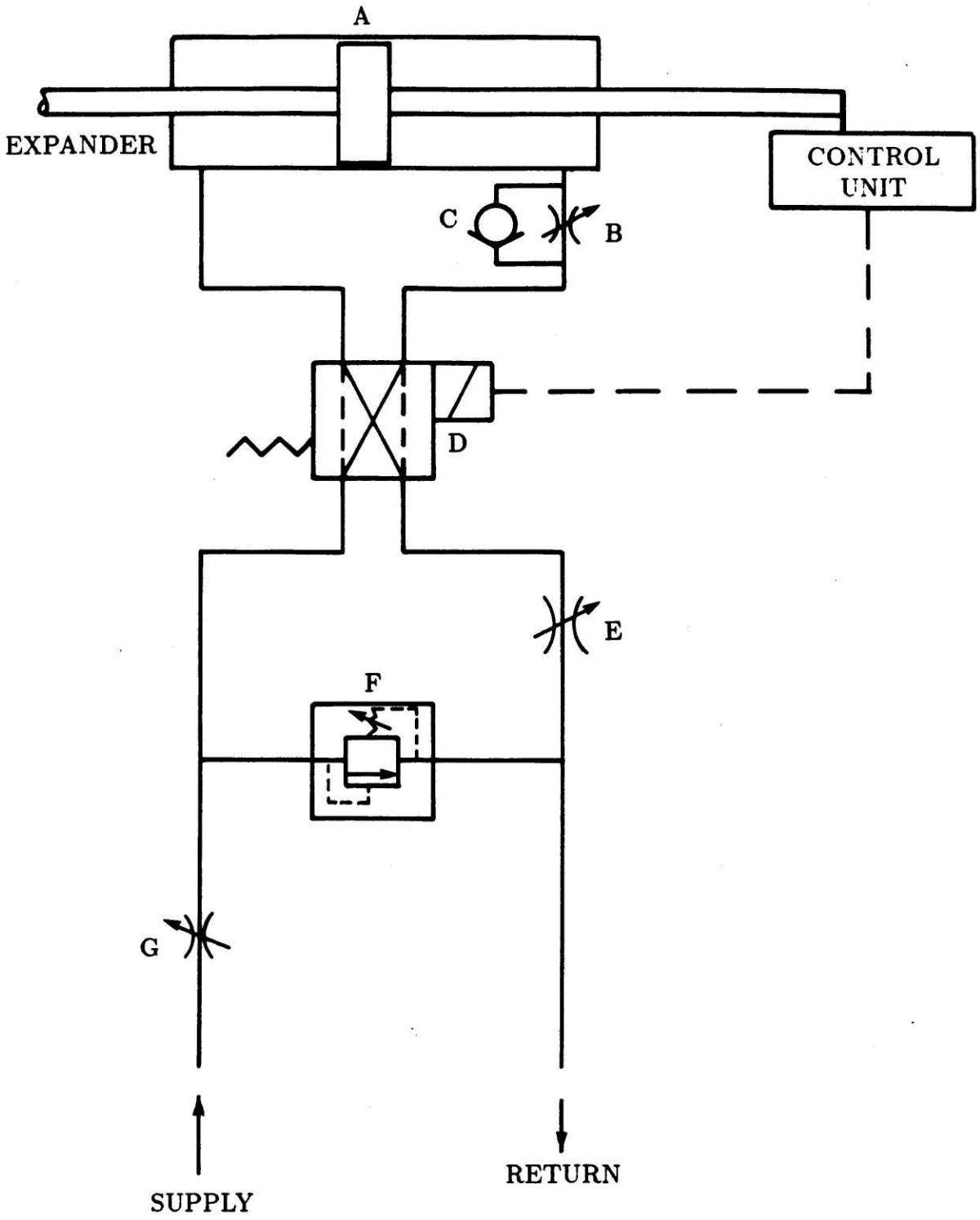

Fig. (4.17) Schematic of hydraulic system with accompanying legend.

Legend for Figure (4.17).

	Part No.	Description
A	1-KJB3LLUS14/19AX1.050	hydraulic cylinder
B	FR101S050	pressure compensated valve
C	C200S	check valve
D	D1VW20BY	directional control valve
E	N200S	needle valve
F	RA101K10	relief valve
G	FR101S100	pressure compensated valve

4.4 Electronic Control System

Timing among the hydraulic directional control valve, inlet valve, and exhaust valve was controlled electronically by a single control unit, as shown in Figure (4.18). Each of the three valves was operated using a similar sub-circuit. The position of the displacer was measured continuously using a Longfellow Motion Position Transducer model SLF-S-SO-D-1. For each valve, two LM311 comparators were used with potentiometers to adjust when the valve would be energized and de-energized. This type of control requires use of an electronic memory device. Outputs from the two comparators were, thus, connected to a flip-flop using transistor-transistor logic (TTL). The flip-flops used were made by combining two 74LS00 NAND gates.

Initial results from the experiment indicated a need for a short delay when the displacer was in the position of minimum volume. At this position, the inlet valve opened. A delay had to be built into the controls so that the dead volume between the displacer and cylinder could be pressurized before the displacer began to move. When no delay was used, the maximum usable intake pressure was less than 40 atm because resistance to flow through the inlet valve and displacer-to-cylinder gap resulted in slow pressurization of the working volume after displacer motion began. The pressure in the dead volume and working space when the inlet valve closes must be low enough to allow expansion to near the return side pressure. The required delay was obtained by adding a monostable multivibrator in conjunction with a NOR gate to the circuit described in the preceeding paragraph. The monostable

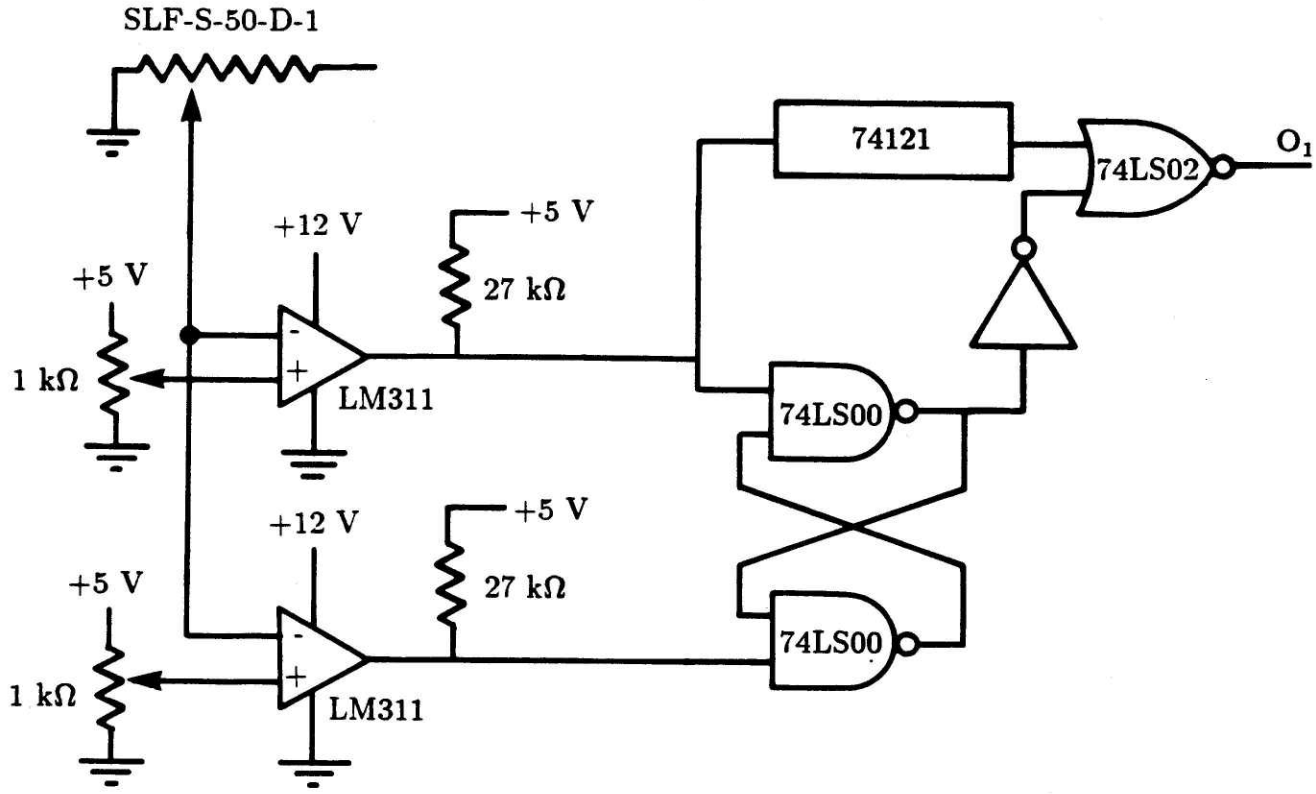

Fig. (4.18)(a) Schematic of electronic control circuit for hydraulic directional control valve.

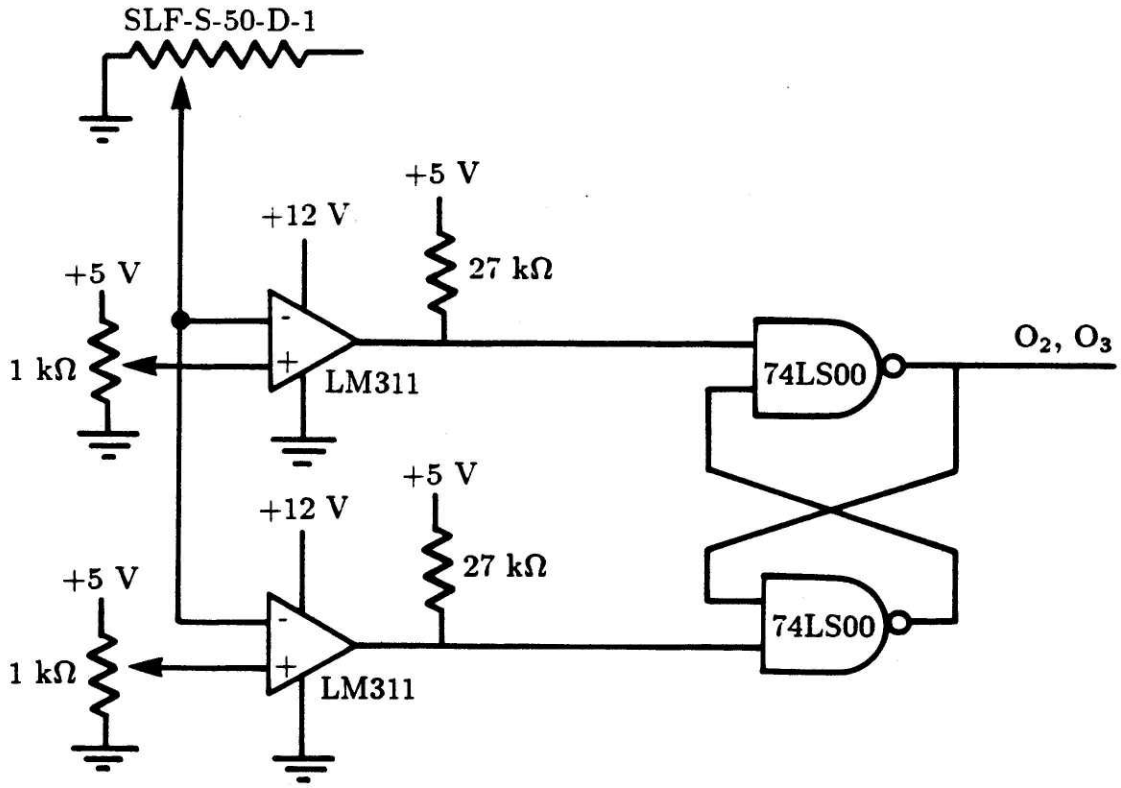

Fig. (4.18)(b) Schematic of the electronic control circuit for the inlet and exhaust valve solenoids.

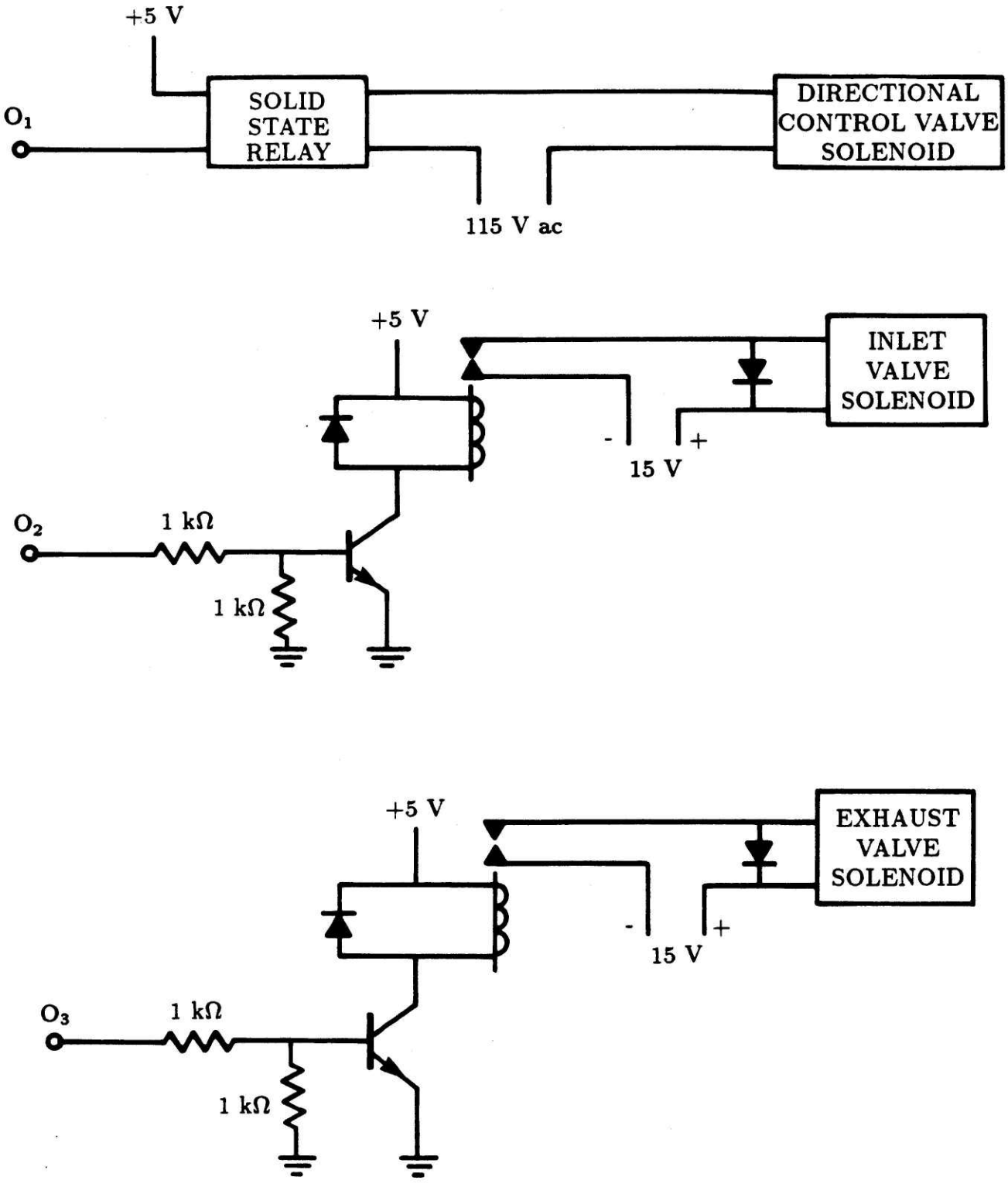

Fig. (4.18)(c) Relay circuit between the electronic control unit and the solenoids.

multivibrator allowed an adjustable pause after the hydraulic piston bottomed onto its seat. During this pause, the dead volume was charged to 40 atm. The non-retriggerable monostable multivibrator selected for the modification was a 74121 using a 10 μF capacitor and a 0 to 100 kΩ multi-turn potentiometer to obtain the appropriate time constants. The NOR gate was a SN74LS02.

The output from each TTL circuit was input to a relay. The relay circuit is shown in Figure (4.18)(c). Since the hydraulic control valve uses 120 V ac, the relay used for the hydraulic control valve is solid state. The inlet and exhaust valves both used mechanical relays from Radio Shack. A 5 V dc power source was used in conjunction with an npn transistor to switch both the mechanical and solid state relays from TTL. Several filters were used to diminish the effects of noise and to reduce the magnitude of ground spikes.[38]

4.5 Experimental Results

The experimental procedure had two objectives. First, magnitudes of the heat leaks due to axial conduction and displacer motion were measured. During these measurements, no refrigeration was produced. The information obtained was used to test the analytical models developed and to get actual values for the magnitudes of heat leaks. The second objective was to determine the refrigeration capacity of the single-stage cryocooler both with and without liquid nitrogen auxiliary cooling.

In order to avoid any confusion of terminology used, each part of the expander cycle was defined using Fig. (4.19). When the exhaust portion of the stroke was complete, the exhaust valve closed and recompression begun. Recompression was complete when the displacer was approximately 0.15 mm from touching the cylinder head. At this position, the dead volume consisted of the displacer-to-cylinder gap volume, the volume between the displacer crown and cylinder head, and any other volume that was pressurized and depressurized that was not a part of the working volume. After recompression, the intake valve opened so that the dead volume was pressurized. After pressurization, the displacer began to move so that additional gas flowed into the working volume at constant pressure until the intake valve closed. The displacer position where the intake valve closed was referred to as the cut-off position. Expansion then began and continued until the displacer reached the position of maximum volume. At this point, the exhaust valve opened. Blowdown consisted of the depressurization of the dead volume and working volume from the pressure at the time the exhaust valve opened to the pressure of the surge volume. Gas was removed from the working volume while the exhaust valve was open.

Throughout the experiment, the inlet and exhaust valve timing was adjusted repeatedly to obtain the desired mass flow rate for the particular data point. As explained earlier, the displacer position was continuously monitored using an electronic position transducer. Comparators were used to set valve timing with respect to displacer position. In this way, the valves could be set to open and close at any displacer position. Valve timing for each of the valves was set independently by

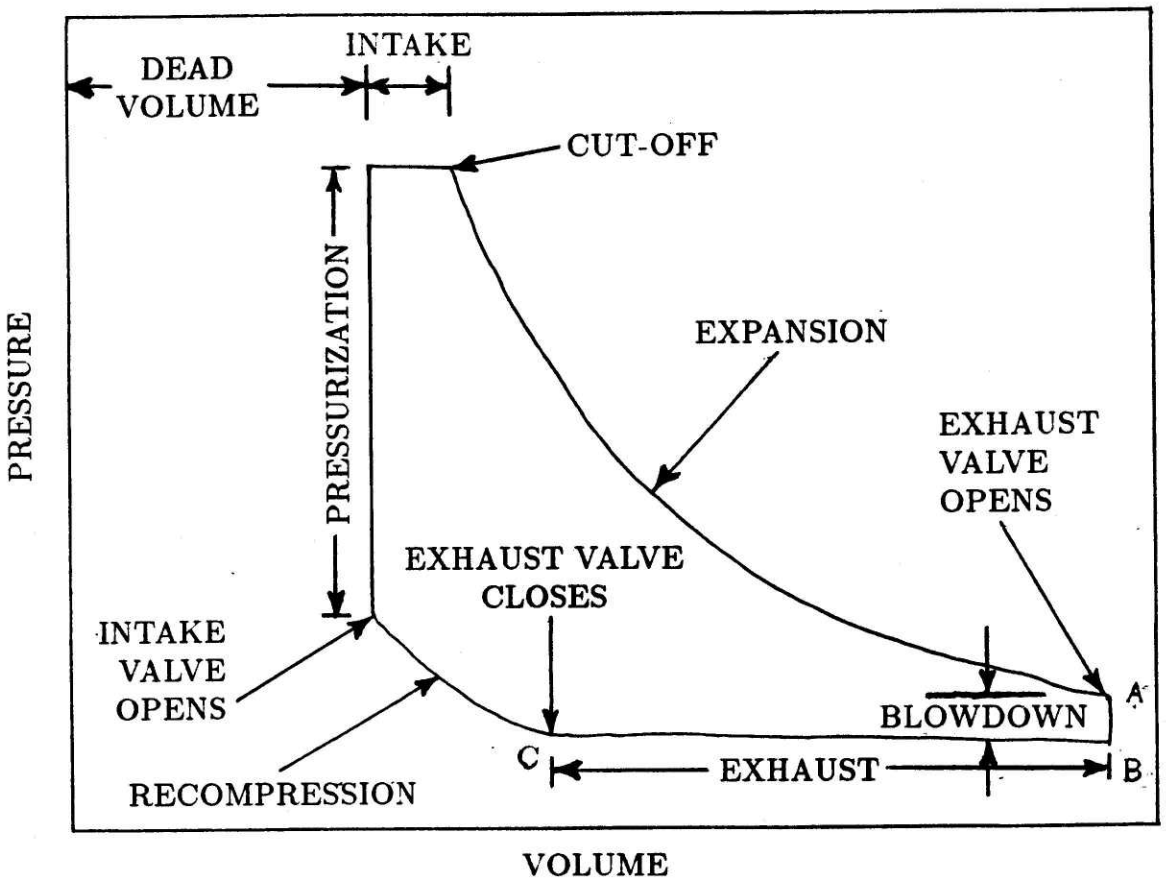

Fig. (4.19) Representative pressure versus volume plot used to define each part of the cycle.

adjusting a potentiometer used in conjunction with the comparator.

The mass flow rate was therefore selected by adjusting the valve timing. The amount of blowdown was set by adjusting the cut-off point for the inlet flow. More blowdown resulted as the inlet valve closed later. The amount of constant pressure exhaust mass flow was set by adjusting when the exhaust valve closed (*i.e.*, when recompression began). A method of computing the amount of mass flow during blowdown and during constant pressure exhaust was given earlier in Section (4.1.1). This method of computing the mass flow rate did not include the additional blowdown due to the displacer-to-cylinder gap dead volume. In this section, the same method of computing mass flow was used except that the dead volume effects were included.

An important parameter for the expansion engine was the volume ratio, defined as

$$E_V = \frac{V_C}{V_W} \tag{4.5}$$

where V_C was the clearance or dead volume and V_W was the working volume. The dead volume was made up primarily of the volume in the displacer-to-cylinder gap and the displacer crown to cylinder head gap when the displacer was at the position of minimum volume. Also included in the dead volume was other small volumes such as in a capillary tube used to connect a pressure transducer to the engine. The total dead volume was approximately 6 cc. The volume displaced by the displacer during the total stroke was the working volume, which was 14.5 cc. The volume ratio was then computed to be 0.41.

As a final comment before giving the experimental results, the independent adjustment of the valve timing allowed the start of recompression and the cut-off point to be selected by simply adjusting a potentiometer. One should note that the engine efficiency was expected to be dependent on the amount of recompression. As the amount of recompression was reduced, the engine efficiency was expected to decrease. The experimental results that follow identify the optimal amount of recompression.

4.5.1 Measured Heat Leaks

Axial conduction along the heat exchanger and radiation heat leak from the vacuum jacket comprise the static heat leak. An experiment was performed that isolated this heat leak from other losses encountered during operation as a refrigerator. The experiment consisted of cooling the surge volume of the cryocooler to near liquid nitrogen temperature and then measuring the amount of energy that must be removed from the surge volume in order to maintain a constant temperature. During the measurements, helium was not circulated through the heat exchanger and the displacer remained stationary. The exhaust valve was kept open to maintain constant pressure in the engine.

The heat leak due to displacer motion was measured by stroking the displacer while keeping the exhaust valve open to maintain constant pressure in the engine and heat exchanger. The magnitude of displacer motion heat leak is the difference between the energy removed from the surge volume in order to maintain constant temperature and the static heat leak measurement. As indicated by the results of Chapter 3, the displacer motion heat leak is relatively independent of engine speed. For this reason, operating the engine at different speeds indicated whether heat was being generated due to friction between the displacer and cylinder wall. Heat generated due to friction is directly proportional to the engine speed.

Figure (4.20) shows the experimental set-up used to measure static and displacer motion heat leaks. To make the heat leak measurements, slightly superheated nitrogen gas passes through a copper coil that is silver brazed to the surge volume to form a heat exchanger. The gas temperature was measured at the entrance to and exit from the heat exchanger by placing diode temperature transducers on the copper coil (see Appendix C for instrumentation details). The mass flow of nitrogen through the heat exchanger was measured at room temperature using a Datametrics model 800-LM flow meter and a model 100-10K hotwire sensor. The meter was factory calibrated for this measurement. The magnitude of heat leak may then be calculated using

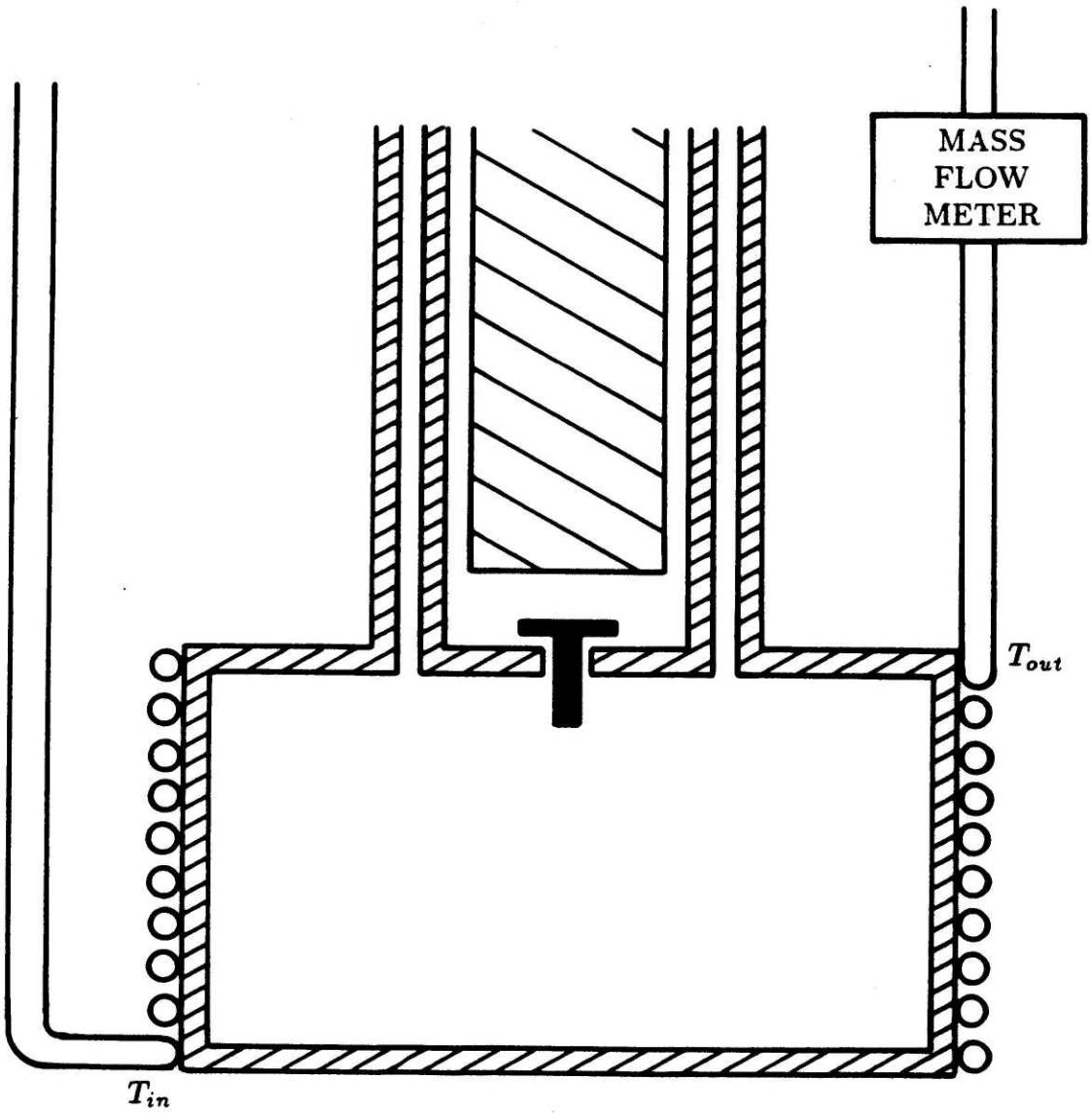

Fig. (4.20) Experimental set-up used to measure static and displacer motion heat leaks.

$$q = m_N (h_{out} - h_{in}) \tag{4.6}$$

where m_N is the mass flow rate of nitrogen and $(h_{out} - h_{in})$ is the enthalpy change. The experiment had to cool for approximately 10 hours before steady state temperatures were reached along the heat exchanger. The cooling down period was shortened by opening the inlet and exhaust valves and allowing helium to flow through the experiment. The following losses were recorded:

Static heat leak = 1.18 W

Displacer motion heat leak (95 RPM) = 1.50 W

The magnitude of displacer motion heat leak varied very little between 35 RPM and 110 RPM.

4.5.2 Cryocooler Performance

This section gives results obtained from the single-stage cryocooler operating from room temperature. The method used to find the minimum temperature that could be reached by the cryocooler will be described first and several results will be given. The result of adding various heat loads to the cold end will then be described.

An iterative method was used to determine the minimum temperature the cryocooler could reach. The adjustable variables were the speed of the engine and the time-averaged mass flow rate. To set the total amount of mass flow, the cut-off point was used to adjust the blowdown mass flow and the start of recompression point was used to adjust the amount of constant pressure mass flow. Figures (4.21) and (4.22) illustrate the method used. Figure (4.21) shows data points collected at a constant engine speed of 105 RPM while varying the mass flow rate. After finding the optimal time-averaged mass flow rate at one engine speed, the engine speed was varied while maintaining the optimal mass flow rate as shown in Fig. (4.22). This iterative procedure was continued until a minimum refrigeration temperature was found. The minimum exhaust temperature recorded was 35 K at an engine speed of 90 RPM and time-averaged mass flow rate of 0.107 g/s.

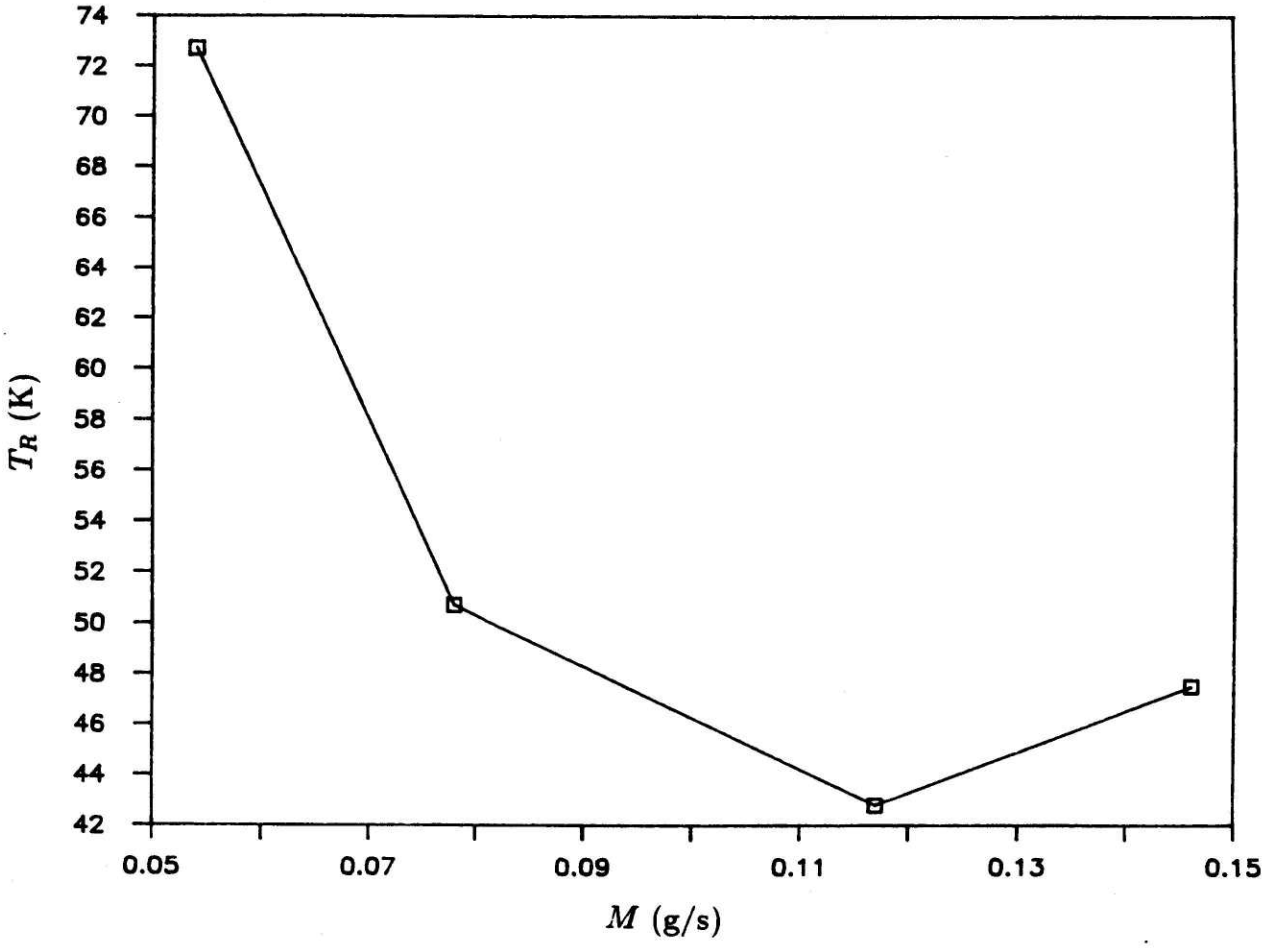

Fig. (4.21) Refrigeration temperature versus time-averaged mass flow rate at constant engine speed for the case of no heat load and no precooling.

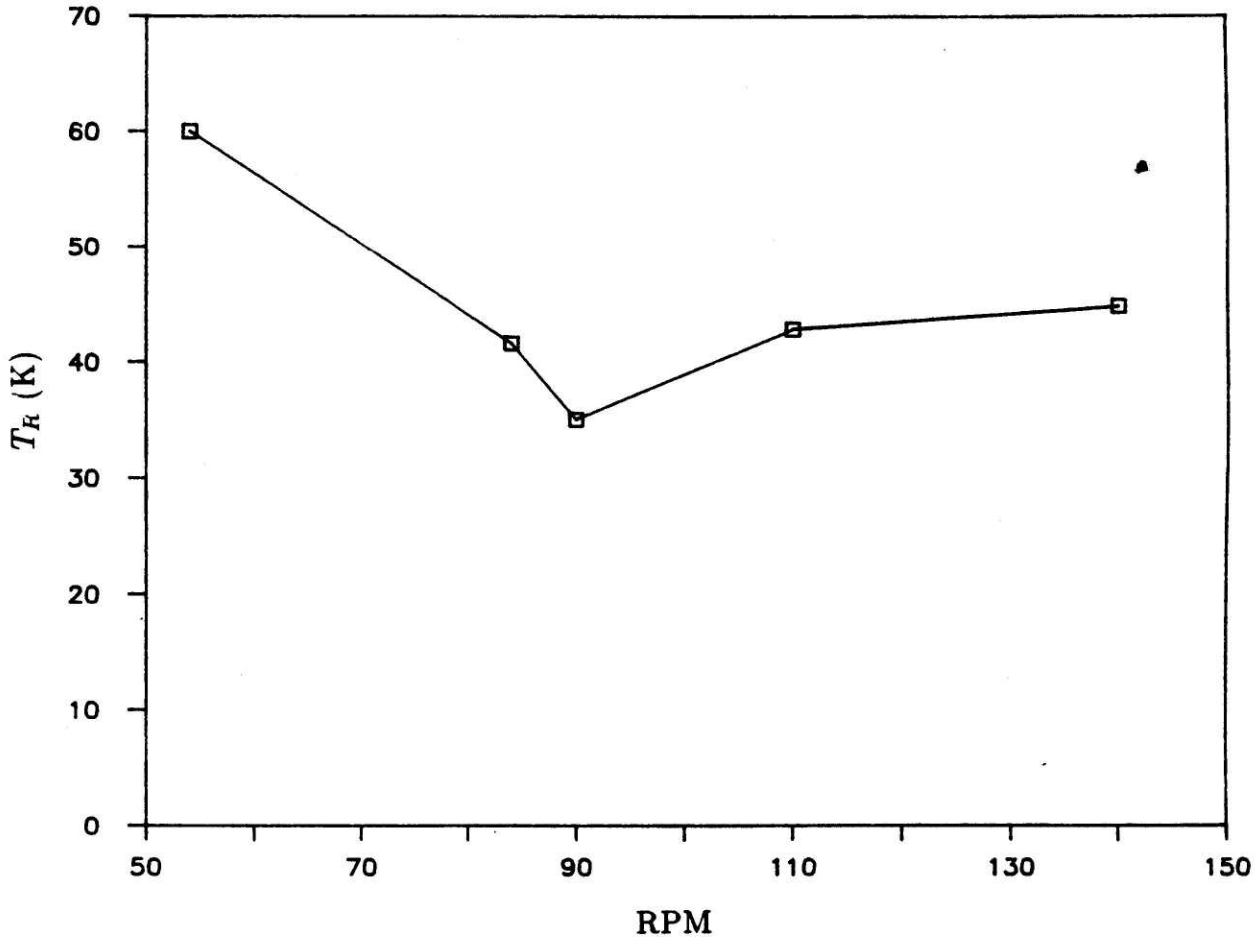

Fig. (4.22) Refrigeration temperature versus engine speed at constant mass flow rate for the case of no heat load and no precooling.

Much information was obtained while operating at the minimum temperature. A pressure versus volume plot is shown in Fig. (4.23). Integration reveals that the indicated work was approximately 18.1 W. The indicated work was the amount of work done on the displacer by the gas. The plot indicates that the optimal running condition required substantial recompression. From the plot, one may also observe an erratic behavior when the expansion stroke began. This behavior was due to slow response of the pressure compensated flow control valve, B, of Fig. (4.17) when the directional control valve switched to begin the expansion stroke. As explained earlier, the electronic control system delayed displacer motion while the dead volume was charged to 40 atm. A plot of position versus time is shown in Fig. (4.24). Charging of the dead volume to the 40 atm inlet pressure placed a large axial force on the displacer, which resulted in sudden displacer motion when the directional control valve switched to begin the expansion stroke. The ripples in the p-v plot are the result of the pressure compensated flow control valve adjusting to the new conditions.

The cryocooler was designed to display RC characteristics on the low-pressure return side. Maintaining a finite mass flow allowed counterflow heat exchange during the intake and expansion portions of the cycle, thereby reducing the cryocooler's vulnerability to diminishing wall heat capacity at the lower temperatures. A plot of the mass flow rate versus time is shown in Fig. (4.25). This mass flow was measured at room temperature at the exit from the low-pressure side of the heat exchanger. The plot indicates that the flow rate varies from 0.086 g/s to 0.133 g/s. The exhaust pressure at room temperature was kept approximately constant at 4 atm using a back-pressure regulator. The pressure difference over the return passage between the cold end at the refrigeration temperature and the room temperature outlet is shown in Fig. (4.26). The plot indicates a swing in pressure difference between 0.22 atm and 0.65 atm. The value of pressure drop measured was approximately the same as the design value discussed earlier in Section (4.1.1).

Temperature was measured at various locations along the heat exchanger and in the surge volume using diode temperature sensors (see Appendix C). A plot of

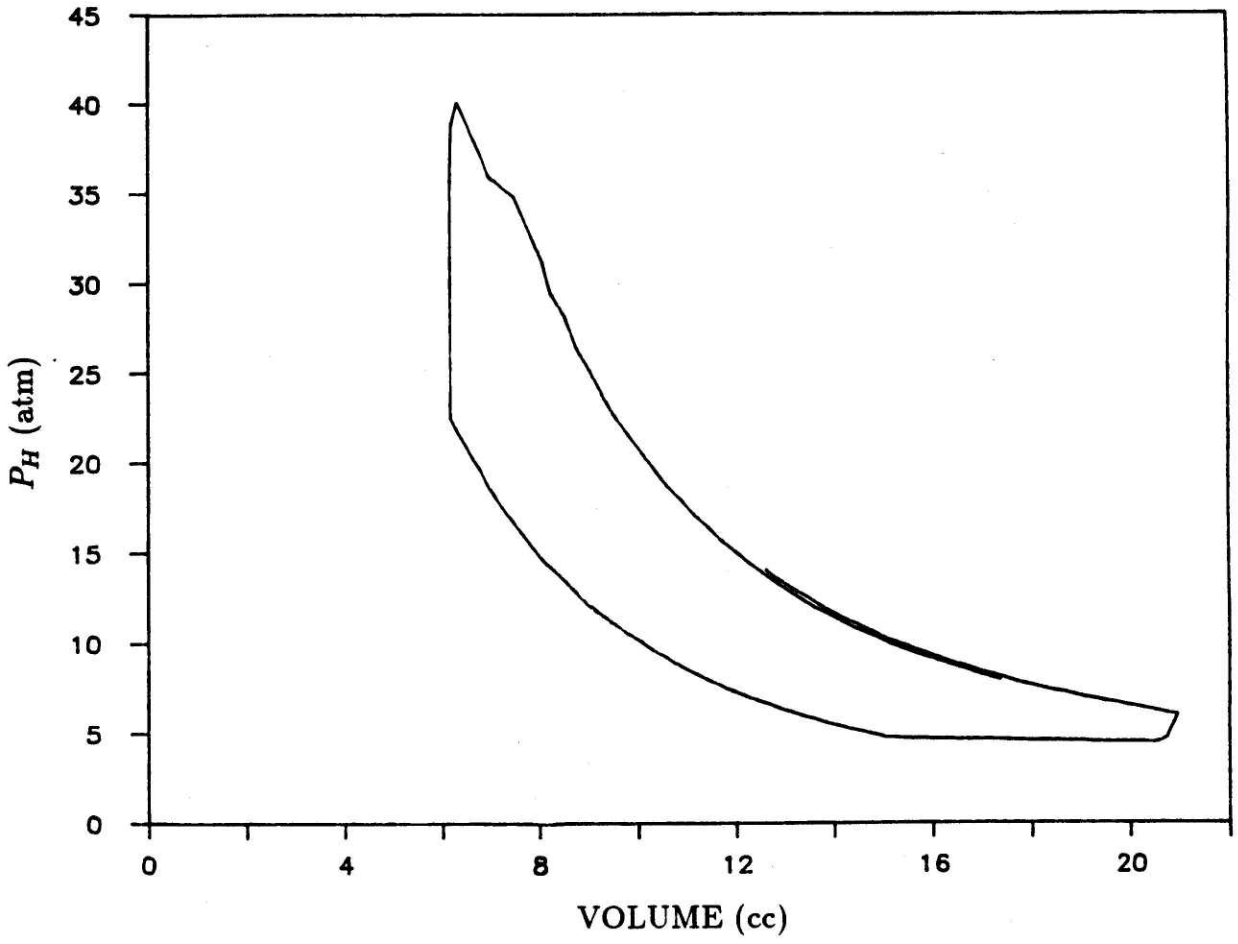

Fig. (4.23) Pressure versus volume for the case of no heat load and no precooling.

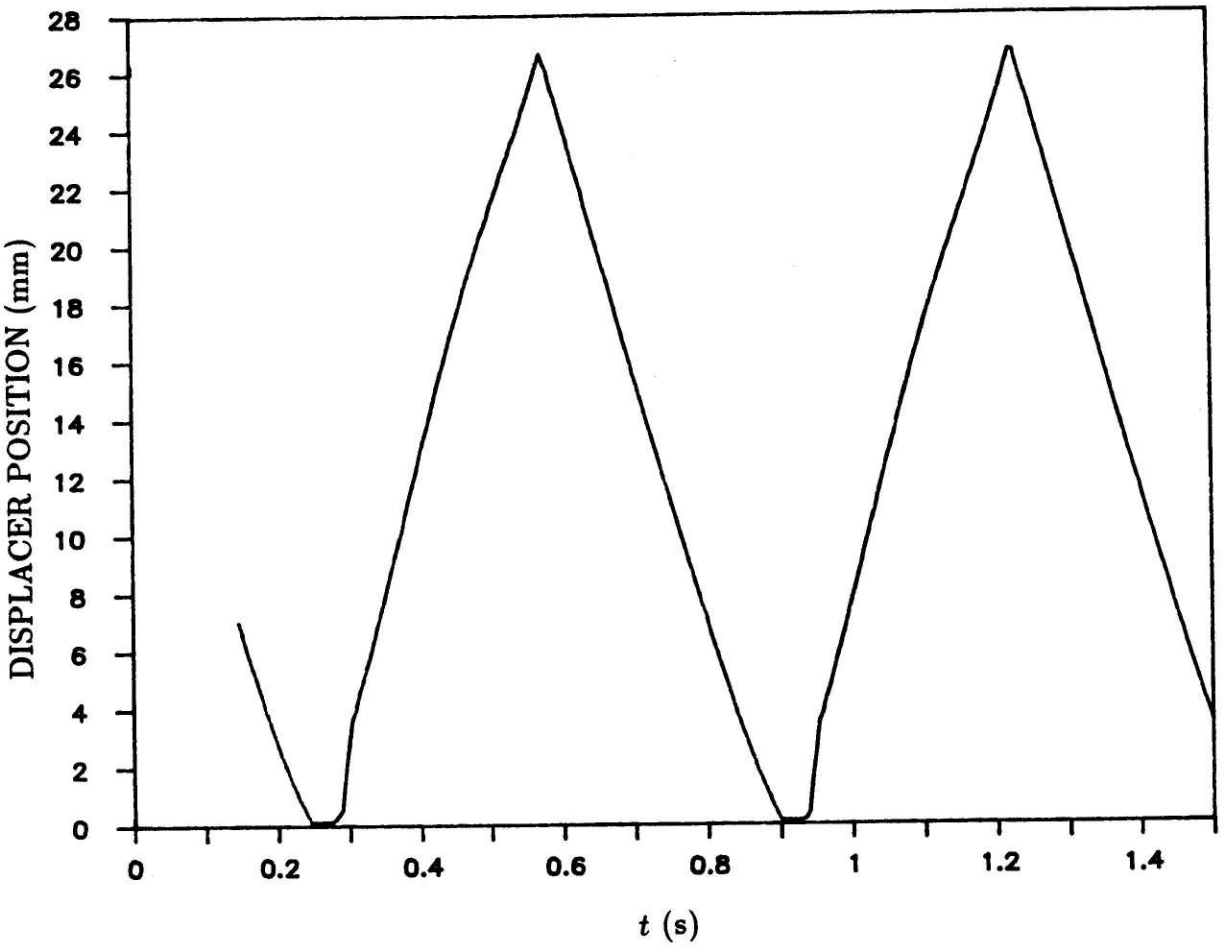

Fig. (4.24) Displacer position versus time for the case of no heat load and no precooling.

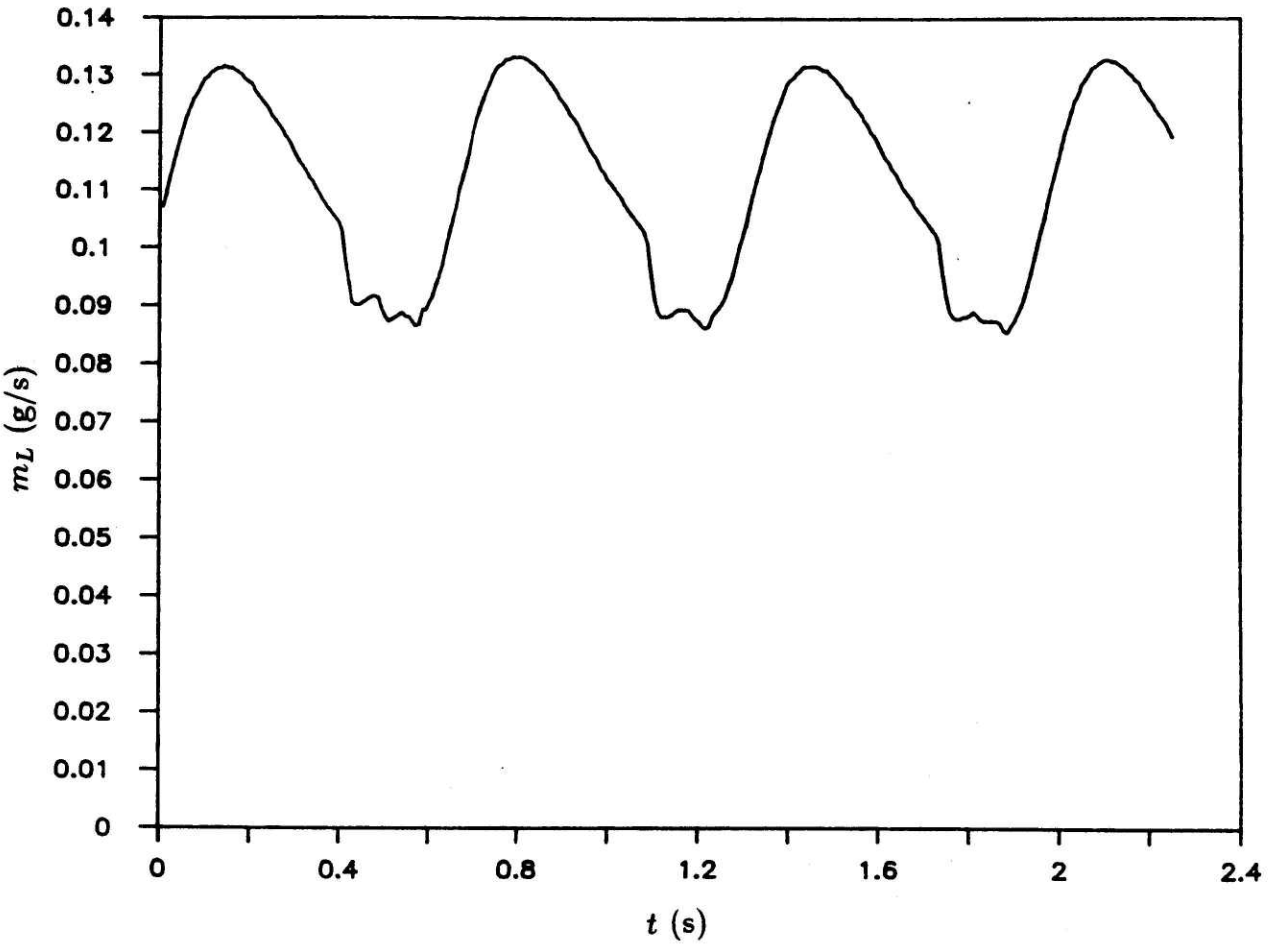

Fig. (4.25) Low-pressure mass flow rate at room temperature versus time for the case of no heat load and no precooling.

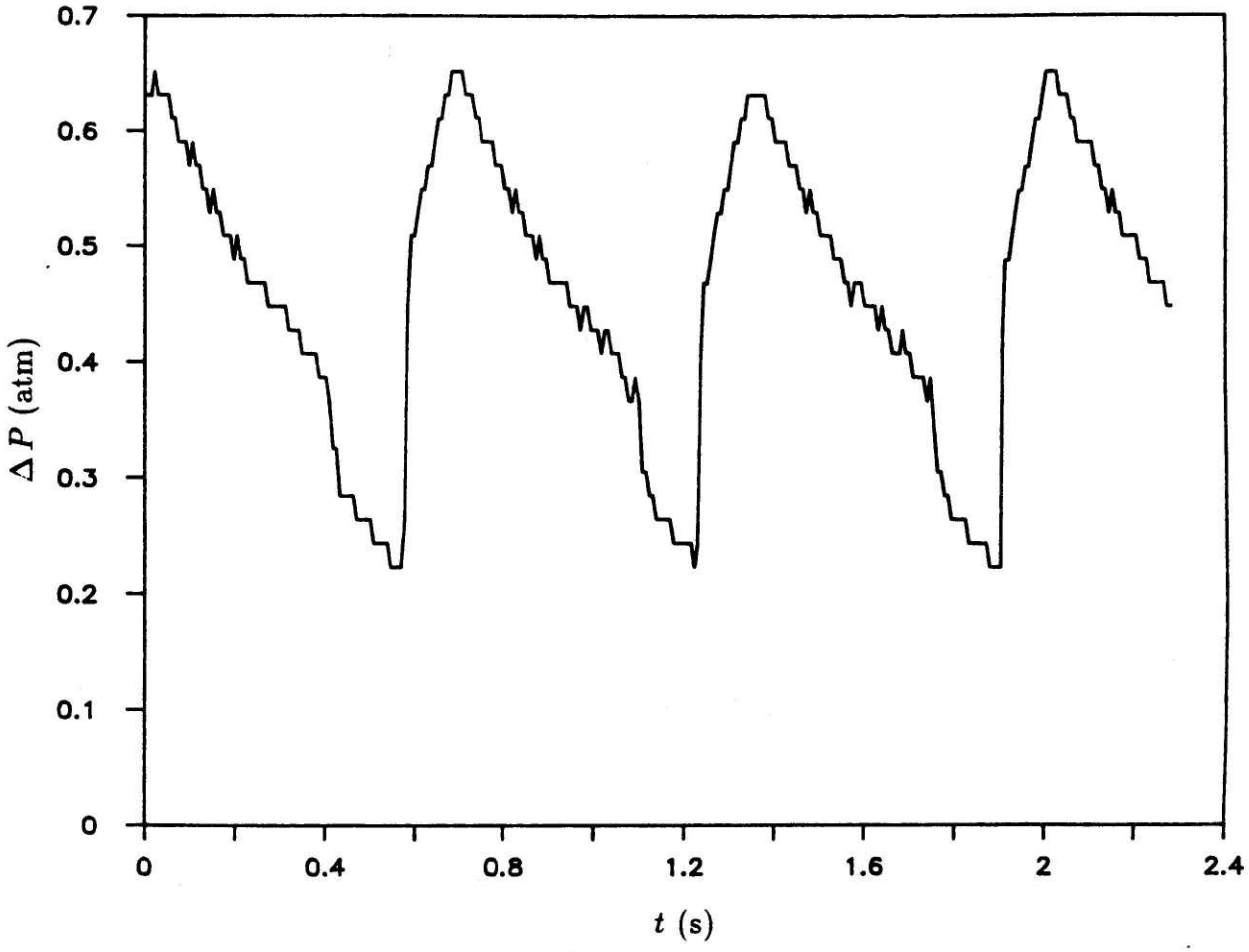

Fig. (4.26) Pressure drop over the low-pressure return passage versus time for no heat load and no precooling.

temperature versus position along the heat exchanger is shown in Fig. (4.27). The temperature distribution along the length was linear except at the cold end. Also, the temperatures along the heat exchanger and on the outside of the surge volume varied a negligible amount with time. Inside the surge volume, two sensors were used to measure temperature fluctuations. One sensor was positioned to measure the temperature of the gas stream flowing through the exhaust valve and another sensor was positioned to measure the gas temperature entering the low-pressure return side of the heat exchanger. In both cases only the sensor and approximately 8 mm of lead wire was exposed to the gas. The remainder of the wire was thermally grounded to stainless steel. For this reason, the temperature swings measured with these two sensors were smaller than the actual temperature swings. The exhaust temperature was observed to vary between 34.7 K and 36.8 K while the temperature at the inlet to the heat exchanger varied between 40.8 K and 41.6 K. The resulting temperature difference between the exhaust and exchanger inlet varied between 4.0 K and 6.9 K.

The data discussed so far is for cryocooler operation with no heat load. To measure the performance with heat loads, two Minco thermofoil heaters were placed inside the surge volume. Starting from the no load condition discussed in previous paragraphs, several heat loads were added to the cold end while maintaining engine speed at 90 RPM and average mass flow rate at 0.107 g/s. Again, constant mass flow rate was maintained by adjusting valve timing to render the appropriate amount of time for constant pressure exhaust and the cut-off point to yield an appropriate blowdown. Figure (4.28) is a plot of these results. Figure (4.29) is the p-v plot for a heat load of 11 W. The indicated work obtained from the plot was 22.4 W. At this load, very little recompression could be used. Also, the inlet pressure could be maintained at only 34 atm because the cut-off point was not adjusted so that less volume was displaced during intake. Although the inlet valve was de-energized shortly after the displacer motion began, the response of the valve was not quick enough to reduce the displaced volume at cut-off. Using a higher inlet pressure would have resulted in larger blowdown; however, the maximum blowdown that

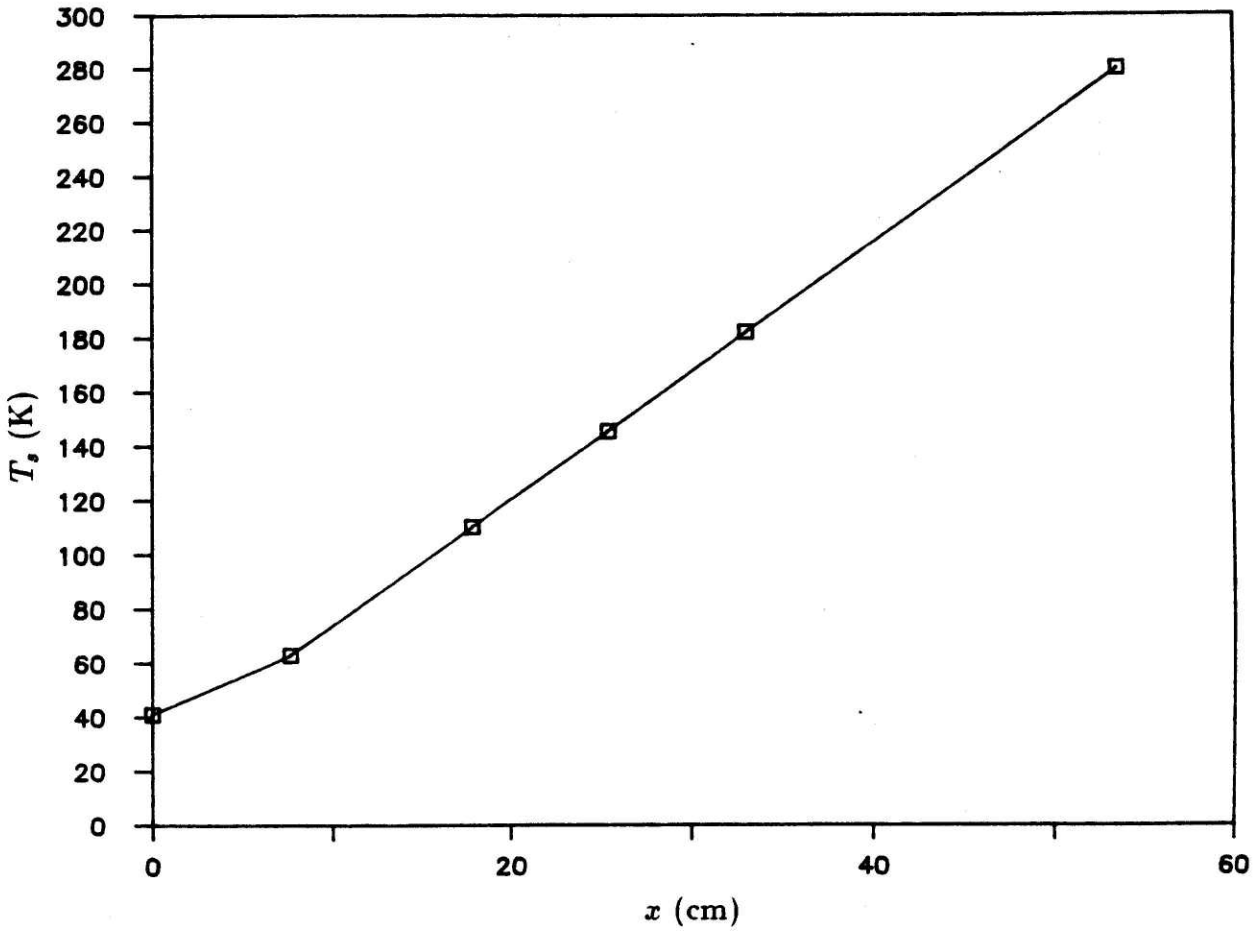

Fig. (4.27) Outer shell wall temperature versus position for the case of no heat load and no precooling.

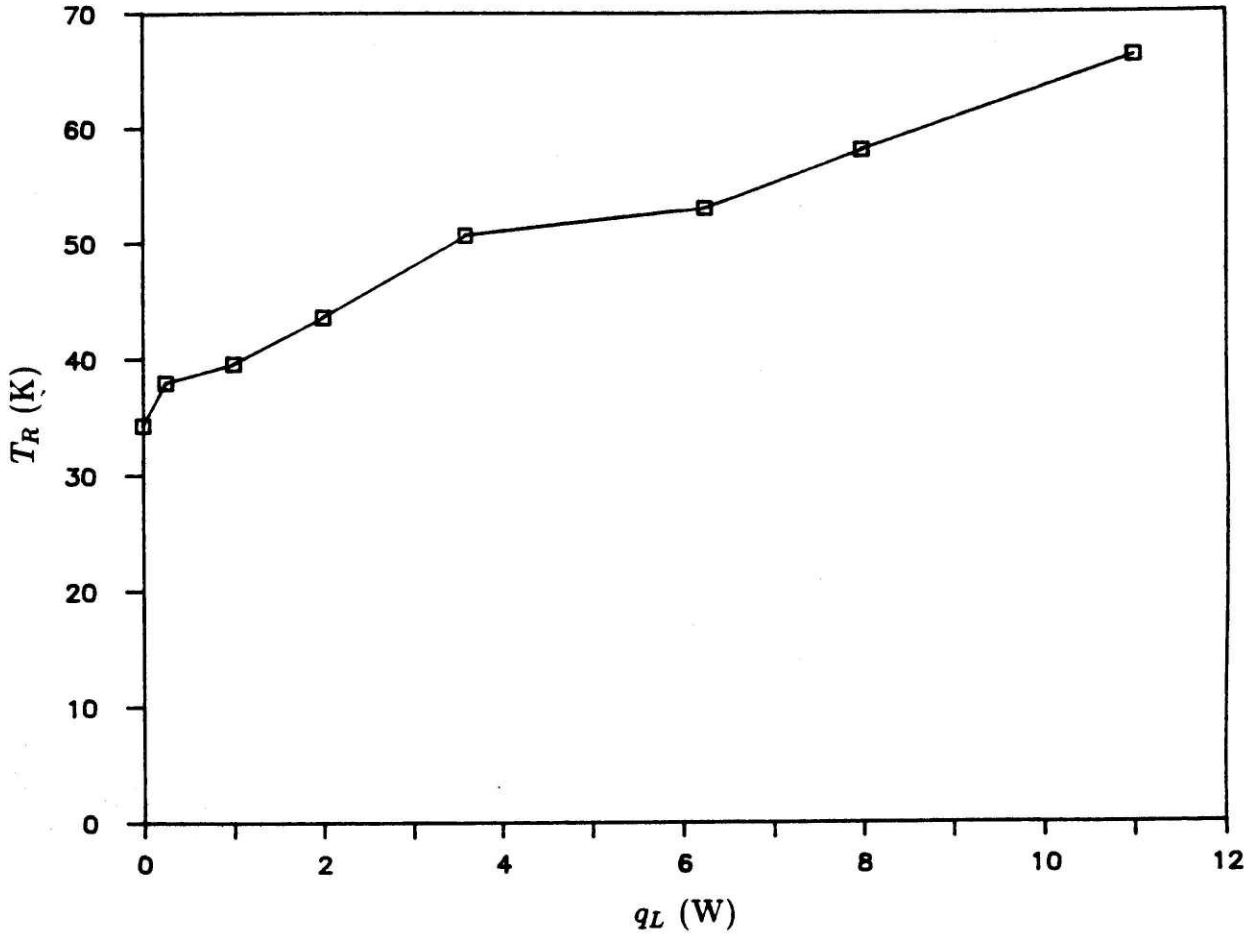

Fig. (4.28) Refrigeration temperature versus heat load for the case of no precooling.

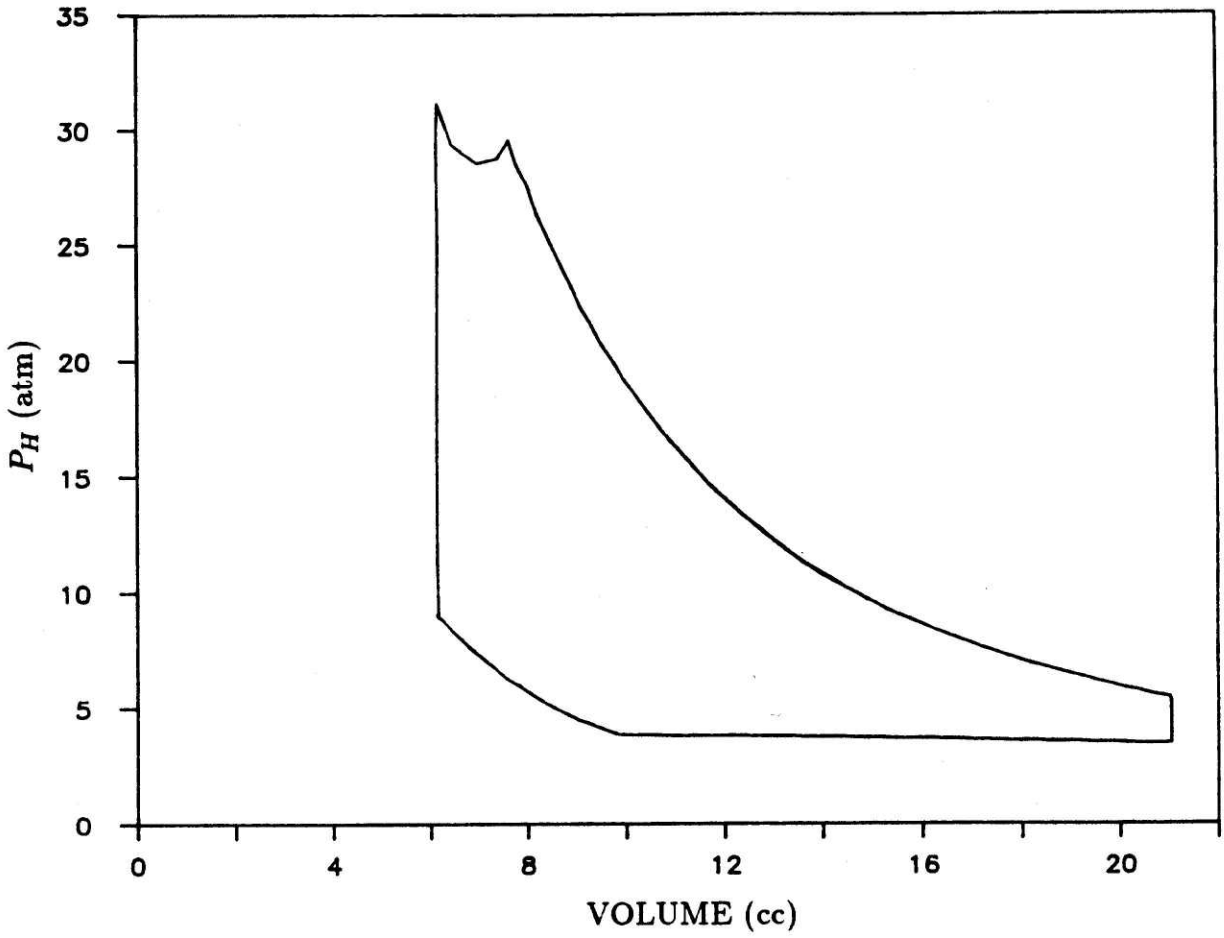

Fig. (4.29) Pressure versus volume for the case of 11 W load and no precool.

could be used was about 3 atm, above which the exhaust valve solenoid could not supply enough force to push the valve off its seat.

4.5.3 Cryocooler Performance with Precooling

Experiments were next performed using liquid nitrogen in a precooling heat exchanger and radiation shield. Figure (4.1) shows the position of the precooling heat exchanger. The liquid nitrogen cooled radiation shield extended from approximately the center of the precooling heat exchanger to enclose the colder parts of the cryocooler. Aluminized mylar superinsulation was used to cover the radiation shield and to completely enclose the colder parts of the cryocooler. The information obtained using the precooling heat exchanger and liquid nitrogen cooled radiation shield was very useful in understanding how a multistage cryocooler might perform. Results will be given in the same order as in the previous section.

An iterative method was used to determine the minimum temperature the cryocooler could reach. As with operation without precooling, data was taken at different engine speeds while maintaining constant time-averaged mass flow rate and at different mass flow rates while maintaining constant engine speed. The mass flow was varied the same as before, by proper adjustment of the valve timing. The mass flow due to blowdown was set by adjusting the cut-off point and the mass flow at constant exhaust pressure was set by adjusting when the exhaust valve closed. Figure (4.30) is a plot of temperature versus engine speed at a constant time-averaged mass flow rate of 0.097 g/s. Figure (4.31) gives temperature versus mass flow rate at 65 RPM. Both of these plots indicate that the cryocooler was not particularly sensitive to either mass flow rate or engine speed. The minimum exhaust temperature reached was 19.5 K at an average flow rate of 0.151 g/s and an engine speed of 65 RPM.

Results obtained while the cryocooler was operating at its minimum temperature are given in Figs. (4.32) to (4.34). The p-v plot shown in Fig. (4.32) may be compared with the p-v plot in Fig. (4.23) for operation without liquid nitrogen precool. In both cases, the lowest refrigeration temperature was reached using ap-

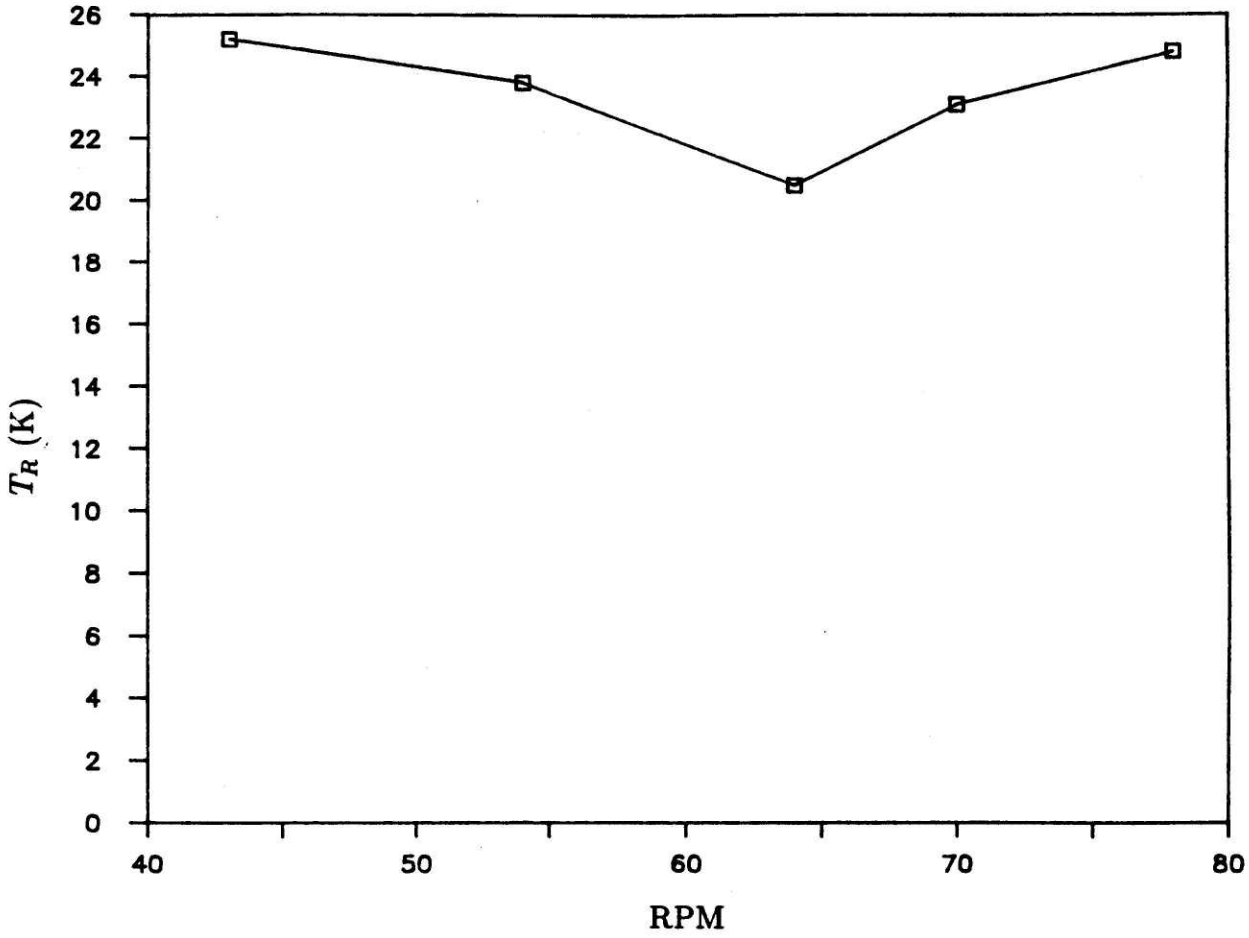

Fig. (4.30) Refrigeration temperature versus engine speed at a constant time-averaged mass flow rate for the case of liquid nitrogen precooling and no load.

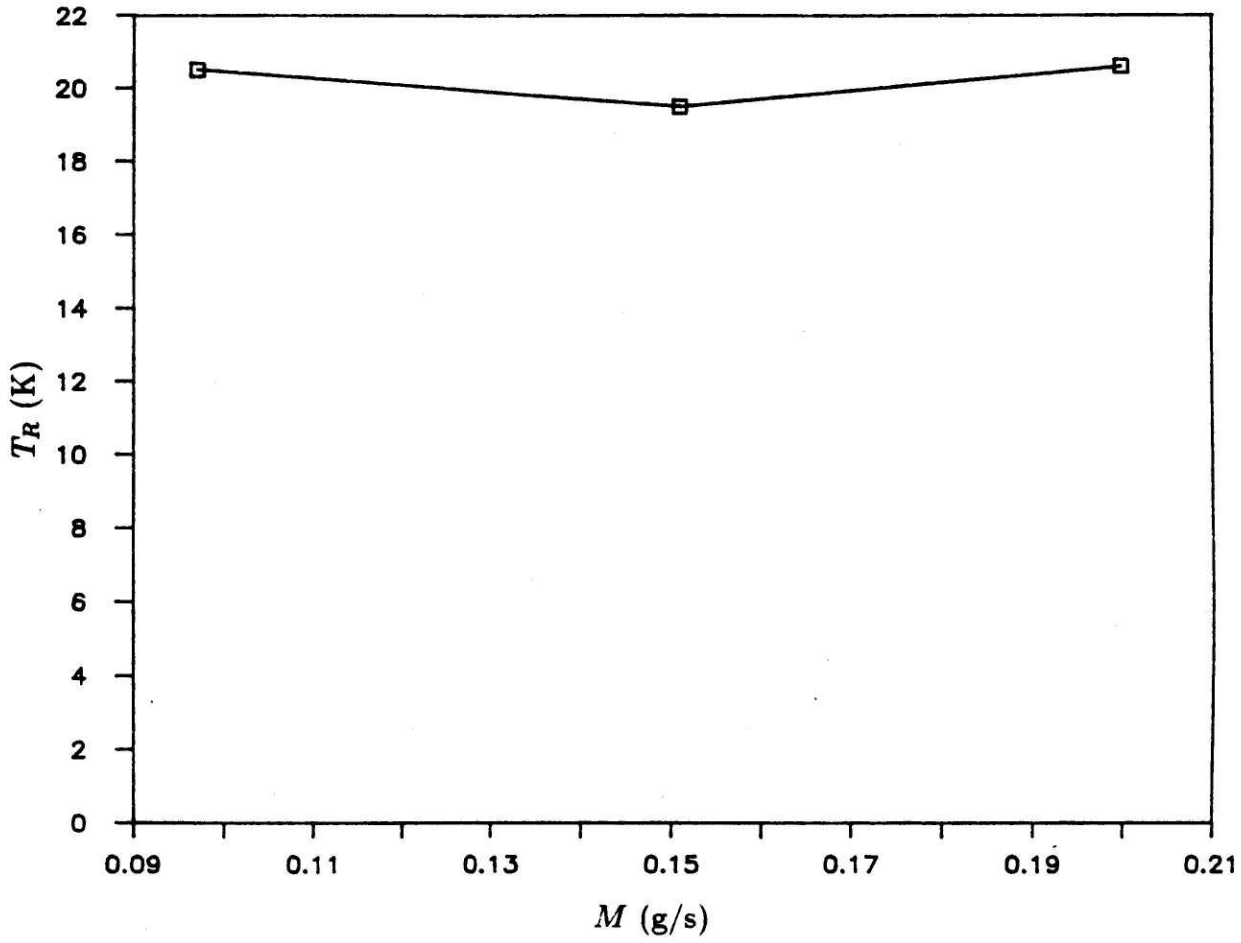

Fig. (4.31) Refrigeration temperature versus time-averaged mass flow rate at constant engine speed for LN_2 precooling and no heat load.

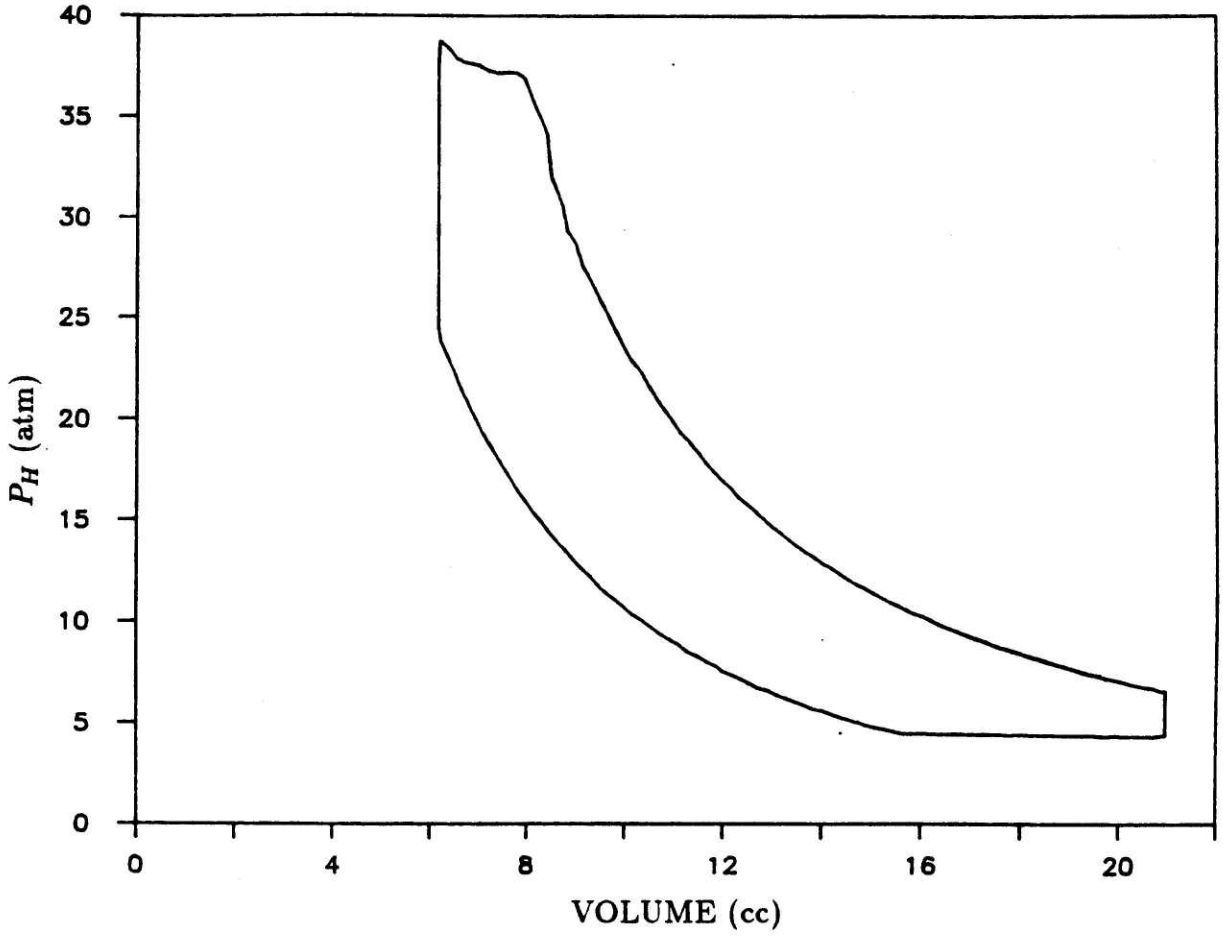

Fig. (4.32) Pressure versus volume with liquid nitrogen precooling and no heat load.

proximately the same amount of recompression. The work indicated by the p-v plot is 13.7 W. Effectiveness of the RC design on the low-pressure return was reduced with liquid nitrogen precooling. A reduction in the effectiveness of the RC design on the low-pressure return with liquid nitrogen precooling may be identified in Figs. (4.33) and (4.34). Figure (4.33) is a plot of low-pressure mass flow rate at room temperature versus time and Fig. (4.34) is a plot of return side pressure difference between the surge volume and room temperature versus time. These plots indicate that, as predicted, the return side flow resistance was substantially reduced by cooling to liquid nitrogen temperature.

Temperature along the heat exchanger is shown in Fig. (4.35). Only the 33 cm of heat exchanger between the surge volume and the precooling heat exchanger are considered in this plot. Temperature variations, as measured by the diode sensors, along the heat exchanger and on the surge volume were negligible after steady state conditions were reached. The exhaust temperature was observed to vary between 19.5 K and 21.3 K during a single cycle, while the temperature at the inlet to the heat exchanger varied between 22 K and 24.5 K. Based on these temperatures, the temperature difference between the exhaust and exchanger inlet varied between 1.1 K and 4.8 K. Again, these temperatures are actually some average of the sensor and wall temperatures.

Heat loads were applied to the cold end in an effort to better predict performance of a multistage device. Heat loads of up to 6.25 W were applied while maintaining the average mass flow rate at 0.151 g/s and the engine speed at 65 RPM. Figure (4.36) shows the minimum exhaust temperature reached at different heat loads. Mass flow rate was maintained constant by adjusting the valve timing to give appropriate magnitudes of blowdown mass flow and constant pressure exhaust mass flow. A pressure versus volume plot is given in Fig. (4.37) for a 6.25 W heat load. The indicated work was 13.4 W.

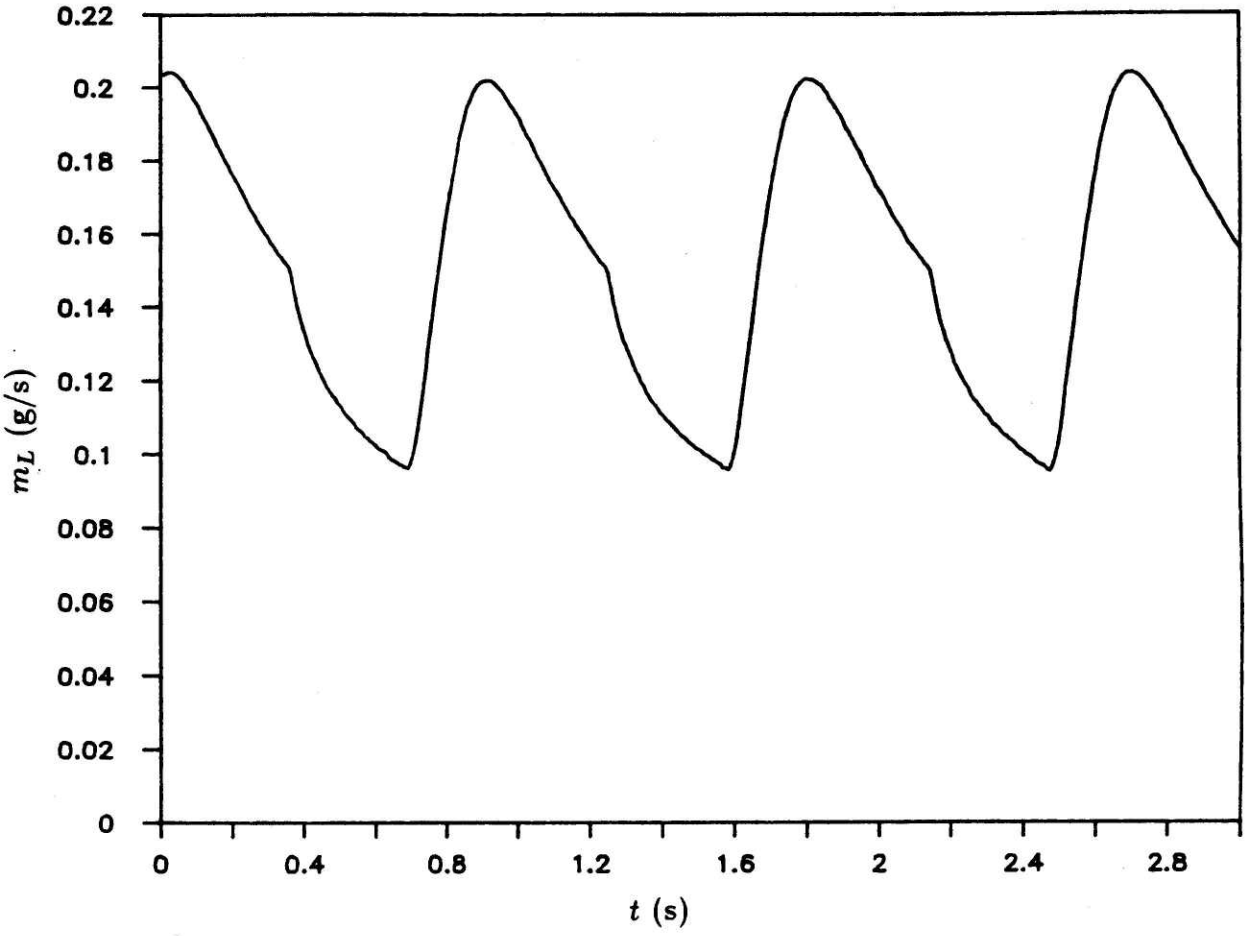

Fig. (4.33) Low-pressure mass flow rate at room temperature versus time for LN_2 precooling and no heat load.

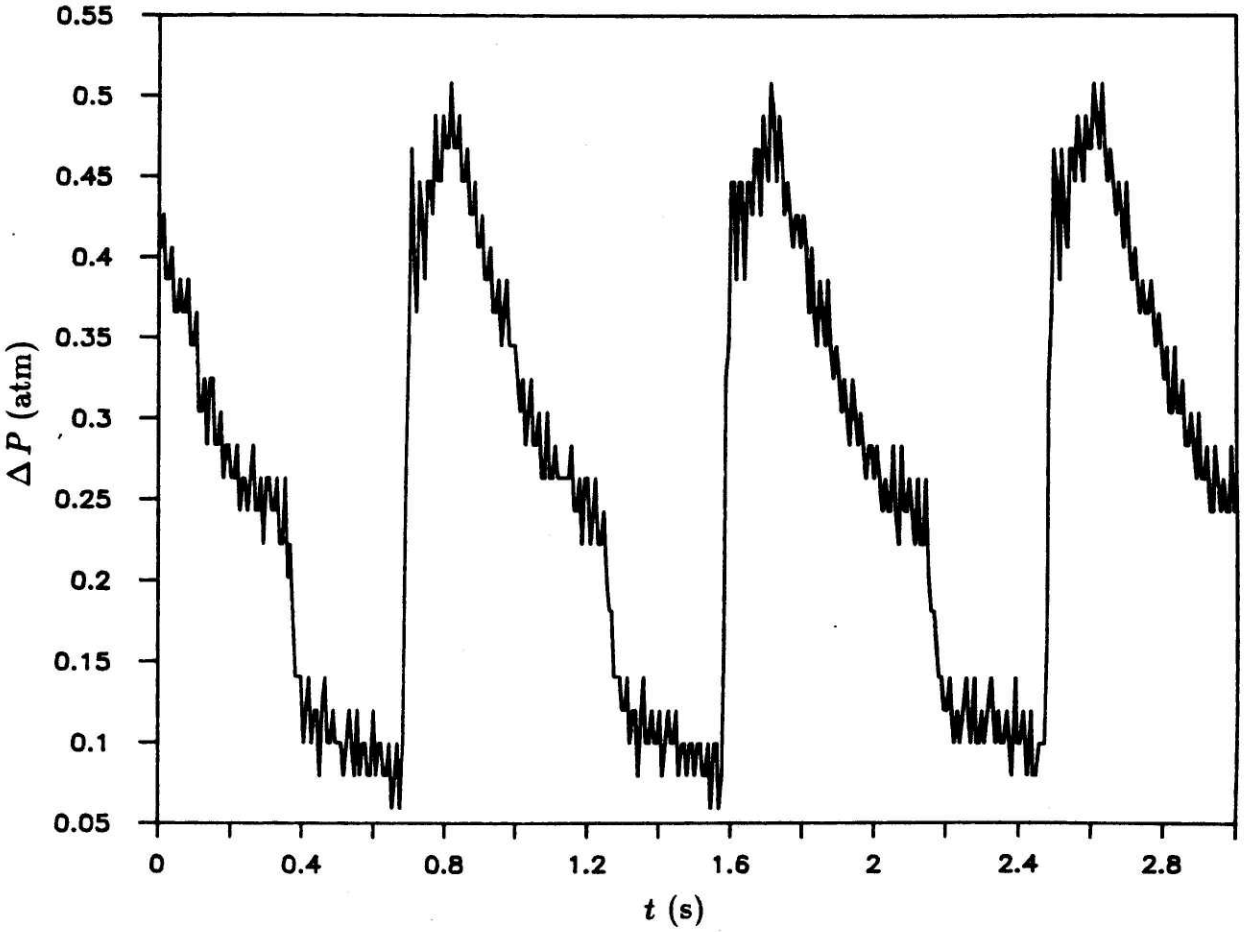

Fig. (4.34) Pressure drop over the low-pressure return passage versus time for LN_2 precooling and no heat load.

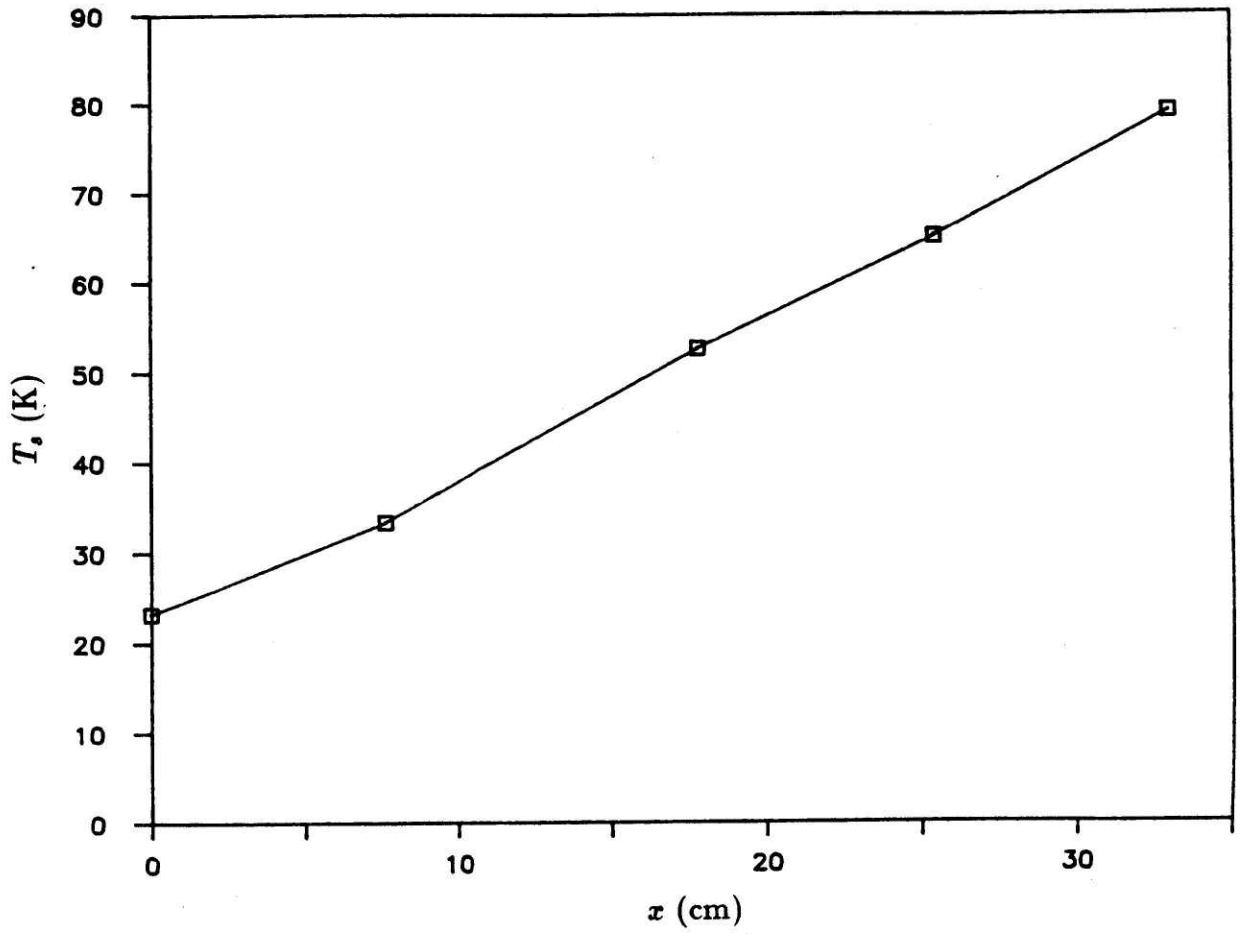

Fig. (4.35) Outer shell wall temperature versus position for the case of LN_2 pre-cooling and no heat load.

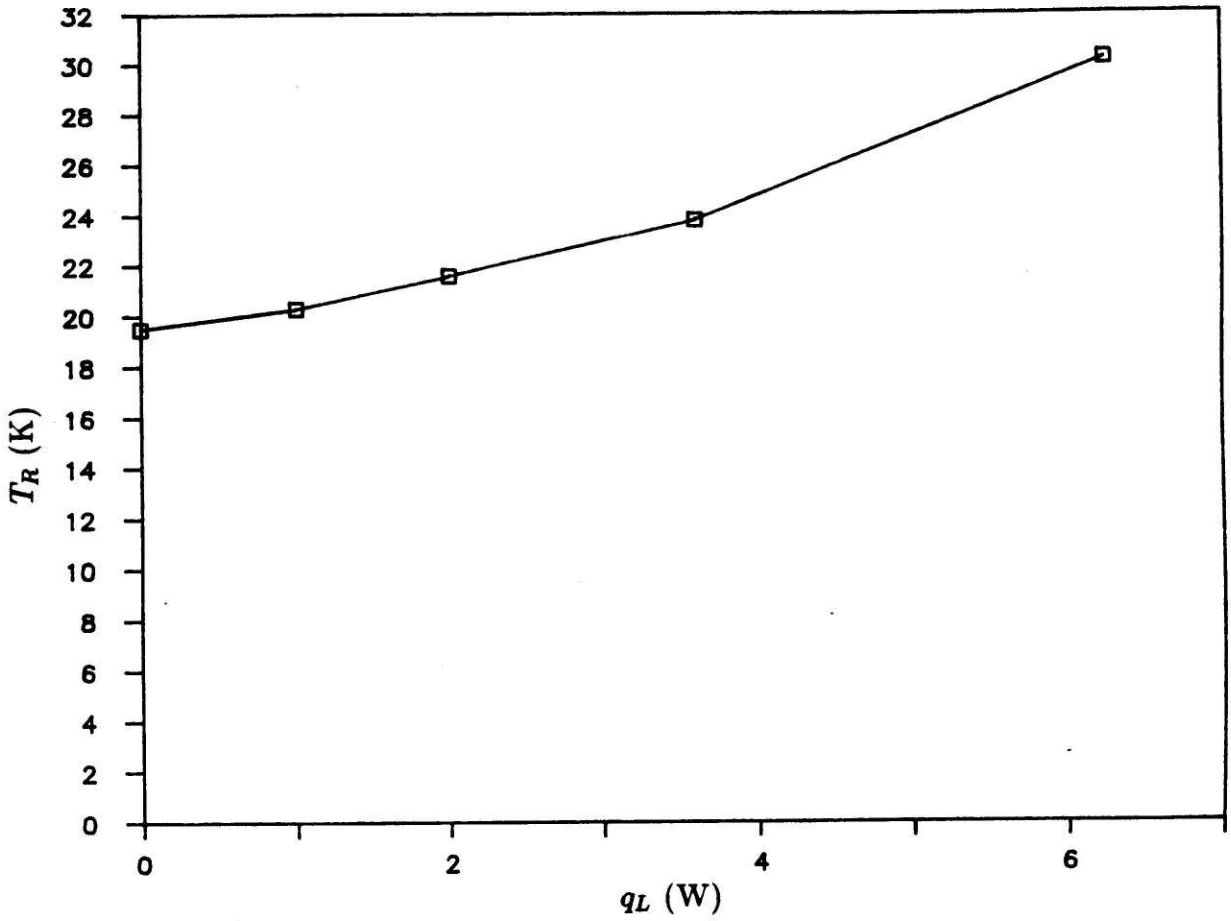

Fig. (4.36) Refrigeration temperature versus heat load for the case of LN_2 pre-cooling.

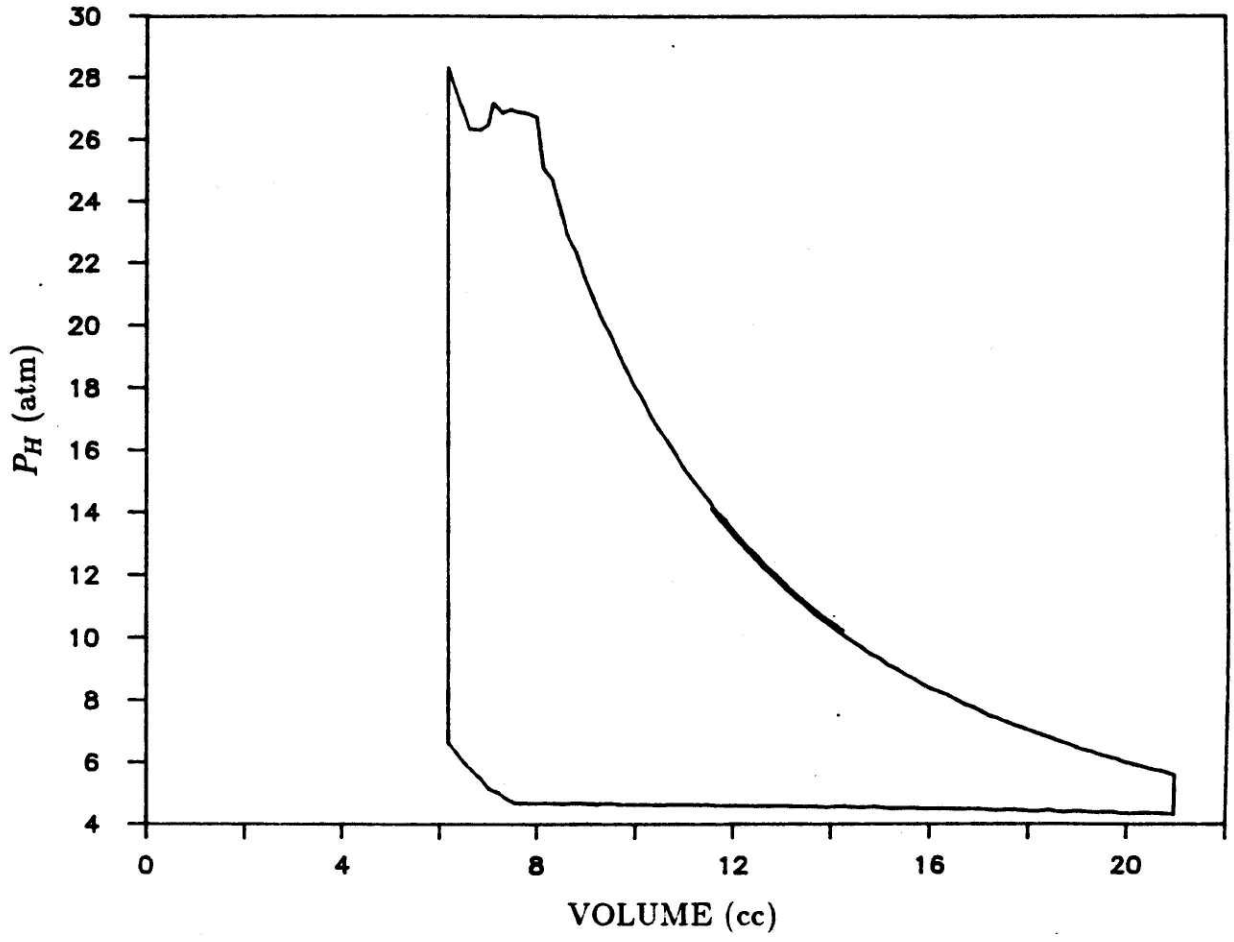

Fig. (4.37) Pressure versus volume for the case of liquid nitrogen precooling and 6.25 W heat load.

4.5.4 Calculations of Experimental Efficiencies

In this subsection, the experimental results were used to compute performance parameters for the single-stage cryocooler. The most important performance parameters computed were the adiabatic engine efficiencies and the heat exchange temperature differences at different operating conditions. The procedure used to compute the efficiencies is given in the following paragraphs. The experimental data point for the case of no precooling and no heat load is used as a representative example. Experimentally determined efficiencies for four data points are compared with results from the performance algorithm in the Section (4.6). A summary of all the results is given in Tables (4.3) to (4.6). The results are divided into two columns. The first column lists values obtained from the experiment. Values listed in the tables from "P_H" to "T measured at exhaust (K)" (*i.e.*, the first eight values) are experimentally measured values. The measured temperatures were helpful in determining whether the computed exhaust temperatures and low-pressure return inlet temperatures were reasonable. One should note, however, that the value of "T measured at the exhaust" was influenced by the applied heat load, since the temperature sensor was located very close to the resistance heaters. The remaining values in the first column are computed based on these measured values. The second column of values were obtained by using the performance algorithm described in Chapter 3. A discussion of these values from the performance algorithm is given in Section (4.6).

The temperatures of the gas flowing through the exhaust valve during the exhaust portion of the stroke were computed based on the time-average of the measured mass flow through the cryocooler. An iterative procedure was necessary. The result was a mass-averaged enthalpy for the exhaust, h_{exh}. The value of this mass-averaged enthalpy, h_{exh}, was then used to compute several performance parameters such as an adiabatic expansion efficiency for the cryocooler. To illustrate the procedure, the experimental data point for the case of no precooling and no heat load is used in the following discussion. The iterated variable was the temperature of the

Table (4.3) Experimental and theoretical values for the case of no precool and no heat load.

Parameter	Experimental	Theoretical
P_H (atm)	41	41
P_L (atm)	4	4
RPM	90	90
M (g/s)	0.107	0.107
q_L (W)	0	0
W_{ind} (W)	18.1	18.1
T measured at return inlet(K)	41.2	—
T measured at exhaust (K)	34.7	—
q_C (W)	1.1	1.1
T_A (K)	38	—
T_B (K)	34	36
$T_H(0,0)$ (K)	66	63
W_{rev} (W)	23.1	—
$T_L(0,0)$ (K)	41	41
$\Delta T)_{h0}$ (K)	25	26
η_E	0.78	0.76
$\Delta T)_{h0}$ swing (K)	—	16 - 36
h_c (W)	—	2.1
h_{nc} (W)	—	14.8
C_F	0.64	0.63

gas in the displaced volume when blowdown began. In the discussion that follows, values from the final iteration are given.

The total mass flow per stroke was computed using

$$\gamma = M\,\tau \tag{4.6}$$

where M is the time-averaged mass flow rate and τ is the cycle period. For the case of no precooling and no heat load, the time-averaged mass flow rate was $M = 0.107$ g/s and the period for one cycle at the 90 RPM engine speed was $\tau = 0.67$ s. The total mass flow per cycle was then $\gamma = 0.071$ g. This total mass flow per cycle was

Table (4.4) Experimental and theoretical values for the case of no pre-cool and 11 W heat load.

Parameter	Experimental	Theoretical
P_H (atm)	32	32
P_L (atm)	4	4
RPM	90	90
M (g/s)	0.107	0.107
q_L (W)	11	11.2
W_{ind} (W)	22.4	22.4
T measured at return inlet(K)	82.6	—
T measured at exhaust (K)	66.2	—
q_C (W)	1.1	1.1
T_A (K)	55	—
T_B (K)	48	45
$T_H(0,0)$ (K)	88	82
W_{rev} (W)	28.8	—
$T_L(0,0)$ (K)	75	70
$\Delta T)_{h0}$ (K)	13	12
η_E	0.78	0.76
$\Delta T)_{h0}$ swing (K)	—	4.4 - 22
h_c (W)	—	2.3
h_{nc} (W)	—	7.7
C_F	0.9	0.88

then divided into two parts:

$$\gamma = \gamma_b + \gamma_e \tag{4.7}$$

where γ_b is the mass flow through the exhaust valve during blowdown and γ_e is the mass flow during constant pressure exhaust. To avoid confusion, Fig. (4.19) is used to indicate points on the p-v plot where blowdown and constant pressure exhaust occur. Points A and B indicate the beginning and end of blowdown, respectively. Points B and C indicate the beginning and end of constant pressure exhaust, respectively. Computation of these mass flows follows.

Table (4.5) Experimental and theoretical values for the case of liquid nitrogen precool and no heat load.

Parameter	Experimental	Theoretical
P_H (atm)	40	40
P_L (atm)	4	4
RPM	65	65
M (g/s)	0.151	0.151
q_L (W)	0	0
W_{ind} (W)	13.7	13.8
T measured at return inlet(K)	23.2	—
T measured at exhaust (K)	19.5	—
q_C (W)	0.2	0.2
T_A (K)	20	—
T_B (K)	18	18
$T_H(0,0)$ (K)	36	33
W_{rev} (W)	17.3	—
$T_L(0,0)$ (K)	19	19
$\Delta T)_{h0}$ (K)	17	14
η_E	0.79	0.78
$\Delta T)_{h0}$ swing (K)	—	13 - 19
h_c (W)	—	0.5
h_{nc} (W)	—	12.7
C_F	0.65	0.59

The mass flow during blowdown, γ_b, was due to blowdown from the displacement volume, $\gamma_{b,D}$, and from the clearance volume, $\gamma_{b,C}$, as follows

$$\gamma_b = \gamma_{b,D} + \gamma_{b,C} \tag{4.8}$$

The blowdown from the displacement volume, $\gamma_{b,D}$, was computed using

$$\gamma_{b,D} = \frac{(\rho_A - \rho_B)\,\pi\, D_p^2\, s}{4} \tag{4.9}$$

where D_p is the displacer diameter and s is the total stroke. The densities ρ_A and ρ_B were evaluated based on the temperature and pressure of the displaced volume

Table (4.6) Experimental and theoretical values for the case of liquid nitrogen precool and 6.25 W heat load.

Parameter	Experimental	Theoretical
P_H (atm)	29	29
P_L (atm)	4	4
RPM	65	65
M (g/s)	0.151	0.151
q_L (W)	6.25	6.3
W_{ind} (W)	13.4	13.2
T measured at return inlet(K)	38.8	—
T measured at exhaust (K)	30.2	—
q_C (W)	0.2	0.2
T_A (K)	26	—
T_B (K)	23	23
$T_H(0,0)$ (K)	40	39
W_{rev} (W)	17.8	—
$T_L(0,0)$ (K)	32	32
$\Delta T)_{h0}$ (K)	8	7
η_E	0.75	0.74
$\Delta T)_{h0}$ swing (K)	—	5.5 - 10
h_c (W)	—	0.4
h_{nc} (W)	—	6.2
C_F	0.86	0.84

at points A and B of Fig. (4.19), respectively. An adiabatic expansion process from points A to B of Fig. (4.19) was assumed. The efficiency of this expansion process was expressed in terms of the ratio of temperatures before and after expansion from point A to point B, as follows

$$\epsilon = \frac{T_A / T_B}{T_A / T_{B,s}} = \frac{T_{B,s}}{T_B} \tag{4.10}$$

where T is the gas temperature, subscripts A and B refer to points A and B of Fig. (4.19), and subscript s indicates the state after isentropic expansion from state A. The expansion process was assumed to have an efficiency of $\epsilon = 0.95$. (Even

moderate error in this estimated expansion efficiency resulted in a small change in the final computed value of the mass-averaged exhaust enthalpy, h_{exh}.) To use Eqns. (4.9) and (4.10) to compute the mass flow due to blowdown, the temperature at the start of blowdown (point A) must be estimated. This temperature, referred to as T_A, was the iteration variable. The final value, after iteration, for the case of no precool and no heat load was $T_A = 38$ K. The pressure in the displaced volume before blowdown was approximately $P_A = 6$ atm, as indicated by Fig. (4.23). The exhaust pressure, P_L, was at approximately $P_B = P_C = 4$ atm. Based on these values, Eqn. (4.10) was used to compute the temperature of the displaced volume at point B of Fig. (4.19). Point B was the beginning of constant pressure exhaust, which was also assumed to occur at constant temperature, so that $T_B = T_C$. The computed value of this exhaust temperature was $T_B = 34$ K. At this point, all information needed to determine the densities of Eqn. (4.9) was known. The stroke was 26.7 mm and the displacer diameter was 26.3 mm. The mass flow per cycle due to blowdown of the displaced volume of the displacer for the case of no precool and no heat load was then $\gamma_{b,D} = 0.028$ g.

The blowdown mass flow due to the clearance volume was computed assuming isothermal expansion (*i.e.*, the work of expansion was negligible compared to the heat capacity of the walls). Another assumption used to simplify the calculation was that the gas leaving the displacer-to-cylinder gap does not mix with or change the temperature of the gas in the displaced volume. The equation used was

$$\gamma_{b,C} = (\rho_{L,A} - \rho_{L,B})\, V_C \tag{4.11}$$

where V_C is the clearance volume, $\rho_{L,A}$ is the gas density in the displacer-to-cylinder gap at point A of Fig. (4.19) averaged over the displacer length, and $\rho_{L,B}$ is the gas density in the displacer-to-cylinder gap at point B of Fig. (4.19) averaged over the displacer length. These average gas densities were computed by taking the average of the inverse of the gas temperatures at each end of the displacer-to-cylinder gap, since density is inversely proportional to temperature for an ideal gas. At this average temperature, densities $\rho_{L,A}$ and $\rho_{L,B}$ were determined at $P_A = 6$ atm and

$P_B = 4$ atm, the pressures before and after blowdown, respectively. The clearance volume was $V_C = 6$ cc. Using this procedure, the mass flow due to blowdown in the clearance volume was computed to be $\gamma_{b,C} = 0.009$ g.

The mass flow through the exhaust valve after blowdown was computed next. Although the pressure in the surge volume rose slightly during this portion of the exhaust, the pressure between points B and C of Fig. (4.19) was assumed constant. The amount of mass flow due to constant pressure exhaust, γ_e, was computed using

$$\gamma_e = \frac{\rho_B \pi D_p^2 s_e}{4} \tag{4.12}$$

where ρ_B was defined earlier. This mass flow takes place at the minimum exhaust temperature computed earlier to be $T_B = T_C = 34$ K. The distance traveled by the displacer at the constant exhaust pressure, s_e, was determined using the p-v plot shown in Fig. (4.23). The mass flow due to constant pressure exhaust was computed to be $\gamma_e = 0.034$ g. At this point, the total mass flow due to both blowdown and constant pressure exhaust may be determined using Eqns. (4.7) and (4.8) to be $\gamma = 0.071$ g, which agrees with the value computed using Eqn. (4.6). Another iteration would be required if these two values did not agree. The iteration would consist of choosing a new value for T_A and determining new values for the individual mass flows. Using this procedure resulted in values of gas temperatures at the points A, B, and C of Fig. (4.19). Knowledge of these temperatures allowed determination of a mass-averaged exhaust enthalpy.

A mass-averaged exhaust enthalpy was computed using the following equation:

$$h_{exh} = \frac{\gamma_{b,D}}{\gamma} h_{AB} + \frac{\gamma_{b,C}}{\gamma} h_A + \frac{\gamma_e}{\gamma} h_B \tag{4.13}$$

where h_{AB} is the average enthalpy leaving the displaced volume during blowdown, h_A is the enthalpy leaving the displacer-to-cylinder gap during blowdown, and h_B is the enthalpy during constant pressure exhaust. The value of h_{AB} was computed using the average temperature and pressure during blowdown, so that

$$h_{AB} = h_{AB}\left(\frac{P_A + P_B}{2}, \frac{T_A + T_B}{2}\right) \tag{4.14}$$

The value of h_A was computed based on T_A and P_A, since the gas leaving the displacer-to-cylinder gap was at constant temperature for large wall heat capacity. The value of h_B was computed based on T_B and P_B. For the case of no precooling and no heat load, the mass-averaged exhaust enthalpy was $h_{exh} = 197$ J/g.

The mass-averaged exhaust enthalpy, h_{exh}, was the starting point for defining an adiabatic engine efficiency. The adiabatic efficiency was based on a control volume that consisted of only the displaced volume. In addition, the adiabatic efficiency was defined for the case of no clearance volume (*i.e.*, the displacer-to-cylinder gap, $z_H = 0$). Assuming no clearance volume resulted in an efficiency that did not include the irreversibility due to pressurization of the clearance volume during the pressurization portion of the cycle, as shown in Fig. (4.19). In the following paragraphs, an adiabatic engine efficiency will be developed based on these assumptions. To better understand why the assumptions were made, the effects of having a finite displacer-to-cylinder gap will be discussed first. Then, the enthalpy of the gas entering the displaced volume will be determined. At that point, the adiabatic efficiency will be calculated. Finally, an effort will be made to better quantify the irreversibility due to pressurization of the finite clearance volume in the cryocooler experiment, which will be compared with the irreversibility due to adiabatic expansion when assuming no clearance volume.

When defining an adiabatic engine efficiency, the assumption of no clearance volume was made in an effort to simplify the calculation. Allowing for a finite clearance volume would result in a more cumbersome calculation for two main reasons. First, if clearance volume effects were included, the pressure of the gas entering the displaced volume during expansion would change with displacer position. For this reason, some mass-averaged intake pressure would have to be defined. In addition, for a finite clearance volume, an energy balance on the displaced volume would include two mass flows exiting the displaced volume during the exhaust and recompression portion of the cycle: one into the exhaust valve while the exhaust valve was open and another into the displacer-to-cylinder gap during recompression. Assuming no clearance volume required consideration of only two time-averaged flow

streams. One flow entering the control volume was assumed to be at constant pressure. All of the mass entering the control volume was expanded and then exhausted through the exhaust valve.

The assumption of no clearance volume was made in an effort to simplify the calculation of an expansion efficiency. Such an assumption, however, ignored several sources of thermodynamic irreversibility that were present in the real physical device. For example, a throttling irreversibility occurred during pressurization of the clearance volume. This throttling irreversibility will be shown later in this section to be substantial when compared to the irreversibility incurred during adiabatic expansion with the assumption of no clearance volume. Several irreversibilities due to mixing of gases at different temperatures were also ignored by assuming no clearance volume. One such mixing irreversibility was due to flow from the warmer isothermal displacer-to-cylinder gap to the cooler adiabatic displaced volume during expansion. As another example, during recompression, the gas temperature in the displaced volume was different than the temperature of the displacer-to-cylinder gap. Still another mixing irreversibility ignored was that due to mixing of warmer gas leaving the displacer-to-cylinder to enter the cooler displaced volume during exhaust blowdown.

The enthalpy of the gas entering the displaced volume was determined as a first step in computing an adiabatic engine efficiency. The mass-averaged exhaust enthalpy, h_{exh}, was used along with the measured indicated work and the time-average of the measured mass flow to determine the enthalpy of the gas entering the working volume. The control volume used for this analysis included only the working volume (*i.e.*, the volume displaced by the displacer). As stated earlier, the analysis assumed no clearance volume. However, one should note that, since clearance volume was present in the actual device, the effects of clearance volume are not completely decoupled from the calculated enthalpy entering the working volume. Another assumption was that no net enthalpy flow resulted from displacer motion at the control volume boundary. An energy balance on the working volume,

assuming adiabatic expansion, was written as

$$W_{ind} = M\left(h_H(0,0) - h_{exh}\right) \tag{4.15}$$

where M is the time-averaged mass flow rate, and $h_H(0,0)$ is the average enthalpy entering the working volume at the inlet pressure, P_H. In this equation, the unknown value was $h_H(0,0)$, which corresponds to the average inlet temperature to the working volume, $T_H(0,0)$. As discussed in Chapter 3, the inlet temperature to the working volume was not constant, but varied with the position of the displacer. In Chapter 3, this average inlet temperature was defined as $T_H(0,0)$. For comparative purposes in Section (4.6), the same terminology was used here. The value of $T_H(0,0)$ was not needed here to determine an engine efficiency, but was computed for computation of a heat exchange temperature difference and for comparison with values given in Section (4.6) from the performance algorithm. The value of $T_H(0,0)$ was determined from helium tables using the value of $h_H(0,0)$ and the inlet pressure, P_H. For the experimental case of no precooling and no heat load, the indicated work output was 18.1 W, the time-averaged mass flow rate was 0.107 g/s, and, from earlier results, the constant pressure exhaust enthalpy was 197 J/g. From Eqn. (4.15), the average enthalpy entering the working volume was $h_H(0,0) = 366$ J/g.

At this point, an adiabatic engine efficiency was defined. The terms of this efficiency were based upon results from Eqn. (4.15), which was for a control volume that included only the displaced volume. The adiabatic engine efficiency was defined as

$$\eta_E = \frac{h_H(0,0) - h_{exh}}{h_H(0,0) - h_{exh,s}} \tag{4.16}$$

where $h_{exh,s}$ was the isentropic expansion state. This enthalpy after isentropic expansion, $h_{exh,s}$, was computed based on isentropic expansion from $h_H(0,0)$ and the maximum inlet pressure, P_H. When computing the value of isentropic enthalpy change, no clearance volume was assumed. For the case of no precooling and no heat load, the computed isentropic efficiency was 0.78. Examination of the adiabatic

efficiencies listed in Tables (4.3) to (4.6) reveals that the value of efficiency did not vary much for different operating conditions.

The throttling irreversibility during pressurization of the control volume was excluded from the determination of the reversible change in enthalpy for the adiabatic engine efficiency by assuming no clearance volume. Since this throttling irreversibility was quite substantial, it will now be investigated. The amount of throttling irreversibility increased as the amount of recompression decreased. The amount of recompression had to be adjusted when heat loads were added to the cold end in order to maintain a constant mass flow rate, as discussed in the results section. Decreasing the amount of recompression resulted in a larger throttling irreversibility during pressurization of the clearance volume.

In an effort to better quantify the magnitude of irreversibility due to pressurization of the displacer-to-cylinder gap after recompression, some approximate calculations were made. The irreversibility due to pressurization was due to the pressure drop between the supply pressure at room temperature and the pressure of the displaced volume. To decouple entropy generation due to pressure drop from other modes of entropy generation and to simplify the calculation, the pressure drop was assumed to occur only at room temperature, over the inlet valve and over the 90° turn from the inlet valve port to the displacer-to-cylinder gap. No pressure drop was assumed to occur in the displacer-to-cylinder gap. The situation was modelled as flow through an adiabatic valve at room temperature; thus, for ideal gas conditions, the process was isothermal. The entropy generation over the adiabatic valve per cycle was expressed as

$$d\,S_{gen,P} = d\,\gamma_{in}\,(s_{out} - s_{in}) \tag{4.17}$$

where γ_{in} is the amount of mass flow during pressurization, s_{out} is the entropy of the gas leaving the valve, and s_{in} is the entropy of the gas entering the valve. The amount of mass flow during pressurization, γ_{in}, was calculated based on the amount of gas required to pressurize the clearance volume, γ_P, since

$$d\,\gamma_{in} = d\,\gamma_P$$

The magnitude of γ_P was computed assuming isothermal compression (*i.e.*, the work of compression due to pressurization was small compared to the heat capacity of the exchanger walls). The temperature gradient along the exchanger was linear as shown in Fig. (4.27). The value of γ_P was computed by taking the average of the inverse of the gas temperatures at each end of the displacer-to-cylinder gap, since density is inversely proportional to temperature for an ideal gas. The cold end temperature used was $T_H(0,0)$. The magnitude of this effective temperature of the displacer-to-cylinder gap was defined as T_{eff}. The equation used to calculate the amount of mass flow during pressurization was based on the ideal gas equation as follows

$$P_{gap}\, V_C = \gamma_P\, R\, T_{eff}$$

where P_{gap} is the displacer-to-cylinder gap pressure, V_C is the clearance volume, and R is the universal gas constant. Equation (4.17) was now integrated using these criteria to obtain

$$S_{gen,P} = \frac{V_C\, P_H}{T_{eff}} \left(1 - \frac{P_R}{P_H}\left(1 - \ln \frac{P_R}{P_H}\right)\right) \tag{4.18}$$

where V_C is the clearance volume, P_H is the inlet pressure and the final gap pressure, and P_R is the gap pressure at the end of recompression. The magnitude of entropy generation due to pressure drop over at room temperature was computed for two cases for comparison: 1. no precool, no heat load; 2. no precool, 11 W heat load. The results are summarized in the following table:

Case	P_H (atm)	P_R (atm)	T_{eff} (K)	$S_{gen,P}$(J/K)	$S_{gen,E}$(J/K)	$\frac{S_{gen,P}}{S_{gen,E}}$
1	40	22	100	0.029	0.114	0.25
2	32	9	130	0.054	0.127	0.43

For comparative purposes, the table also includes the entropy generation in the displaced volume, which corresponds to the adiabatic engine efficiency of Eqn. (4.16). The equation used was

$$S_{gen,E} = \gamma \left(s_H(0,0) - s_{exh}\right) \tag{4.19}$$

where $s_H(0,0)$ is the entropy based on $h_H(0,0)$ and the inlet pressure P_H, and s_{exh} is based on h_{exh} at the exhaust pressure P_L. The results indicate that throttling during pressurization was a major irreversibility that increased substantially as the amount of recompression decreased.

The heat exchange temperature difference, $\Delta T)_{h0}$, was computed as

$$\Delta T)_{h0} = T_H(0,0) - T_L(0,0) \tag{4.20}$$

where $T_L(0,0)$ was the gas temperature after the lumped heat leak at the cold end. This terminology is the same as that used in Chapter 3. The value of $T_L(0,0)$ was computed based on the corresponding enthalpy, $h_L(0,0)$, using

$$M\big(h_L(0,0) - h_{exh}\big) = h_c + q_L + q_C \tag{4.21}$$

Here, the heat leak to the cold end was considered to be a lumped heat leak consisting of the average enthalpy flow due to displacer motion, h_c, the heat load, q_L, and the conduction heat leak, q_C. This lumped heat leak was added to the gas after expansion. Values of q_C and h_c were not experimentally measured, so values were estimated for Eqn. (4.21). The heat conduction was estimated using an integrated value of conductivity over the temperature span. The value of h_c was estimated using results from the performance algorithm, as given in Tables (4.3) to (4.6). In other words, results from the performance algorithm were used as inputs to Eqn. (4.21) because the enthalpy flow due to displacer motion was not measured. As discussed in the next section, the performance algorithm gave results that match the values measured from the experiment quite well. For this reason, the value obtained from the performance algorithm for the enthalpy flow due to displacer motion was accurate enough for this computation. For the case of no precooling and no heat load, the conduction heat leak was computed to be approximately 1.1 W, the enthalpy flow due to displacer motion was 2.1 W, and there was no applied heat load. Based on these values and values established earlier, the low-pressure return enthalpy was $h_L(0,0) = 227$ J/g. At 4 atm, this enthalpy corresponds to 41 K. Thus, from Eqn. (4.20), the heat exchange temperature difference was $\Delta T)_{h0} = 25$ K.

Another performance parameter that is included in Tables (4.3) to (4.6) is a flow coefficient. A value for the flow coefficient is given based on a definition as follows:

$$C_F = \frac{M_{act}}{\rho_{exh,s} V_W} \tag{4.22}$$

where M_{act} is the actual mass flow rate and V_W is the displacement volume. The density $\rho_{exh,s}$ is the exhaust density after reversible, adiabatic expansion from $h_H(0,0)$ and the maximum inlet pressure, P_H. One may note that reversible, adiabatic expansion was assumed to begin from the same initial state as that assumed for the expansion efficiency of Eqn. (4.16). The displacement volume was $V_W = 14.5$ cc. For the case of no precooling and no heat load, the density was $\rho_{exh,s} = 0.0078$ g/cc. The flow coefficient was then $C_F = 0.64$.

The above procedure was used to compute performance parameters for four of the data points that have already been discussed: 1. No precool, no load; 2. No precool, 11 W load; 3. Liquid nitrogen precool, no load; 4. Liquid nitrogen precool, 6.25 W load. Each data point is described in Tables (4.3) to (4.6), respectively. Also included in Tables (4.3) to (4.6) are results from the performance algorithm of Chapter 3. A discussion of the experimental results and a comparison with the theoretical results from the performance algorithm is given in the next section.

4.6 Discussion of Results

A discussion of cryocooler performance is given in this section. Problems encountered during cryocooler testing that have not yet been described are given first. Then, the trends in cryocooler performance are discussed. The usefulness of the performance algorithm in predicting cryocooler performance is included by comparing the experimental results. Finally, counterflow heat exchange degradation due to the slow response of the hydraulic drive mechanism is evaluated.

4.6.1 Problems with the Cryocooler

Two problems encountered during cryocooler operation have already been identified. First, the control system had to be modified to provide a delay in displacer

motion so that the dead volume could charge to 40 atm before displacer motion began. Second, the hydraulic drive mechanism was slow to respond to changing conditions. This problem will be discussed in more detail later in this section. A problem that has not been discussed involves gas contamination.

A significant problem encountered during cryocooler testing involved gas contamination. As the temperature decreased at the cold end of the cryocooler, contaminants condensed both on the exhaust valve seat and in the valve passages. Contaminants on the valve seat resulted in valve leakage. Contaminants between the exhaust valve plunger and the valve guide resulted in valve sticking. The problem was solved by installing an additional adsorption filter in the high-pressure flow line at room temperature. The adsorbant was liquid-nitrogen-cooled activated charcoal. After the filter was added, no additional contamination problems occurred; however, the cryocooler was operated no more than 12 hours during a single run.

4.6.2 Discussion of Cryocooler Performance

Performance parameters computed earlier using the experimental results were used in the performance algorithm for two reasons. First, the accurateness of the performance algorithm was validated by comparing theoretical and experimental values. Second, after the performance algorithm was shown to be reasonably accurate, results from the experiment that could not be measured were examined by looking at the values from the performance algorithm.

A convenient way to compare the different loss mechanisms was by using a first law energy balance on the cold end as shown in Fig. (3.3). The energy balance was

$$W = h_c + h_{nc} + q_L + q_C \tag{4.23}$$

where W is the expander work, h_c is the enthalpy flow rate due to displacer motion, h_{nc} is the enthalpy flow due to counterflow heat exchange, q_L is applied heat load, and q_C is the heat leak due to conduction. The value of each term on the right side of Eqn. (4.23) represents a loss in expander work. For a given amount of

expander work, the minimum temperature reachable by the cryocooler increased as the terms on the right increased. Also, the expander adiabatic efficiency affected the minimum refrigeration temperature. The difference between the reversible work output and the measured work output represented a thermodynamic loss. As the difference increased, the minimum refrigeration temperature increased.

Experimental results were compared with the theoretical results from the performance algorithm, as shown in Tables (4.3) to (4.6). When looking at the tables, the reader may wish to refer to Table (3.1) of Chapter 3 in order to distinguish inputs and outputs in the performance algorithm. One may also wish to note that for comparative purposes in Chapter 3, a single value of heat exchange performance was used to compute all values of $\Delta T)_{h0}$. Here, the value of $\Delta T)_{h0}$ was an input to the algorithm. The outputs listed in Tables (4.3) to (4.6) were obtained by adjusting η_E and $\Delta T)_{h0}$ until the theoretical values best matched the experimental values. A comparison of experimental and theoretical values in the tables reveals the correlation to be quite reasonable. For this reason, values that could not be experimentally measured but were outputs from the performance algorithm were used to better understand cryocooler performance. The variation in temperature with time of the displacer, cylinder, and outer shell at the cold end was examined in this way.

The experimental and theoretical adiabatic engine efficiencies are given in Tables (4.3) to (4.6). Both values were computed using Eqn. (4.16). The value of adiabatic efficiency was approximately the same for both with and without liquid nitrogen precooling and for all applied heat loads. As heat load was increased, the amount of recompression that could be used to maintain a constant mass flow rate decreased. As explained in Subsection (4.5.4), the adiabatic efficiency remained approximately constant as the amount of recompression decreased apparently because of compensating effects from changes in the intake pressure, P_H, and the refrigeration temperature, T_R. A separate calculation indicated that the irreversibility due to throttling during pressurization was a major loss that increased as the amount of recompression decreased.

The magnitude of reversible adiabatic work is listed in the tables for comparison with the indicated work from the experiment. The difference between the reversible and indicated work was the lost work due to inefficiencies. The magnitude of this lost work was compared with the average enthalpy flow due to counterflow heat exchange, h_{nc}, to reveal that the heat exchange loss was dominant. The heat exchange loss became less dominant, however, as the heat load was increased.

Time-averaged values of the heat exchange temperature difference are given in the tables. Because the temperature change of the gas during the expansion process decreased as the expander inlet temperature decreased, the value of $\Delta T)_{h0}$ was smaller when operating at the lower temperatures (*i.e.*, with liquid nitrogen precooling). This result was predicted by the first law balance on the cold end given in Eqn. (4.23). In Eqn. (4.23), the magnitudes of h_c, q_L, and q_C were not directly dependent on the expander inlet temperature, as were W and h_{nc}. Also, the value of $\Delta T)_{h0}$ decreased as the applied heat load was increased. This trend was predicted by Eqns. (4.20) and (4.21).

The heat exchange temperature difference, $\Delta T)_{h0}$, was not a constant with time. The magnitude of variation of the temperature difference with time was not measured in the experiment. Since the theoretically predicted values in Tables (4.3) to (4.6) agree well with the experimentally determined values measured, the temperature versus time plots for the displacer, cylinder, and outer shell were assumed to be predicted reasonably by the performance algorithm. The temperature versus time plot for the case of no precooling and no load is shown in Fig. (4.38). The temperatures plotted are for the cross section $x = 0$ at the cold end; thus, the displacer temperature plotted is the temperature seen by the cylinder at the stationary position $x = 0$. The heat exchange temperature difference varied between 16 K and 36 K. Both the time-averaged temperature difference along with the maximum and minimum values are given in the tables.

Another performance parameter listed in the tables is the flow coefficient, C_F, as defined in Eqn. (4.22). The measured values of C_F were approximately equal for optimal operation at the minimum refrigeration temperature for the cases of with

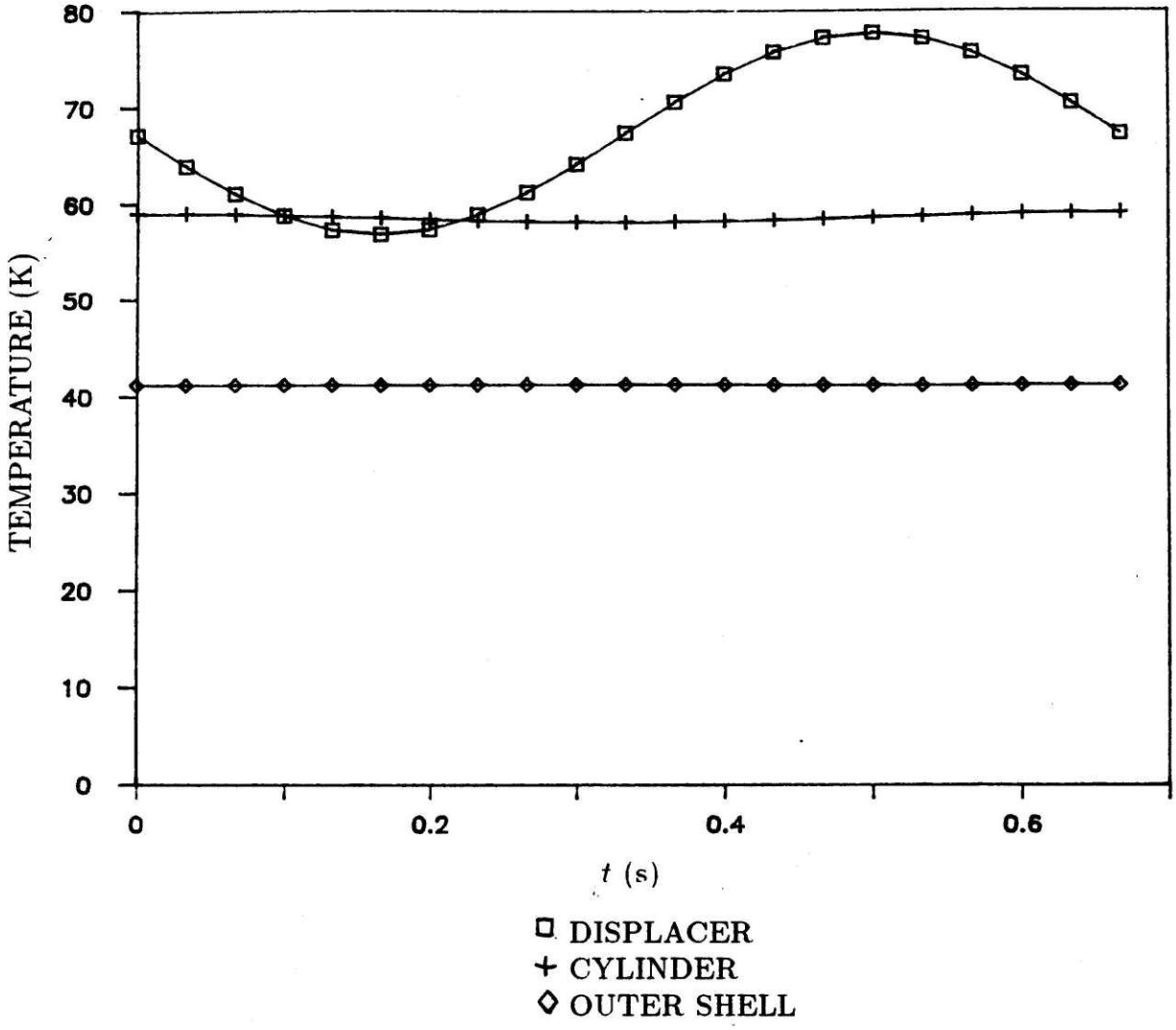

Fig. (4.38) Temperature versus time at the cold end for the case of no precool and no load.

and without liquid nitrogen precooling. Also, the value of C_F increased as the heat load was increased and less recompression was used.

One observation should be made concerning the performance algorithm in terms of a design algorithm. In this section, the theoretically determined values were shown to agree quite well with the experimental values, which raised the question of whether the performance algorithm should be used as a design algorithm for future cryocoolers using the integral expander and exchanger. The problem with using the performance algorithm to design future integral expander and exchanger units was that two performance efficiencies were inputs to the algorithm. These efficiencies were the adiabatic expander efficiency and the heat exchange efficiency. Thus, a good prediction of expander and exchanger efficiencies must be available before the performance algorithm can be used with confidence to design cryocoolers.

4.6.3 A Discussion of Heat Exchange Performance

Counterflow heat exchange was the dominant loss mechanism in the single-stage cryocooler experiment. A primary reason for the larger than expected counterflow heat exchange loss was the very high mass flow rate at the cold end immediately after the hydraulic directional control valve switched to begin the expansion stroke. This very high mass flow rate was explained with use of Fig. (4.39), which is Fig. (4.23) with the data points indicated. The data points were taken at 5 ms intervals. Again, this plot was for the case of no precool and no load, where the time-averaged mass flow rate was 0.107 g/s and the engine speed was 90 RPM. Only this case is included in this discussion. When the inlet valve opened, the pressure began to build in the dead volume. As described earlier, a delay was built into the electronic control system to allow the pressure in the dead volume to reach the full intake pressure before displacer motion began. After the dead volume was charged, the controls switched the hydraulic directional control valve. The initial motion was very fast because the pressure compensated flow control valve used to control displacer motion during expansion reacted slowly. The result was a very large mass flow rate into the cold volume during the initial portion of the expansion stroke.

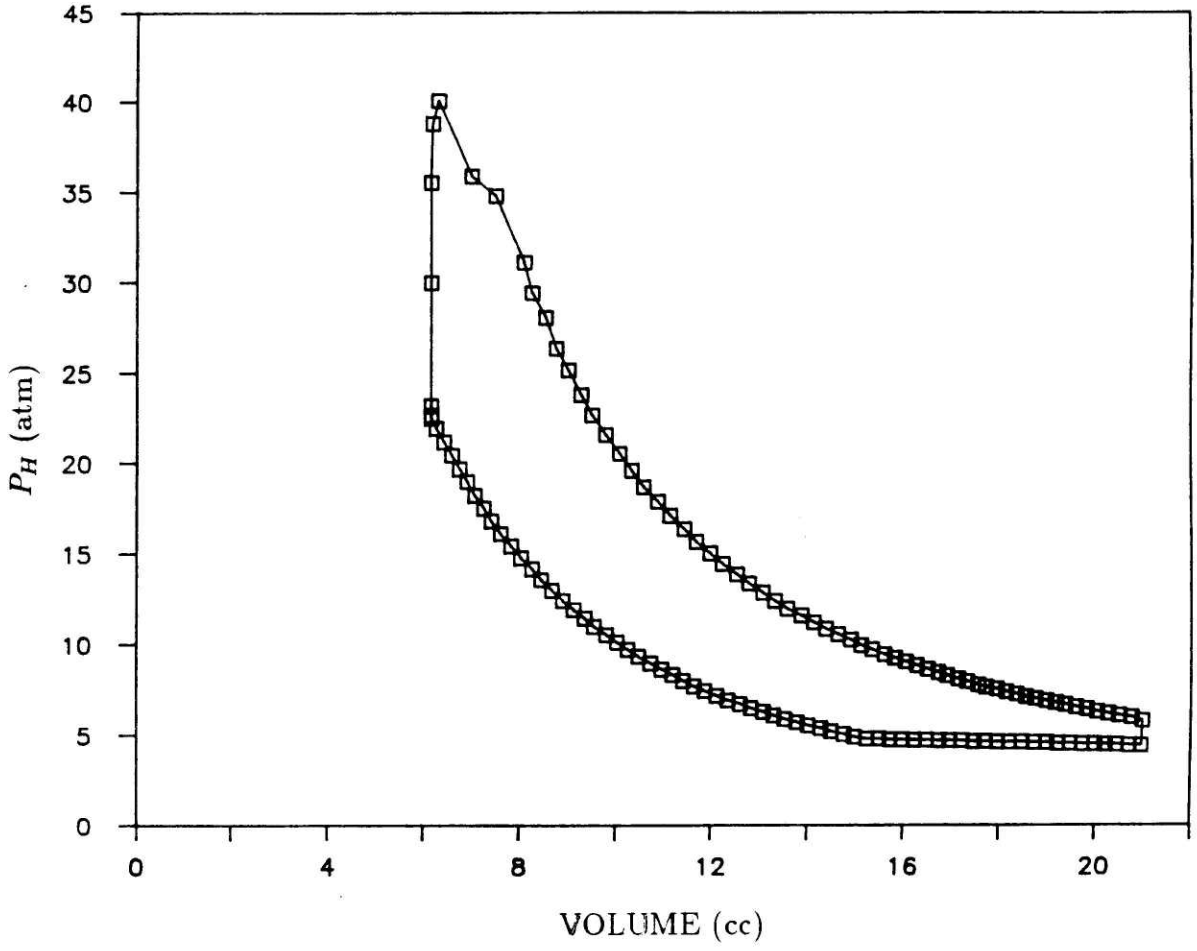

Fig. (4.39) Pressure versus volume with data points included for the case of no precooling and no heat load.

Figure (4.39) indicates this high initial mass flow rate. The larger separation in the data points during the initial portion of the expansion stroke indicates a quick displacement of cold-end volume and, thus, a large quantity of mass quickly flowing into the cold end. To quantify this mass flow and to better understand the mass flow during the entire expansion stroke, some calculations were made. The mass flows computed were those while the inlet valve was open. During these times, the exhaust valve was closed. The displacer was stationary during the charging of the dead volume. The first mass flow of interest was of the mass flow into the dead volume during the pressurization stage, γ_P. This calculation was done in Eqn. (4.18) of Subsection (4.5.4), so it will not be repeated here. The mass that flowed into the dead volume during pressurization was approximately $\gamma_P = 0.048$ g. The total mass flow per cycle, γ, was computed using

$$\gamma = M\,\tau \tag{4.24}$$

where M was the time-averaged mass flow rate and τ was the period for one cycle. The mass flow per cycle was approximately $\gamma = 0.071$ g. Thus, over half of the mass flow per cycle occurred during the dead volume pressurization. One should note that the mass flow rate during pressurization was maximum at room temperature and zero at the cold end. The amount of mass flow at the cold end after pressurization and before the cut-off point, γ_C, was computed using

$$\gamma_C = \Delta V\ \rho_0 \tag{4.25}$$

where ΔV was the volume displaced before cut-off and ρ_0 was the density at the cold end during the intake portion of the stroke. This density is based on the average intake pressure indicated by Fig. (4.39) and the average temperature at the cold end during intake as indicated by Fig. (4.38). The exact location of the cut-off point in Fig. (4.39) was not clear. Cut-off was assumed at a stroke of 2.6 mm. The average pressure during the intake portion of the stroke was taken to be 35 atm. The average intake temperature was taken as 68 K. The magnitude of γ_C was 0.033 g. Figure (4.39) shows the p-v plot with data points taken at 5 ms

intervals. The 0.033 g flowed into the cold end in less than 20 ms, which is a mass flow rate of 1.65 g/s (which may be compared with the time-averaged mass flow rate of 0.107 g/s for the complete cycle). These results indicate that approximately half of the total mass flow per cycle flowed into the cold end within the first 20 ms of the expansion stroke. This very high initial mass flow rate resulted in poor counterflow heat exchange.

These results indicated methods of improving the counterflow heat exchange by making the displacer-to-cylinder gap mass flow rate more constant throughout the cycle. First, the hydraulic valve used to control the displacer motion during expansion must react quickly to changing conditions in the working volume, as has already been discussed. Counterflow heat exchange would also be improved by throttling the mass flow during the pressurization stage. Even greater gains would be realized by making the initial displacer motion at the start of expansion very slow and letting the displacer speed increase as the expansion stroke progressed. This modification would provide a more constant mass flow rate during the expansion stroke to improve counterflow heat exchange.

Finally, an observation concerning regenerative heat exchange was made. A reason for regenerative heat exchange degradation at the cold end when operating at the lower temperatures may be due to the decrease in wall heat capacity. This phenomena may be illustrated by considering the charging of the gap between the displacer and cylinder at the cold end. As the gap charges, the walls and gas temperatures equilibrate very quickly due to high heat exchange. At warmer temperatures, the walls have a much larger heat capacity than the gas, so, as the pressure rises, the walls can accommodate the energy added to the gas without an appreciable temperature rise. At colder temperatures, the walls cannot accommodate the energy added to the gas without an associated temperature rise. In the cryocooler tested, calculations indicate that, for no mass flow on the low-pressure side, the temperature rise of the displacer, cylinder, and gas-filled gap would be about 5 K for pressurization from 4 atm to 40 atm, starting from 20 K. Gas flow on the low-pressure side was always present, however, as shown in Fig. (4.33). With the

low-pressure mass flow included, performing the same calculations results in a temperature rise of less than 2 K for pressurization from 4 atm to 40 atm, starting from 20 K. This 2 K temperature swing due to pressurization seems small when compared to the theoretical heat exchange temperature difference of 16 K for the case of liquid nitrogen precooling and no heat load, as indicated in Table (4.5). These results suggest that, although the reduction of wall heat capacity with temperature reduced cryocooler performance, the primary loss mechanism in the experiment was the enthalpy flow at the cold end due to heat exchange temperature difference.

Chapter 5
Conclusions and Recommendations

5.1 Summary of Analytical Results

This project identified a cryocooler configuration that exploits the high thermodynamic efficiency of the SVC cycle while being constructed with practical components. The primary specifications for the cryocooler were 1 W of refrigeration at 4.2 K and a physical size constraint of 60 cm high with 20 cm sides. To realize a practical configuration for these specifications, both cycle and component analyses were performed. The cycle analysis consisted of a computerized parametric optimization study of the SVC cycle that included entropy generation calculations for the individual components. The study was performed by examining SVC cycle performance with different heat exchanger and expansion engine configurations. Specific losses considered were expander and compressor inefficiencies, heat exchange temperature difference, fluid friction, heat conduction, and radiation heat leak. The optimization study identified a cryocooler design that incorporated the integration of a heat exchanger and expansion engine in a concentric tube configuration.

Evolution of this concentric tube configuration led to a modification of the SVC cycle configuration which has several advantages. First, the inlet valve operates at room temperature. This design reduces potential reliability problems present with valves operating at the refrigeration temperature, while allowing additional room for the cold exhaust valve. The design also reduces axial conduction by using the displacer wall as an inner shell for the heat exchanger. The result is an exchanger using regenerative heat exchange due to pressure cycling in the displacer-to-cylinder gap and counterflow heat exchange.

Since the cycle analysis did not provide enough information for detailed design of the integral expander and exchanger, a performance algorithm was developed in Chapter 3 which involved modeling of displacer motion and counterflow heat exchange in conjunction with the expansion process. Variations in important design parameters were investigated to determine appropriate values for such dimensions

as the heat exchange gap widths. The performance algorithm was used not only to design a prototype cryocooler to be tested but also to investigate the feasibility of the integral expander and exchanger design for shorter single-stage cryocooler lengths.

5.2 Summary of Experimental Results

A single-stage cryocooler was designed, assembled and tested. The prototype machine produced refrigeration of 1 W at 40 K without precooling and at 20 K with liquid nitrogen precooling. The results indicate that a high pressure ratio single-stage cryocooler, using a combination of regenerative and counterflow heat exchange, is a viable component in a multi-stage miniature liquid helium temperature refrigerator.

Methods were devised to compute performance parameters for the single-stage cryocooler. An adiabatic engine efficiency was defined for the displaced volume at the cold end. This efficiency deliberately ignored irreversibilities associated with clearance volume by assuming no clearance volume. A separate analysis then quantified the throttling irreversibility due to pressurization of the clearance volume. In this way, the magnitude of entropy generation due to adiabatic expansion with no clearance volume was compared with the entropy generation due to pressurization of the clearance volume. The calculations indicated that the irreversibility due to pressurization was substantial when compared to the adiabatic engine irreversibility and that the irreversibility due to pressurization increased a considerable amount as the amount of recompression decreased. Another performance parameter determined was the heat exchange temperature difference for the counterflow streams. The heat exchange temperature difference varied greatly, depending on the operating conditions. Operation at higher refrigeration temperatures resulted in a larger heat exchange temperature difference than at lower temperatures. Applying a heat load resulted in a lower heat exchange temperature difference.

A primary observation was that counterflow heat exchange performance limited the cryocooler performance. One cause of the heat exchange degradation was a very

high mass flow rate on the high-pressure side during the initial part of the expansion stroke. This high mass flow rate was the result of the slow response of a hydraulic pressure-compensated flow control valve used to control the speed of the exhaust stroke.

5.3 Recommendations

This document presents the first development stage for a new type of liquid helium temperature cryocooler. Several short- and long-term projects must be completed before a viable system will be realized. In the short term, lucrative results should be obtained from modifying the drive mechanism to better regulate the mass flow rate between the displacer and cylinder. Best performance would result if the high-pressure mass flow were of the same order of magnitude as the low-pressure flow throughout the cycle. One way to help average the flow rate would be to have slow displacer motion during the intake portion of the stroke. Additional averaging of the flow rate might be obtained by throttling at the inlet valve during the initial pressurization of the dead volume; this would, however, require complex valve action to prevent throttling during the intake stroke. One way to obtain this valve action might be to modify the displacer so that when the inlet valve opens, the displacer constricts the inlet flow; after the dead volume is charged, the displacer would begin to move, removing the flow constriction.

Another area that must receive continued attention throughout cryocooler development involves both cycle and component analyses, which will ultimately evolve into a single analysis. The performance algorithm presented here could be used to verify the case of only one set of physical dimensions. Future experiments will provide additional data points that will be used to build algorithms to better predict performance.

A long-term goal that is scheduled to follow this project involves development of a practical exhaust valve. The exhaust valve used in this project had two major problems. First, it was very vulnerable to contamination. Contaminants that condensed on the valve seat resulted in valve leakage. Condensation between the sliding

plunger and the plunger housing resulted in sticking. These results indicate a need to find an inexpensive, efficient way to eliminate or, at least, reduce contamination in the gas. Valve design should employ a seat that could mechanically break up and remove small amounts of contamination. Sliding surfaces used to guide the plunger should be eliminated. One way to do this is to rigidly attach the plunger to a bistable diaphragm.

The second major problem with the exhaust valve was due to the use of a room temperature solenoid to drive the cold valve. The design required flexible connections at the room temperature vacuum jacket because of dimensional changes of the cold parts when cooled down. Also, conduction heat leak through the mechanical connection between the warm solenoid and cold valve had to be kept minimal by using small diameter, fragile tubes. The result was a bulky exhaust valve that was very vulnerable to any accidental movement of the warm solenoid housing. A much better design will use a cold drive mechanism for the plunger. One design would use a bistable diaphragm/plunger that would be powered by high-pressure helium actuated by the use of a small, cold solenoid.

A major challenge in future development will be multi-staging of the single-stage cryocooler. This development could proceed by building single-stage units of different lengths and thermally connecting the stages to form a cycle configuration like that of Fig. (2.13). A more elegant design would use a single displacer of different diameters to form the stages. This design would involve challenges in exhaust valve design and in plumbing among the stages. Interfacing with the cold compressor would also be very challenging.

Miniaturization of the cold compressor would be most efficient if no direct connections to room temperature were necessary. The power removed from the expansion engines is more than adequate to provide power to the cold compressor. The compressor drive shaft cannot easily be mechanically connected directly to the expansion engine drive shaft, however, because cold seals would be necessary. Magnets could probably be used to provide the connection since the force required to pressurize the gas to the return flow pressure could be designed to be small.

Appendix A
Computer Program Descriptions
with Results for the System Analysis

This appendix is separated into two sections. The first section is a description of the computer programs used in Chapter 2. The second section uses the computer programs to supply details for some of the results that were given in Chapter 2.

A.1 Computer Program Descriptions for the System Analysis

This section is a description of the computer programs used to analyze cryocoolers employing the SVC and Collins cycles. These programs enable the user to determine optimal operating conditions with respect to dry expander inlet temperatures which the user manually inputs to the program. The remainder of the parameters must be read into the program via storage files. Table (A.1) is a listing of the inputs and outputs to the main program, SYSITER, and the main subprogram, SYSLEAK. Note that the parameter symbols used in this appendix may differ from those used in the remainder of the document. For this reason, all terms are defined in this appendix, either in the computer programs or in the written text.

Program SYSITER will first be described. SYSITER is used to compute the thermodynamic state properties and mass flow rates. Engine entropy generations in both dry expanders, the wet expander, and the vapor compressor are also computed. A description of subprogram SYSLEAK will then be given. SYSLEAK is used to place physical dimensions on the dry expansion engines and heat exchangers. Using these dimensions SYSLEAK then computes the heat leaks due to radiation and axial conduction, along with the corresponding entropy generations. SYSLEAK also computes entropy generation in the helium gas due to fluid friction pressure drop and heat exchange temperature difference.

Subprogram PINCH is called by SYSITER to locate the pinch points in the coldest heat exchanger. Several other function subprograms are used to compute the properties of helium. Most of the subprograms were obtained from the National

Table (A.1) Inputs and outputs to program SYSITER and subroutine SYSLEAK

PROGRAM SYSITER

Required Inputs:

PH	The pressure (atm) at each state point on the high-pressure side.
PQ	The pressure (atm) at the inlet to the wet expander or before the J-T valve.
PL	The pressure (atm) at each state point on the low-pressure side
PC	The pressure (atm) after the vapor compressor or after the refrigeration zone.
QE	The lumped heat input (W) before each dry expander.
QW	The lumped heat input (W) before the wet expander or before the J-T valve.
QRL	The lumped heat input (W) at the refrigeration zone that does not include the refrigeration load.
NN	The number of dry expansion engines.
IEXP	This input is 1 if a wet expander is used or 0 if a J-T valve is used.
ICOMP	This input is 1 if a vapor compressor is used or 0 if not.
QR	The refrigeration load (W).
TR	The refrigeration temperature (K).
PR	The refrigeration pressure (atm). Note that only on input is required to establish the state of the helium in the refrigeration zone, either TR or PR.
DTPIN	The minimum value of the ratio of heat exchange temperature difference to the low-pressure side temperature in the heat exchangers. One value is used for all exchangers.
FWE	The adiabatic efficiency of the wet expander.

FVC The adiabatic efficiency of the vapor compressor.

FE The adiabatic efficiency of each dry expander.

TE The temperature (K) at the inlet to each expansion engine.

Outputs:

MR The mass flow rate (g/s) through the refrigeration zone.

ME The mass flow rate (g/s) through each dry expansion engine.

MCOMP The mass flow rate (g/s) through the warm compressor.

TH The temperature (K) of the high-pressure stream at each state point.

TL The temperature (K) of the low-pressure stream at each state point.

SGENWE The entropy generated (W/K) in the wet expander.

SGENDE The entropy generated (W/K) in each dry expander.

SGENCO The entropy generated (W/K) in the vapor compressor

Subroutine SYSLEAK

Additional Inputs Required:

RPM The speed of the engines in revolutions per minute; all engines are assumed to operate at the same speed.

R The ratio of bore to stroke, taken to be the same for all engines.

ZH The radial gap (in) between the displacer and the cylinder.

ZL The radial gap (in) between the cylinder and outer shell.

TPIS The thickness of the displacer tube (in).

TCYL The thickness of the cylinder tube (in).

TSHELL The thickness of the outer shell (in).

ANG The helix angle (degrees) of the spiral spacer measured from the axis of the engine.

TCAN The temperature (K) of the vacuum shell.

E The emissivity of all the surfaces.

Outputs:

PH Updated values of the pressure (atm) at each state point on the high-pressure side.

PL Updated values of the pressure (atm) at each state point on the low-pressure side.

B The bore (in) of each dry expansion engine.

S The stroke (in) of each dry expansion engine.

L The length of each counterflow heat exchanger.

QER The lumped radiation heat leak (W) before each dry expander.

QEC The lumped conduction heat leak (W) before each dry expander.

SGENER The entropy (W/K) generated before each dry expansion engine due to radiation heat leak.

SGENEC The entropy (W/K) generated before each dry expansion engine due to conduction heat leak.

SGGAS The entropy (W/K) generated in the helium gas due to pressure drop and to heat exchange temperature difference.

Bureau of Standards. The subprograms used to compute helium properties which were not obtained from NBS include CALCUP and CALCPS. A complete list of subprograms is given in Table (A.2).

Dictionaries are included in the introductions to SYSITER and to SYSLEAK. These dictionaries include variables which are used most often during the computations. Variables not included in the dictionaries will be defined in the text.

Exhibit (A.1), at the end of this appendix, is a printout of SYSITER and SYSLEAK, which includes line numbers. Throughout the program descriptions, specific line numbers will be referenced.

A.1.1 PROGRAM SYSITER

Program SYSITER first reads the type of cryocooler to be analyzed, the specified physical dimensions, the operating load, the refrigeration temperature or pressure, and the component efficiencies. Values which remain constant for each iteration are next computed. The user is then asked to input the values of expander inlet temperatures to be used as the first iteration. All output values are then computed. The program then returns to the read statement to ask the user for new expander inlet temperatures. Note that a single set of expander inlet temperatures should be inputed approximately three times to obtain correct results. This is because the outputs from each run through the program are the inputs to the next run.

The numbering system used throughout SYSITER begins at state point 1 located at the exit from the coldest dry expander and proceeds in the direction of increasing temperature. The dry expansion engines are numbered so that the coldest dry expander is number 1. Figure (A.1) illustrates the numbering system.

Lines 128-146 are standard fortran statements including dimension and read statements. All inputs to the program are read here except $TE(1)$ and $TE(2)$, which are read later. The inputs are also shown in Table (A.1).

Line 147 sets the temperature of the helium gas at the exit from the warm compressor after-cooler, which is the gas temperature at the entrance to the warm end of the heat exchanger stack at 300 K.

Table (A.2) Subprograms of program SYSITER

Subroutines:

CALCPS	Computes density (g/cc) and temperature (K) given pressure (atm) and entropy (J/gm-K). Estimates of density and temperature must be included as inputs.
CALCUP	Computes density (g/cc) and temperature (K) given pressure (atm) and enthalpy (J/g). Estimates of density and temperature must be included as inputs.

Functions:

CONDT	Computes thermal conductivity (W/cm-K) given density (moles/liter) and temperature (K).
CP	Computes the specific heat at constant pressure (J/mole-K) when given density (moles/liter) and temperature (K).
DENF	Computes density (kg/m^3) given pressure (Pa) and temperature (K).
DPH	Computes the density (moles/liter) given pressure (atm) and enthalpy (J/mole).
DSATL	Computes the saturated liquid density (moles/liter) given temperature (K).
DSATV	Computes the saturated vapor density (moles/liter) given temperature (K).
ENTHAL	Computes enthalpy (J/g) given density (kg/m^3) and temperature (K).
ENTROP	Computes entropy (J/mole-K) given density (moles/liter) and temperature (K).
SAPH	Computes entropy (J/kg-K) given pressure (Pa) and enthalpy (J/kg).
SYSLEAK	Determines the physical dimensions of the internal cryocooler components. Also computes the entropy generations due to various mechanisms.

VISCDT Computes viscosity (g/cm-s) given density (moles/liter) and temperature (K).

VPN Computes the saturation pressure (atm) given temperature (K).

VPTEMP Computes the saturation temperature (K) given pressure (atm).

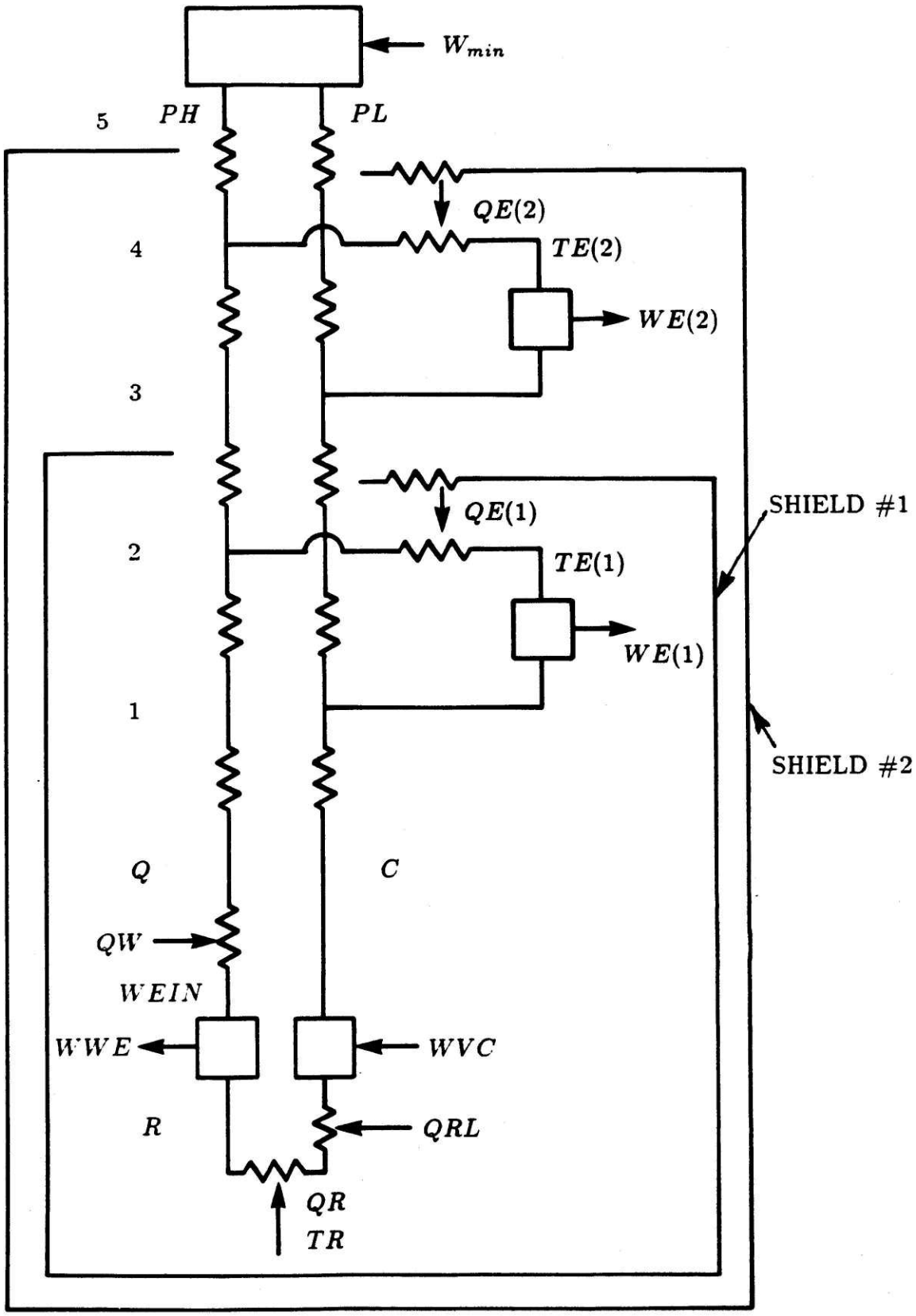

Fig. (A.1) Numbering system for SVC cycle.

Lines 151-164 compute the saturation properties of helium at the refrigeration temperature or pressure, whichever is input in the read statement.

Lines 166-180 use the saturated vapor properties of helium, the vapor compressor adiabatic efficiency, and the low-side pressure to compute the properties at the exit from the cold compressor. The adiabatic efficiency is

$$FVC = \frac{HCS - HV}{HC - HV} \tag{A.1}$$

where HC is the actual enthalpy at the exit from the cold compressor, HCS is the enthalpy at the exit from the cold compressor for isenthalpic compression, and, for use in CALCUP, DC is the density. Note that to use subprograms CALCUP and CALCPS, estimates of the outputs must be included as inputs to be used as a first iteration. These subprograms usually converge within a few iterations. If the Collins cycle is used then this section of the program is skipped by going directly to line 181.

At this point the dry expander inlet temperatures are read. The program is set up at this time to read temperatures for a cryocooler using two dry expanders.

Lines 187-205 compute the outlet states for all of the dry expanders. The outlet density, internal energy, entropy, and isentropic expansion enthalpy are called DO, UO, SO, and HOS, respectively. The adiabatic efficiency used to compute the outlet state is

$$FE = \frac{HE - HL}{HE - HOS} \tag{A.2}$$

Line 204 computes the change in entropy between engine inlet and exit states, $DELSEXP$, which will be used later to compute the entropy generation in the dry expanders.

Lines 206-213 compute the high-pressure side temperatures corresponding to the outlets of the dry expanders by assuming these to be heat exchange pinch points. The high-side enthalpies at these pinch points are also calculated. The high-side temperatures are computed using

$$TH = TL\,(1 + DTPIN) \tag{A.3}$$

The program next checks to see whether a heat exchanger is needed between the exit from the coldest dry expander and the cold compressor. If so, the enthalpy, HQ, before the lumped heat input QW is computed at line 218; if not, HQ is equal to $HH(1)$. The temperature, TQ, before the lumped heat input QW, is next computed using CALCUP at line 224.

Lines 227-258 use subprogram PINCH to locate the pinch points in the coldest heat exchanger. The program first assumes the pinch point to be located at the exit from the coldest dry expander. The temperatures TQ, TC, and $TL(1)$ are set by other system inputs. So, if the assumed pinch point location is incorrect, the program places the pinch point at the proper location and recomputes $TH(1)$ for the new conditions. Note that, under the conditions used for all systems considered in this analysis, the pinch points for the warmer exchangers are located at the assumed positions.

The mass flow rate through the wet expander is next determined by an iterative procedure. Lines 259-285 compute the mass flow rate for the SVC cycle while lines 286-302 are for the Collins cycle.

The computation of the mass flow rate for the SVC cycle will now be described (lines 259-285). An iteration is required to determine the mass flow rate because of the heat leak QW. Since an initial estimate of the mass flow rate is needed, the heat leak QW is first set equal to zero and the mass flow rate required for no heat leak is calculated. The same procedure as that which follows is used to compute this mass flow rate except that QW is set equal to zero. To compute the mass flow rate including QW, the following equations are used:

$$MR\,(HHI - HQ) = QW \tag{A.4}$$

to obtain HHI, where HHI is the enthalpy before the wet expander and HQ is the enthalpy before the heat input. For $FWE = 1.0$:

$$XS = \frac{SH - SF}{SFG} \tag{A.5}$$

where SH is the enthalpy before the wet expander. Using XS,

$$HRS = HF + XS\ HFG \tag{A.6}$$

where HRS is the enthalpy of the two-phase helium exiting the wet expander. Next obtain the actual HR using

$$FWE = \frac{HHI - HR}{HHI - HRS} \tag{A.7}$$

to obtain HR. The actual quality is then

$$X = \frac{HR - HF}{HFG} \tag{A.8}$$

where,

$$MV = \frac{X}{1 - X} ML \tag{A.9}$$

$$ML = \frac{QR + QRL}{HFG} \tag{A.10}$$

$$MR = ML + MV \tag{A.11}$$

This value for MR is compared with the value used in the first equation to see if the difference is negligible.

Lines 306-308 compute the entropy generated in the wet expander and cold compressor using the previous results.

The mass flow rate over the J-T valve for the Collins cycle is computed much the same way as for the SVC cycle (lines 286-302). The mass flow rate for $QW = 0$ is first computed using the same procedure as below except that $QW = 0$. To compute the mass flow rate including the heat leak, the following equations are used:

$$MR\,(\,HHI - HQ\,) = QW \tag{A.12}$$

$$X = \frac{HHI - HF}{HFG} \tag{A.13}$$

$$MV = \frac{X}{1 - X}\,ML \tag{A.14}$$

$$ML = \frac{QR + QRL}{HFG} \tag{A.15}$$

$$MR = ML + MV \tag{A.16}$$

The value of MR computed in the last equation is compared with the initial value to determine if additional iterations are required.

Lines 315-323 compute the enthalpies, which will be used later, at the warm entrance to and exit from the heat exchanger stack.

Once MR is known, the mass flow rate through each dry expander required to match the heat capacity rates of the high-pressure and low-pressure sides may be determined. This computation is performed in lines 324-344. In the following equations, state i is at the point where gas is extracted from the high-pressure stream for the dry expander j, where $j = i/2$. The equations which must be solved simultaneously for $ME(j)$ by eliminating $WE(j)$ are:

$$WE(j) = ME(j)\,(\,HE(j) - HL(i-1)\,) \tag{A.17}$$

and,

$$QE(j) - WE(j) + (M(j) + ME(j))\,(HH(i+1) - HL(i+1))$$

$$+M(j)\,(HL(i-1) - HH(i-1)) = 0 \tag{A.18}$$

These equations are solved in lines 330-331 to determine $ME(j)$. Lines 332-333 compute the enthalpies on the low-pressure and high-pressure sides at the state point i. The equations used are:

$$QE(j) = ME(j)\left(HE(j) - HH(i)\right) \tag{A.19}$$

and,

$$HL(i+1) - HL(i) = HH(i+1) - HH(i) \tag{A.20}$$

Subprogram CALCUP is then used to compute the temperatures on the high-pressure and low-pressure sides at state point i.

The entropy generated in each dry expander is next computed on line 347 by using the change in entropy computed in lines 203-204 and the mass flow rates computed above.

Several write statements to the terminal screen and to file 10 are followed by subprogram SYSLEAK.

A.1.2 Subprogram SYSLEAK

This subprogram is used to compute physical dimensions for a cryocooler based on the state points computed in program SYSITER. After physical dimensions are found, values of heat leaks, pressure drops, and other sources of entropy generation are computed.

Lines 106-120 include standard fortran statements. Lines 122-123 compute the sine and cosine of the helix angle, ANG.

Lines 126-144 compute the bore and stroke of the dry expansion engines. The mass of helium gas in the cylinder during each stroke, $MEXP$, is first calculated using the mass flow rate and the speed of the expansion engine. The exit density is next computed so that the bore and stroke may be determined.

In order to facilitate sizing of the heat exchangers, lines 146-232 change the numbering of the state points. The state points referred to as C and Q located at

the exit from the cold compressor and before the lumped heat leak QW, respectively, are renumbered to be state point 1. Thus, state point i in SYSITER becomes state point $i + 1$ in SYSLEAK.

Lines 235-269 compute several of the gas properties required to design the heat exchangers. Lines 242-250 compute the enthalpies at the newly defined state points. Lines 253-269 compute average properties using the average temperatures and pressures on the high-side and low-side. Here, the integer i refers to the heat exchanger, where $i = 1$ indicates the coldest heat exchanger.

The subroutine next completes the designs of the heat exchangers by finding their lengths. Heat transfer coefficients are computed first so that an equation can be used to determine the length. Then the pressure drop over the exchanger is computed. Since a concentric tube counterflow heat exchanger is being used, the equations listed are well established in the literature.[39]

Lines 283-284 determine the Reynolds number for the high- and low-pressure sides. The equations used are

$$REH = \frac{2\,MEH}{\pi\,DIAH\;\;VH} \tag{A.21}$$

$$REL = \frac{2\,MEL}{\pi\,DIAL\;\;VL\;\;CO} \tag{A.22}$$

where, in the equation for low-pressure side Reynolds number, the term

$$CO = \cos\,(\,ANG\,)$$

is needed because of the spiral flow passage shape.

The heat transfer coefficients are now computed. The high-pressure side is not likely to encounter turbulent flow. The low-pressure side, however, will be turbulent, at least in the warmer heat exchangers. For this reason, the choice of equation for heat transfer coefficient on the low-pressure side depends on the magnitude of the Reynolds number. Lines 286 and 290 compute the coefficient of heat transfer for

laminar flow for the high- and low-pressure sides, respectively. The equations used are

$$HHP = \frac{NU\ KH}{ZH} \tag{A.23}$$

$$HLP = \frac{NU\ KL}{ZL} \tag{A.24}$$

where,

$$NU = 8.23 \tag{A.25}$$

Turbulent flow conditions are assumed to begin at Reynolds numbers greater than 2000. If the low-pressure flow is turbulent, the equation used is

$$HLP = \frac{KL}{2\,ZL}\left(1 + 3.5\,\frac{2\,ZL}{DIAL}\right)(0.75)\,(0.023)\,REL^{.08}\,PRL^{0.4} \tag{A.26}$$

The heat exchanger length is next computed on lines 304-310 using the following relations:

$$Q = MEH\,(HIN - HOUT). \tag{A.27}$$

$$Q = U\,A\,\frac{DTA - DTB}{\ln\left(\frac{DTA}{DTB}\right)} \tag{A.28}$$

where,

$$DTA = TEH(i+1) - TEL(i+1) \tag{A.29}$$

$$DTB = TEH(i) - TEL(i) \tag{A.30}$$

The overall coefficient of heat transfer is

$$UCONV = \frac{HHP\ HLP}{HHP + HLP} \tag{A.31}$$

By combining the above equations, the heat exchanger length is

$$L = \frac{MEH\ (HIN - HOUT)\ \ln\left(\frac{DTA}{DTB}\right)}{(DTA - DTB)\,\pi\,DCI\ UCONV} \tag{A.32}$$

Using the Reynolds numbers computed above, the program finds the pressure drop over the heat exchanger for the high- and low-pressure side for laminar or turbulent flow. The definition of fluid friction coefficient, f, used here is from reference (39):

$$\Delta P = 4 f \frac{L}{D_e} \frac{\rho V^2}{2} \tag{A.33}$$

In this equation, ρ is the fluid density, V is the fluid velocity, and the equivalent diameter, D_e, is defined as

$$D_e = 2 Z \tag{A.34}$$

where Z is the radial gap width. The velocity in Eqn. (A.33) is eliminated using the mass flow rate:

$$M = \rho V A \tag{A.35}$$

where A is the cross sectional area for flow. On the high-pressure side,

$$AHP = \pi\,DIAH\ \ ZH \tag{A.36}$$

and on the low-pressure side

$$ALP = \pi\,DIAL\ \ ZL\ \ CO \tag{A.37}$$

where the thickness of the spiral spacer is assumed negligible.

The value of the fluid friction coefficient, f, depends on whether the flow is laminar or turbulent. For laminar flow in the annular space between concentric tubes:

$$f = \frac{24}{Re} \tag{A.38}$$

For turbulent flow, the equation used for the range of Re encountered in this analysis is

$$f = \frac{0.046}{Re^{0.2}} \tag{A.39}$$

Combining the above information, the equations for pressure drop given on lines 312-325 may be written in terms of variables used in the program. For the high-pressure side, only laminar flow conditions will be considered:

$$DELPH = \frac{12\,L\ VH\ MEH}{ZH^3\,DH\,\pi\,DIAH} \tag{A.40}$$

In this equation, DH is the high-pressure side density. A similar equation is used for laminar flow on the low-pressure side, except that the length of the flow passage must be modified.

$$DELPL = \frac{12\,L\ VL\ MEL}{ZL^3\,DL\,\pi\,DIAL\ CO^2} \tag{A.41}$$

For turbulent flow conditions on the low-pressure side, the equation used is

$$DELPL = \frac{0.046\,MEL^2\,L}{REL^{0.2}\,DL\ ZL^3\,\pi^2\,DIAL^2\,CO^3} \tag{A.42}$$

The new value for the absolute pressure at each state point may now be computed by starting with the input pressures, $PEL(1)$ and $PEH(n+2)$, and subtracting the pressure drop for each heat exchanger. This is done on lines 329-345.

At this point in the programs, the heat exchanger dimensions are known. The lumped heat leaks before each of the engines will now be computed by determining the heat leaks due to radiation and axial conduction.

Lines 381-388 determine the heat exchanger area exposed to radiation heat leak. The amount of cold box area exposed to radiation is assumed to be that of a cylinder with a diameter and length of three times the bore of the coldest dry expander. The view factor calculated on line 400 is for infinite gray parallel plates.

Fig. (A.1) will be helpful in the following discussions when the description of each control volume under investigation is given.

Line 404 gives the magnitude of radiation heat leak to be lumped as a heat input to the refrigeration zone. This heat leak is equal to the total amount of radiation received by the refrigeration zone from the radiation shield # 1. The radiation shields are assumed to operate at the entrance temperature to their respective dry expander. The refrigeration zone is assumed to be at 4.5 K.

Lines 406-408 compute an average outer shell temperature for each heat exchanger by using the inlet and outlet low-pressure gas temperatures, since this gas is in contact with the outer shell.

Lines 410-413 compute the heat leak lumped at the inlet to the wet expander. The heat leak QWR is divided into two parts which will be used later in entropy generation computations. This heat leak is equal to the total amount of radiation received by heat exchangers # 1 and # 2 from radiation shield # 1.

The radiation heat leak lumped at the inlet to dry expander # 1 is computed in lines 415-420. The magnitudes of EE, FF, and GG will be used later in entropy generation computations. The value of $QER(1)$ is determined by adding the heat leaks to the radiation shield # 1 and to the heat exchangers # 3 and # 4. In words, the heat leak $QER(1)$ is equal to: the radiation emitted by radiation shield # 2 and absorbed by heat exchangers # 3 and # 4 (which is the sum of EE and FF); plus the radiation emitted by radiation shield # 2 and absorbed by radiation shield # 1 (which is written as GG); less the radiation emitted by radiation shield # 1 to the colder components.

The heat leak $QER(2)$ is computed by adding the heat leak to radiation shield # 2 and the heat leak to exchanger # 5, on lines 423-427. In words, the value of $QER(2)$ is equal to: the radiation emitted by the cryocooler can and absorbed by

heat exchanger # 5 (written as UU); plus the radiation emitted by the cryocooler can and absorbed by radiation shield # 2 (written as VV); less the radiation emitted by radiation shield # 2 to the colder components.

The entropy generation due to radiation heat leak is computed on lines 485-493. To compute this entropy generation, the cryocooler is divided into several control volumes so that the entropy generation may be computed for each. The entropy generated in the volume between radiation shield # 1 and the refrigeration zone, $SGENRL$, is computed on line 486. The entropy generated in the volume between radiation shield # 1 and heat exchangers # 1 and # 2, $SGENWR$, is computed on line 488. The value of $SGENE1R$ consists of two volumes: i) the volume between radiation shield # 1 and radiation shield # 2, and ii) the volume between radiation shield # 2 and heat exchangers # 3 and # 4. The value of $SGENE2R$ also consists of two volumes: i) the volume between heat exchanger # 5 and the cryocooler can, and ii) the volume between the radiation shield # 2 and the can.

The conduction heat leak is computed on lines 430-466. The cross-sectional area for conduction is computed on lines 432-434. Lines 445-447 compute an average temperature of the cross-section at both ends of each heat exchanger. Line 448 computes an average temperature of the complete heat exchanger to be used in the stainless steel conductivity calculation. Lines 450-452 use a third order logarithmic equation to compute the conductivity of the stainless steel. Using a linear temperature gradient assumption, line 454 computes an average axial conduction heat leak for each heat exchanger. Lines 459-460 compute an average heat leak for integral exchanger combinations. This average heat leak is based on the length of the heat exchangers. Lines 462-466 compute the amount of conduction heat leak removed at each dry expander inlet. The heat leak lumped at an expander is the difference between the average axial conduction heat leak in the heat exchanger combination above the expander inlet temperature and that in the exchanger combination below the expander inlet temperature.

The entropy generation due to axial conduction is computed on lines 495-500. The control volume selected for $SGENWC$ contains heat exchangers # 1 and # 2;

the control volume selected for $SGENE1C$ contains heat exchangers # 3 and # 4; and, the control volume selected for $SGENE2C$ contains heat exchanger # 5. In each case the entropy generated is equal to the entropy leaving the heat exchanger stainless steel tubes and walls at the lower temperature minus that entering the heat exchanger at a higher temperature.

Lines 468-473 sum the heat leaks lumped at the engine inlets due to radiation and axial conduction. Line 475 calculates the total radiation heat leak to be used in a later calculation of the total entropy generation.

The entropy generation in the helium gas is next calculated in each heat exchanger using real gas properties from the NBS programs. In heat exchangers 3, 4, and 5, ideal gas equations are also used to compute the entropy generation so that the individual contributions of temperature changes and pressure drops to the total entropy generation may be compared. Lines 517-522 compute the properties to be used in the real gas entropy computations. Lines 525-527 compute the entropy generation in each heat exchanger, where i refers to the heat exchanger number. Lines 529-538 compute the entropy generation using ideal gas relationships. Lines 532-533 compute the entropy generation due to irreversible temperature changes; lines 534-535 compute the entropy generation due to irreversible pressure changes; and, line 537 is sum of the two.

The final computation in SYSLEAK is that of total entropy generation in the cryocooler components operating below 300 K. The expression on line 545 is for a control volume that encloses the entire cryocooler.

Table (A.3) SVC cycle considered in Section A.2

Parameter	Value
Refrigeration load	1 W
Refrigeration temperature	4.2 K
High pressure	40 atm
Low pressure	4 atm
$\Delta T / T$	0.05
Wet expander efficiency	0.80
Vapor compressor efficiency	0.80
Dry expander efficiencies	0.75

A.2 Results From Computer Analysis

In this section, computer results given in Section 2.4.1 of Chapter 2 will be developed in more detail. The results given here pertain to optimal selections of the dry expander inlet temperatures and the sensitivity of cycle performance to variations in engine efficiencies. The trends to be observed in this section are not dependent on the specific components chosen for the cryocooler and are generally valid for any cryocooler using the SVC cycle. The inputs needed for this analysis are listed in Table (A.3). The cycle configuration is shown in Figure (A.1). The heat inputs before the engines are all set equal to zero. The only irreversibilities included in the following results are those due to heat exchange temperature difference and due to engine inefficiency. Including the heat inputs before the engines and the irreversibilities not considered here does not affect the trends of the results.

Figure (A.2) is a plot of mass flow rate at the warm compressor versus the temperature at the inlet to the warmer dry expander for several values of inlet temperature to the colder dry expander. This plot is illustrative of the type of iteration required to determine the optimal dry expander inlet temperatures. As indicated by the figure, the mass flow rate at the warm compressor is more sensitive to changes in the inlet temperature to the warmer dry expander than to the cooler one. The reason for this trend is that the capacity flow rates are more nearly matched at the warmer temperatures without the use of any dry expander. All of

the data points for the theoretical trends reported in Chapter 2 were based these optimal expander inlet temperatures.

Individual variations in the isentropic efficiency of the wet expander, vapor compressor, or dry expanders result in varying magnitudes of effect on the warm compressor mass flow rate. Each data point in the following results was obtained for optimally placed dry expander inlet temperatures. Figures (A.3) and (A.4) are plots of flow rate versus wet expander efficiency and vapor compressor efficiency, respectfully. In both cases only the efficiency under investigation was varied. These plots indicate that variations in the wet expander efficiency effect the flow rate more significantly than the vapor compressor.

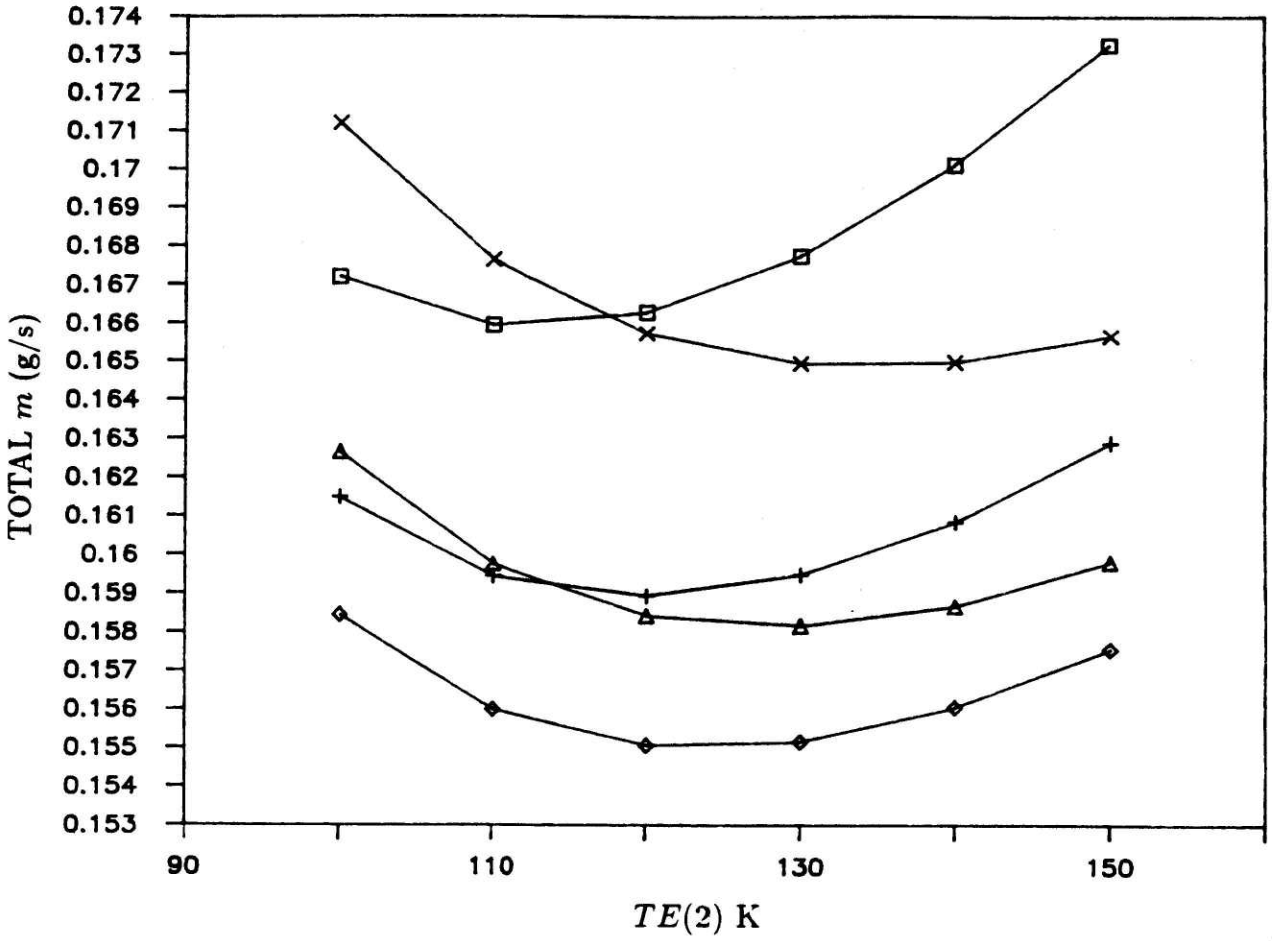

Fig. (A.2) Mass flow rate at the warm compressor versus dry expander #2 inlet temperature.

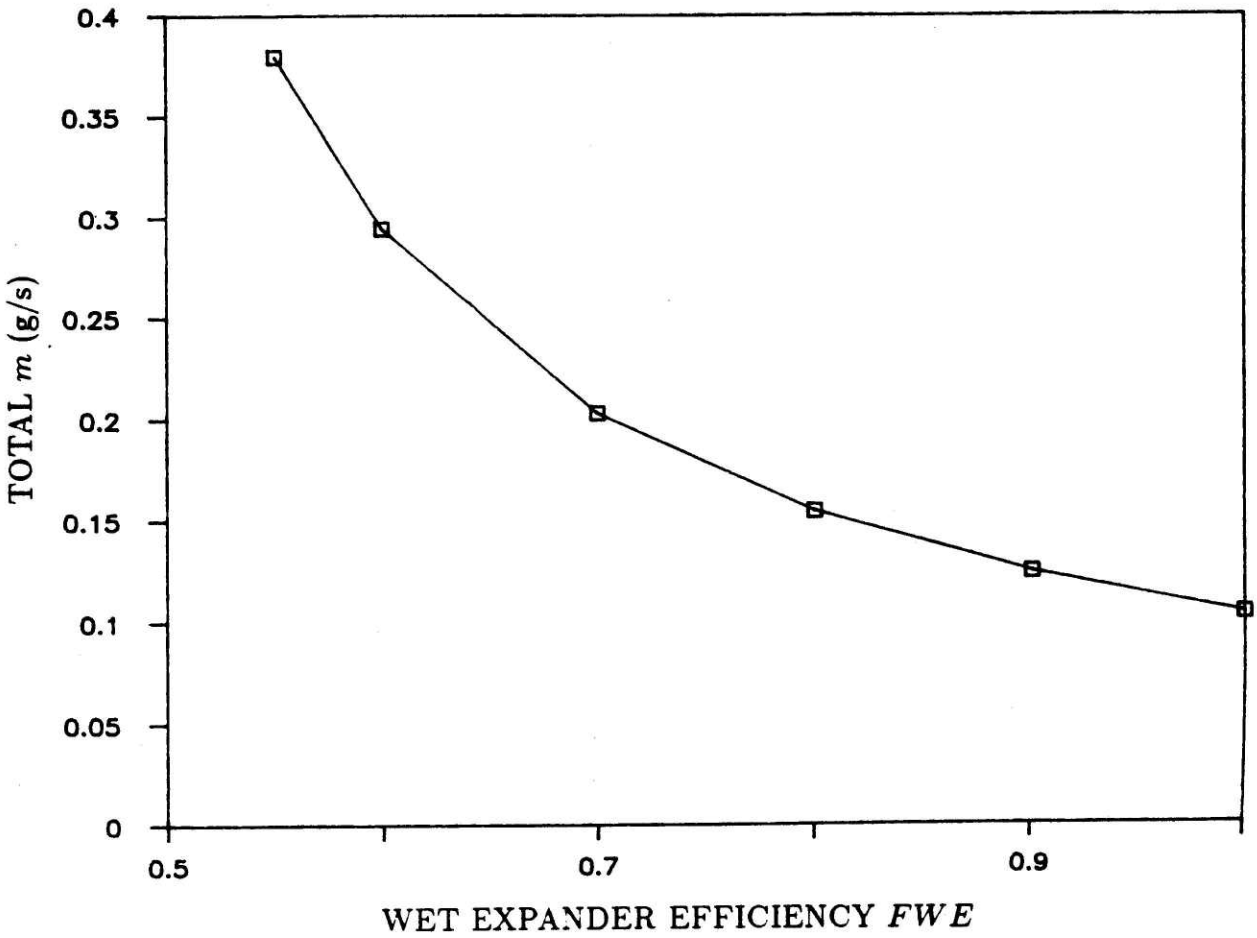

Fig. (A.3) Mass flow rate at the warm compressor versus the adiabatic engine efficiency for the wet expander.

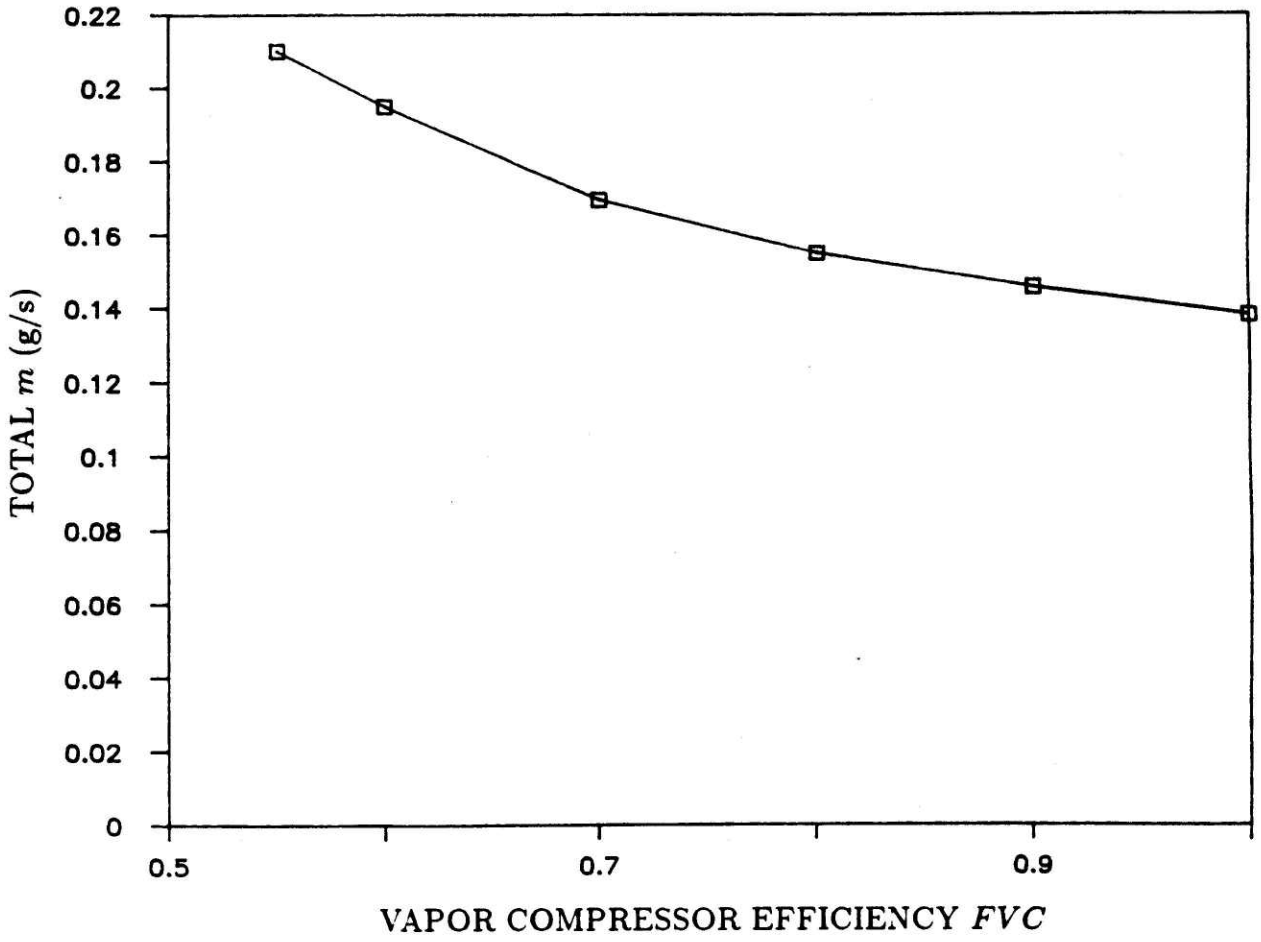

Fig. (A.4) Mass flow rate at the warm compressor versus the adiabatic efficiency for the vapor compressor.

Exhibit (A.1) Computer programs for system analysis.

```
0001    c************************** PROGRAM SYSITER *****************
0002    c
0003          program sysiter
0004    c
0005    c  This program is used to compute the thermodynamic state
0006    c  properties, mass flow rates, and entropy generation for
0007    c  SVC cycle and Collins cycle cryocoolers.  A subprogram
0008    c  computes physical dimensions of the cryocooler and the
0009    c  corresponding heat leaks based on these dimensions.
0010    c
0011    c  A subprogram named PINCH is used to locate the pinch
0012    c  points in the coldest heat exchanger.  Several
0013    c  subroutines are used to compute the properties of helium.
0014    c  Most of the subroutines were obtained from the National
0015    c  Bureau of Standards.  The subroutines used to compute
0016    c  helium properties which were not obtained from NBS include
0017    c  CALCUP and CALCPS.  The subprogram used to compute the
0018    c  dimensions of the heat exchangers, dry expanders, wet
0019    c  expander, and cold compressor is called SYSLEAK.
0020    c
0021    c  The program first reads the type of cryocooler to be
0022    c  analysed, the specified dimensions such as tube diameter,
0023    c  the operating load and temperature or pressure, and the
0024    c  component efficiencies.  Values which remain constant
0025    c  throughout the program are next computed.  The program then
0026    c  asks the user to input the values of expander inlet temp-
0027    c  erature to be used as the first iteration.  All output
0028    c  parameters are then computed.  The program returns to
0029    c  the read statement to ask the user for new expander inlet
0030    c  temperatures.  Note that a single set of expander inlet
0031    c  temperatures should be inputed approximately three times
0032    c  to obtain correct results.  This is because the outputs
0033    c  from each run through the program are the inputs to the
0034    c  next run.
0035    c
0036    c
0037    c  DICTIONARY
0038    c
0039    c  TE(i)    -inlet temperature to the dry expansion engines
0040    c
0041    c  QE(i)    -lumped heat leak added to the high pressure
0042    c            stream just before the dry expansion engine
0043    c
0044    c  DE(i)    -density of the high pressure stream at the
0045    c            inlet to the dry expansion engine
0046    c
0047    c  HE(i)    -enthalpy of the high pressure stream at the
0048    c            inlet to the dry expansion engine
0049    c
0050    c  SE(i)    -entropy of the high pressure stream at the
0051    c            inlet to the dry expansion engine
0052    c
0053    c  TH(i)    -temperature of the high pressure stream at
```

```
0054     c            the i state point
0055     c
0056     c  TQ       -temperature of the high pressure stream before
0057     c            a lumped heat leak is added before the gas
0058     c            is expanded to liquid helium temperature
0059     c
0060     c  TWEIN    -temperature of the high pressure stream after
0061     c            a lumped heat leak is added before the gas is
0062     c            expanded to liquid helium temperature
0063     c
0064     c  TL(i)    -temperature of the low pressure stream at the
0065     c            i state point
0066     c
0067     c  TC       -temperature of the low pressure stream exiting
0068     c            the refrigeration zone.  If a cold compressor
0069     c            is used, then this temperature is that of the
0070     c            gas exiting the cold compressor.
0071     c
0072     c  M(i)     -mass flow rate in the low pressure side which
0073     c            corresponds to the section in the exchanger
0074     c            stack operating the temperature of dry
0075     c            expander # i
0076     c
0077     c  ME(i)    -mass flow rate through dry expander # i
0078     c
0079     c  MR       -mass flow rate through the refrigeration zone
0080     c
0081     c  FE(i)    -adiabatic efficiency of dry expander # i
0082     c
0083     c  FVC      -adiabatic efficiency of the vapor compressor
0084     c
0085     c  FWE      -adiabatic efficiency of the wet expander
0086     c
0087     c  PH(i)    -high pressure at state point i
0088     c
0089     c  PQ       -pressure before expansion to refrigeration zone
0090     c
0091     c  PL(i)    -low pressure at state point i
0092     c
0093     c  PC       -pressure exiting the refrigeration zone.  If a
0094     c            cold compressor is used, then this is the pressure
0095     c            at the exit from the cold compressor
0096     c
0097     c  QR       -refrigeration load
0098     c
0099     c  TR       -refrigeration temperature
0100     c
0101     c  PR       -refrigeration pressure;  note that only TR or PR
0102     c            must be read, with the other value being input
0103     c            as zero
0104     c
0105     c  QW       -the heat leak before expansion to TR
0106     c
0107     c  QRL      -the heat leak to the refrigeration zone
```

```
0108     c
0109     c  DTPIN    -the temperature ratio delta T/T
0110     c
0111     c  NN       -the number of dry expansion engines
0112     c
0113     c  N        -twice the number of dry expansion engines
0114     c
0115     c  CO,SI    -cosine and sine of the heat exchanger tube helix
0116     c            angle
0117     c
0118     c  IEXP     -the number of wet expanders; 0 or 1
0119     c
0120     c  ICOMP    -the number of vapor compressors; 0 or 1
0121     c
0122     c  In general, variables of entropy, enthalpy, and density
0123     c  will begin with S, H, and D, respectively.  Variables of
0124     c  entropy generation will begin with SGEN.
0125     c
0126     c
0127     c
0128           dimension te(12),qe(11),de(12),he(12),se(12),
0129          &hh(12),hl(12),th(12),tl(12),m(12),me(12),
0130          &fe(11),ph(11),pl(11),delsexp(12),sgendex(12)
0131           real m,me,mv,ml,mr,mrqw,mtol
0132           common thin,tq,tc,tlout,pq,pc,dtpin,icomp,hg,
0133          &ph,pl,qe,qw,qrl,
0134          &nn,iexp,rpm,r,zh,zl,ang,tcan,e,
0135          &tpis,tcyl,tshell,
0136          &qr,tr,pr,fwe,fvc,fe,
0137          &mr,me,th,tl,te,co,si
0138           read(7,1000)ph,pq,pl,pc,qe,qw,qrl
0139           read(8,2000)nn,iexp,icomp,rpm,r,zh,zl,tpis,tcyl,tshell,
0140          &ang,tcan,e
0141           read(9,3000)qr,tr,pr,dtpin,fwe,fvc,fe
0142     c
0143      1000 format(11f6.2/f6.2/11f6.2/f6.2/11f6.3/f10.6/f10.6)
0144      2000 format(i2/i2/i2/f6.1/f4.2/f6.4/f6.4/f6.4/f6.4/f6.4
0145          &/f4.1/f6.2/f5.3)
0146      3000 format(f8.2/f8.2/f8.2/f7.5/f6.4/f6.4/11f5.3)
0147           to=300.
0148     c
0149           n=nn*2
0150     c
0151     c  Find the saturation properties of helium
0152     c  at the refrigeration T or P.
0153           if(tr.eq.0.)go to 101
0154           pr=vpn(tr)
0155           go to 102
0156       101 tr=vptemp(pr)
0157       102 drl=dsatl(tr)*4.0026/1000.
0158           drv=dsatv(tr)*4.0026/1000.
0159           hf=enthal(drl*1000.,tr)/1000.
0160           hg=enthal(drv*1000.,tr)/1000.
0161           sf=entrop(drl*1000./4.0026,tr)/4.0026
```

```
0162          sg=entrop(drv*1000./4.0026,tr)/4.0026
0163          hfg=hg-hf
0164          sfg=sg-sf
0165    c
0166    c  Find the properties at the exit from the
0167    c  cold compressor or the refrigeration zone.
0168          if(icomp.eq.0)go to 111
0169          d=.03146
0170          tc=8.
0171          call calcps(pc,sg,d,tc)
0172          hcs=enthal(d*1000.,tc)/1000.
0173          hc=(hcs-hg)/fvc+hg
0174          dc=dph(pc,hc*4.0026)*4.0026/1000.
0175          uc=hc-.101325*pc/dc
0176    c The output of calcup will be the actual value of tc
0177          call calcup(uc,pc,dc,tc)
0178          sc=entrop(dc*1000./4.0026,tc)/4.0026
0179          delscom=sc-sg
0180          go to 112
0181        111 tc=tr
0182          hc=hg
0183    c  Read the inlet temperatures to expanders 1 & 2
0184        112 print *,'Input TE(1) and TE(2):'
0185          read(5,*)te(1),te(2)
0186          if(te(1).eq.0.)stop
0187    c Find outlet state of all expanders
0188          do 2 i=2,n,2
0189          j=i/2
0190          de(j)=denf(ph(j)*101325.,te(j))
0191          he(j)=enthal(de(j),te(j))/1000.
0192          se(j)=entrop(de(j)/4.0026,te(j))/4.0026
0193    c Initial estimates of tout and dout
0194          tt=te(j)/2.
0195          dd=denf(pl(i-1)*101325.,tt)/1000.
0196          call calcps(pl(i-1),se(j),dd,tt)
0197          hos=enthal(dd*1000.,tt)/1000.
0198          hl(i-1)=he(j)-fe(j)*(he(j)-hos)
0199          do=dph(pl(i-1),hl(i-1)*4.0026)*4.0026/1000.
0200          uo=hl(i-1)-.101325*pl(i-1)/do
0201          tl(i-1)=tt
0202          call calcup(uo,pl(i-1),do,tl(i-1))
0203          so=entrop(do*1000./4.0026,tl(i-1))/4.0026
0204          delsexp(j)=so-se(j)
0205        2 continue
0206    c Find the high pressure side temperatures at the expander
0207    c outlet state assuming these to be pinch points
0208          th(n+1)=to
0209          tl(n+1)=th(n+1)/(1.+dtpin)
0210          do 3 i=1,n+1,2
0211          th(i)=(1.0+dtpin)*tl(i)
0212          dh=denf(ph(i)*101325.,th(i))
0213        3 hh(i)=enthal(dh,th(i))/1000.
0214    c Check whether a heat exchanger is needed between the coldest
0215    c expansion engine and the wet expander
```

```
0216          dtmax=0.2
0217          if((tl(1)-tc).lt.dtmax) go to 4
0218          hq=hh(1)+hc-hl(1)
0219          go to 5
0220        4 hq=hh(1)
0221        5 dq=dph(pq,hq*4.0026)*4.0026/1000.
0222          uq=hq-.101325*pq/dq
0223          tq=tc
0224          call calcup(uq,pq,dq,tq)
0225          thin=th(1)
0226          tlout=tl(1)
0227          call pinch(tlpin)
0228          xx=.05
0229          if(abs((tlpin-tl(1))/tl(1)).lt.xx)go to 262
0230          thpin=(1.+dtpin)*tlpin
0231          if(abs(tlpin-tc).gt.xx)go to 260
0232          dhpin=denf(pq*101325.,thpin)
0233          hhpin=enthal(dhpin,thpin)/1000.
0234          hq=hhpin
0235          hh(1)=hhpin+hl(1)-hc
0236          tq=thpin
0237          dhh1=dph(ph(1),hh(1)*4.0026)*4.0026/1000.
0238          uhh1=hh(1)-.101325*ph(1)/dhh1
0239          call calcup(uhh1,ph(1),dhh1,th(1))
0240          thin=th(1)
0241          go to 261
0242      260 pal=(pc+pl(1))/2.
0243          pah=(pq+ph(1))/2.
0244          dlpin=denf(pal*101325.,tlpin)
0245          dhpin=denf(pah*101325.,thpin)
0246          hlpin=enthal(dlpin,tlpin)/1000.
0247          hhpin=enthal(dhpin,thpin)/1000.
0248    c
0249          hh(1)=hhpin+hl(1)-hlpin
0250          hq=hc+hhpin-hlpin
0251          dhh1=dph(ph(1),hh(1)*4.0026)*4.0026/1000.
0252          dq=dph(pq,hq*4.0026)*4.0026/1000.
0253          uhh1=hh(1)-.101325*ph(1)/dhh1
0254          uq=hq-.101325*pq/dq
0255          call calcup(uhh1,ph(1),dhh1,th(1))
0256          call calcup(uq,pq,dq,tq)
0257          thin=th(1)
0258      261 call pinch(tlpin)
0259      262 if(iexp.eq.0)go to 77
0260    c Iterate to find the mass flow rate through the wet expander
0261    c required to sustain the required load.  Start the iteration
0262    c with the flowrate obtained when qw=0.
0263          ml=(qr+qrl)/hfg
0264          ss=saph(pq*101325.,hq*1000.)/1000.
0265          xs=(ss-sf)/sfg
0266          hs=hf+xs*hfg
0267          h=hq-fwe*(hq-hs)
0268          x=(h-hf)/hfg
0269          mv=x*ml/(1.-x)
```

```
0270          mr=ml+mv
0271          if(qw.eq.0.) go to 10
0272      c Start iteration
0273          mtol=.005
0274        6 mrqw=mr
0275          hhi=hq+qw/mrqw
0276          sh=saph(pq*101325.,hhi*1000.)/1000.
0277          xs=(sh-sf)/sfg
0278          hrs=hf+xs*hfg
0279          hr=hhi-fwe*(hhi-hrs)
0280          if(hr.ge.hg)go to 7
0281          x=(hr-hf)/hfg
0282          mv=x*ml/(1.-x)
0283          mr=ml+mv
0284          if(abs(mrqw-mr)/mr.le.mtol)go to 91
0285          go to 6
0286      c  Start iteration for J-T valve using QW=0.
0287       77 ml=(qr+qrl)/hfg
0288          if(hq.ge.hg)go to 7
0289          x=(hq-hf)/hfg
0290          mv=x*ml/(1.-x)
0291          mr=ml+mv
0292          if(qw.eq.0.)go to 10
0293      c  Add QW and iterate.
0294       66 mrqw=mr
0295          hhi=hq+qw/mrqw
0296          if(hhi.ge.hg)go to 7
0297          x=(hhi-hf)/hfg
0298          mv=x*ml/(1.-x)
0299          mr=ml+mv
0300          mtol=.0001
0301          if(abs(mrqw-mr)/mr.le.mtol)go to 9
0302          go to 66
0303        7 write(6,8)
0304        8 format(1h1,'no liquid helium produced using this cycle')
0305          go to 112
0306       91 sgencom=mr*delscom
0307          sr=x*sfg+sf
0308          sgenwex=mr*(sr-sh)
0309        9 dh=dph(pq,hhi*4.0026)*4.0026/1000.
0310          uh=hhi-.101325*pq/dh
0311          twein=tc
0312          call calcup(uh,ph,dh,twein)
0313          go to 11
0314       10 twein=tq
0315      c Find the enthalpys at the exit from the warm compressor and
0316      c on the corresponding low pressure side
0317       11 tol=to/(dtpin+1.)
0318          doh=denf(ph(n+1)*101325.,to)
0319          dol=denf(pl(n+1)*101325.,tol)
0320          hh(n+1)=enthal(doh,to)/1000.
0321          hl(n+1)=enthal(dol,tol)/1000.
0322          th(n+1)=to
0323          tl(n+1)=tol
```

```
0324    c Starting at the cold end, first calculate the mass flow
0325    c through each expansion engine and then find properties
0326    c before the heat input.
0327          m(1)=mr
0328          do 100 i=2,n,2
0329          j=i/2
0330          aaa=hh(i+1)-hl(i+1)+hl(i-1)
0331          me(j)=-(m(j)*(aaa-hh(i-1))+qe(j))/(aaa-he(j))
0332          hh(i)=he(j)-qe(j)/me(j)
0333          hl(i)=hh(i)+hl(i+1)-hh(i+1)
0334          m(j+1)=m(j)+me(j)
0335          dh=dph(ph(i),hh(i)*4.0026)*4.0026/1000.
0336          uh=hh(i)-.101325*ph(i)/dh
0337    c initial estimate of th(i)
0338          th(i)=te(j)
0339          call calcup(uh,ph(i),dh,th(i))
0340          dl=dph(pl(i),hl(i)*4.0026)*4.0026/1000.
0341          ul=hl(i)-.101325*pl(i)/dl
0342    c initial estimate of tl(i)
0343          tl(i)=th(i)
0344          call calcup(ul,pl(i),dl,tl(i))
0345    c
0346    c  Find the entropy generated in each dry expander:
0347          sgendex(j)=me(j)*delsexp(j)
0348      100 continue
0349          l=n/2
0350          write(6,400)te(1),te(2)
0351      400 format(//4x,'TE(1)=',f5.1,'K'/
0352         &4x,'TE(2)=',f5.1,'K')
0353          write(6,500)mr
0354      500 format(4x,'mr=',f8.5,'gm/sec')
0355          do 610 i=1,nn
0356          write(6,600)i,me(i)
0357      600 format(' ',3x,'me(',i1,')=',f8.5,'gm/sec')
0358      610 continue
0359          write(6,700)m(l+1)
0360      700 format(' ',3x,'mcomp=',f8.5,'gm/sec'//)
0361    c
0362          write(6,800)sgenwex,sgencom
0363      800 format(3x,'sgenwex=',f7.5,'W/K'/
0364         &       3x,'sgencom=',f7.5,'W/K')
0365    c
0366          do 901 i=1,nn
0367          write(6,900)i,sgendex(i)
0368      900 format(3x,'sgendryexp(',i1,')=',f7.5,'W/K')
0369      901 continue
0370    c
0371          write(6,902)
0372      902 format(/)
0373    c  Open a new file and store the outputs of this program to be
0374    c  used in SYSLEAK, if SYSLEAK is not a subprogram.
0375    c
0376          open (unit=10,file='out.dat',status='new')
0377          write(10,999)mr,me,th,tl,tc,tq,te
```

```
0378       999 format(f8.5/12f8.5/12f6.2/12f6.2/f6.2/f6.2/12f6.2)
0379     c
0380           call sysleak
0381           go to 112
0382           end
```

```
0001    c************************* PROGRAM SYSLEAK ********************
0002    c
0003    c
0004          subroutine sysleak
0005    c
0006    c
0007    c  This subprogram designs the internal components of the system
0008    c  specified by SYSITER.  The components designed include the
0009    c  dry expansion engines, vapor compressor, wet expander, and
0010    c  heat exchangers.  Also computed are the heat leaks due to
0011    c  axial conduction and radiation.  These heat leaks are added
0012    c  to obtain the lumped heat leak to be added before their
0013    c  respective engine.
0014    c
0015    c  DICTIONARY:
0016    c
0017    c  Many of the same variables used in SYSITER are again used here.
0018    c  Thus, only the new variables will be defined. Note that many
0019    c  of the variables defined below are necessary to renumber the
0020    c  state points for easy bookkeeping throughout the program.
0021    c  Also, in this program variables beginning with SG are used
0022    c  to designate entropy generation(e.g., SGGAST is the entropy
0023    c  generation in the gas due to temperature changes).
0024    c  The heat exchangers are numbered from 1 to n+1, where
0025    c  1 refers to the coldest heat exchanger located between
0026    c  the refrigeration zone and the exit from the coldest
0027    c  dry expansion engine.
0028    c
0029    c  MEH(i)  -mass flow rate on the high pressure side through
0030    c           heat exchanger i
0031    c
0032    c  MEL(i)  -mass flow rate on the low pressure side through
0033    c           heat exchanger i
0034    c
0035    c  TEH(i)  -temperature on the high pressure side at state point i
0036    c
0037    c  TEL(i)  -temperature on the low pressure side at state point i
0038    c
0039    c  PEH(i)  -pressure on the high pressure side at state point i
0040    c
0041    c  PEL(i)  -pressure on the low pressure side at state point i
0042    c
0043    c  VH(i)   -viscosity of the gas at high-side state point i
0044    c
0045    c  VL(i)   -viscosity of the gas at low-side state point i
0046    c
0047    c  KH(i)   -gas thermal conductivity at high-side state point i
0048    c
0049    c  KL(i)   -gas thermal conductivity at low-side state point i
0050    c
0051    c  CPL(i)  -gas specific heat at constant pressure at low-side
0052    c           state point i
0053    c
```

```
0054     c  PRL(i)  -Prandtl number at low-side state point i
0055     c
0056     c  Hhp     -convective heat transfer coefficient on the H-P side
0057     c
0058     c  Hlp     -convective heat transfer coefficient on the L-P side
0059     c
0060     c  REH     -Reynolds number on the high-pressure side
0061     c
0062     c  REL     -Reynolds number on the low-pressure side
0063     c
0064     c  L(i)    -length of heat exchanger i
0065     c
0066     c  LTOT    -total heat exchanger length
0067     c
0068     c  ATOT    -total heat exchanger area
0069     c
0070     c  B(i)    -bore of dry expander i
0071     c
0072     c  tpis    -wall thickness for piston
0073     c
0074     c  tcyl    -wall thickness for cylinder
0075     c
0076     c  tshl    -wall thickness for outer shell
0077     c
0078     c  zh      -width of high-pressure gap
0079     c
0080     c  zl      -width of low-pressure gap
0081     c
0082     c  Dp      -outer diameter of piston
0083     c
0084     c  Dci     -inner diameter of cylinder
0085     c
0086     c  Dco     -outer diameter of cylinder
0087     c
0088     c  Dsi     -inner diameter of shell
0089     c
0090     c  Dso     -outer diameter of shell
0091     c
0092     c  DIAh    -mean diameter of high-pressure radial gap
0093     c
0094     c  DIAl    -mean diameter of low-pressure radial gap
0095     c
0096     c  ANG     -helix angle for the spiral spacer
0097     c
0098     c  Tcan    -temperature of the vacuum jacket
0099     c
0100     c  e       -emissivity of all surfaces
0101     c
0102     c  DelPL(i)-low-pressure side pressure drop over heat exchanger i
0103     c
0104     c  DelPH(i)-high-pressure side pressure drop over heat exchanger i
0105     c
0106           dimension me(12),th(12),tl(12),teh(12),tel(12),te(12),
0107          &meh(12),mel(12),hin(12),hout(12),kh(12),kl(12),the(12),
```

```
0108          &vh(12),vl(12),cpl(12),prl(12),l(12),b(12),s(12),fe(11)
0109           dimension dhe(12),ahe(12),qer(12),qc(12),qcc(12),qec(12),
0110          &ph(11),pl(11),pel(12),peh(12),dh(12),dl(12),
0111          &sh(12),sl(12),sggas(12),sggast(12),sggasp(12),sgpgas(12)
0112           dimension dp(12),dci(12),dco(12),dsi(12),dso(12),dial(12),
0113          &diah(12),reh(12),rel(12),ac(12),delpl(12),delph(12),qe(11)
0114           real me,mr,meh,mel,kh,kl,l,nu,ltot,ln,mexp
0115           common thin,tq,tc,tlout,pq,pc,dtpin,icomp,hg,
0116          &ph,pl,qe,qw,qrl,
0117          &nn,iexp,rpm,r,zh,zl,ang,tcan,e,
0118          &tpis,tcyl,tshell,
0119          &qr,tr,pr,fwe,fvc,fe,
0120          &mr,me,th,tl,te,co,si
0121           pi=3.14159
0122           co=cos(ang*pi/180.)
0123           si=sin(ang*pi/180.)
0124           n=nn*2
0125      c
0126      c  Size the dry expansion engines
0127           do 2 i=2,n,2
0128           j=i/2
0129           mexp=(me(j)/rpm)*60.
0130           den=denf(pl(j)*101325.,tl(j))
0131           b(j)=(((4.*r*mexp)/(den*pi))**(1./3.))*(10./2.54)
0132           s(j)=b(j)/r
0133           write(6,27)j,b(j)
0134       27  format(3x,'BORE(',i1,')=',f6.3,' in')
0135           dp(j)=b(j)-2.*zh
0136           dci(j)=b(j)
0137           diah(j)=(dp(j)+dci(j))/2.
0138           dco(j)=dci(j)+2*tcyl
0139           dsi(j)=dco(j)+2*zl
0140           dial(j)=(dco(j)+dsi(j))/2.
0141           dso(j)=dsi(j)+2*tshell
0142        2  continue
0143           write(6,28)
0144       28  format(/)
0145      c
0146      c  Change the numbering of the diameters to match the heat
0147      c  exchangers. Note that all of these diameters are not
0148      c  used in this version of SYSLEAK.
0149      c
0150           b1=b(1)
0151           b2=b(2)
0152           b(2)=b1
0153           b(3)=b1
0154           b(4)=b2
0155           b(5)=b2
0156      c
0157           dp1=dp(1)
0158           dp2=dp(2)
0159           dp(2)=dp1
0160           dp(3)=dp1
0161           dp(4)=dp2
```

```
0162            dp(5)=dp2
0163      c
0164            dci1=dci(1)
0165            dci2=dci(2)
0166            dci(2)=dci1
0167            dci(3)=dci1
0168            dci(4)=dci2
0169            dci(5)=dci2
0170      c
0171            write(6,687)dci(1),dci(4)
0172        687 format(3x,'DCI(1)=',f6.3,'in'/3x,'DCI(4)=',f6.3,'in')
0173      c
0174            dco1=dco(1)
0175            dco2=dco(2)
0176            dco(2)=dco1
0177            dco(3)=dco1
0178            dco(4)=dco2
0179            dco(5)=dco2
0180      c
0181            dsi1=dsi(1)
0182            dsi2=dsi(2)
0183            dsi(2)=dsi1
0184            dsi(3)=dsi1
0185            dsi(4)=dsi2
0186            dsi(5)=dsi2
0187      c
0188            dso1=dso(1)
0189            dso2=dso(2)
0190            dso(2)=dso1
0191            dso(3)=dso1
0192            dso(4)=dso2
0193            dso(5)=dso2
0194      c
0195            diah1=diah(1)
0196            diah2=diah(2)
0197            diah(2)=diah1
0198            diah(3)=diah1
0199            diah(4)=diah2
0200            diah(5)=diah2
0201      c
0202            dial1=dial(1)
0203            dial2=dial(2)
0204            dial(2)=dial1
0205            dial(3)=dial1
0206            dial(4)=dial2
0207            dial(5)=dial2
0208      c
0209      c  Change the state point numbering to reduce programing steps
0210            te1(1)=tc
0211            pe1(1)=pc
0212            teh(1)=tq
0213            peh(1)=pq
0214            do 3 i=1,n+1
0215            te1(i+1)=t1(i)
```

```
0216          pel(i+1)=pl(i)
0217          teh(i+1)=th(i)
0218          peh(i+1)=ph(i)
0219        3 continue
0220    c
0221    c
0222    c  Find the mass flow rate for the high-side and low-side
0223    c  for each heat exchanger
0224          meh(1)=mr
0225          mel(1)=mr
0226          do 4 i=2,n,2
0227          j=i/2
0228          meh(i)=meh(i-1)
0229          mel(i)=mel(i-1)+me(j)
0230          meh(i+1)=mel(i)
0231          mel(i+1)=mel(i)
0232        4 continue
0233    c
0234    c
0235    c  Find the helium properties required for heat exchanger
0236    c  dimensioning.  First define the symbols:
0237    c       KH,KL=thermal conductivity of high-side and low-side
0238    c       VH,VL=viscosity on high-side and low-side
0239    c       CPL=specific heat on low-side
0240    c       HIN,HOUT=enthalpy in and out on high-side
0241    c
0242    c  First compute the enthalpies. Note that "i" in the DO statement
0243    c  refers to the newly defined state points.
0244          dout=denf(101325.*peh(1),teh(1))
0245          hout(1)=enthal(dout,teh(1))/1000.
0246          do 5 i=2,n+2
0247          din=denf(101325.*peh(i),teh(i))
0248          hin(i-1)=enthal(din,teh(i))/1000.
0249          hout(i)=hin(i-1)
0250        5 continue
0251    c
0252    c
0253    c  Calculate the remainder of properties using the average
0254    c  temperature of the high-side and low-side for each exchanger.
0255    c  Here the "i" in the DO statement refers to the exchanger.
0256          do 6 i=1,n+1
0257          thh=(teh(i)+teh(i+1))/2.
0258          phh=(peh(i)+peh(i+1))/2.
0259          tll=(tel(i)+tel(i+1))/2.
0260          pll=(pel(i)+pel(i+1))/2.
0261          dh(i)=denf(101325.*phh,thh)/4.0026
0262          dl(i)=denf(101325.*pll,tll)/4.0026
0263          kh(i)=condt(dh(i),thh)
0264          kl(i)=condt(dl(i),tll)
0265          vh(i)=viscdt(dh(i),thh)
0266          vl(i)=viscdt(dl(i),tll)
0267          cpl(i)=cp(dl(i),tll)
0268          prl(i)=(cpl(i)*vl(i))/(kl(i)*4.0026)
0269        6 continue
```

```
0270     c
0271     c
0272     c  Next calculate the heat transfer coefficients for the heat
0273     c  exchanger on the high- and low-pressure sides.  Then use
0274     c  this information to place dimensions on the exchanger.
0275     c  On the low-pressure side, turbulent flow conditions are
0276     c  likely.  For this reason, the low-pressure side Reynolds
0277     c  number is computed so that the appropriate equations will
0278     c  be used to compute the coefficient of heat transfer and
0279     c  the pressure drop.
0280           nu=8.23
0281           do 7 i=1,n+1
0282     c
0283           reh(i)=(2.*meh(i))/(pi*2.54*diah(i)*vh(i))
0284           rel(i)=(2.*mel(i))/(pi*2.54*dial(i)*vl(i)*co)
0285     .c
0286           hhp=(nu*kh(i)/zh)*((2.54*144.)/(0.293*1.8))
0287     c
0288           if(rel(i).ge.2000)go to 10
0289     c
0290           hlp=(nu*kl(i)/zl)*((2.54*144.)/(0.293*1.8))
0291           go to 69
0292     c
0293        10 hlp=((kl(i)/(2.*zl))*(1.+3.5*(2.*zl/dial(i)))
0294          &*0.75*0.023*rel(i)**0.8*prl(i)**0.4)*
0295          &((2.54*144.)/(0.293*1.8))
0296     c
0297        69 write(6,25)i,hhp,i,hlp
0298        25 format(3x,'hhp(',i2,')=',f5.0,'Btu/hr-ft2-F',10x,
0299          &'hlp(',i2,')=',f5.0,'Btu/hr-ft2-F')
0300     c
0301     c  Next combine equations for UA and solve for the length
0302     c  of the exchanger.
0303     c
0304           dta=teh(i+1)-tel(i+1)
0305           dtb=teh(i)-tel(i)
0306           delh=hin(i)-hout(i)
0307           uconv=1./(1./hhp+1./hlp)
0308           ln=alog(dta/dtb)
0309           l(i)=((meh(i)*delh*ln)/(uconv*pi*dci(i)*
0310          &(dta-dtb)))*(144./(1.8*0.293))
0311     c
0312           if(rel(i).ge.2000.)go to 29
0313     c
0314           delpl(i)=((12.*vl(i)*l(i)*mel(i))/
0315          &(co**2*zl**3*dl(i)*pi*dial(i)))*
0316          &(1000./(4.0026*453.6*32.2*12.*2.54**2*14.7))
0317           go to 26
0318     c
0319        29 delpl(i)=((0.046*mel(i)**2*l(i))
0320          &/(rel(i)**0.2*dl(i)*zl**3*pi**2*dial(i)**2*co**3))
0321          &*(1000./(2.54**3*4.0026*453.6*32.2*12.*14.7))
0322     c
0323        26 delph(i)=((12.*l(i)*vh(i)*mel(i))/
```

```
0324          &(zh**3*dh(i)*pi*diah(i)))*
0325          &(1000./(4.0026*453.6*32.2*12.*2.54**2*14.7))
0326     c
0327          7 continue
0328     c
0329     c  Compute the absolute pressure at each state point.
0330             do 15 i=2,n+2
0331             pel(i)=pel(i-1)-delpl(i-1)
0332          15 continue
0333             pc=pel(1)
0334             do 16 i=2,n+2
0335             pl(i)=pel(i+1)
0336          16 continue
0337     c
0338             ph(n+1)=peh(n+2)
0339             j=-1
0340          17 j=j+1
0341             i=n-j
0342             ph(i)=ph(i+1)-delph(i+1)
0343             if(i.eq.1)go to 20
0344             go to 17
0345          20 pq=ph(1)-delph(1)
0346     c
0347             write(6,28)
0348     c  Write the lengths and the Reynolds numbers.
0349             do 9 i=1,n+1
0350             write(6,8)i,l(i),reh(i),rel(i)
0351           8 format(3x,'L(',i1,')=',f5.2,'in',5x,'Re(hi-pres)=',f6.0,5x,
0352            &'Re(lo-pres)=',f6.0)
0353           9 continue
0354             ltot=0.
0355             do 13 i=1,n+1
0356             ltot=ltot+l(i)
0357          13 continue
0358             write(6,12)ltot
0359          12 format(3x'LTOTAL=',f5.1,'in'/)
0360     c
0361     c  Determine and write the total area for heat exchange.
0362     c
0363             atot=0.
0364             do 14 i=1,n+1
0365             atot=atot+pi*dci(i)*l(i)
0366          14 continue
0367     c
0368             write(6,21)atot
0369          21 format(3x,'ATOTAL=',f5.1,'square inches'/)
0370     c
0371             write(6,22)pq,pc
0372          22 format(3x,'pq=',f9.5,'atm'/3x,'pc=',f9.5,'atm')
0373             do 18 i=1,n+1
0374             write(6,19)i,ph(i),i,pl(i)
0375       19 format(3x,'ph(',i2,')=',f9.5,'atm'/3x,'pl(',i2,')=',f9.5,'atm')
0376          18 continue
0377     c
```

```
0378     c  The above results will now be used to calculate the heat leak
0379     c  to be removed before each dry expander.
0380     c
0381     c  Determine the heat exchanger container area exposed to
0382     c  radiation heat leak.
0383           do 101 i=1,n+1
0384     c
0385     c
0386     c
0387           ahe(i)=pi*l(i)*dso(i)
0388         101 continue
0389     c
0390     c  Determine an area for the cold box to be used in determination
0391     c  of QRLR (which is QRL due to radiation).
0392     c  Assume the cold box to be a cylinder with a diameter and
0393     c  length of 3 times the bore of the coldest dry expander.
0394     c  Later assume both the inner and outer shields are of the same
0395     c  diameter.
0396     c
0397           acb=pi*((3.*b(1))**2)/4.+3.*b(1)*pi*3.*b(1)
0398     c
0399     c  View factor:
0400           f=1./(2./e-1.)
0401     c
0402     c  Radiation heat leak to refrigeration zone:
0403           sigma=.1713e-8
0404           qrlr=sigma*acb*f*(te(1)**4-4.5**4)*(1.8**4)*(.2931/144.)
0405     c
0406           do 102 i=1,n+1
0407           the(i)=(tel(i)+tel(i+1))/2.
0408         102 continue
0409     c
0410          qwrhe1=sigma*f*ahe(1)*(te(1)**4-the(1)**4)*(1.8**4)*(.2931/144.)
0411          qwrhe2=sigma*f*ahe(2)*(te(1)**4-the(2)**4)*(1.8**4)*(.2931/144.)
0412     c
0413           qwr=qwrhe1+qwrhe2
0414     c
0415           ee=sigma*f*ahe(3)*(te(2)**4-the(3)**4)*(1.8**4)*(.2931/144.)
0416           ff=sigma*f*ahe(4)*(te(2)**4-the(4)**4)*(1.8**4)*(.2931/144.)
0417           gg=sigma*f*(pi*3.*b(1)*(l(1)+l(2))+acb)*
0418          &                    (te(2)**4-te(1)**4)*(1.8**4)*(.2931/144.)
0419     c
0420           qer(1)=ee+ff+gg-qwr-qrlr
0421     c
0422     c
0423           uu=sigma*f*ahe(5)*(tcan**4-the(5)**4)*(1.8**4)*(.2931/144.)
0424           vv=sigma*f*(pi*3.*b(1)*(l(1)+l(2)+l(3)+l(4))+acb)*
0425          &                   (tcan**4-te(2)**4)*(1.8**4)*(.2931/144.)
0426     c
0427           qer(2)=uu+vv-qer(1)
0428     c
0429     c
0430     c  Compute the conduction heat leak area.
0431     c
```

```
0432          do 103 i=1,n+1
0433          ac(i)=pi*(dp(i)*tpis+dco(i)*tcyl+dso(i)*tshell)
0434        103 continue
0435    c
0436    c  Find the heat leak for each exchanger.
0437    c
0438    c  The following constants are for a polynomial used to compute
0439    c  the stainless steel wall conductivity.
0440          a=-2.18837
0441          bb=4.442795
0442          c=-1.518
0443          d=.1668444
0444    c
0445          do 104 i=1,n+1
0446          tavehi=(teh(i)+tel(i))/2.
0447          tavelo=(teh(i+1)+tel(i+1))/2.
0448          tk=(tavehi+tavelo)/2.
0449    c
0450          xt=alog10(tk)
0451          xkk=a+bb*xt+c*xt**2+d*xt**3
0452          xk=10.**xkk
0453    c
0454          qc(i)=-ac(i)*xk*((tavehi-tavelo)/l(i))*2.54/1000.
0455        104 continue
0456    c
0457    c  Find the average heat leak for exchanger combinations.
0458    c
0459          do 105 i=2,n,2
0460        105 qcc(i)=(1./(l(i)+l(i-1)))*(l(i)*qc(i)+l(i-1)*qc(i-1))
0461    c
0462    c  Find the heat removed at each expander:
0463    c
0464          qwc=qcc(2)
0465          qec(1)=qcc(4)-qwc
0466          qec(2)=qc(5)-qcc(4)
0467    c
0468    c  Total heat leak to each expander at the refrigeration load:
0469    c
0470          qrl=qrlr
0471          qw=qwr+qwc
0472          qe(1)=qer(1)+qec(1)
0473          qe(2)=qer(2)+qec(2)
0474    c
0475          qrtot=qrlr+qwr+qer(1)+qer(2)
0476    c
0477          write(6,50)qrl,qw,qe(1),qe(2)
0478       50 format(3x,'qrl=',f7.4,'W'/
0479         &       3x,'qw=',f7.4,'W'/
0480         &       3x,'qe(1)=',f7.4,'W'/
0481         &       3x,'qe(2)=',f7.4,'W')
0482    c
0483    c  Compute the entropy generated in the heat exchangers:
0484    c
0485    c  Radiation:
```

```
0486          sgenrl=qrl*(1./4.22-1./te(1))
0487    c
0488          sgenwr=qwrhe1*(1./the(1)-1./te(1))+qwrhe2*(1./the(2)-1./te(1))
0489    c
0490          sgene1r=ee*(1./the(3)-1./te(2))+ff*(1./the(4)-1./te(2))+
0491         &        gg*(1./te(1)-1./te(2))
0492    c
0493          sgene2r=uu*(1./the(5)-1./tcan)+vv*(1./te(2)-1./tcan)
0494    c
0495    c   Conduction:
0496          sgenwc=qwc*(1./tel(1)-1./tel(3))
0497    c
0498          sgene1c=qcc(4)*(1./tel(3)-1./tel(5))
0499    c
0500          sgene2c=qc(5)*(1./tel(5)-1./tel(6))
0501    c
0502    c   Total entropy generated due to radiation and conduction:
0503          sgenw=sgenwr+sgenwc
0504    c
0505          sgene1=sgene1r+sgene1c
0506    c
0507          sgene2=sgene2r+sgene2c
0508    c
0509    c
0510    c   Next calculate the entropy generation in the helium gas.  In ex-
0511    c   changers "1" and "2", the entropy generation will be calculated
0512    c   using properties of helium from the NBS program.  The higher
0513    c   temperature heat exchangers will use an ideal gas relation so
0514    c   that a comparison may be made between entropy generation due to
0515    c   temperature and pressure gradients.
0516    c
0517          do 60 i=1,6
0518          dsh=denf(peh(i)*101325.,teh(i))/4.0026
0519          sh(i)=entrop(dsh,teh(i))/4.0026
0520          dsl=denf(pel(i)*101325.,tel(i))/4.0026
0521          sl(i)=entrop(dsl,tel(i))/4.0026
0522       60 continue
0523    c
0524    c
0525          do 61 i=1,5
0526          sggas(i)=meh(i)*(sh(i)-sh(i+1))+mel(i)*(sl(i+1)-sl(i))
0527       61 continue
0528    c
0529          r=8.315/4.0026
0530          cpp=5.2
0531          do 70 i=3,5
0532          sggast(i)=meh(i)*(cpp*alog(teh(i)/teh(i+1)))
0533         &          +mel(i)*(cpp*alog(tel(i+1)/tel(i)))
0534          sggasp(i)=-meh(i)*(r*alog(peh(i)/peh(i+1)))
0535         &           -mel(i)*(r*alog(pel(i+1)/pel(i)))
0536
0537          sgpgas(i)=sggast(i)+sggasp(i)
0538       70 continue
0539    c
```

```
0540            tr=vptemp(pr)
0541            dintop=denf(101325.*peh(n+2),teh(n+2))/4.0026
0542            doutop=denf(101325.*pel(n+2),tel(n+2))/4.0026
0543            sintop=entrop(dintop,teh(n+2))/4.0026
0544            soutop=entrop(doutop,tel(n+2))/4.0026
0545            sgentot=meh(n+1)*(soutop-sintop)-qrtot/tcan-qr/tr
0546      c
0547            write(6,80)sgenrl,sgenwr,sgenwc,sgenw,
0548           &sgene1r,sgene1c,sgene1,
0549           &sgene2r,sgene2c,sgene2
0550           80 format(3x,'sgenrl=',f7.5,'W/K'/
0551           &3x,'sgenwr= ',f7.5,'W/K',4x,
0552           &   'sgenwc= ',f7.5,'W/K',4x,
0553           &   'sgenw= ',f7.5,'W/K'/
0554           &3x,'sgene1r=',f7.5,'W/K',4x,
0555           &   'sgene1c=',f7.5,'W/K',4x,
0556           &   'sgene1=',f7.5,'W/K'/
0557           &3x,'sgene2r=',f7.5,'W/K',4x,
0558           &   'sgene2c=',f7.5,'W/K',4x,
0559           &   'sgene2=',f7.5,'W/K')
0560      c
0561            do 23 i=1,5
0562            write(6,71)i,sggas(i)
0563           71 format(3x,'sggas(',i1,')=',f7.5,'W/K')
0564           23 continue
0565      c
0566            do 73 i=3,5
0567            write(6,72)i,sggast(i),i,sggasp(i),i,sgpgas(i)
0568           72 format(3x,'sggast(',i1,')=',f7.5,'W/K',
0569           &       4x,'sggasp(',i1,')=',f7.5,'W/K',
0570           &       4x,'sgpgas(',i1,')=',f7.5,'W/K')
0571           73 continue
0572      c
0573            write(6,74)sgentot
0574           74 format(3x,'total generated entropy=',f7.5,'W/K')
0575      c
0576            open(unit=11,file='sys7.dat',status='new')
0577            write(11,5000)ph,pq,pl,pc,qe,qw,qrl
0578         5000 format(11f6.2/f6.2/11f6.2/f6.2/11f6.3/f10.6/f10.6)
0579      c
0580            return
0581            end
```

```
0001    c************************* PINCH POINT ANALYSIS ******************
0002    c
0003          subroutine pinch(tlpin)
0004    c
0005    c
0006    c  This program computes temperatures on the high- and low-pressure
0007    c  sides of the coldest heat exchanger.  The temperatures,
0008    c  temperature differences, and temperature ratios are computed
0009    c  at incremental temperatures along each exchanger.  This program
0010    c  assumes the pinch point to be at the same position as previously
0011    c  assumed in SYSITER.  This assumed position of the pinch point is
0012    c  checked in this program and if the position assumed was
0013    c  incorrect then the new pinch point location is transferred back
0014    c  to SYSITER.
0015    c
0016    c
0017          dimension me(12),th(12),tl(12),te(12),fe(11),
0018         &b(11),c(11),qe(11)
0019          real mh,ml
0020          common thin,thout,tlin,tlout,ph,pl,dtpin,icomp,hg,
0021         &b,c,qe,qw,qrl,
0022         &nn,iexp,rpm,r,zh,zl,a,tcan,e,
0023         &tpis,tcyl,tshell,
0024         &qr,tr,pr,fwe,fvc,fe,
0025         &mr,me,th,tl,te,co,si
0026          delta=8.
0027          dhout=denf(ph*101325.,thout)
0028          hhout=enthal(dhout,thout)/1000.
0029          if(icomp.eq.1)go to 50
0030          hlin=hg
0031          go to 51
0032       50 dlin=denf(pl*101325.,tlin)
0033          hlin=enthal(dlin,tlin)/1000.
0034       51 r=1.
0035          s=hlin-r*hhout
0036          write(6,100)
0037      100 format(//26x,'PINCH POINT ANALYSIS'//8x,'THX(K)',
0038         &8x,'TLX(K)',8x,'DELTA T(K)',8x,'DELTA T/T'/)
0039          x=thout-tlin
0040          ys=x/tlin
0041          p=ys
0042          if(ys.le.dtpin)go to 300
0043          ys=dtpin
0044          go to 301
0045      300 tlpin=tlin
0046      301 write(6,101)thout,tlin,x,p
0047      101 format(8x,f6.2,8x,f6.2,10x,f6.3,12x,f6.4)
0048          n=(tlout-tlin)/delta
0049          if(n.eq.0)go to 20
0050          do 10 i=1,n
0051          tlx=tlin+i*delta
0052          dlx=denf(pl*101325.,tlx)
0053          hlx=enthal(dlx,tlx)/1000.
```

```
0054           hhx=(hlx-s)/r
0055           dhx=dph(ph,hhx*4.0026)
0056           uhx=hhx-(101.325*ph)/(dhx*4.0026)
0057           thx=tlx
0058           call calcup(uhx,ph,dhx*.0040026,thx)
0059           x=thx-tlx
0060           y=x/tlx
0061           if(y.lt.ys)go to 200
0062           go to 201
0063       200 tlpin=tlx
0064           ys=y
0065       201 write(6,9)thx,tlx,x,y
0066         9 format(8x,f6.2,8x,f6.2,10x,f6.3,12x,f6.4)
0067        10 continue
0068        20 x=thin-tlout
0069           y=x/tlout
0070           if(y.ge.ys)go to 12
0071           tlpin=tlout
0072        12 write(6,13)thin,tlout,x,y
0073        13 format(8x,f6.2,8x,f6.2,10x,f6.3,12x,f6.4)
0074           if(tlpin.gt.0.)go to 11
0075           tlpin=tlout
0076        11 write(6,8)
0077         8 format(/)
0078           return
0079           end
```

Appendix B

Detailed Development of the Performance Algorithm

A performance algorithm for the integral heat exchanger and expansion engine is described in Chapter 3. This algorithm contains heat exchange terms that include an enthalpy flow rate, a heat leak due to conduction, and a refrigeration load. In this appendix, details of the performance algorithm will be given. An expression for the average rate of enthalpy flow at a cross section will first be developed. These equations include both steady-cyclic terms and non-cyclic terms. The steady-cyclic terms are referred to in the literature[40] as shuttle heat transfer. The non-cyclic terms are due to the heat exchange temperature difference between the high-pressure and low-pressure streams.

After finding an expression for the average rate of enthalpy flow at a cross section, the performance algorithm will be described. The model will include a lumped heat leak after adiabatic expansion from high to low pressure.

B.1 The Average Enthalpy Flow Rate at a Cross Section

The performance algorithm requires an expression for the average rate of enthalpy flow at a cross section, which will be developed in this section. This expression for enthalpy flow requires solving energy balance equations for a cross section that includes the displacer, cylinder, and shell walls along with the high- and low-pressure gaps. After several simplifying assumptions are listed, the expression for enthalpy flow will be given. Then, the differential equations satisfying the first law of thermodynamics will be solved and the results will be substituted in the equation for enthalpy flow.

The steady-cyclic heat transfer has been solved for the case of reciprocating engines.[40-43] The task here is to extend the work done for reciprocating machines to the integral heat exchanger and expansion engine being developed. An approach similar to that used by Rios in reference (40) will be used.

B.1.1 Simplifying Assumptions

In an effort to find solutions to the problem that may be easily applied, several simplifying assumptions have been made:

Assumption 1 The displacer is long. This assumption asserts that end effects are negligible on overall system performance. Also, for a long displacer, the temperature gradient over a short length may be approximated as a straight line.

Assumption 2 The thermal conductivity of the gas and walls is negligible in the direction of flow. This allows axial conduction to be neglected.

Assumption 3 The walls have infinite thermal conductivity in the radial direction; thus, the walls are assumed to be at a single temperature so that the temperature gradient in the walls in the radial direction is zero. This assumption is useful only if the wall thickness is smaller than the thermal wavelength, ℓ_T, where

$$\ell_T = 2\pi \sqrt{\frac{2\,\alpha}{\omega}} \qquad (B.1)$$

where α is the thermal diffusivity and ω is the circular frequency.

Assumption 4 The work of compression is small when compared to the heat capacity of the walls. A result of this assumption is that the effects of gas compressibility are negligible.

Assumption 5 Flow in the annular spaces is laminar. Thus, with assumption 4, the gas can be considered to have an average temperature equal to the mean of its enclosing walls.

Assumption 6 Material properties are constant over a length of displacer equal to the stroke.

Assumption 7 The flow on the low-pressure side is non-periodic. This means that a surge volume has been built at the exit from the exhaust valve.

B.1.2 Net Enthalpy Flow Through a Plane

In this section, an expression for the net enthalpy flow through any plane perpendicular to the piston motion will be developed. This net enthalpy flow includes both steady-cyclic and non-cyclic terms that comprise most of the heating load that must be removed from the cold end by way of expansion work.

The coordinate system shown in Figure (B.1) is described in terms of a stationary coordinate system, x, and a moving coordinate system, y, which is attached to the displacer. The displacer motion is given by a periodic function, $\xi(t)$. When $t = 0$, the x and y coordinates coincide. The directions of x and y are defined as positive in the direction of increasing temperature so that the derivative of cylinder temperature with respect to x is a positive number. Also, in accordance with the stated assumptions, the position of $x = 0$ is located midway between the warm end and the cold end in order to escape end effects.

The enthalpy flow through a plane for one cycle may be expressed as:

$$\Delta H = \oint m_H \, c_p \, T_H(x,t) \, dt - \oint m_L \, c_p \, T_L(x,t) \, dt - \oint \rho_m \, A_{cd} \, c_m \, T_d(-\xi,t) \, \frac{d\xi}{dt} \, dt \qquad (B.2)$$

In this equation, the enthalpy flow is defined as positive toward the cold end. The last term is the enthalpy flow of the solid displacer. For convenience, an enthalpy per unit length of displacer will be defined as

$$h_d = \rho_m \, A_{cd} \, c_m \, T_d(-\xi,t) \qquad (B.3)$$

For a length equal to the stroke, the axial temperature distributions for the displacer, cylinder, and outer shell are given by straight lines. These linear temperature distributions require that the heat transfer at any time between the displacer and cylinder be identical at any x. For the displacer, this may be written as

$$\frac{dq_1}{dy} \neq f(y) \qquad (B.4)$$

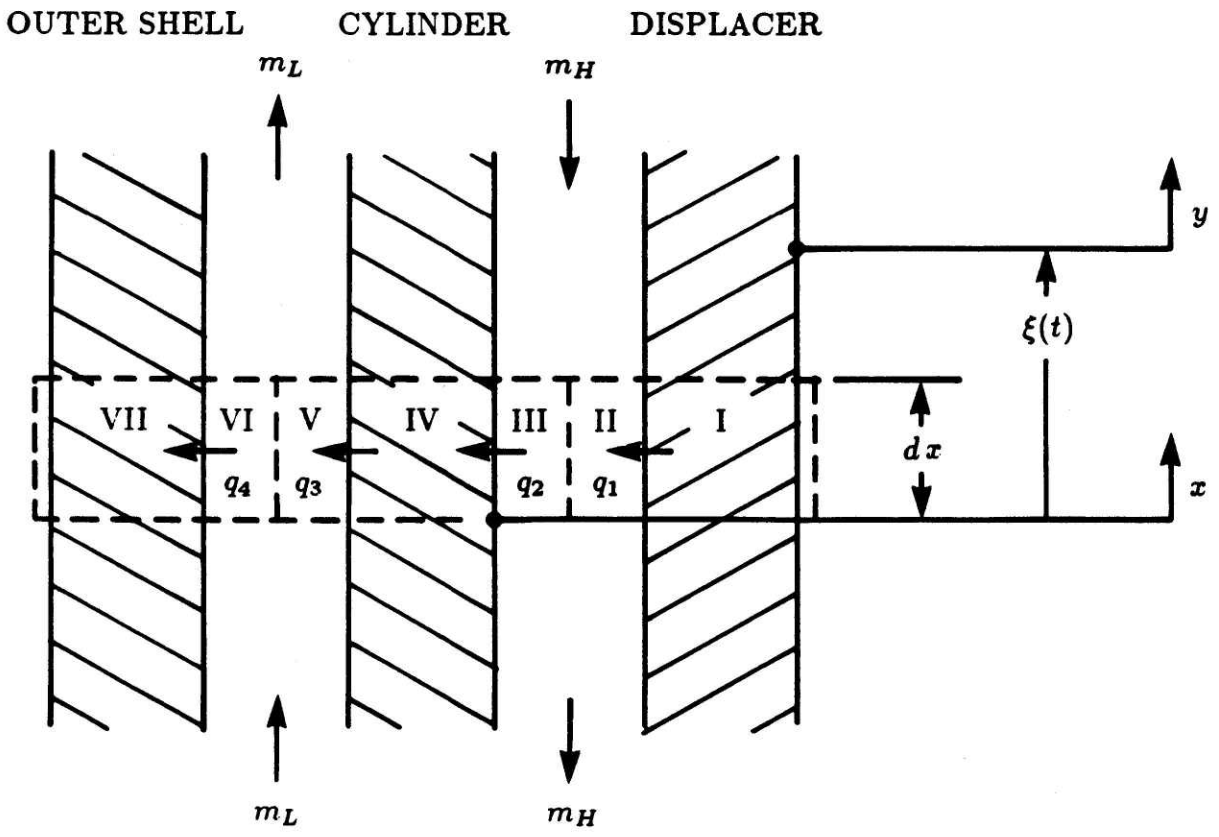

Fig. (B.1) Control volumes for the heat transfer equations.

By applying the first law to a length dy on the displacer, one obtains

$$-d\,q_1 = \rho_m\, A_{cd}\, c_m\, \frac{\partial T_d}{\partial t}\, dy \qquad (B.5)$$

Integrating Eqn. (B.5) from 0 to t yields

$$h_d = h_{d0} - \int_0^t \frac{d\,q_1}{d\,y}\, d\,t \qquad (B.6)$$

where

$$h_{d0} = h_d(y, t = 0) \qquad (B.7)$$

By substituting Eqn. (B.6) into Eqn. (B.2) using Eqn. (B.4), one obtains

$$\Delta H = \oint m_H\, c_p\, T_H(x,t)\, dt - \oint m_L\, c_p\, T_L(x,t)\, dt - \oint h_{d0}\, d\xi + \oint \left(\int_0^t \frac{d\,q_1}{d\,y}\, dt \right) \frac{d\,\xi}{d\,t}\, dt \qquad (B.8)$$

where the term

$$\oint h_{d0}\, d\xi = 0$$

because ξ is periodic and h_{d0} is a constant.

The above equation is the enthalpy flow per cycle. The average rate of enthalpy flow at any cross section may be written as

$$h = h_g + h_d \qquad (B.9)$$

where

$$h_g = \frac{\omega}{2\,\pi} \oint m_H\, c_p\, T_H(x,t)\, dt - \frac{\omega}{2\,\pi} \oint m_L\, c_p\, T_L(x,t)\, dt \qquad (B.10)$$

and

$$h_d = \frac{\omega}{2\,\pi} \oint \left(\int_0^t \frac{d\,q_1}{d\,y} dt \right) \frac{d\,\xi}{d\,t} dt \qquad (B.11)$$

In these expressions, m_H, m_L, ω, and ξ are inputs, along with the gas properties. The temperatures T_H and T_L are represented by Fourier series.

In the next section, an expression for dq_1 / dy will be developed that will be substituted into Eqn. B.11.

B.1.3 Derivation of the Energy Equations

Figure B.1 shows a cross section of the integral heat exchanger and expansion engine. This cross section has been divided into seven control volumes as shown. In this section, the energy equations for each of the seven control volumes will be derived. Then, Fourier series will be used to represent the temperature fluctuations of the displacer, cylinder, and outer shell. Fourier series will also be used to represent the high-pressure side mass flow rate, an input to the solution.

For each of the seven control volumes, the energy equation may be written as

$$\frac{\partial E_{CV}}{\partial t} = E_{IN} - E_{OUT} \qquad (B.12)$$

This equation is a statement that the rate of change of energy within the control volume must equal the difference between the energy flux into and the energy flux out of the control volume.

For control volume I, the energy equation written for the moving position at $y = 0$ on the displacer is

$$\frac{dq_1}{dy} = -\rho_m c_m \pi D_d t_d \frac{\partial T_d}{\partial t}\Bigg)_{y=0} \qquad (B.13)$$

For control volume II, the energy equation for the moving control volume at $y = 0$ is

$$\frac{dq_1}{dy} = \frac{k_g \pi D_H}{z_H}(T_d(0,t) - T_c(\xi,t)) - \frac{m_H c_p}{2}\frac{\partial T_H}{\partial y}\Bigg)_{y=0} \qquad (B.14)$$

In accordance with assumption 4, this equation does not include the rate of change of energy for the gas in the control volume. An order of magnitude comparison of

the terms in the equation reveal that at 100 K, the magnitude of the neglected term is less than 5% of the terms included.

The remainder of the energy equations will be written for control volumes located at the stationary position $x = 0$. For control volume III,

$$\frac{d\,q_2}{d\,x} = \frac{k_g\,\pi\,D_H}{z_H}\,(T_d(-\xi,t) - T_c(0,t)) + \frac{m_H\,c_p}{2}\,\frac{\partial T_H}{\partial x}\Bigg)_{x=0} \qquad (B.15)$$

For control volume IV,

$$\frac{d\,q_2}{d\,x} - \frac{d\,q_3}{d\,x} = \rho_m\,c_m\,\pi\,D_c\,t_c\,\frac{\partial T_c}{\partial t}\Bigg)_{x=0} \qquad (B.16)$$

For control volume V,

$$\frac{d\,q_3}{d\,x} = \frac{k_g\,\pi\,D_L}{z_L}\,(T_c(0,t) - T_s(0,t)) + \frac{m_L\,c_p}{2}\,\frac{\partial T_L}{\partial x}\Bigg)_{x=0} \qquad (B.17)$$

For control volume VI,

$$\frac{d\,q_4}{d\,x} = \frac{k_g\,\pi\,D_L}{z_L}\,(T_c(0,t) - T_s(0,t)) - \frac{m_L\,c_p}{2}\,\frac{\partial T_L}{\partial x}\Bigg)_{x=0} \qquad (B.18)$$

Finally, for control volume VII,

$$\frac{d\,q_4}{d\,x} = \rho_m\,c_m\,\pi\,D_s\,t_s\,\frac{\partial T_s}{\partial t}\Bigg)_{x=0} \qquad (B.19)$$

The temperature distributions in the displacer, cylinder, and outer shell have all been assumed to be straight lines for a length equal to the stroke, s. Thus, at steady-cyclic state and with Eqn. (B.4), the temperature gradients at any position along a length equal to the stroke may be simplified as

$$\frac{\partial T}{\partial x} = \frac{\partial T_d}{\partial y} = \frac{\partial T_c}{\partial x} = \frac{\partial T_s}{\partial x} = \frac{\partial T_H}{\partial x} = \frac{\partial T_L}{\partial x} \qquad (B.20)$$

and the temperature difference between the displacer and cylinder is

$$T_d(-\xi,t) - T_c(0,t) = T_d(0,t) - T_c(\xi,t) \qquad (B.21)$$

Now that the energy equations have been written, expressions for the inputs will be defined. The periodic motion of the displacer will be

$$\frac{\xi}{s} = \sum_{n=1}^{\infty} G_n \sin n\omega t \qquad (B22)$$

The high-pressure side mass flow rate involves both periodic and constant terms. In non-dimensional form, this flow rate may be written as

$$\frac{m_H c_p z_H}{2\pi D_H s k_g} = \sum_{n=1}^{\infty} (H_n \cos n\omega t + I_n \sin n\omega t) + \frac{M_H c_p z_H}{2\pi D_H s k_g} \qquad (B.23)$$

where M_H is the non-periodic inlet mass flow rate which is equal to the time-average flow rate.

As stated in assumption 7, the low-pressure side mass flow rate is assumed to be a non-periodic term. This mass flow rate is defined as M_L. Continuity requires that the time-average high-pressure side flow rate must equal the low-pressure side flow rate so that

$$M_H = M_L$$

The temperatures of the walls and gas streams will be changing with time. These changes will be periodic and may be represented by Fourier series. The temperatures at a location $x = 0$ for the displacer, cylinder, and outer shell may be represented as

$$T_d(-\xi,t) - T_d(-\xi,0) = s\frac{\partial T}{\partial x}\sum_{n=1}^{\infty}\left(A_n \cos n\omega t + B_n \sin n\omega t\right) \qquad (B.24)$$

$$T_c(0,t) - T_c(0,0) = s\frac{\partial T}{\partial x}\sum_{n=1}^{\infty}\left(C_n \cos n\omega t + D_n \sin n\omega t\right) \qquad (B.25)$$

$$T_s(0,t) - T_s(0,0) = s\frac{\partial T}{\partial x}\sum_{n=1}^{\infty}\left(E_n \cos n\omega t + F_n \sin n\omega t\right) \qquad (B.26)$$

Now that expressions for the displacer, cylinder, and outer shell temperatures are available, the energy equation for each control volume may be rewritten by using the appropriate substitution. For control volume I, the resulting equation is

$$\frac{d\,q_1}{d\,y} = \rho_m\, c_m\, \pi\, D_d\, t_d\, s\, \omega\, \frac{\partial T}{\partial x} \sum_{n=1}^{\infty} \left(-n\, B_n\, \cos n\,\omega\, t + n\, A_n\, \sin n\,\omega\, t\right) \qquad (B.27)$$

In order to rewrite Eqn. (B.14) using the expressions for periodic temperature, a relation for the temperature difference between the displacer and cylinder must be found. By definition of the linear temperature distribution, one may write

$$\frac{T_d(-\xi,0) - T_d(0,0)}{s\,(\partial T\,/\,\partial x)} = -\frac{\xi}{s}$$

By substituting this equation into Eqns. (B.22) and (B.24), the displacer temperature may be written as

$$\frac{T_d(-\xi,t) - T_d(0,0)}{s\,(\partial T\,/\,\partial x)} = \sum_{n=1}^{\infty} \left(A_n\, \cos n\,\omega\, t + (B_n - G_n)\, \sin n\,\omega\, t\right) \qquad (B.28)$$

Now Eqns. (B.23), (B.25), and (B.28) may be substituted into Eqn. (B.14) using Eqn. (B.21) to find an expression for the energy balance on control volume II:

$$\frac{d\,q_1}{d\,y} = \frac{k_g\,\pi\, D_H\, s}{z_H}\, \frac{\partial T}{\partial x} \sum_{n=1}^{\infty} \left((A_n - C_n - H_n)\, \cos n\,\omega\, t + (B_n - D_n - G_n - I_n)\, \sin n\,\omega\, t\right)$$

$$+ \frac{k_g\,\pi\, D_H\, \alpha_H}{z_H} - \frac{M_H\, c_p}{2}\, \frac{\partial T}{\partial x} \qquad (B.29)$$

In this expression,

$$\alpha_H = T_d(0,0) - T_c(0,0) \qquad (B.30)$$

is the temperature difference when

$$n\,\omega\, t = m\,\pi \qquad (B.31)$$

where m is an integer. At these times, $\xi = 0$. In other words, α_H may be thought of as the heat exchange temperature difference that would exist when the piston is stationary, the mass flow on the high- and low-pressure sides is constant, and the heat removal at the cold end is supplied by an outside source. Moreover, the first term in Eqn. (B.29) represents the heat transfer resulting from piston motion, while the second and third terms result from a time-averaged heat exchange temperature difference.

In a similar fashion the energy equation for control volume III may be written as

$$\frac{d\,q_2}{d\,x} = \frac{k_g\,\pi\,D_H\,s}{z_H}\,\frac{\partial T}{\partial x}\sum_{n=1}^{\infty}\Big((A_n - C_n + H_n)\cos n\,\omega\,t + (B_n - G_n - D_n + I_n)\sin n\,\omega\,t\Big) + \frac{k_g\,\pi\,D_H\,\alpha_H}{z_H} + \frac{M_H\,c_p}{2}\,\frac{\partial T}{\partial x} \qquad (B.32)$$

The energy balances for the remaining control volumes require straight forward substitution of the equations developed so far. For control volume IV,

$$\frac{d\,q_2}{d\,x} - \frac{d\,q_3}{d\,x} = \rho_m\,c_m\,\pi\,D_c\,t_c\,s\,\omega\,\frac{\partial T}{\partial x}\sum_{n=1}^{\infty}\left(n\,D_n\cos n\,\omega\,t - n\,C_n\sin n\,\omega\,t\right) \qquad (B.33)$$

For control volume V,

$$\frac{d\,q_3}{d\,x} = \frac{k_g\,\pi\,D_L\,s}{z_L}\,\frac{\partial T}{\partial x}\sum_{n=1}^{\infty}\Big((C_n - E_n)\cos n\,\omega\,t + (D_n - F_n)\sin n\,\omega\,t\Big) + \frac{k_g\,\pi\,D_L\,\alpha_L}{z_L} + \frac{m_L\,c_p}{2}\,\frac{\partial T}{\partial x} \qquad (B.34)$$

where, similar to Eqn. (B.30),

$$\alpha_L = T_c(0,0) - T_s(0,0) \qquad (B.35)$$

is a time-averaged temperature difference due to heat exchange between the high- and low-pressure sides.

The energy equation for the remainder of the low-pressure side is

$$\frac{d\,q_4}{d\,x} = \frac{k_g\,\pi\,D_L\,s}{z_L}\,\frac{\partial T}{\partial x}\sum_{n=1}^{\infty}\Big((C_n - E_n)\cos n\,\omega\,t + (D_n - F_n)\sin n\,\omega\,t\Big)$$

$$+\frac{k_g\,\pi\,D_L\,\alpha_L}{z_L} - \frac{m_L\,c_p}{2}\,\frac{\partial T}{\partial x} \qquad (B.36)$$

The energy equation for control volume VII is

$$\frac{d\,q_4}{d\,x} = \rho_m\,c_m\,\pi\,D_s\,t_s\,s\,\omega\,\frac{\partial T}{\partial x}\sum_{n=1}^{\infty}(n\,F_n\cos n\,\omega\,t - n\,E_n\sin n\,\omega\,t) \qquad (B.37)$$

The energy equations developed so far in this section involve periodic and non-periodic terms that are independent of each other. The non-periodic terms will first be considered. By combining Eqn. (B.27) and Eqn. (B.29), the non-periodic result is

$$\frac{M_H\,c_p}{2}\,\frac{\partial T}{\partial x} - \frac{k_g\,\pi\,D_H\,\alpha_H}{z_H} = 0 \qquad (B.38)$$

Combining Eqns. (B.32), (B.33), and (B.34) yields

$$\frac{k_g\,\pi\,D_H\,\alpha_H}{z_H} + \frac{M_H\,c_p}{2}\,\frac{\partial T}{\partial x} - \frac{k_g\,\pi\,D_L\,\alpha_L}{z_L} - \frac{M_L\,c_p}{2}\,\frac{\partial T}{\partial x} = 0 \qquad (B.39)$$

Combining Eqn. (B.36) and Eqn. (B.37) yields

$$\frac{M_L\,c_p}{2}\,\frac{\partial T}{\partial x} - \frac{k_g\,\pi\,D_L\,\alpha_L}{z_L} = 0 \qquad (B.40)$$

Eqns. (B.38), (B.39), and (B.40) may be combined in several ways to give the usual results for non-periodic heat transfer. For example, by substituting Eqn. (B.38) and Eqn. (B.39) into Eqn. (B.40), one finds that

$$\frac{\alpha_H}{\alpha_L} = \frac{D_L}{D_H}\,\frac{z_H}{z_L} \qquad (B.41)$$

This result will be used later in the performance algorithm to determine the average cylinder temperature.

The periodic terms in the energy equations may be combined in a similar fashion. The result is a set of six equations with six unknowns:

$$A_n + U\,B_n - C_n = H_n \tag{B.42}$$

$$U\,A_n - B_n + D_n = -G_n - I_n \tag{B.43}$$

$$-Z_H\,A_n + Z\,C_n + V\,D_n - Z_L\,E_n = Z_H\,H_n \tag{B.44}$$

$$Z_H\,B_n + V\,C_n - Z\,D_n + Z_L\,F_n = Z_H\,G_n - Z_H\,I_n \tag{B.45}$$

$$C_n - E_n - W\,F_n = 0 \tag{B.46}$$

$$D_n + W\,E_n - F_n = 0 \tag{B.47}$$

The constants in these equations are defined as follows:

$$U = \frac{\rho_m\,c_m\,t_d\,\omega\,z_H\,n}{k_g} \tag{B.48}$$

$$V = \frac{\rho_m\,c_m\,t_c\,\omega\,D_c\,n}{k_g} \tag{B.49}$$

$$W = \frac{\rho_m\,c_m\,t_s\,\omega\,z_L\,n}{k_g} \tag{B.50}$$

$$Z_H = \frac{D_H}{z_H} \tag{B.51}$$

$$Z_L = \frac{D_L}{z_L} \tag{B.52}$$

$$Z = Z_H + Z_L \tag{B.53}$$

Another constant that can be defined now is

$$Q = \frac{1}{U} \tag{B.54}$$

These simultaneous equations are being solved in an effort to find the average enthalpy flux at any cross section. Since this enthalpy flux involves $d\,q_1 \,/\, d\,y$, other constants will be defined now to expedite solving the simultaneous equations. The energy equation for control volume II will now be rewritten to define these constants:

$$\frac{d\,q_1}{d\,y} = \frac{k_g\,\pi\,D_H\,s}{z_H}\,\frac{\partial T}{\partial x}\sum_{n=1}^{\infty}\left(J_n\,\cos n\,\omega\,t + K_n\,\sin n\,\omega\,t\right) + \frac{k_g\,\pi\,D_H\,\alpha_H}{z_H} - \frac{M_H\,c_p}{2}\,\frac{\partial T}{\partial x} \tag{B.55}$$

where

$$J_n = A_n - C_n - H_n \tag{B.56}$$

and

$$K_n = B_n - D_n - G_n - I_n \tag{B.57}$$

In Section B.1.4, an expression will be needed for K_n in order to solve for the enthalpy flux. The equations developed so far may be solved to yield an expression for K_n as follows:

$$K_n = \frac{-G_n + (L\,\Delta - M\,N\,\Delta + Q)H_n + \left(L\,\Sigma - M\left(N\,\Sigma + 2\,\frac{Z_H}{V\,W}\right) - 2\,\frac{Z_H}{Z_L} - 1\right)I_n}{1 + Q^2 + \frac{Z_H}{Z_L} - L\,\beta + M\,N\,\beta + \frac{M\,Z_H}{V\,W}} \tag{B.58}$$

In this equation, several constants must be defined:

$$L = Q - \frac{V}{Z_L} \tag{B.59}$$

$$M = Q\,W - \frac{V\,W}{Z_L} - 1 \tag{B.60}$$

$$N = \frac{Z_L\,W + V}{V\,W} \tag{B.61}$$

$$\beta = \frac{V\,W\,(Z_L\,Z_H\,Q - V\,Z_H) + P\,Z_H}{V\,W\,(Z_L\,Z_H + V^2) - P\,(Z_L\,W + V)} \tag{B.62}$$

$$\Delta = \frac{V\,W\,Z_L\,Z_H}{V\,W\,(Z_L\,Z_H + V^2) - P\,(Z_L\,W + V)} \tag{B.63}$$

$$\Sigma = \frac{2\,P\,Z_H - 2\,W\,Z_H\,V^2}{V\,W\,(Z_L\,Z_H + V^2) - P\,(Z_L\,W + V)} \tag{B.64}$$

where, in these equations,

$$P = Z_L\,Z\,W + V^2\,W + Z_L\,V \tag{B.65}$$

To obtain temperature versus time for the displacer, cylinder, and outer shell, expressions for the constants in Eqns. (B.24), (B.25), and (B.26) have been determined as a set of equations to be solved in order. (For example, the value of E_n must be known before solving for F_n.) The set of equations follows:

$$E_n = \beta\,K_n + \Delta\,H_n + \Sigma\,I_n \tag{B.66}$$

$$F_n = -N\,E_n - \frac{Z_H}{V\,W}\,K_n - \frac{2\,Z_H}{V\,W}\,I_n \tag{B.67}$$

$$B_n = Q\,E_n + Q\,W\,F_N + Q\,H_n - Q^2\,K_n \tag{B.68}$$

$$D_n = \frac{V}{Z_L} E_n + \left(\frac{V W}{Z_L} + 1 \right) F_n + \frac{Z_H}{Z_L} K_n + 2 \frac{Z_H}{Z_L} I_n \qquad (B.69)$$

$$C_n = E_n + W F_n \qquad (B.70)$$

$$A_n = Q K_n \qquad (B.71)$$

This section has developed energy equations for the heat exchanger along with several constants to be used to determine temperature versus time plots. In the next section, the results from the energy equations will be used to determine the enthalpy flux at any cross section.

B.1.4 Substitution of Energy Equations into Enthalpy Flux Equation

In this section, the results from the preceeding two sections will be combined to yield the average rate of enthalpy flow through a plane perpendicular to the axis of the integral heat exchanger and expander. This enthalpy flow consists of terms for both the gas motion and the piston motion. An expression will first be developed for the gas motion.

For convenience, the average rate of enthalpy flow for the gas will be rewritten:

$$h_g = \frac{\omega}{s\,\pi} \oint m_H\, c_p\, T_H(0,t)\, dt - \frac{\omega}{s\,\pi} \oint m_L\, c_p\, T_L(0,t)\, dt \qquad (B.10)$$

In this equation, m_H, T_H, and T_L consist of both periodic and non-periodic terms. From assumption 5, the high- and low-pressure gas streams each have a temperature equal to the mean of their enclosing wall temperatures. Also, from an earlier result,

$$m_L = M_L = M_H \qquad (B.72)$$

where M_H is the time-averaged mass flow rate on the high-pressure side. Integration of Eqn. (B.10) using the equations for temperature and mass flow rate will therefore result in periodic and non-periodic terms.

By using the average of Eqns. (B.24) and (B.25) for the high-pressure side temperature, T_H, and the average of Eqns. (B.24) and (B.25) for the low-pressure side temperature, T_L, along with Eqn. (B.23) for the high-pressure side periodic mass flow rate, one may integrate Eqn. (B.10) in a straight forward fashion to yield

$$h_g = \frac{\pi D_H s^2 k_g}{2 z_H} \frac{\partial T}{\partial x} \sum_{n=1}^{\infty} \left((A_n + C_n) H_n + (B_n + D_n - G_n) I_n \right)$$

$$+ M_L c_p (T_H(0,0) - T_L(0,0))$$

In this equation, A_n, B_n, C_n, and D_n are coefficients describing the amplitude of the temperature change on the displacer and cylinder with respect to time, while G_n is related to the amplitude of temperature swing due to displacer motion as seen by an observer that is stationary on the cylinder. Since the amplitude of temperature change over time is small compared to (dT/dx), the coefficients A_n, B_n, C_n, and D_n are usually negligible when compared to G_n. This assumption would be valid for any heat exchanger with practical values of displacer to cylinder gap. In this development however, these coefficients will be included so that results for cases with very small displacer to cylinder gaps may be examined in order to enhance the understanding of theoretical trends. To simplify the previous expression for h_g, define

$$S_n = (A_n + C_n) H_n + (B_n + D_n - G_n) I_n \qquad (B.73)$$

A final expression for the average rate of enthalpy flow due to the gas is

$$h_g = \frac{\pi D_H s^2 k_g}{2 z_H} \frac{\partial T}{\partial x} \sum_{n=1}^{\infty} S_n + M_L c_p (T_H(0,0) - T_L(0,0)) \qquad (B.74)$$

The average rate of enthalpy flow due to piston motion remains to be determined. This enthalpy was found in Section B.1.2 to be

$$h_d = \frac{\omega}{2\pi} \oint \left(\int_0^t \frac{dq_1}{dy} dt \right) \frac{d\xi}{dt} dt \qquad (B.11)$$

By substituting Eqn. (B.55) and Eqn. (B.22) into Eqn. (B.11), one may integrate to obtain

$$h_d = -\frac{\pi\, D_H\, s^2\, k_g}{2\, z_H}\, \frac{\partial T}{\partial x} \sum_{n=1}^{\infty} G_n\, K_n \qquad (B.75)$$

The average rate of enthalpy flow at any cross section of the integral heat exchanger and expansion engine may now be written according to Eqn. (B.9) by summing Eqns. (B.74) and (B.75):

$$h = \frac{\pi\, D_H\, s^2\, k_g}{2\, z_H}\, \frac{\partial T}{\partial x} \sum_{n=1}^{\infty} (S_n - G_n\, K_n) + M_L\, c_p\, (T_H(0,0) - T_L(0,0)) \qquad (B.76)$$

This equation is valid at any position along the heat exchanger. So far in this analysis, the temperature gradient has been assumed linear over an axial length equal to the stroke. For the entire length, the temperature gradient may vary due to the effect of finite gas specific heat and changing gas properties. For this reason, the present analysis will now include different temperature gradients on each end of the heat exchanger. In order to proceed, the coordinate system will be redefined so that the position $x = 0$ is located at the cold end of the heat exchanger and the position $x = L$ is located at the warm seal. The temperature distribution will be assumed to be a polynomial of the form

$$\frac{T - T_0}{\Delta T} = \Theta\, (\frac{x}{L})^2 + (1 - \Theta)\, \frac{x}{L} \qquad (B.77)$$

where T_0 is the temperature at the cold end of the heat exchanger, and ΔT is the temperature difference between $x = 0$ and $x = L$.

An energy balance requires the enthalpy flux at the ends of the heat exchanger to be equal. Using this condition and substituting Eqn. (B.77) into Eqn. (B.76) allows Θ to be determined:

$$\Theta = \frac{k_{g0} \sum_{n=1}^{\infty} (\, S_{n0} - G_{n0}\, K_{n0}\,) - k_{gL} \sum_{n=1}^{\infty} (\, S_{nL} - G_{nL}\, K_{nL}\,)}{k_{g0} \sum_{n=1}^{\infty} (\, S_{n0} - G_{n0}\, K_{n0}\,) + k_{gL} \sum_{n=1}^{\infty} (\, S_{nL} - G_{nL}\, K_{nL}\,)} \qquad (B.78)$$

where the subscripts 0 and L refer to the positions $x = 0$ and $x = L$, respectively.

In Section B.2, the average enthalpy flow due to mass flow and displacer motion will be used to develop a performance algorithm for the integral heat exchanger and expansion engine. An expression for enthalpy flow at $x = 0$ will be needed. The equation is

$$h_0 = \frac{\pi D_H s^2 k_{g0}}{2 z_H} \frac{\partial T}{\partial x}\Big)_0 \sum_{n=1}^{\infty} (S_{n0} - G_{n0} K_{n0}) + M_L c_p \left(T_H(0,0) - T_L(0,0)\right) \quad (B.79)$$

where

$$\frac{\partial T}{\partial x}\Big)_0 = \frac{\Delta T}{L}(1 - \Theta) \quad (B.80)$$

Both periodic and non-periodic terms are included in Eqn. (B.79). Later in this analysis, these terms will be separated as follows:

$$h_0 = h_{c0} + h_{nc0} \quad (B.81)$$

where

$$h_{c0} = \frac{\pi D_H s^2 k_{g0}}{2 z_H} \frac{\partial T}{\partial x}\Big)_0 \sum_{n=1}^{\infty} (S_{n0} - G_{n0} K_{n0}) \quad (B.82)$$

$$h_{nc0} = M_L c_p \left(T_H(0,0) - T_L(0,0)\right) \quad (B.83)$$

B.2 Performance Algorithm with Computer Code

Results from Section B.1 will be used along with two major performance specifications in an effort to predict performance trends for the integral exchanger and expander configuration. The two performance specifications that must be estimated are the time-averaged heat exchange temperature difference and the efficiency of the dry expansion engine. This section will outline the details of the performance algorithm.

The control volume used in this analysis, which includes only the cold end, is shown in Fig. (B.2). The boundaries of the control volume extend downward from a plane at $x = 0$, which is also top dead center for the displacer, to include the working space volume and the surge volume. The exact location of the plane at $x = 0$ is somewhat arbitrary since end effects of the heat exchanger are not taken into consideration. Heat inputs to the control volume include the enthalpy flow computed in Section B.1 (h_0), the refrigeration load (q_L), and the axial conduction (q_C). The work removed by the expansion engine is W.

Two major performance specifications must be estimated. These are the expander efficiency in terms of η_E and the heat exchanger performance in terms of a heat exchange temperature ratio at the cold end, $\Delta T / T)_{h0}$. The expander is assumed to be adiabatic in the model. The adiabatic engine efficiency is

$$\eta_E = \frac{h_{in} - h_{out}}{h_{in} - h_{out,s}} \qquad (B.84)$$

In the computer analysis to be described later, this efficiency will be taken as $\eta_E = 0.75$.

The heat exchange performance will be specified here in terms of a temperature ratio. This ratio is the heat exchange temperature difference at a cross section (here the cross section is at $x = 0$) divided by the low-pressure side temperature:

$$\frac{\Delta T}{T}\Big)_{h0} = \frac{T_H(0,0) - T_L(0,0)}{T_L(0,0)} \qquad (B.85)$$

This performance parameter is not yet experimentally determined for the heat exchanger in this analysis, so an estimate is necessary. An efficient heat exchanger may perform with a temperature ratio of 0.15 at 80 K. Since the exchanger being investigated here will have an equivalent diameter equal to twice the radial gap width, heat transfer coefficients will be high, resulting in efficient heat exchange. The following reference point located at $x = 0$ will be used for comparative results from the computer:

$$\frac{\Delta T}{T}\Big)_{h0,ref} = 0.15$$

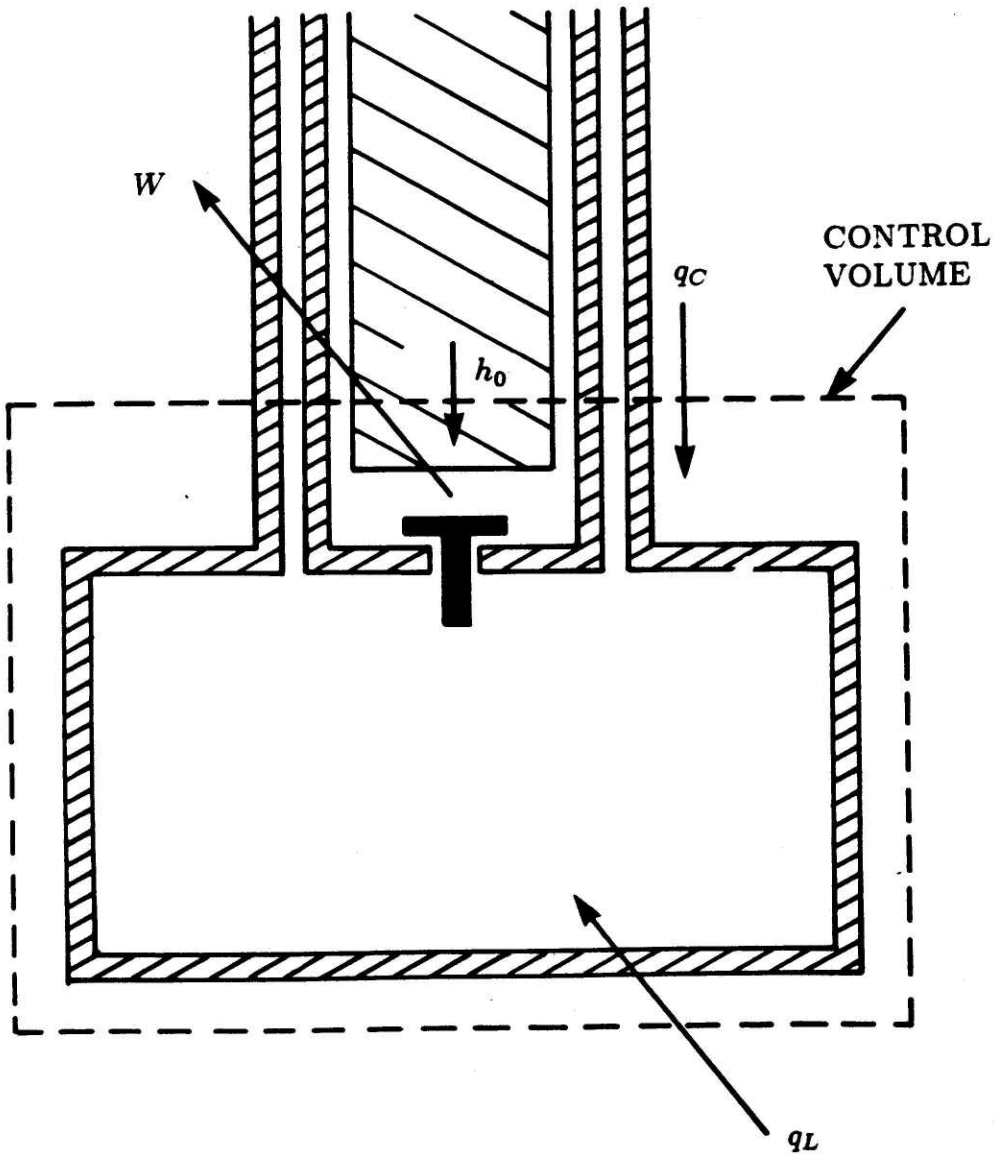

Fig. (B.2) Control volume used for the cold-end energy balance of the performance algorithm.

for the case of

$z_{H,ref} = 0.127\,\text{mm}$

$z_{L,ref} = 0.254\,\text{mm}$

Since flow is laminar, only z_H and z_L are required to specify the heat exchange temperature difference for a given heat exchanger length and diameter and for a given temperature change from end to end, as will be shown next. For this reason, the heat exchange temperature difference for other values of radial gap widths may be specified using Eqn. (B.88), which developed as follows.

For a differential length of heat exchanger, the heat exchange from stream to stream may be written as:

$$\frac{d\,q}{d\,A} = U\,(\,T_H - T_L\,) \tag{B.86}$$

where

$$\frac{d\,q}{d\,A} = \text{constant} = M\,c_p\,\Delta\,T)_{ee}$$

for a heat exchanger of specified heat exchange area, mass flow rate, M, and temperature change from end to end, $\Delta\,T)_{ee}$. The laminar heat transfer coefficient for the gas is

$$h = \frac{Nu\,k_g}{2\,z}$$

The overall coefficient of heat transfer may be written as:

$$U = \frac{Nu\,k_g}{2\,z_H + 2\,z_L} \tag{B.87}$$

for laminar flow and constant gas thermal conductivity at a cross section. For a cross section located at the cold end ($x = 0$), the temperature difference as a function of radial gap width may be written as:

$$\Delta\,T)_{h0} = \frac{z_H + z_L}{z_{H,ref} + z_{L,ref}}\,(T_{H0} - T_{L0})_{ref} \tag{B.88}$$

This equation indicates that the magnitude of $\Delta T)_{h0}$ is different from the reference value if the radial gap widths change. This equation is linear as a function of z_H if z_L is held constant.

A lumped heat input will be added to the gas stream after adiabatic expansion from the average high-pressure side temperature at the cold end, $T_H(0,0)$, to an adiabatic expansion temperature which is never actually obtained in the working volume. The work output obtained by adiabatic expansion is computed using Eqn. (B.84) and the equation

$$W = M_L \left(h_{H0} - h_{out}\right) \tag{89}$$

The gas temperature after the lumped heat input is the temperature of the gas entering the low-pressure side of the heat exchanger, $T_L(0,0)$, which is also the refrigeration temperature, T_R. The lumped heat input is the sum of the enthalpy flow rate at $x = 0$, the conduction heat leak, and the refrigeration load. In this algorithm, the refrigeration load is an output computed using

$$q_L = W - h_0 - q_c \tag{B.90}$$

As a part of the computer algorithm, the temperatures of the displacer, cylinder, and outer shell will be determined as a function of time using Eqns. (B.24) through (B.26) with the coefficients from Eqns. (B.66) through (B.71). The average temperature of the cylinder is given by Eqn. (B.41).

A computer program was written in order to compare the effect of varying physical dimensions such as the gap width between the displacer and cylinder, z_H. Inputs and outputs to the computer program are listed in Table (B.1). The variables that are fed into the program manually are the gap widths between the displacer and cylinder and between the cylinder and outer shell. As discussed in Chapter 3, the Fourier series are evaluated for the case of $n = 1$. Most of the helium properties are computed using a set of programs obtained from the National Bureau of Standards. The remaining programs to compute helium properties were developed as part of

Table (B.1) Inputs and outputs to performance algorithm

Input Parameters

Parameter	Definition
D_H	diameter of high-pressure stream gap
D_L	diameter of low-pressure stream gap
D_c	mean diameter of cylinder
t_d	displacer wall thickness
t_c	cylinder wall thickness
t_s	outer shell wall thickness
ω	circular frequency of displacer
s	stroke
η_E	adiabatic engine efficiency
$\left(\frac{\Delta T}{T}\right)_{h0,ref}$	heat exchanger performance parameter
ρ_m	wall density
c_m	wall specific heat
M_L	time averaged mass flow rate
L	overall exchanger length
q_C	axial conduction heat leak
P_H	mean high-pressure side pressure
P_L	low-pressure side pressure
ΔT	end-to-end temperature difference
T_R	refrigeration temperature
z_H	high-pressure side radial gap
z_L	low-pressure side radial gap

this project, as discussed in Appendix A.

The computer program given in Exhibit (B.1) will be described next. It is set up so that the user may input high- and low-pressure side heat exchange gaps for several systems without exiting the program. Several of the parameters are not written exactly as they are in this text; they are written in a form that should be recognizable to the reader, however. The subscripts 1 and 2 for the various

Table (B.1) (cont.)

Output Parameters

Parameter	Definition
h_{c0}	periodic enthalpy flow at $x = 0$
h_{nc0}	non-periodic enthalpy flow at $x = 0$
h_0	enthalpy flow at $x = 0$
q_L	refrigeration load
W	work output of expansion engine
$T_d(-\xi, t)$	displacer temperature at $x = 0$
$T_c(0, t)$	cylinder temperature at $x = 0$
$T_s(0, t)$	outer shell temperature at $x = 0$

coefficients refer to the cold and warm ends, respectively. The program first reads specifications to be used for the systems of interest. The algorithm then consists of the following step-by-step procedure:

Step 1 Input the gap width between the displacer and cylinder and between the cylinder and outer shell. Then use these gap widths to compute the heat exchange temperature difference by using Eqn. (B.89).

Step 2 Evaluate the gas properties k_g and c_p at $x = 0$ and at $x = L$ based on the mean of the high- and low-pressure sides. The helium property programs are used here.

Step 3 Subroutine KCALC is called. This subroutine first computes the periodic terms of Eqn. (B.79), which include S_n and K_n for the case of $n = 1$ evaluated at $x = 0$ and at $x = L$. Also computed at this time are the coefficients for the temperature versus time equations for the displacer, cylinder, and outer shell.

Step 4 KCALC then uses a function subprogram called ACOM to find a value for Θ in Eqn. (B.78). Then Θ is used to compute the temperature gradient at $x = 0$.

Step 5 The subroutine next computes a value for the periodic enthalpy flow rate, h_{c0}. Note that the value of H_{10} in Eqn. (B.23) is taken as zero so that the high-pressure side mass flow rate is a sinusoidal input. Also, the input coefficient in Eqn.

(B.22) for displacer motion is set at $G_1 = 0.5$, as it must be for sinusoidal motion.

Step 6 The last computation in subroutine KCALC is the displacer, cylinder, and outer shell temperatures as functions of time. The average cylinder temperature is computed using Eqn. (B.41).

Step 7 The main program is used to compute the non-periodic term for the enthalpy flow rate equation. The refrigeration temperature and the heat exchange temperature difference at the cold end are inputs to the program, so the high-pressure side temperature leaving the heat exchanger (which is also the inlet temperature to the expansion engine) may be computed:

$$T_H(0,0) = T_R + \Delta T)_{h0} \qquad (B.91)$$

where $T_R = T_L(0,0)$.

Step 8 Equation (B.84) is used to compute the enthalpy of the gas after adiabatic expansion. The work output is then computed using Eqn. (B.89).

Step 9 The refrigeration load needed to obtain the refrigeration temperature that is specified can now be computed using Eqn. (B.90).

EXHIBIT (B.1) COMPUTER PROGRAMS FOR PERFORMANCE ALGORITHM.

```
      program perform
      dimension kg(2),cpg(2),den(2)
c
      real kg,lnth,ml,ne
c
      common dh,dl,dc,zzh,zzl,tp,tc,ts,
     &ww,s,rom,cm,ml,tr,delthe,
     &lnth,txeql,hc,dtmax
c
      read(9,1) dh,dl,dc,tp,tc,ts,ww,s,ne,rom,cm,ml,
     &lnth,qcond,ph,pl,txeql,tr
c
    1 format(3f11.3/3f11.6/f9.4/f8.6/f8.6/f8.5/f8.5/
     &f9.6/f5.1/f8.3/2f8.1/2f8.1)
c
c Read the values not included in the read statement.
c
      open (unit=8,file='plot.dat',status='new')
c
   15 print *,'Input the high- and low-pressure side gaps'
      read(5,*)zzh
      if(zzh.eq.0.0)stop
      read(5,*)zzl
c
c  An estimate of the heat exchange performance must now be
c  made. Only one estimate is necessary for all heat
c  exchange configurations  under consideration. The
c  estimate made is that for zzh=0.005 in and zzl=0.010 in.
c  The heat exchange ratio was 0.15 at 80 K.
c  Based on this single data point, heat
c  exchange differences
c  for different values of zzh and zzl may be made. This
c  value of temperature difference occurs when the displacer
c  is at its midpoint position. For this reason, the actual
c  temperature difference will be different than delthe for
c  most of the cycle.
c
      delthe=((zzh+zzl)/(0.005+0.010))*12.
c
c  Compute values of thermal conductivity and specific heat
c  at constant pressure for the gas.
c
      pave=(ph+pl)/2.
      den(1)=denf(pave*101325.,tr)/4.0026
      den(2)=denf(pave*101325.,txeql)/4.0026
c
      kg(1)=condt(den(1),tr)*1000.
      kg(2)=condt(den(2),txeql)*1000.
c
      cpg(1)=cp(den(1),tr)/4.0026
      cpg(2)=cp(den(2),txeql)/4.0026
c
```

```
      call kcalc(kg,cpg)
c
c  The enthalpy flow due to counterflow heat exchange
c  through a plane located at x=0 is based on the
c  temperature difference when the displacer is at its mid
c  position.
c
      thxeqo=tr+delthe
c
c  The gas temperature entering the working volume during
c  the expansion stroke is estimated to be the average of
c  temperatures when the pistion is at x=0 and at x=s.
c  This value is again the refrigeration temperature plus
c  the temperature difference when the displacer is at its
c  midpoint.
c
      thexp=tr+delthe
c
c  Now compute the non-periodic heat transfer due to heat
c  exchange temperature difference. It is assumed that the
c  average high-side pressure is half of its maximum value.
c
      dhxeqo=denf(0.5*ph*101325.,thxeqo)
      hhxeqo=enthal(dhxeqo,thxeqo)/1000.
      dref=denf(pl*101325.,tr)
      href=enthal(dref,tr)/1000.
c
      hnc=ml*(hhxeqo-href)
c
c  The total rate of enthalpy flow located at a plane at
c  x=0:
c
      hzero=hc+hnc
c
      write(6,30)hnc,hzero
   30 format(3x,'hn=',f4.1,'W'/3x,'ho=',f4.1,'W')
c
c
c  Next use the adiabatic engine efficiency to find the
c  exhaust temperature.  The enthalpy before expansion is
c  calculated first.
c
      dhexp=denf(ph*101325.,thexp)
      hhexp=enthal(dhexp,thexp)/1000.
      s2s=entrop(dhexp/4.0026,thexp)/4.0026
c
c  Make initial estimates of density and temperature for the
c  isentropic state for the subroutine.
c
      t2s=thexp*(pl/ph)**0.4
      d2s=denf(pl*101325.,t2s)/1000.
c
      call calcps(pl,s2s,d2s,t2s)
c
```

```
      h2s=enthal(d2s*1000.,t2s)/1000.
c
      h2=hhexp-ne*(hhexp-h2s)
c
      d2=dph(p1,h2*4.0026)*4.0026/1000.
c
      u2=h2-0.101325*p1/d2
c
      t2=thexp-ne*(thexp-t2s)
c
      call calcup(u2,p1,d2,t2)
c
      write(6,29)t2
c
   29 format(3x,'Minimum adiabatic temperature = ',f5.1,'K')
c
c  The total work removed by the engine may now be computed:
c
      work=m1*(hhexp-h2)
c
      qload=work-hzero-qcond
c
      write(6,45)work
   45 format(3x,'work output = ',f6.1,'W')
c
      write(6,31)dtmax,qload
   31 format(3x,'Maximum Delta T for heat exchange at
     &(x=0) =',f4.1,'K'/
     &3x,'Heat Load =',f8.1,'W'//)
c
      write(8,1000)zzh,qload,hc,hnc,hzero,qcond,work,dtmax
c
 1000 format(f9.6,f9.4,f9.4,f9.4,f9.4,f9.4,f9.4,f9.4)
c
      go to 15
c
c
      end

      function acom(a1,a2,b1,b2,c1,c2,d)
c
      acom=(a1*(c1-d*b1)-a2*(c2-d*b2))
     &/(a1*(c1-d*b1)+a2*(c2-d*b2))
c
      return
      end


      subroutine kcalc(kg,cp)
c
      dimension kn(2),in(2),kg(2),cp(2),copre(3),sipre(3),
     &temp(3),tss(3),v(2),w(2),p(2),q(2),n(2),sn(2),
     &aa(2),bb(2),cc(2),dd(2),ee(2),ff(2),ddtmax(50)
c
```

```
      real kg,kn,in,l,m,n,ml,lnth
c
      common dh,dl,dc,zzh,zzl,tp,tc,ts,ww,s,rom,
     &cm,ml,tr,delthe,
     &lnth,txeql,hc,dtmax
c
c  The main function of this subroutine is to compute all
c  the constants defined in Appendix B.
c
      do 10 i=1,2
c
      u=((rom*cm*tp*ww*zzh)/kg(i))*(1000.*453.6/2.54)
c
      v(i)=((rom*cm*dc*tc*ww)/kg(i))*(1000.*453.6/2.54)
c
      w(i)=((rom*cm*ts*ww*zzl)/kg(i))*(1000.*453.6/2.54)
c
      zh=dh/zzh
c
      zl=dl/zzl
c
      z=zh+zl
c
      q(i)=1./u
c
      p(i)=zl*z*w(i)+w(i)*v(i)**2+zl*v(i)
c
      bot=v(i)*w(i)*(zl*zh+v(i)**2)-p(i)*(zl*w(i)+v(i))
c
      sig=(2.*p(i)*zh-2.*w(i)*zh*v(i)**2)/bot
c
      del=v(i)*w(i)*zl*zh/bot
c
      bet=(v(i)*w(i)*(zl*zh*q(i)-v(i)*zh)+p(i)*zh)/bot
c
      l=q(i)-v(i)/zl
c
      m=q(i)*w(i)-v(i)*w(i)/zl-1.
c
      n(i)=(zl*w(i)+v(i))/(v(i)*w(i))
c
      hpre=l*del-m*n(i)*del+q(i)
c
      xipre=l*sig-m*(n(i)*sig+2.*zh/(v(i)*w(i)))-1.-2.*zh/zl
c
      botkn=1.+q(i)**2+zh/zl-
     &l*bet+m*(n(i)*bet+zh/(v(i)*w(i)))
c
      pi=3.14159
c
      in(i)=-(ml*cp(i)*zzh*1000.)/(pi*2.*dh*s*kg(i)*2.54)
c
      gn=0.5
c
```

```
      hn=0.
c
      kn(i)=(-gn+hpre*hn+xipre*in(i))/botkn
c
      pi=3.14159
c
c  Compute the coefficients for the tempertures of the
c  displacer, cylinder, and shell as functions of time.
c
      eebot=v(i)*w(i)*(zl*zh+v(i)**2)-p(i)*(zl*w(i)+v(i))
c
      ekn=(v(i)*w(i)*(zl*zh*q(i)-v(i)*zh)+p(i)*zh)*kn(i)
c
      ein=(2.*p(i)*zh-2.*w(i)*zh*v(i)**2)*in(i)
c
      ee(i)=(ekn+ein)/eebot
c
      ff(i)=-n(i)*ee(i)-zh*kn(i)/(v(i)*w(i))-
     &2.*zh*in(i)/(v(i)*w(i))
c
      bb(i)=q(i)*ee(i)+q(i)*w(i)*ff(i)-kn(i)*q(i)**2
c
      dd(i)=bb(i)-gn-in(i)-kn(i)
c
      cc(i)=w(i)*ff(i)+ee(i)
c
      aa(i)=q(i)*kn(i)
c
      sn(i)=(aa(i)+cc(i))*hn+(bb(i)+dd(i)-gn)*in(i)
c
   10 continue
c
      write(6,32)in(1),kn(1)
   32 format(3x,'Ino =',f10.8/3x,'Kno =',f10.8)
c
c
      write(6,35)aa(1),bb(1),cc(1),dd(1),ee(1),ff(1)
   35 format(/3x,'A1=',f10.8
     &       /3x,'B1=',f10.8
     &       /3x,'C1=',f10.8
     &       /3x,'D1=',f10.8
     &       /3x,'E1=',f10.8
     &       /3x,'F1=',f10.8//)
c
      a=acom(kg(1),kg(2),kn(1),kn(2),sn(1),sn(2),gn)
c
      dtdxo=((txeql-tr)/lnth)*(1-a)
c
c  Now compute the total periodic rate of enthalpy flow.
c  The non-periodic enthalpy flow will be computed in the
c  main program.
c
      hc=(pi/2.)*(dh/zzh)*s**2*kg(1)*dtdxo
     &*((aa(1)+cc(1))*hn+
```

```
     &(bb(1)+dd(1)-gn)*in(1)
     &-gn*kn(1))*(2.54/1000.)
c
      copre(1)=aa(1)
      copre(2)=cc(1)
      copre(3)=ee(1)
      sipre(1)=bb(1)-gn
      sipre(2)=dd(1)
      sipre(3)=ff(1)
c
c  Compute the temperatures for the displacer, cylinder, and
c  shell when the displacer is at its midpoint.
c
      tss(1)=tr+delthe
      tss(2)=(tss(1)/zzh+tr/zzl)/(1./zzl+1./zzh)
      tss(3)=tr
c
c  The temperatures of the displacer, cylinder, and shell
c  will now be computed with respect to time.
c
      write(6,110)
  110 format(3x,' T(SEC) ',3X,' TPIS(K)',3x,'  TP-TC ',3X,
     &' TCYL(K)',3X,'  TC-TS ',3X,' TSHL(K)',3x,'DEL T
     & (K)'/)
c
      open (unit=10,file='out.dat',status='new')
c
      tau=2.*pi/ww
      tstep=tau/20.
      time=0.
      ddtmax(1)=0.
      do 200 i=1,21
c
      ang=ww*time
c
      do 100 j=1,3
c
      temp(j)=tss(j)+s*dtdxo*(copre(j)*cos(ang)+
     &sipre(j)*sin(ang))
c
c
  100 continue
c
      tpc=temp(1)-temp(2)
      tcs=temp(2)-temp(3)
c
      ddtmax(i+1)=tpc+tcs
      if(ddtmax(i+1).gt.ddtmax(i))dtmax=ddtmax(i+1)
c
      write(6,120)time,temp(1),tpc,temp(2),
     &tcs,temp(3),ddtmax(i+1)
c
      write(10,130)time,temp(1),temp(2),temp(3)
c
```

```
      time=time+tstep
c
  200 continue
c
  120 format(3x,f8.5,3x,f8.4,3x,f8.4,3x,f8.4,
     &3x,f8.4,3x,f8.4,3x,f9.4)
c
  130 format(f9.5,f9.4,f9.4,f9.4)
c
      write(6,36)dtdxo,hc
   36 format(/3x,'dtdxo=',f6.2,'K/in'
     &       /3x,'hc=',f4.1,'W')
c
      return
c
      end
```

Appendix C

Details of the Single-Stage Cryocooler Experiment

This appendix first describes the instrumentation used to measure pressure, temperature, and helium mass flow in the single-stage cryocooler experiment. The information supplied includes choice of sensor, calibration data, and sensor location. The second part of this appendix describes the helium compression system.

Figure (C.1) with an accompanying legend locates all instruments and heaters with connections into the vacuum jacket through a 35 pin hermetic lead through mounted on the top plate. The pairing letters are identified on the lead through.

C.1 Instrumentation and Data Acquisition

An ACRO data acquisition system was used with a COMPAC personal computer to obtain all electronic measurements. Several BASIC programs were available from the ACRO manual which were easily modified to obtain programs for relatively slow data intake of measurements such as temperature and for faster data collection required for p-v plots. Calibration curves for the electronic pressure transducers and the mass flow meter are given in Table (C.1).

Table (C.1) Pressure and mass flow rate calibration curves.

Sensor	Measurement	V_{in}	Equation
CEC	inlet pressure	5 V	$P(\text{psig}) = 52640\, V_{out}\,(\text{mV}) - .07$
Omega	surge vol. pres.	12 V	$P(\text{psia}) = 30.05\, V_{out}\,(\text{V}) - 28.28$
Omega	warm exit pres.	12 V	$P(\text{psia}) = 30.08\, V_{out}\,(\text{V}) - 29.22$
Datametrics	nitrogen flow	–	$\dot{m}(\text{g/s}) = 0.0537\, V_{out}\,(\text{V})$
Datametrics	helium flow	–	$\dot{m}(\text{g/s}) = .03948 V_{out}(\text{V}) - .00931$

C.1.1 Pressure Instrumentation

The absolute pressure in the intake line was measured both electronically and mechanically. The electronic measurement was made with a CEC 0-1000 psig transducer. A calibration equation is given in Table (C.1). A Bourdon tube pressure

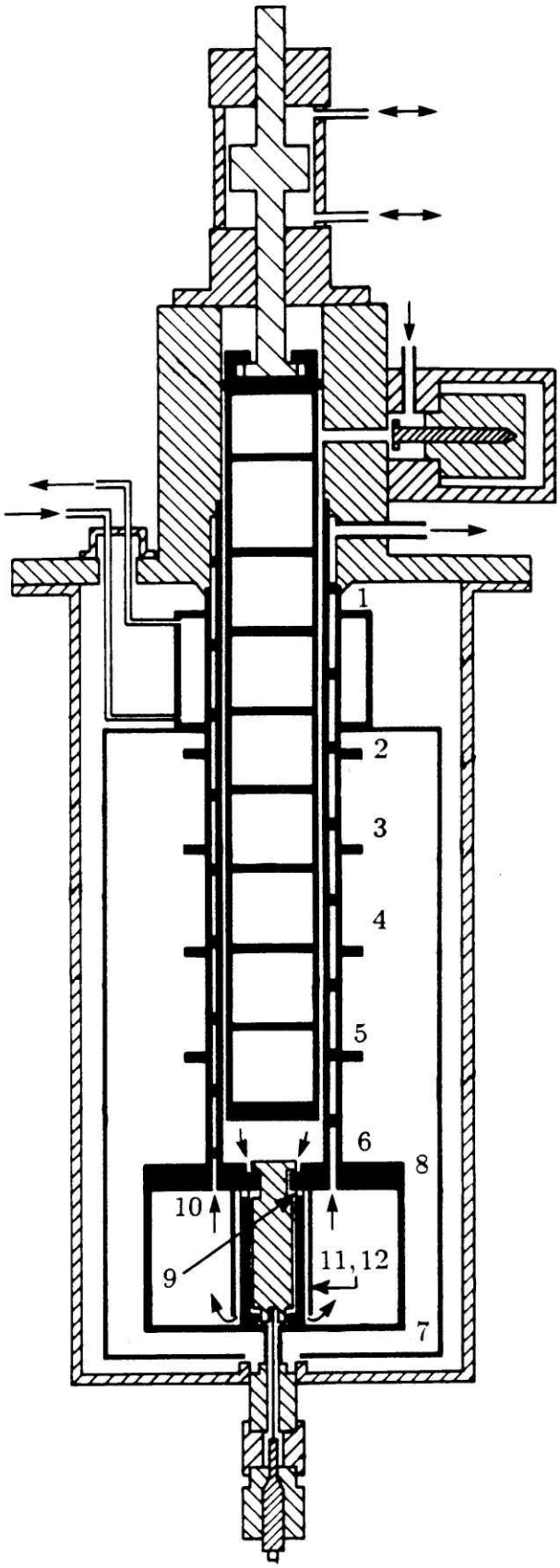

Fig. (C.1) Temperature sensor and heater locations with legend.

Legend for Fig. (C.1)

#	Pair	Instrument	Location
1	A,B	thermocouple	between LN_2 exchanger and top plate
2	P,R	SNO-230 diode	33 cm above surge volume top flange
3	R,S	SNO-238 diode	25 cm above surge volume top flange
4	S,T	SNO-229 diode	18 cm above surge volume top flange
5	T,U	SNO-207 diode	8 cm above surge volume top flange
6	U,V	thermocouple	1.3 cm above surge volume top flange
7	D,F	SNO-217 diode	entrance to LN_2 exchanger
8	C,D	SNO-236 diode	exit from LN_2 exchanger
9	C,W	SNO-216 diode	exhaust valve passage
10	G,W	SNO-201	low-pressure return inlet
11	K,L	heater	outside exhaust guide tube
12	H,J	heater	inside exhaust guide tube
–	M,N	heater	inside LN_2 reservoir

gage was also used. This gage provided a visual pressure measurement that was always available, such as when adjusting the pressure regulator for the appropriate inlet pressure.

Pressure in the working volume was measured using a Dytran model 2300C4 piezoelectric pressure transducer, which is a 0 to 1000 psi unit with a nominal sensitivity of 0.35 pC/psi. The sensor was mounted to the top flange of the surge volume using mounting adaptor model 6522. A capillary tube approximately 7 cm long with a 1.3 mm I.D. connected the transducer to the cylinder head. A Kistler Instruments charge amplifier converted the transducer output to a voltage signal. A piezoelectric sensor provides only a relative pressure measurement. For this reason, a second pressure sensor was needed in the surge volume to provide an absolute pressure measurement. An Omega Engineering, Inc. model PX-304-150A-5V operated at room temperature by mounting the transducer on the top plate and connecting the transducer to the surge volume using a capillary tube.

Pressure drop through the low-pressure return passage was measured using the

Omega pressure sensor connected to the surge volume in conjunction with a second Omega model PX-304-150A-5V mounted outside the cryocooler in the exhaust line at room temperature. Mechanical measurement of the exhaust line pressure was provided by a Bourdon tube pressure gage, which expedited proper adjustment of the back-pressure regulator.

C.1.2 Temperature Instrumentation

Temperature sensors were mounted at the locations indicated in Fig. (C.1). Most of the temperature measurements were made using Southampton Miniature Diode Thermometers from Sonder Instrument, Inc. Calibration data for a representative thermometer is given in Exhibit (C.1). This choice of sensor was based primarily upon convenience and price. The sensors were received three weeks after ordering and cost $75. each. The claimed accuracy was ± 0.2 K from 4.2 K to 30 K and ± 0.5 K from 30 K to 180 K. This sensor is not intended to provide extreme accuracy; rather, the sensor is a quick and easy way to avoid very expensive calibration costs and long delivery times when measurements not requiring high accuracy are needed. The diodes are made in a batch process so that all sensors in the batch have the same operating sensitivity; then, a few sensors are calibrated to obtain a representative calibration curve for the entire batch. Each sensor is then tested at three representative points: liquid helium, liquid nitrogen,and room temperatures. These data points are given in Table (C.2).

Care had to be taken when mounting the sensors to avoid getting mounting material on the diode sensing element. Temperatures above 100 C also had to be avoided. Two sensors were destroyed during the mounting process: one by excessive heat during a welding procedure and another by breaking a fragile lead on the diode surface. How delicate these sensors were cannot be overemphasized. No sensors failed, however, after being mounted successfully.

Temperature sensors along the heat exchanger were mounted on the outside of the outer shell in the vacuum space. The leads were wrapped around the shell approximately 7 turns and then epoxied to the shell using Stycast 2850 epoxy from

Typical temperature vs forward voltage data, with 10 μA excitation current, for Southampton Miniature Diodes

Temp K	Forward voltage V	Temp K	Forward voltage V
1.3119	1.82808	13.0342	1.29437
1.4848	1.82509	14.0094	1.26880
1.5968	1.82274	15.0224	1.24492
1.8133	1.81742	16.0128	1.22394
2.0012	1.81199	17.0214	1.20467
2.2065	1.80522	18.1551	1.18484
2.4003	1.79803	19.0702	1.16936
2.5941	1.79019	20.0112	1.15235
2.7871	1.78165	22.2508	1.121468
3.0069	1.77121	25.5305	1.11013
3.2137	1.76073	27.322	1.10660
3.3905	1.75144	29.629	1.10261
3.5937	1.74030	33.266	1.09703
3.8085	1.72802	35.111	1.09441
4.0119	1.71615	37.708	1.090463
4.2228	1.70354	40.0864	1.086755
4.3418	1.69721	45.1737	1.078749
4.4205	1.69248	49.852	1.071306
4.6040	1.68046	55.423	1.062358
4.8031	1.66778	60.028	1.054925
5.0443	1.65251	65.361	1.046299
5.2278	1.64089	69.943	1.038859
5.4177	1.62883	75.425	1.029855
5.6047	1.61706	80.186	1.021965
5.8167	1.60379	85.063	1.013772
6.0108	1.59179	90.139	1.005107
6.2284	1.57847	95.308	0.996139
6.4294	1.56651	100.289	0.987383
6.6372	1.55435	112.884	0.964690
7.0707	1.53003	125.013	0.942030
7.5449	1.50461	137.202	0.918653
8.0709	1.47807	150.167	0.893062
8.5699	1.45435	163.092	0.867054
9.0266	1.43382	175.191	0.842082
9.4998	1.41365	187.799	0.815698
10.0076	1.393299	200.334	0.789183
10.5030	1.374588	213.211	0.761649
11.0124	1.356520	225.306	0.735572
12.0057	1.32428	237.8	0.708406
		250.465	0.680713
		261.576	0.656242
		273.111	0.630408
		291.570	0.589728
		300.599	0.569511

Exhibit (C.1) Sample calibration points for diode temperature sensors.

Table (C.2) Forward diode sensor voltage (in volts) at the specified temperature for a 10 μA current

sensor	room	LN_2	LHe
SNO-201	0.5839	1.02634	1.7148
SNO-207	0.588	1.027	1.7146
SNO-216	0.593	1.0278	1.7137
SNO-217	0.5885	1.0272	1.7126
SNO-229	0.588	1.0266	1.7130
SNO-230	0.5871	1.0274	1.7133
SNO-236	0.5844	1.0269	1.7132
SNO-238	0.586	1.0271	1.7138

Emerson Cummings. The sensor was grounded to the shell only by conduction through the leads. Each sensor was protected by a couple of layers of tape that did not actually touch the sensor but provided some shielding from the surroundings. Approximately five layers of aluminized mylar insulation were wrapped around the outer shell, enclosing the temperature sensors. As indicated in Fig. (C.1), two copper-constantan thermocouples were mounted on the outer shell, just in case the diode sensors failed. These sensors were not used.

Additional diode sensors were mounted inside the surge volume to measure the gas temperature and outside the surge volume to measure heat leaks. The exact locations and a discussion of these temperature measurements are given in Chapter 4.

C.1.3 Mass Flow Rate Measurement

A Datametrics model 800-LM flowmeter and a model 100-10K hotwire sensor were used to measure nitrogen flow at 1 atm and helium flow at 4 atm. Both measurements were made at room temperature. To make sure the measurements were made at room temperature, the gas was passed through a copper tube submerged in a room temperature pale of water. The meter was factory calibrated to measure the nitrogen flow. Calibration for the 4 atm helium flow was done at this lab using an

American AC-250-C Aluminumcast integrating flowmeter. The calibration curves are given in Table (C.1).

C.2 Compression System

A compression system was constructed to provide the 40 atm intake and 4 atm exhaust pressures. A schematic of the system is shown in Fig. (C.2) with an accompanying legend. The compressor used an Ingersoll-Rand, Type 30, Model 4R15X built in 1963. This is a 15 hp compressor with a flow capacity of 7 ℓ/s. Since the Ingersoll-Rand compressor has a much higher rated flow capacity than that required by the cryocooler experiment, the arrangement shown in Fig. (C.2) was necessary. The low-pressure storage tank has a volume of approximately 1000 ℓ, while two helium bottles provide approximately 110 ℓ for the high-pressure storage.

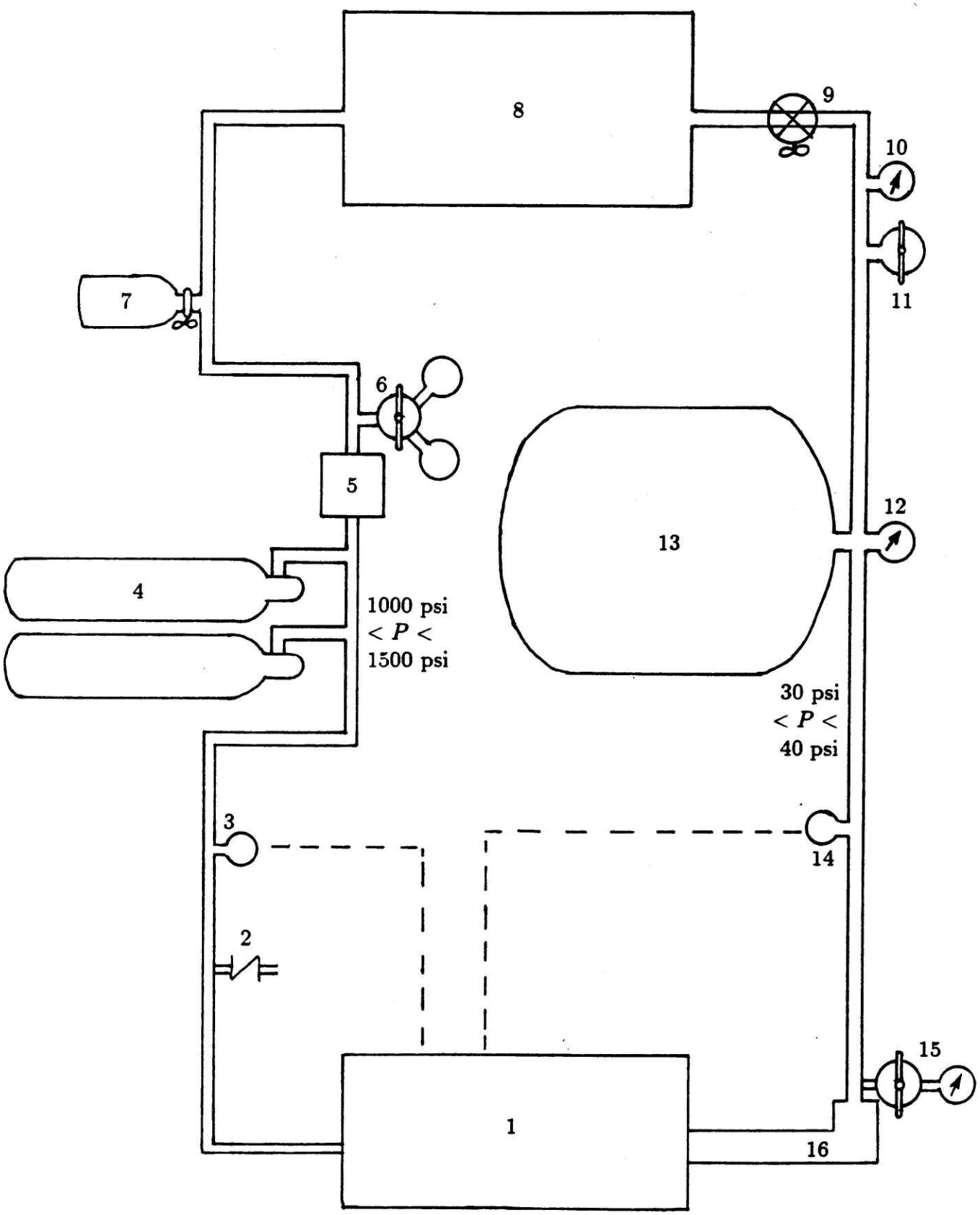

Fig. (C.2) Schematic of the compression system.

Legend for Fig. (C.2).

Item	Component
1	Ingersoll-Rand Air Compressor
2	High-pressure relief valve
3	Pressure transducer—output to controller
4	High-pressure helium tanks
5	LN_2 cooled charcoal filter
6	Matheson pressure regulator model #3
7	Surge volume tank
8	Cryocooler
9	Needle valve
10	Matheson pressure gage #63-3112
11	Conoflow back-pressure regulator #H30
12	Matheson pressure gage #63-3112
13	Low-pressure helium tank
14	Microswitch PVC 0100CA pressure transducer
15	Matheson line regulator #342
16	2.54 cm O.D. X 0.38 mm wall copper tube

REFERENCES

1. J.L. Smith, Jr., G.Y. Robinson, Jr., Y. Iwasa, "Survey of the state of the art of miniature cryocoolers for superconductive devices," Jan. 1984; U.S. Navy Contract N0001483K 0327.
2. R.B. Scott, *Cryogenic Engineering*, Van Nostrand, Princeton, 1959.
3. R.F. Barron, *Cryogenic Systems*, McGraw-Hill, NY, 1966.
4. Graham Walker, *Cryocoolers, Part 1 and Part 2*, Plenum Press, 1983.
5. W.H. Higa, E. Wiebe, "One million hours at 4.5 Kelvin," NBS Special Publications 508, p. 99, 1978.
6. B.A. Benedict, "Computer simulation of a cascade J-T refrigerator system using three fluids: helium, hydrogen, and nitrogen," Ball Aerospace Systems Division, P.O. Box 1062, Boulder, Colorado 80306.
7. C.K. Chan, "Dynamic design of gas sorption J-T refrigerator," Advances in Cryogenic Engineering, Vol. 31, p. 819, 1986.
8. H. Sixsmith, J. Valenzuela, W.L. Swift, "Small turbo-Brayton cryocoolers," Creare Inc., Hanover, New Hampshire.
9. C.G.B. Garret, *Magnetic Cooling*, Harvard University Press, John Wiley & Sons, Inc., 1954.
10. Tausczik, C.P., *Magnetically Active Regeneration*, MIT, Ph.D. thesis, 1986.
11. F.F. Chellis, "Design compromises in the selection of closed-cycle cryocoolers," NBS Special Publication 508, p109, 1978.
12. M.B. Simmonds, "Cryocoolers for use with superconducting instruments: some estimates of requirements," NBS Special Publication 508, p. 207, 1978.
13. R.H. Hubbell, W.M. Toscano, "Thermodynamic optimization of helium liquefaction cycles," Advances in Cryogenic Engineering, Vol. 25, p. 551, 1980.
14. F.W. Pirtle, P.A. Lessard, J.M. Kaufman, P.J. Kerney, "Thermodynamic aspects of small 4.2 K Cryocoolers," Advances in Cryogenic Engineering, Vol. 27, p. 595, 1982.
15. R.B. Fleming, "The effect of flow distribution in parallel channels of counter-

flow heat exchangers," Advances in Cryogenic Engineering, Vol. 12, p. 352, 1967.

16. R.B. von Rohr, J.L. Smith, Jr., "Criteria for scaling of heat exchangers to miniature size," MIT Cryogenic Engineering Laboratory, Rm. 41-204, Cambridge, Massachusetts 02139.

17. K. Chowdhury, S. Sarangi, "Effects of finite thermal conductivity of the separating wall on the performance of counterflow heat exchangers," Cryogenics, April, 1983, Vol. 23, Number 4.

18. W.C. Kratz, "The effect of temperature of impurity adsorption from hydrogen on activated carbon and silica gel," Advances in Cryogenic Engineering, Vol. 25, p. 597, 1980.

19. A.J. Kidnay, M.J. Hiza, P.F. Dickson, "The adsorption isotherms of methane, nitrogen, hydrogen and their mixtures on charcoal at 76 K," Advances in Cryogenic Engineering, Vol. 13, p. 397, 1968.

20. A.J. Kidnay, M.J. Hiza, "High pressure adsorption isotherms of neon, hydrogen, and helium at 76 K," Advances in Cryogenic Engineering, Vol. 12, p. 730, p. 730, 1967.

21. M.J. Hiza, A.J. Kidnay, "A comparison of the low-temperature adsorption of nitrogen and methane from hydrogen gas on three different adsorbents," Advances in Cryogenic Engineering, Vol. 8, p. 174, 1963.

22. Graham Walker, *Cryocoolers, Part 2: Applications*, pp. 119-120, Plenum Press, New York, 1983.

23. Ronald White, William Haskin, "Development approaches for long-life cryocoolers," NBS Special Publications 607, p. 21, May, 1981.

24. E.B. Qvale, J.L. Smith, Jr., "Mathematical model for steady operation of Stirling-type engines," Transactions of ASME, Journal of Engineering for Power, 90:A1, 1968.

25. P.A. Rios, E.B. Qvale, J.L. Smith, Jr., "An analysis of the Stirling cycle refrigerator," Advances in Cryogenic Engineering, Vol. 14, 1969.

26. E.B. Qvale, J.L. Smith, Jr., "An approximate thermal performance of a Stirling

engine generator," Transactions of ASME, Journal of Engineering for Power, 91:A2, 1969.

27. P.A. Rios, J.L. Smith, Jr., "An analytical and experimental evaluation of the pressure-drop losses in the Stirling-cycle," Transactions of ASME, Journal of Engineering and Power, 92:A2, 1970.

28. J.L. Smith, Jr., "Some aspects of the selection of regenerators," Cryogenics, 5:6, 1965.

29. S.N. Rea, J.L. Smith, Jr., "The influence of pressure cycling on thermal regenerators," Transactions of ASME, Journal of Engineering for Industry, 89:B3, 1967.

30. W.S. Harris, P.A. Rios, J.L. Smith, Jr., "The design of thermal regenerators for Stirling-type refrigerators," Advances in Cryogenic Engineering, Vol. 16, 1971.

31. J.W. Colangelo, E.E. Fitzpatrick, S.N. Rea, J.L. Smith, Jr., "An analysis of the performance of the pulse tube refrigerator," Advances in Cryogenic Engineering, Vol. 13, 1968.

32. J.L. Smith, Jr., "A metal bellows expansion engine," Advances in Cryogenic Engineering, Vol. 12, 1967.

33. M. Minta, *Analytical and Experimental Studies of an Optimal Helium Liquifaction Cycle*, Sc.D. thesis, MIT, 1984.

34. M. Minta, J.L. Smith, Jr., "Helium liquifier cycles with saturated vapor compression," Advances in Cryogenic Engineering, Vol. 27, p. 603, 1982.

35. M. Minta, J.L. Smith, Jr., "An entropy flow optimization technique for helium liquefaction cycles," Advances in Cryogenic Engineering, Vol. 29, 1984.

36. M. Minta, J.L. Smith, Jr., "An optimum cold end configuration for helium liquefaction cycles," Advances in Cryogenic Engineering, Vol.29, p479, 1984.

37. M. Minta, *Study of Helium Liquefaction Cycles at Elevated Pressures*, MSME thesis, MIT, 1981.

38. P. Horowitz, W. Hill, *The Art of Electronics*, Cambridge University Press, Cambridge, 1980.

39. W.M. Rohsenow, H. Choi, *Heat, Mass, and Momentum Transfer*, Prentice-Hall, Inc., Englewood Cliffs, New Jersey, 1961.

40. P.A. Rios, "An approximate solution to the shuttle heat-transfer losses in a reciprocating machine," Journal of Engineering for Power, p. 177, April 1971.

41. F.J. Zimmerman, R.C. Longsworth, "Shuttle heat transfer," Advances in Cryogenic Engineering, Vol. 16, p. 342, 1971.

42. S.N. Rea, *A Study of Thermal Regenerators Subjected to Rapid Pressure and Flow Cycling*, Ph.D. thesis, MIT, 1966.

43. E.B. Qvale, *An Analytical Model of Stirling-Type Engines*, Ph.D. thesis, MIT, 1967.

BIOGRAPHICAL NOTE

Buren Crunkleton always advised his son, Alan, to focus his efforts on school, but in high school, Alan's education took a back seat to his passion for racing motorcycles. Alan was probably the only MIT PhD who skipped out of the SAT midway through the exam in order to enter a Saturday afternoon motocross race.

It wasn't until his senior year in high school that Alan took an interest in developing his aptitude in mathematics, guided by the enthusiasm of his math teacher, Mrs. Hayes.

He attended the Georgia Institute of Technology, as did many of his classmates from Toccoa, Georgia. It was at Georgia Tech that Alan became interested in MIT. During his sophomore year, he set his goal: to graduate from MIT with a PhD in Mechanical Engineering. In the year between college and graduate school, Alan worked as a consultant at the Georgia Tech Engineering Experiment Station, doing energy audits for medium sized companies which had energy intensive operations. He enrolled at MIT in the fall of 1982.